Determining the best apparent resistivity versus frequency definition for a magnetotelluric sounding : a comparison between two statistical techniques

By

JANINE COLE

Submitted in partial fulfilment of the requirements for the degree of

MAGISTER SCIENTIAE

in the Faculty of Science
University of Pretoria

PRETORIA

2001

ABSTRACT

Various different statistical reduction techniques were used to determine the best curves that would fit through apparent resistivity and impedance phase versus frequency data. The major problem in processing magnetotelluric data is the presence of manmade electromagnetic noise. This noise causes outliers to appear on the data and as a result does not always have a Gaussian distribution. Most of the conventional reduction techniques like those based on the L_1- and L_2 -norm assume that the noise in the data is normally distributed. To address this problem two additional techniques were applied to the data, namely the robust M-estimation technique, and the L_p norm technique. The robust M-estimation technique minimises a loss function with a known distribution. Different weights are applied to the impedance data depending on the position in the error distribution. The adaptive L_p norm technique uses the real distribution of the data to determine the value of p used in the reduction.

These methods were first tested on synthetic data and then applied to real data collected in the Northern Cape Province of South Africa. The synthetic tests showed the L_1 – norm and L_p – norm to provide good results. It also became clear that the adaptive L_p-norm method is more susceptible to the starting impedance values than the robust M-estimation technique. When applied to real magnetotelluric data, very similar results were obtained from all the techniques when the data quality was relatively good. For bad quality data, the robust M-estimation method gave the best results. It is clear that the effectiveness of the statistical techniques is dependent on the quality of the data.

CONTENTS **PAGE**

LIST OF FIGURES

LIST OF TABLES

GLOSSARY OF SYMBOLS

Symbol	Description	mks units
B	Magnetic induction	T
H	Magnetic intensity	A/m
D	Electric displacement	C/m^2
E	Electric field	V/m
J	Current density	A/m^2
q	Charge	C
t	Time	s
f	Frequency	hz
ε_0	Electric permittivity of free space	F/m
P	Polarisation	C/m^2
Φ	Magnetic flux	Wb
ξ	Electromotive force	V
σ	Conductivity	mho/m
μ_0	Magnetic permeability of free space	H/m
ω	Angular frequency	rad/s
δ	Skindepth	m
$\mathbf{Z}_{ij}$	Impedance	ohm
ρ_{ij}	Apparent resistivity	ohm.m
ϕ_{ij}	Phase	degree

CHAPTER 1
OVERVIEW

1.1. INTRODUCTION

The magnetotelluric method provides the geophysicist with a frequency domain electromagnetic tool that is not hampered by the presence of conductive overburden or sampling frequencies that do not allow for deep penetration. Variations in the earth's natural magnetic field supply frequencies ranging from nearly DC to several kilohertz, thus giving one the ability to study the electric substructure of the earth to great depths. The final results of magnetotelluric soundings are log-log plots showing apparent resistivity as a function of depth calculated from large amounts of data collected during a sounding. One of the main problems affecting the quality of the results is the presence of artificial electromagnetic sources that are too close to satisfy the assumption that the electromagnetic energy consists of plane waves. Statistical reductions of the data aim to minimise the effect of this 'noise'. Unfortunately, most of the basic minimisation techniques assume noise with a Gaussian distribution. In reality this is not the case and this leads to poor quality results. The aim of this study is to compare two statistical minimisation techniques that try to take the actual distribution of the noise into consideration.

1.2. SUMMARY OF CONTENTS

Chapter 2 gives a brief description of various sources of natural electromagnetic energy. It is important to be aware of the different sources since this will indicate the optimal time to do magnetotelluric soundings. The distance of the sources means that the electromagnetic energy is in the form of plane waves. This is one of the fundamental assumptions made in the deduction of the magnetotelluric theory. Chapter 3 starts with this assumption and uses Maxwell's equations to derive wave equations that describe the propagation of plane electromagnetic waves through the earth. By applying the wave equations to various geological models, it is possible to arrive at the equations describing the relation between the electric and magnetic fields measured at a sounding

station. These fields are related via the impedance tensor and it is the noise in this tensor that needs to be minimised.

Data acquisitioning and basic processing techniques are described in Chapter 4. One of the final results in this chapter shows the relation between apparent resistivity and impedance.

Chapter 5 contains a discussion on various statistical methods used to minimise the effect of noise in data. It starts out with the L_1- and L_2 norms that make the assumption of normally distributed noise. Two methods that address this problem are the Robust M-estimation and adaptive L_p norm techniques. The robust M-estimation method uses a weight function to ignore outliers in the data. This effectively causes the actual distribution to approach a normal distribution. With the adaptive L_p norm technique the actual distribution of the noise is used to determine the value of p that will be used to minimise the error. These methods are applied to synthetic data with both normal and non-normal error distributions and the results are compared.

Statistical reduction methods discussed in Chapter 5 are applied to real data in Chapter 6. Data for the case study were collected between Sishen and Keimoes along a traverse that crosses a number of tectonic boundaries. The final model calculated is compared to a deep reflection seismic line that ran along the same traverse. Chapter 7 discusses the final results obtained with the various statistical techniques.

CHAPTER 2

NATURAL SOURCES OF ELECTROMAGNETIC ENERGY

2.1. GENERAL

Cagnaird (1953) based the theory of the magnetotelluric method on two important assumptions:

- The source is a natural electromagnetic plane wave propagating vertically downward into the Earth and
- The Earth has a one dimensional electrical substructure.

The naturally occurring electromagnetic plane wave originates from a variety of sources and may comprise a wide range of frequencies, depending on the origin. The higher frequency component mainly emanates from meteorological activities such as lightning. Variations in the Earth's magnetic field linked to solar activity are responsible for a low frequency field.

2.2. SOURCES RELATED TO SOLAR ACTIVITIES

It is well known that the geomagnetic field is composed of three parts - the main field that originates from an internal source, the external field originating outside the earth and local variations in the main field caused by magnetic material in the earth's crust (Telford et al., 1976). The variable nature of the external field is of particular interest to us since it induces currents in the ionosphere which act as sources of natural electromagnetic energy

Pulkkinen and Baker (1997) describe geomagnetic activity as 'the general term used to define variations in the Earth's surface magnetic field caused by sources external to the Earth.' They point out that these variations are caused by fluctuations in current systems within the ionosphere and magnetosphere controlled by the variable nature of the solar wind, the interplanetary magnetic field (IMF) or the geometrical relation of the sun and earth.

2.1.1. Solar wind

The close relationship between geomagnetic variations and solar activity warrants a quick look at the basic morphology of the sun. Frazier (1985) describes the sun as 'a series of concentric layers that interact continuously.' Figure 2.1 shows a schematic diagram depicting these concentric layers.

In the solar core at extreme temperatures of 15 000 000°C and pressure 200 billion times the pressure at the earth's surface, hydrogen atoms are fused together to form helium, releasing massive amounts of energy during this process. As the energy passes through the radiation zone, decreases in temperature and pressure and a change in wavelength transform the gamma rays into X-rays and from there into ultraviolet and visible light. The convection zone consists of a cooler, more opaque gas and here the energy is moved upward by convection cells into the photosphere. The energy finally reaches the photosphere from where it is emitted into space. Solar gases are confined by magnetic loops form the sun's atmosphere or corona. Holes in the corona allow the constant movement of gas particles into space thus forming what is known as the solar wind.

The particles emitted by the sun consist mainly of ionized hydrogen that forms a plasma of protons and electrons (Kaufman and Keller, 1981). Experiments with the Lunik space probes four decades ago revealed a flux of positive ions of approximately 2×10^8 particles cm^{-2} sec^{-1} beyond a distance of 39 earth radii (R_E) (Snyder *et al.*, 1963). During the end of 1962 and into the beginning of 1963 the space probe Mariner measured the velocity of the interplanetary plasma for the first time directly and determined an average velocity of 504 km/s during the experiment (Snyder et al., 1963).

2.1.2. Relation between solar wind and geomagnetic activity

The geomagnetic field presents a barrier to the solar wind stopping it at roughly 10 R_E and deflecting it away from and around the earth (Moore and Delcourt, 1995). The protons and electrons are often deflected in opposite

directions causing a magnetic field that cancels the earth's magnetic field where it occurs. The boundary thus formed is known as the magnetopause (Kaufman and Keller, 1981). In the process the solar wind modifies the shape of the geomagnetic field compressing it on the daylight side and causing it to be extended on the opposite side (figure 2.2).

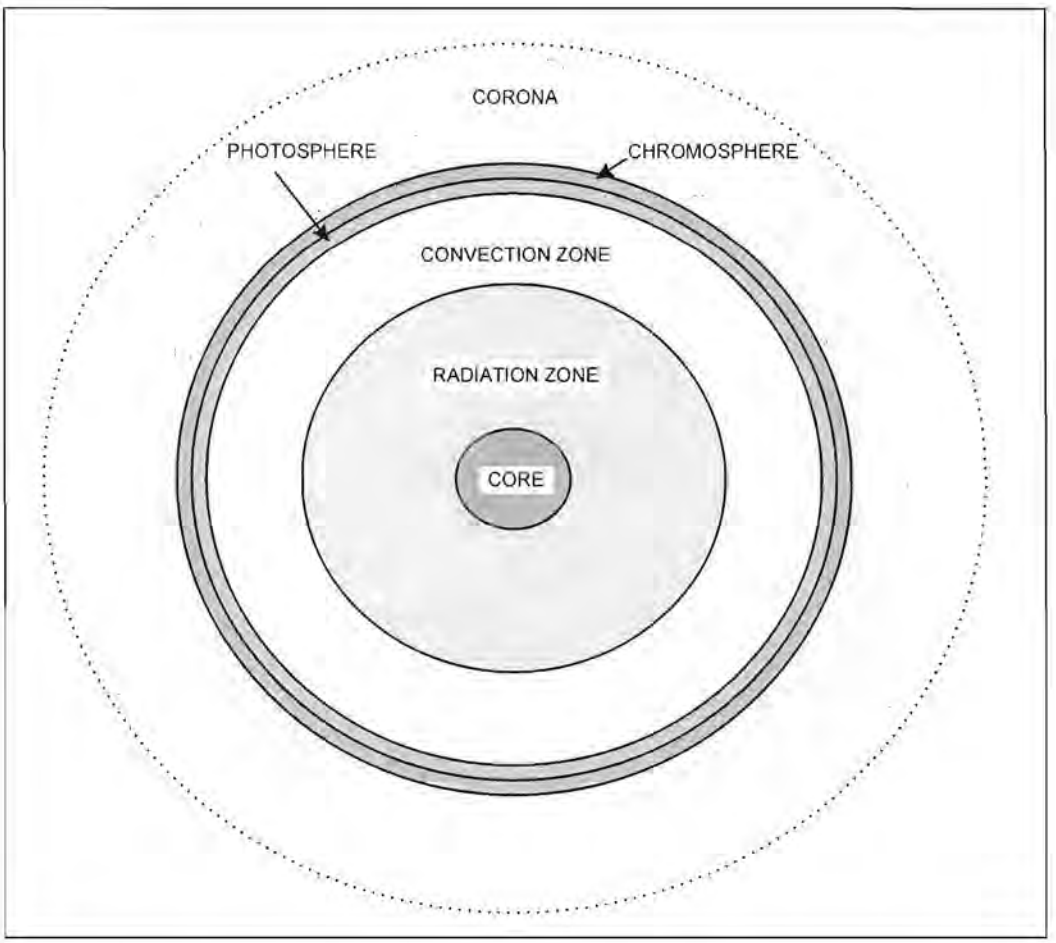

Figure 2.1. Simplified diagram depicting the morphology of the sun (adapted from Frazier, 1985).

The variable nature of the solar wind's strength and velocity cause the magnetopause to fluctuate. The size of the magnetosphere changes and new ionospheric currents form (Pulkkinen and Baker, 1997). When the solar wind is strongly enhanced, stronger magnetic effects known as magnetic storms occur.

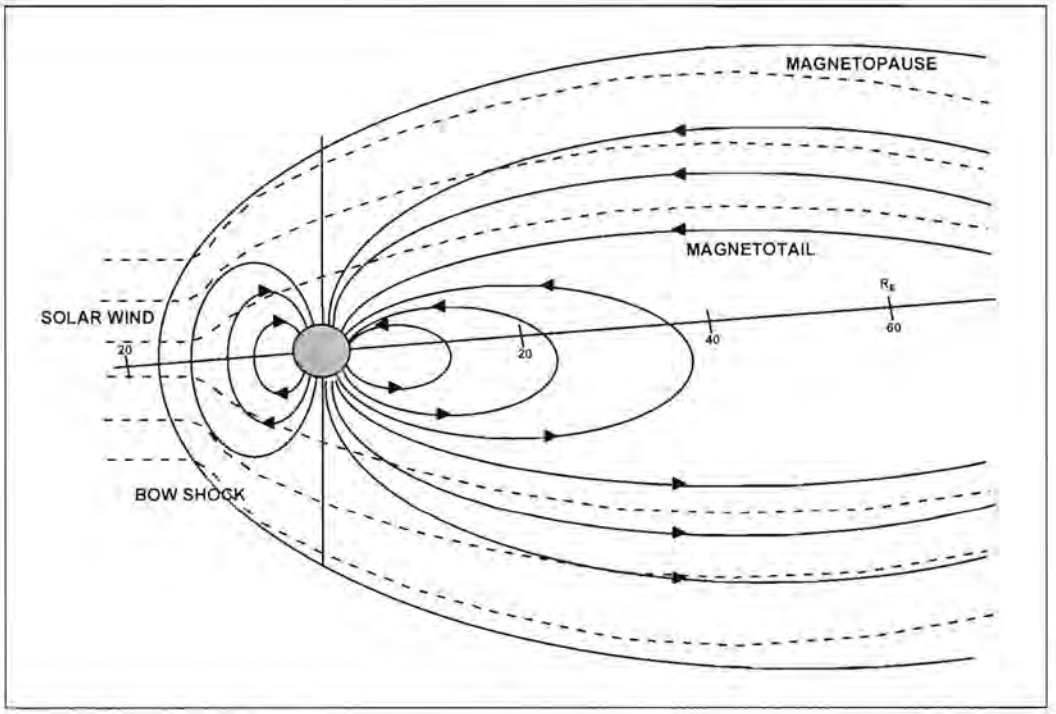

Figure 2.2. The Earth's magnetosphere (Moore, 1994).

2.1.3. Magnetic storms

Sunspots, areas of intense magnetic activity on the surface of the sun, release energy in the form of solar flares and other eruptions. Already in the previous century scientists observed that sunspots waxed and waned in cycles of nearly 11 years. These cycles correlate directly to times of increasing and decreasing geomagnetic activity. This and the fact that increased geomagnetic activity occurs at roughly 27 day intervals (period of the sun's rotation) led to the assumption that solar flares serve as the main instigators of large geomagnetic storms.

Solar flares were held responsible for solar energetic particle (SEP) events even when no flares were visible on the solar disk. These events were believed to result from flares on the back side of the sun. Several models were derived to explain the relatively long duration of most of these events compared with the short lifetime of a flare. One explanation for this

phenomenon was that the solar magnetic field extended through interplanetary space in the form of 'magnetic tubes.' Particles emitted by flares diffused through the solar atmosphere until they reached the tube of force that extended out to the earth at that time, slowly filling it and increasing the flux of particles measured on earth (figure 2.3). Rapid discharge of particles from the tube resulted in magnetic storms (Reid, 1964).

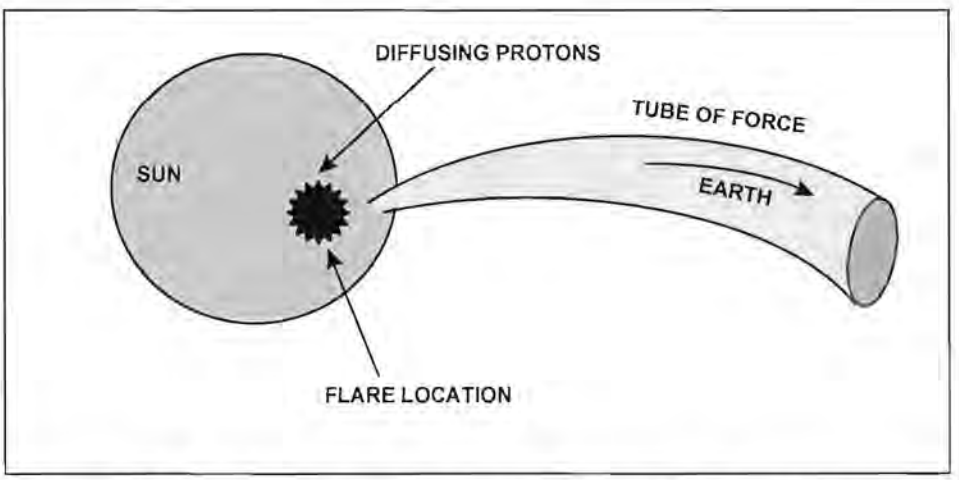

Figure 2.3. Reid's diffusive model for the initial phase of a solar proton event (Reid, 1964).

However, in recent years coronal mass ejections (CMEs) have gained prominence as presenting the crucial link between solar activity and transient interplanetary disturbances that cause large geomagnetic storms (Gosling et al., 1990). During coronal mass ejection events 10^{15} - 10^{16} gms of solar material are suddenly propelled outward into space at speeds ranging from less than 50 km/s to greater than 1200 km/s (Gosling et al., 1991). CMEs are not always observed in association with solar flares but when they are temporally related, CMEs usually begin to lift of from the sun before any substantial flaring activity has occurred (Gosling, 1993).

When CMEs have outward speeds exceeding that of the ambient solar wind a shock forms in front of the ejection and the slower moving plasma ahead is accelerated and deflected from its path (Sheeley et al., 1985). Gosling et al. (1990) show that a strong relation exists between these shock

disturbances, CMEs and large geomagnetic storms. Still, it is important to note that not all CMEs and shock disturbances cause geomagnetic storms. A prerequisite for the formation of major magnetic storms seems to be the presence of an intense, long-duration, southward-directed, interplanetary magnetic field (B_z) within the CME or shock (Tsurutani and Gonzalez, 1992; Lundstedt, 1996; Pulkinnen and Baker, 1997). The strong B_z may be a result of either compression of the ambient interplanetary magnetic field (IMF) by the shock, or of draping of the IMF about the fast CME or a combination of compression and draping (Gosling and McComas, 1987).

2.1.4. Geomagnetic activity as source for MT soundings

Variations in the geomagnetic field induce currents to flow in the ionized layers of the earth's atmosphere (at 80-160 km altitude). These currents in the ionosphere lead to a displacement of mass and together the magnetic and inertial forces give rise to magnetohydrodynamic waves (Kaufman and Keller, 1981). By the time the magnetic effects reach the earth's surface they are strongly modified and classified as micropulsations. These are divided into continuous (Pc) and irregular (Pi) pulsations. They in turn induce currents in conductive layers within the earth. Table 2.1 summarises further subdivisions of the two classes as discussed by Kaufman and Keller (1981).

2.3. SOURCES RELATED TO THUNDERSTORM ACTIVITY

Transient electromagnetic fields (also called atmospherics or sferics) associated with lightning provide the main natural energy at frequencies ranging from 3 Hz to 30 kHz. The electromagnetic field generated by a lightning stroke, shows high energy density at high frequencies when observed relatively nearby. As the energy propagates to greater distances through wave guide propagation, some lower frequencies are enhanced while the higher frequencies are attenuated (Kaufman and Keller, 1981). The measured field is a superposition of individual sferics originating from thunderstorms around the world (Zhang and Paulson, 1997).

Table 2.1. Summary of micropulsation's characteristics.

Classification			Appearance	Time of occurrence	Cause
Pc		Pc-1	Discrete signal with gradually increasing frequency (pearls)	Middle and low latitudes: nights and mornings High latitudes: noon and afternoon	Kinetic instabilities in magnetospheric plasma
		Pc-2	Two maxima on amplitude spectrum	Midday	Disturbance in geomagnetic field
		Pc-3	Two maxima on amplitude spectrum	Midday	Oscillations produced outside magnetosphere
		Pc-4	Two maxima on amplitude spectrum	Mid latitudes: middays High latitudes: night	Generated during onset of magnetic storms
		Pc-5	One maximum on amplitude spectrum	High latitudes: mornings and evenings	Interaction of solar wind with magnetopause
		Pc-6			
Pi	**Pi-1**	PiB	Groups of irregular variations with periods less than 15s	Occur with explosive phase of substorm (22:00-05:00)	Transverse vibration of magnetosphere boundary
		PiC	Irregular variations with dominant period of 5 to 10s	Occur in both explosive and quasi-stable phase of substorm	
		IPDP	Decrease in period during course of occurrence	16:00-01:00	Excited in auroral zone
	Pi-2		Decaying sequence of	Associated with	Related to force lines of

			oscillations with periods of 60-100s and duration of 5-10min	explosive phase of substorm	geomagnetic field along which auroral activity proceeds
	Pi-3		Periods>150s	Night time	Development of Kelvin-Helmholtz instability at boundary of magnetosphere

CHAPTER 3

BASIC THEORY OF THE MAGNETOTELLURIC METHOD

3.1 INTRODUCTION

Cagnaird and Tikhonov developed the theory underlying the magnetotelluric method independent of each other in the 1950's (Tikhonov, 1950; Cagnaird, 1953). They both observed that the electric and magnetic fields associated with telluric currents that flow in the Earth as a result of variations in the Earth's natural electromagnetic field, should relate to each other in a certain way depending on the electrical characteristics of the Earth. Since then tremendous advances have been made in the understanding, processing and interpretation of the data. However, the fundamental principles and assumptions have remained unchanged. This chapter presents the principles that form the basis of the magnetotelluric method.

3.2 MAXWELL'S EQUATIONS

The magnetotelluric method is a frequency domain electromagnetic technique. As with all electromagnetic methods the fundamental principles underlying the technique are summarised in Maxwell's equations given in differential form in equations (3.1) to (3.4) (Reitz et al. 1979).

$$\nabla \cdot \mathbf{B} = 0 \qquad \text{-------- (3.1)}$$

$$\nabla \cdot \mathbf{D} = q \qquad \text{-------- (3.2)}$$

$$\nabla \times \mathbf{E} = -\frac{\partial \mathbf{B}}{\partial t} \qquad \text{-------- (3.3)}$$

$$\nabla \times \mathbf{H} = \mathbf{J} + \frac{\partial \mathbf{D}}{\partial t} \qquad \text{-------- (3.4)}$$

The symbols are declared in the glossary.

It is important to have a clear understanding of these equations and therefore they will be discussed separately in more detail.

3.2.1. $\nabla \cdot \mathbf{B} = 0$

The divergence of a vector (**X**) is the limit of its surface integral per unit volume as the volume (V) enclosed by the surface goes to zero (Reitz, et al., 1979).

$$\nabla \cdot \mathbf{X} = \lim_{V \to 0} \frac{1}{V} \oint_S \mathbf{X} \cdot \mathbf{n} \, da \qquad \text{------- (3.5)}$$

In other words it describes the net flow through a surface enclosing the source of the flow. If $\nabla \cdot \mathbf{X} > 0$, there is a net outflow from the position of **X**. If $\nabla \cdot \mathbf{X} < 0$, there is a net inflow to the position of **X**. If $\nabla \cdot \mathbf{X} = 0$, there is no net inflow or outflow.

Therefore, $\nabla \cdot \mathbf{B} = 0$ indicates that for a closed surface surrounding the source of a magnetic field, the net result of the inflow and outflow per unit volume is zero as the volume goes to zero. This implies that the magnetic source has a negative and positive pole and that isolated magnetic poles do not exist. Figure 3.1 illustrates this point.

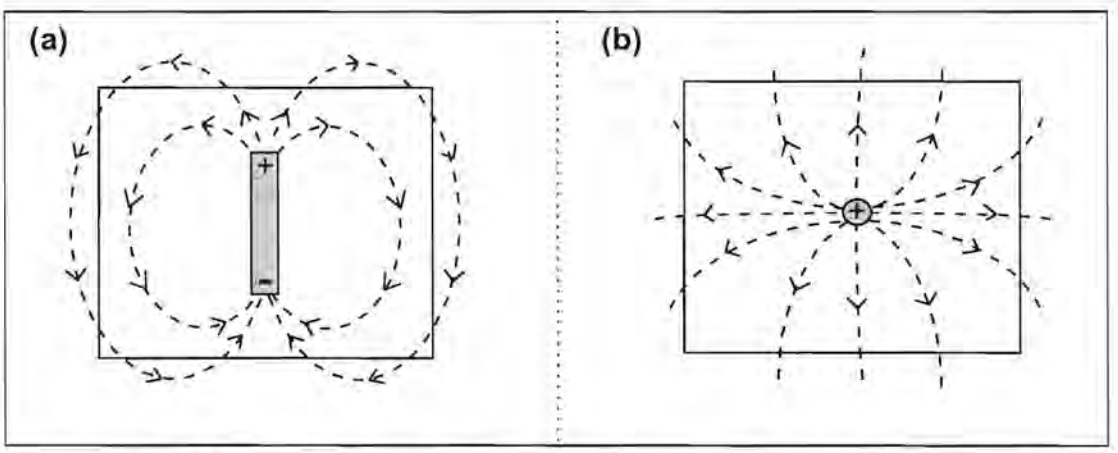

Figure 3.1 Maxwell's equation $\nabla \cdot \mathbf{B} = 0$ implies that the situation depicted in (a) prevails and that single magnetic poles as denoted in (b) cannot occur.

3.2.2. $\nabla \cdot \mathbf{D} = q$ (Gauss' law)

The electric flux across a closed surface is proportional to the net electric charge (q) enclosed by the surface.

$$\mathbf{D} = \varepsilon_0 \mathbf{E} + \mathbf{P} \qquad \text{------- (3.6)}$$

The electric displacement (**D**) includes the charge embedded in the dielectric medium ($\varepsilon_0\mathbf{E}$) as well as the polarisation charge (**P**). Reitz et al. (1979) defines polarisation as follows:

> *A small volume element of a dielectric medium which is electrically neutral has been polarised if a separation of the positive and negative charge has been effected. The volume element is then characterised by an electric dipole moment $\Delta\mathbf{p}$ that determines the electric field produced by the small volume Δv at distant points. **P** is the electric dipole moment per unit volume.*

3.2.3. $\nabla \times \mathbf{E} = -\frac{\partial \mathbf{B}}{\partial t}$ (Faraday's law)

Through experimentation it was found that an electromotive force (ξ) is associated with a change in magnetic flux (Φ) through a circuit.

$$\xi = -\frac{d\Phi}{dt} \qquad \text{------- (3.7)}$$

The EMF is independent of the way in which the flux changes. The minus sign indicates that the direction of the induced EMF is such as to oppose the change that produces it.

Define the EMF around an electric circuit as

$$\xi = \oint_c \mathbf{E} \cdot d\mathbf{l} \qquad \text{------- (3.8)}$$

and the magnetic flux as

$$\Phi = \int_S \mathbf{B} \cdot \mathbf{n}\, da \qquad \text{------- (3.9)}$$

where da is an infinitesimal area and **n** is the unit vector perpendicular to da. Equation (3.9) therefore gives the integral of the normal component of the magnetic field over a surface S.

Substituting (3.8) and (3.9) into (3.7) yield

$$\oint_c \mathbf{E}\cdot d\mathbf{l} = -\frac{d}{dt}\int_s \mathbf{B}\cdot\mathbf{n}\,da \qquad \text{------- (3.10)}$$

Stokes' theorem states that the line integral of a vector around a closed curve is equal to the integral of the normal component of its curl over any surface bounded by the curve ($\oint_c \mathbf{F}.d\mathbf{l} = \int_s \nabla\times\mathbf{F}\cdot\mathbf{n}\,da$). Therefore equation (3.10) can be written as

$$\int_s \nabla\times\mathbf{E}\cdot\mathbf{n}\,da = -\frac{d}{dt}\int_s \mathbf{B}\cdot\mathbf{n}\,da \qquad \text{------- (3.11)}$$

$$\int_s \nabla\times\mathbf{E}\cdot\mathbf{n}\,da = -\int_s \frac{\partial\mathbf{B}}{\partial t}\cdot\mathbf{n}\,da \qquad \text{------- (3.12)}$$

This holds true for all fixed surfaces, therefore

$$\nabla\times\mathbf{E} = -\frac{\partial\mathbf{B}}{\partial t} \qquad \text{------- (3.13)}$$

3.2.4. $\nabla\times\mathbf{H} = \mathbf{J} + \frac{\partial\mathbf{D}}{\partial t}$ (Ampere's law)

This law describes the magnetic field due to a current distribution. **J** is the transport current density that consists of the motion of free electrons or charged ions. The electric displacement **D** was defined in equation (3.6). $\frac{\partial\mathbf{D}}{\partial t}$ gives the variation of the electric displacement with time and is called the displacement current.

It is worthwhile to discuss the definition of the 'curl' and examine this in order to gain a better understanding of Ampere's and Faraday's laws. Reitz et al. (1979) define the curl of a vector as the limit of the ratio of the integral of the vector's cross product with the outward drawn normal over

a closed surface, to the volume enclosed by the surface as the volume goes to zero.

$$\nabla \times \mathbf{F} = \lim_{V \to 0} \frac{1}{V} \oint_S \mathbf{n} \times \mathbf{F} \, da \qquad \text{------- (3.14)}$$

The cross product of two vectors is the product of the magnitudes times the sine of the smallest angle between the two vectors, with the direction of the resultant vector perpendicular to the two vectors according to the right hand screw rule. The curl of a vector can therefore be interpreted as the tendency of a vector to rotate around an axis perpendicular to the vector and the normal (Ellis and Gulick, 1986). Figure 3.2 serves to illustrate this point.

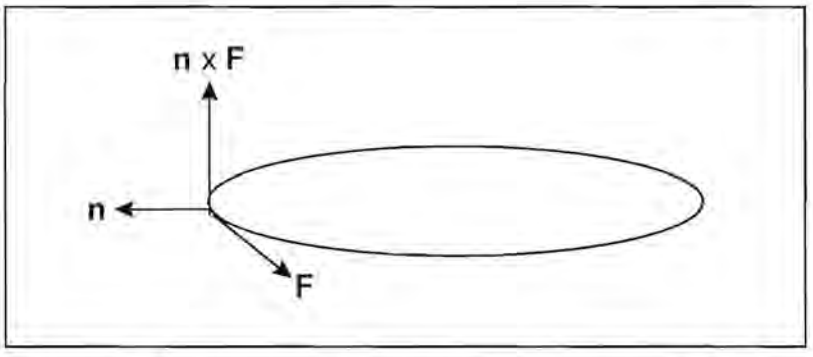

Figure 3.2. The curl of a vector (integration of **n** X **F** over the total closed surface divided by the enclosed volume V as V goes to zero)

3.3. WAVE EQUATIONS

A wave equation describes the wave propagation in a linear medium. To derive the wave equation for the magnetic field, one considers the curl of equation (3.4) (Reitz et al., 1979).

$$\nabla \times \nabla \times \mathbf{H} = \nabla \times \mathbf{J} + \nabla \times \frac{\partial \mathbf{D}}{\partial t} \qquad \text{------- (3.15)}$$

let $\mathbf{D} = \varepsilon \mathbf{E}$, $\mathbf{J} = \sigma \mathbf{E}$ and $\mathbf{B} = \mu_0 \mathbf{H}$ and use (3.3), then

$$\nabla \times \nabla \times \mathbf{H} = \sigma(\nabla \times \mathbf{E}) + \varepsilon \frac{\partial}{\partial t}(\nabla \times \mathbf{E})$$
$$= -\sigma\mu_0 \frac{\partial \mathbf{H}}{\partial t} - \varepsilon\mu_0 \frac{\partial^2 \mathbf{H}}{\partial t^2}$$

Using the identity $\nabla \times \nabla \times \mathbf{X} = \nabla\nabla \cdot \mathbf{X} - \nabla^2 \mathbf{X}$ and (3.1) lead to the wave equation for the magnetic field

$$\nabla^2 \mathbf{H} - \sigma\mu_0 \frac{\partial \mathbf{H}}{\partial t} - \varepsilon\mu_0 \frac{\partial^2 \mathbf{H}}{\partial t^2} = 0 \qquad \text{------- (3.16)}$$

The wave equation for the electric field can be derived similarly by taking the curl of (3.3). In a charge free medium where $\nabla \cdot \mathbf{D} = 0$ this results in

$$\nabla^2 \mathbf{E} - \sigma\mu_0 \frac{\partial \mathbf{E}}{\partial t} - \varepsilon\mu_0 \frac{\partial^2 \mathbf{E}}{\partial t^2} = 0 \qquad \text{------- (3.17)}$$

Equations (3.16) and (3.17) describe the electromagnetic field in a homogeneous, linear medium with no free charge density.

3.4. APPLICATION OF WAVE EQUATIONS IN THE MAGNETOTELLURIC METHOD

In the development of the theory for the magnetotelluric method, we make the following assumptions (Kaufman and Keller, 1981):

- The Earth consists of N horizontal layers, each with resistivity ρ_n and thickness h_n (Figure 3.3).
- A horizontal current sheet located above the surface of the Earth acts as a source for an electromagnetic field that depends only on the vertical (z) coordinate and the distribution of resistivities.

- The horizontal current sheet (j_x) in the source plane induces a uniform primary magnetic field (H_{0y}) that does not vary with z (z is positive downwards).

Temporal fluctuations of the primary magnetic field generate the primary horizontal electric field (E_{0x}). Variations in the primary electric field cause currents to flow in conductive layers in the Earth which in turn serve as source for the secondary electromagnetic field. Since we assume that the Earth consists of homogeneous layers, the current density does not change over the horizontal planes and the secondary electromagnetic field also consists of an electric field in the x-direction and a magnetic field in the y-direction.

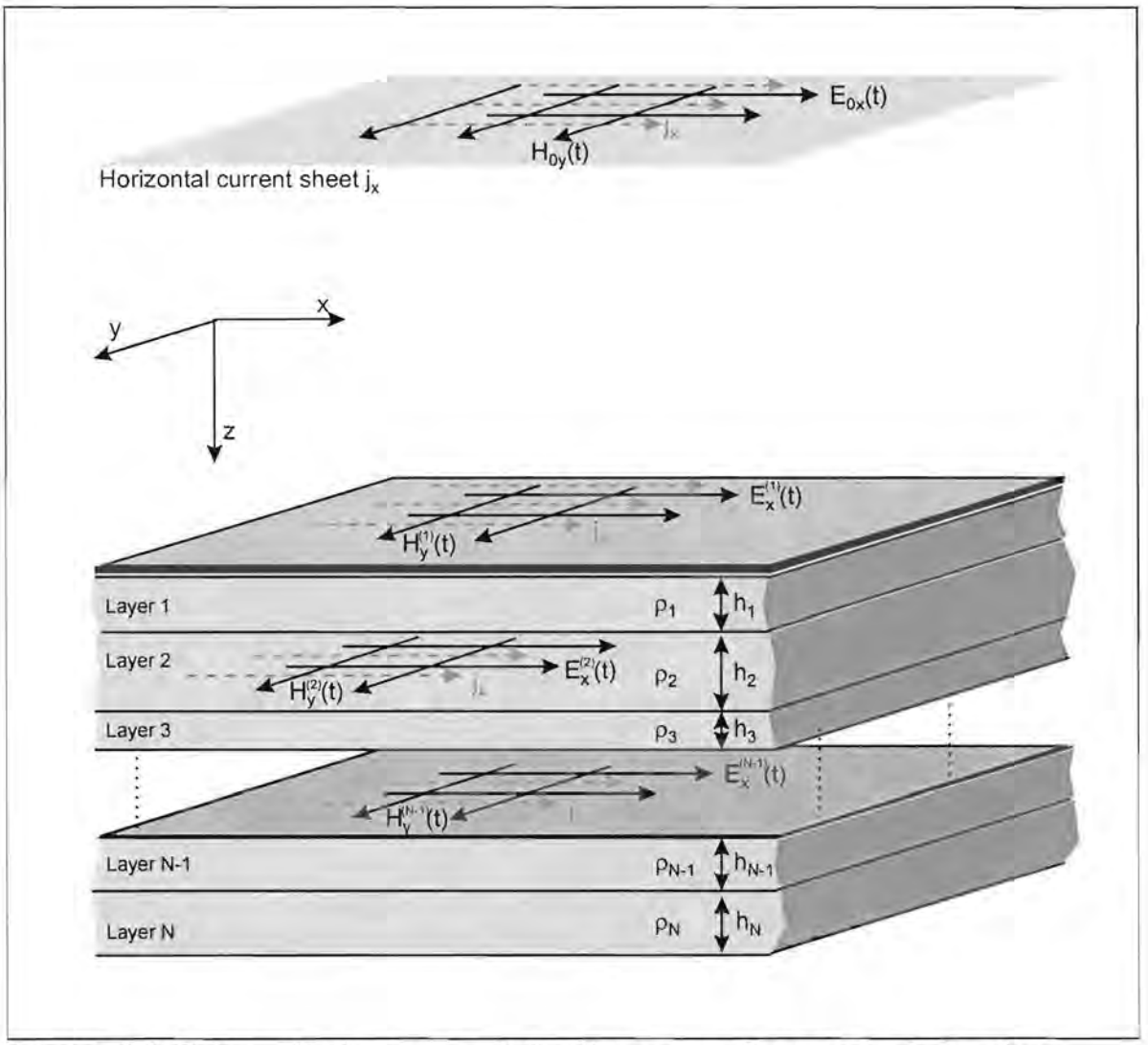

Figure 3.3 Schematic diagram depicting the assumptions made during the development of the MT theory

The total electromagnetic field is time dependant. Assume that the electric and magnetic components can be written as

$$\mathbf{E}(\mathbf{r},t) = E_x e^{-i\omega t} \qquad \text{------- (3.18)}$$

$$\mathbf{H}(\mathbf{r},t) = H_y e^{-i\omega t} \qquad \text{------- (3.19)}$$

In the above equations the time dependency $e^{-i\omega t}=\cos\omega t - i\sin\omega t$ implies an assumption that the fields are continuous harmonic oscillators.

Substitute (3.18) into (3.17) and remember that the electric field varies only in the z-direction. The wave equation for the electric field induced under the assumptions made at the beginning of the section therefore is

$$e^{-i\omega t}\left(\frac{\partial^2 E_x}{\partial z^2} + i\omega\mu\sigma E_x + \omega\mu D_x\right) = 0 \qquad \text{------- (3.20)}$$

According to Kaufman and Keller (1981) the displacement current can be neglected in the MT method. Equation (3.20) then becomes

$$e^{-i\omega t}\left(\frac{\partial^2 E_x}{\partial z^2} + i\omega\mu\sigma E_x\right) = 0 \qquad \text{------- (3.21)}$$

In order to satisfy (3.21) the electric field must have the following form in each layer (n)

$$E_x^{(n)} = e^{-iwt}\left(A_n e^{ik_n z} + B_n e^{-ik_n z}\right) \qquad \text{------- (3.22)}$$

where

$$k = \sqrt{i\omega\mu\sigma} \qquad \text{------- (3.23)}$$

is the wavenumber. Skindepth (δ) and wavenumber are related as follows

$$k = \frac{1+i}{\delta} \qquad \text{------- (3.24)}$$

Use (3.13) and (3.22) to determine the form of the magnetic field in each layer

$$H_y^{(n)} = e^{-iwt}\frac{k_n}{\omega\mu}\left(A_n e^{ik_n z} - B_n e^{-ik_n z}\right) \qquad \text{-------} (3.25)$$

In (3.22) and (3.25) we assume that the tangential components of the electric and magnetic fields are continuous when passing through the interface between two layers. It is now possible to examine the behaviour of the electric and magnetic fields in different geological scenarios.

3.4.1. Uniform half-space

In a uniform half-space the electromagnetic energy must decrease with increasing depth since energy is transformed into heat. Since

$$e^{ikz} = e^{\frac{iz}{\delta}} e^{\frac{-z}{\delta}} \qquad \text{-------} (3.26)$$

and

$$e^{-ikz} = e^{\frac{-iz}{\delta}} e^{\frac{z}{\delta}} \qquad \text{-------} (3.27)$$

it is clear that in both (3.22) and (3.25) the first term between brackets represents the part of the field that decreases with increasing depth and the second term that part of the field that increases with increasing depth. For a uniform half-space, with the assumption that the field should approach 0 as z becomes very large, the electric and magnetic fields therefore reduce to

$$E_x = e^{-iwt}\left(Ae^{ikz}\right) \qquad \text{-------} (3.28)$$

and

$$H_y = e^{-iwt}\frac{k}{\omega\mu}\left(Ae^{ikz}\right) \qquad \text{-------} (3.29)$$

At the surface of the earth where z=0, (3.28) and (3.29) reduce to

$$E_x(0) = e^{-iwt}A \qquad \text{-------} (3.30)$$

and

$$H_y(0) = e^{-iwt}\frac{k}{\omega\mu}A = E_x(0)\frac{k}{\omega\mu} \qquad \text{------- (3.31)}$$

The ratio of the electric field to the magnetic field is known as the impedance, Z.

$$Z_{xy} = \frac{E_x}{H_y} = \frac{\omega\mu}{k} \qquad \text{------- (3.32)}$$

If the electric field is orientated in the y direction, the impedance Z_{xy} can be derived in a similar fashion as

$$Z_{yx} = \frac{E_y}{H_x} = -\frac{\omega\mu}{k} \qquad \text{------- (3.33)}$$

By using (3.23) and the fact that $\frac{1}{\sqrt{i}} = e^{-\frac{i\pi}{4}}$ (see Appendix A for derivation), (3.32) can be written in terms of the apparent resistivity ρ

$$Z_{xy} = 2\pi\sqrt{\frac{\rho}{5T}}\cdot 10^{-3}e^{\frac{-i\pi}{4}} \quad \text{ohm} \qquad \text{------- (3.34)}$$

Since the impedance is complex, it has an amplitude and a phase. The amplitude is given by the modulus of Z

$$\left|Z_{xy}\right| = 2\pi\sqrt{\frac{\rho}{5T}}\cdot 10^{-3} \quad \text{ohm} \qquad \text{------- (3.35)}$$

and the phase by the tangency of the ratio of the imaginary part to the real part.

$$\phi_{xy} = -\frac{\pi}{4} \qquad \text{------- (3.36)}$$

For Z_{yx} the amplitude is the same as for Z_{xy} and the phase is

$$\phi_{yx} = \pi - \frac{\pi}{4} \qquad \text{------- (3.37)}$$

3.4.2. Impedance of a two-layer medium

The impedance for a two-layer medium can be derived from (3.22) and (3.25). Figure 3.4 depicts a model of a two-layer medium.

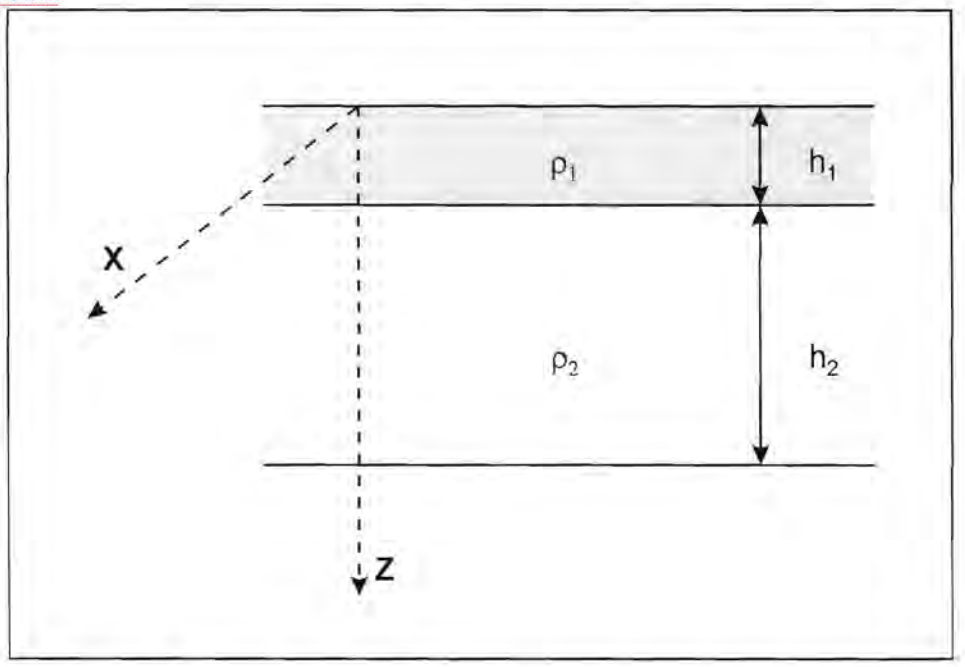

Figure 3.4 Two-layer medium

In the first layer the electric and magnetic fields are

$$E_x^{(1)} = e^{-iwt}\left(A_1 e^{ik_1 z} + B_1 e^{-ik_1 z}\right) \qquad 0 \le z \le h_1 \qquad \text{------- (3.38)}$$

and

$$H_y^{(1)} = e^{-iwt}\frac{k_1}{\omega\mu}\left(A_1 e^{ik_1 z} - B_1 e^{-ik_1 z}\right) \qquad 0 \le z \le h_1 \qquad \text{------- (3.39)}$$

The second layer is considered to be a half-space, and the electric and magnetic fields are

$$E_x^{(2)} = e^{-iwt}\left(A_2 e^{ik_2 z}\right) \qquad z \ge h_1 \qquad \text{------- (3.40)}$$

and

$$H_y^{(2)} = e^{-iwt}\frac{k_2}{\omega\mu}\left(A_2 e^{ik_2 z}\right) \qquad z \ge h_1 \qquad \text{------- (3.41)}$$

Using the impedance ratio and the boundary conditions given in (3.42) and (3.43) the impedance relation (3.44) for a two layer medium can be derived (Kaufman and Keller, 1981).

$$E_x^n = E_x^{n+1} \qquad z = h_n \qquad \text{------- (3.42)}$$

$$H_y^n = H_y^{n+1} \qquad z = h_n \qquad \text{------- (3.43)}$$

$$Z_{xy} = \frac{\omega\mu}{k_1} \frac{1+\left(\frac{1-\sqrt{\rho_1/\rho_2}}{1+\sqrt{\rho_1/\rho_2}}\right)e^{2ik_1h_1}}{1-\left(\frac{1-\sqrt{\rho 1/\rho_2}}{1+\sqrt{\rho_1/\rho_2}}\right)e^{2ik_1h_1}} \qquad \text{------- (3.44)}$$

3.4.3. Electromagnetic fields in the presence of a two-dimensional structure

After developing the impedance for a layered medium, it is important to consider what effects two-dimensional structures will have on the electromagnetic field. Two scenarios will be considered, namely

- electric field parallel to the vertical structure (E - polarisation)
- electric field perpendicular to the vertical structure (H - polarisation)

E-Polarisation

Assume the two-dimensional structure strikes in the x-direction and the primary electric field is directed along the x-axis. The primary electric field does not intersect the surface and the total electric field has only an E_x component. As a result all derivatives with respect to x are zero. Maxwell's equation describing the magnetic field due to a current distribution (3.4) therefore becomes

$$\nabla \times \mathbf{H} = \sigma\mathbf{E} \qquad \text{------- (3.45)}$$

(the displacement current is negligibly small compared to the conduction current for the frequencies and conductivities measured in magnetotellurics (Kaufman and Keller, 1981)).

Equation (3.45) reduces to

$$\sigma E_x = \frac{\partial H_z}{\partial y} - \frac{\partial H_y}{\partial z} \qquad \text{------- (3.46)}$$

and (3.3) together with $\mathbf{H} = H_0 e^{-i\omega t}$ yield

$$H_y = \frac{1}{i\omega\mu}\frac{\partial E_x}{\partial z} \qquad \text{------- (3.47)}$$

and

$$H_z = -\frac{1}{i\omega\mu}\frac{\partial E_x}{\partial y} \qquad \text{------- (3.48)}$$

Therefore, in the case of E-polarisation, the magnetic field has a vertical component.

H-Polarisation

In this case the primary electric field is directed perpendicular to the x-striking two-dimensional structure. Electric charges develop on the structure and the electric field has components E_y and E_z. The electric field does not change in the x-direction and therefore all derivatives with respect to x are zero. Ampere's law (3.45) again gives the magnetic field associated with this current distribution, with

$$\sigma E_y = \frac{\partial H_x}{\partial z} \qquad \text{------- (3.49)}$$

and

$$\sigma E_z = \frac{\partial H_x}{\partial y} \qquad \text{------- (3.50)}$$

These equations are substituted into (3.3) and yield the following equation describing the magnetic field

$$H_x = \frac{1}{i\omega\mu}\left(\frac{\partial E_z}{\partial y} - \frac{\partial E_y}{\partial z}\right) \qquad \text{------- (3.51)}$$

When the electric field is directed perpendicular to the two-dimensional structure, the magnetic field does not have a z-component.

3.4.4. Tensor impedance

From the previous section, it is clear that the relative orientation between structures in the earth and the primary electromagnetic field plays a crucial role in impedance calculations. This is further complicated by the fact that the orientation of the primary electromagnetic field changes with time and several orientations may be present at a certain time resulting in elliptical polarisation. In an attempt to deal with this problem the tensor impedance was derived (Sims et al., 1971; Kaufman and Keller, 1981). In matrix form the tensor repesentation of (3.32) and (3.33) is

$$\begin{bmatrix} E_x \\ E_y \end{bmatrix} = \begin{bmatrix} Z_{xx} & Z_{xy} \\ Z_{yx} & Z_{yy} \end{bmatrix} \begin{bmatrix} H_x \\ H_y \end{bmatrix} \qquad \text{------- (3.52)}$$

Therefore, the electric field in a certain direction may depend on magnetic fields parallel and perpendicular to it and the impedances can vary with time as the polarisation of the source field changes (Swift, 1986).

CHAPTER 4
DATA ACQUISITIONING AND PROCESSING

The collection of magnetotelluric data in the field entails setting up the sounding station and recording until adequate data have been gathered in the appropriate frequency range. Time spent on a sounding depends on the required survey depth and the level of natural electromagnetic activity. Basic processing involves a number of steps, one of the most important being to determine whether natural electromagnetic events occurred.

4.1. DATA ACQUISITIONING

4.1.1. Field Setup

It is clear from the development of the basic theory that inhomogeneities in the substructure of the earth cause secondary electric and magnetic fields that each have components in the x-, y- and z- directions. For this reason it is necessary to measure three perpendicular magnetic components and two horizontal perpendicular electric components. Two horizontal perpendicular magnetic components are also measured at a remote station away from the base station. This is based on the assumption that the noise will be different at the two stations but the events will be the same. A typical field setup is shown in Figure 4.1.

4.1.1.1. Measuring the electric field

To measure the electric field, the potential difference between two electrodes is measured. The electrodes must preferably be made of non-polarising material such as a metal immersed in one of its salts in a porous cup. The voltage difference between a pair of non-polarising electrodes is relatively stable, whereas for metal electrodes potential differences resulting

from electrochemical reactions at the metal surface can be present (Kaufman and Keller, 1981).

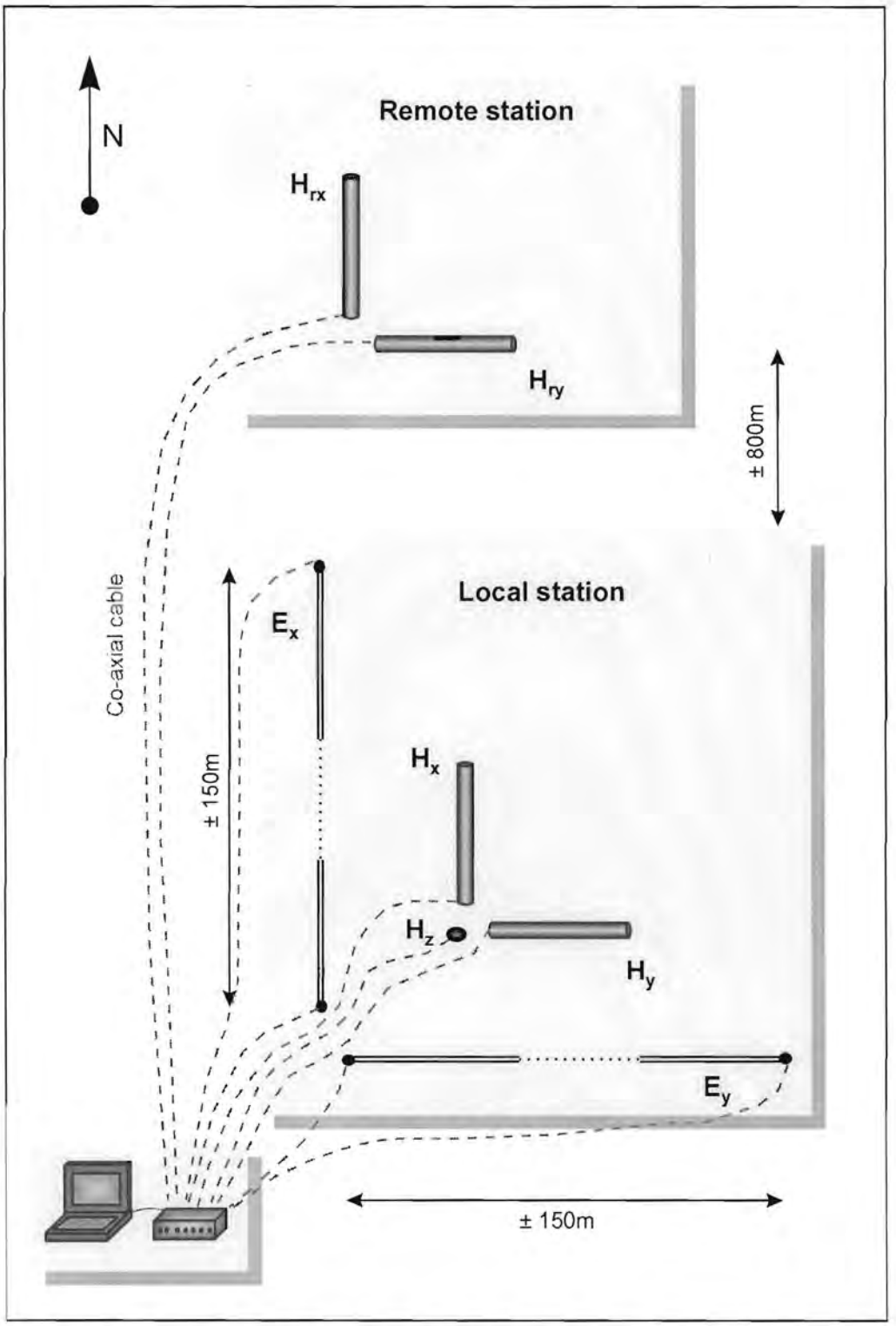

Figure 4.1. Field setup for Magnetotelluric station

Contact resistances at electrodes can cause problems. In a dry soil or bare rock the contact resistance of the electrode may be very high and the soil or rock needs to be saturated with water or sometimes even saltwater to improve the contact. It is also true that when the contact resistances are high electrostatic and electromagnetic noise cause problems.

Electrode intervals vary from site to site. According to Ohm's law potential (V) is proportional to resistance (R):

$$V = I R \qquad \text{------- (4.1)}$$

Therefore, as the resistivity of the geology increases the strength of the measured signal will increase, if the current (I) remains constant. In a conductive earth, the signal will decrease and an increase in electrode spacing is necessary to amplify the signal strength (V = E I). It is important to remember that noise will behave the same as natural signals and consequently the amount of noise present will influence the choice of electrode spacing.

Another important factor in laying out the electrodes is the geological substructure. For a small electrode spacing local variations in resistivity near the surface will negatively influence the measurements. If, for example, the electrodes are placed in a localised shallow conductor, the electric measurements will be strongly influenced by this feature while the magnetic measurements will be almost unaffected. If a longer separation is used between the electrodes, the average electric field will be more characteristic of the dominant electric field and the dominant resistivity in the surface layer.

Coaxial cables are used between the electrodes and the recording equipment. Since motion of the cables must be minimised it should be laid flat on the ground.

4.1.1.2. Measuring the magnetic field

Magnetic induction coils are used to measure the magnetic field intensity. The coil detects the rate of change of the magnetic field and the electromotive force (EMF) induced in the coil is

$$EMF = -nA\left(\frac{dB}{dt}\right)\cos\theta \qquad \text{------- (4.2)}$$

for a coil with negligible resistance, inductance and capacitance (Kaufman and Keller, 1981). In (4.2)

n = number of turns of wire

A = area of the coil (m^2)

B = magnetic induction (T)

θ = angle between the magnetic field **H** and the normal to the plane of the coil.

The voltage measured by an induction loop is proportional to the oscillation frequency or time rate of change of the magnetic field that cuts through the loop.

The coils are buried beneath the earth to minimise the effect of wind and changes in temperature. Care must be taken to level the coils perfectly in the horizontal and vertical positions for the various components respectively.

4.1.2. Data sampling

The aim of a magnetotelluric sounding is to deduce an image of changes in the electrical substructure of the earth with depth. For this reason data are sampled at different frequencies. Frequency relates to depth via the skin depth

$$\delta = \sqrt{\frac{2}{\omega\mu\sigma}} \qquad \text{------- (4.3)}$$

Data are recorded from both the electrodes and the magnetic coils in analog form and need to be digitised. The main problem with digitising a signal is frequency aliasing. The Nyquist criterion states that at least two samples must be taken over each cycle of a frequency to be certain that the frequency can be recognised. The sampling interval must therefore be chosen in such a way that all the frequencies contained in the signal can be recognised and not just those that we are interested in. A possible solution is to filter out unwanted frequencies with an analogue filter before digitising the signal. Unwanted frequencies such as 50Hz and its harmonics can be filtered out before data processing starts.

The range of frequencies finally utilised at a sounding station (and therefore the depth of investigation) depends mainly on the aim of the survey and the geo-electrical substructure. According to the Nyquist criterion the highest frequency that can be identified with a sampling period Δt is

$$f_N = \frac{1}{2\Delta t} \qquad \text{------- (4.4)}$$

For example, if the sampling frequency is 3000 Hz, the highest frequency that can be recovered would be 1500 Hz. The lowest frequency that can be measured with a specific sampling period Δt is

$$f_L = \frac{1}{(n * \Delta t) / 2} \qquad \text{------- (4.5)}$$

where n is the number of points sampled ($n = 2^m$ because the first step of processing is transformation to the frequency domain). Therefore, if we sample 2048 points at a frequency of 3000 Hz, the lowest frequency that

can be identified is approximately 3 Hz. From equation (4.5) it is clear that the range of frequencies can be improved by increasing the number of sampling points.

4.2. DATA PROCESSING

The steps involved in data processing are shown in Figure 4.2. Each of the steps will be discussed in more detail.

4.2.1. Transformation to Frequency Domain

Sampled time series data are transformed to complex amplitude spectra using Fourier transformation. The Fast Fourier Transform is the algorithm most widely used for this operation and the computational form to be implemented is

$$X(n) = \sum_{k=0}^{N-1} x_0(k) e^{\frac{-i2\pi k}{N}}, \qquad n = 0,1,\ldots,N-1 \qquad \text{------- (4.6)}$$

where $x_0(k)$ is the sampled time function.

4.2.2. Auto- and cross power spectra

The auto- and cross spectra are the frequency domain equivalents of auto-correlation and cross-correlation in the time domain. They are defined by Swift (1986) as follows:

Auto-spectra	$\langle E_x E_x^* \rangle$, $\langle E_y E_y^* \rangle$, $\langle H_x H_x^* \rangle$, $\langle H_y H_y^* \rangle$
Cross-spectra	$\langle E_x H_x^* \rangle$, $\langle E_x H_{rx}^* \rangle$, $\langle H_x E_y^* \rangle$, etc.

$E_x = E_x(\omega)$, $E_y = E_y(\omega)$, etc. are the Fourier spectra of the time domain functions and $E_x^* = E_x^*(\omega)$, $E_y^* = E_y^*(\omega)$, etc. are the complex conjugates of

the Fourier spectra. The brackets <> represent an averaging in time for finite bandwidths.

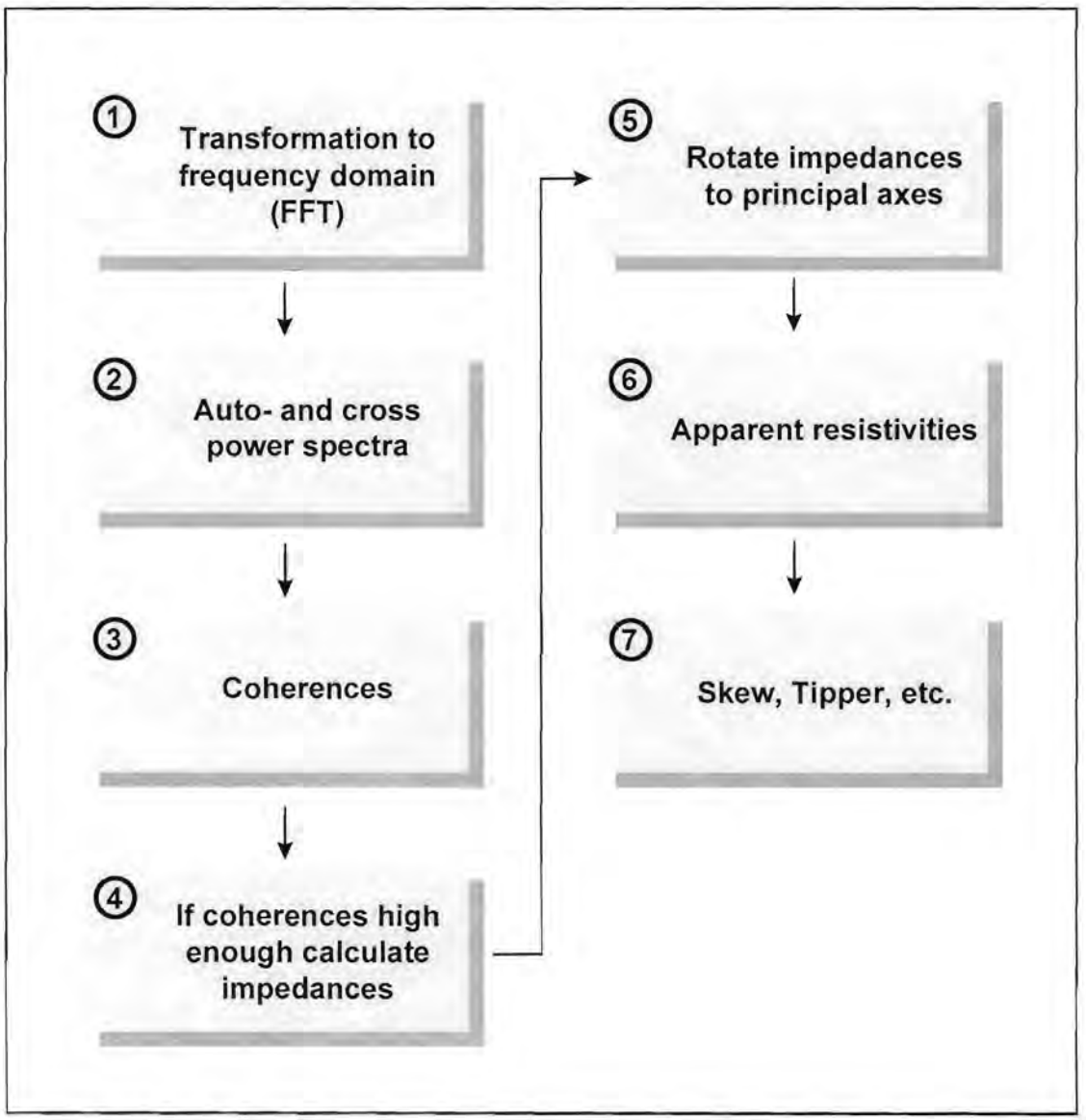

Figure 4.2. Processing steps

4.2.3. Coherences

It is necessary to determine whether a data set contains actual events or only noise. An event must appear simultaneously on at least two related

components, e.g. E_x and H_y but is usually visible on all the components. The following discussion is taken from an article on coherence functions by Reddy and Rankin (1974).

We can view the MT system as a multi-input linear system where H_x and H_y are the inputs, E_x and E_y are the outputs and Z_{zz}, Z_{xy}, Z_{yx} and Z_{yy} are the frequency response functions. Three types of coherence functions can be used to analyse the data quality:

- *Ordinary coherence*: Coherency between the output and each of the inputs, e.g. between E_x and H_x or E_x and H_y. High ordinary coherences between H_x and E_y and between H_y and E_x indicate a linear relation between the inputs and outputs.

$$\mathrm{Coh}(E_x H_x) = \frac{< E_x H_x^* >}{(< E_x E_x^* >< H_x H_x^* >)^{\frac{1}{2}}} \qquad \text{------- (4.7)}$$

- *Multiple coherence*: Coherency between the output and all of the inputs, e.g. between output E_x and inputs H_x and H_y. High multiple coherences indicate good signal to noise ratios.

$$\mathrm{Mcoh}(E_x H_x H_y) =$$

$$\frac{< H_y H_y^* >< H_x E_x^* >^2 + < H_x H_x^* >< H_y E_x^* >^2 - 2\mathrm{Re}(< H_x H_y^* >< H_y E_x^* >< E_x H_x^* >)}{< E_x E_x^* > (< H_x H_x^* >< H_y H_y^* > - < H_x H_y^* >^2)}$$

------- (4.8)

- *Partial coherence*: This is the coherency between the output and a specific input after the effect of the other inputs has been removed by least-squares prediction from the specified output and input. For e.g. between E_x and H_x after the effect of H_y has been removed by least squares prediction from E_x and H_x. High partial coherences between E_x and H_y and between E_y and H_x and corresponding low partial

coherences between E_x and H_x and between E_y and H_y indicate that the rotation angle corresponds to the principal direction. The reason for this being that in the principal direction Z_{xx} and Z_{yy} is close to zero. This means that $E_x = Z_{xx}H_x$ is close to zero and therefore the partial coherency between E_x and H_x is low.

$$Pcoh(H_xE_x) = \frac{<H_xE_x^*>}{(<E_xE_x^*><H_xH_x^*>)^{\frac{1}{2}}} \qquad \text{------- (4.9)}$$

The equation looks similar to (4.7) but it differs in that the effect of the other input (H_y in this case) has been removed. The partial coherency can also be formulated in terms of the multiple and ordinary coherences:

$$Pcoh(H_xE_x) = \frac{Mcoh(E_xH_xH_y) - Coh(H_yE_x)}{1 - Coh(H_yE_x)} \qquad \text{------- (4.10)}$$

4.2.4. Impedances

If the coherences are high enough, indicating that there may be a true event present in the data, we can proceed to calculate the impedance tensor elements. This can be done in two ways, one in which only the components measured at the local station are used and another in which the remote station components are incorporated.

4.2.4.1. Single station impedance

Z_{ij} in equation (3.52) can be estimated in a least squares way (Sims et al., 1971). Young (1962) states the principle of least squares as follows: the most probable value of a quantity is obtained from a set of measurements by choosing the value which minimises the sum of the squares of the deviations of these measurements. Deviation is defined as the difference between any measurement in the set and the mean of the set. For a set of

measurements x_i, the most probable value of x is that which minimises the quantity

$$\sum_{i=1}^{n}(x - x_i)^2$$

For this equation to be a minimum

$$\frac{d}{dx}\sum_{i=1}^{n}(x - x_i)^2 = 0 \qquad \text{------- (4.11)}$$

Apply this to (3.52) (n is the number of measurements at a specific frequency):

$$\Psi = \sum_{i=1}^{n}(E_{xi} - (Z_{xx}H_{xi} + Z_{xy}H_{yi}))^2 \qquad \text{------- (4.12)}$$

Setting the derivatives of Ψ with respect to the real and imaginary parts of Z_{xx} equal to zero yields

$$\sum_{i=1}^{n}E_{xi}H_{xi}^{*} = Z_{xx}\sum_{i=1}^{n}H_{xi}H_{xi}^{*} + Z_{xy}\sum_{i=1}^{n}H_{yi}H_{xi}^{*} \qquad \text{------- (4.13)}$$

Setting the derivatives of Ψ with respect to the real and imaginary parts of Z_{xy} equal to zero yields

$$\sum_{i=1}^{n}E_{xi}H_{yi}^{*} = Z_{xx}\sum_{i=1}^{n}H_{xi}H_{yi}^{*} + Z_{xy}\sum_{i=1}^{n}H_{yi}H_{yi}^{*} \qquad \text{------- (4.14)}$$

The solutions in (4.13) and (4.14) minimise the error caused by noise on E_x. By taking another least-squares estimate the noise on H_x can be minimised. The various least squares estimates results in the following equations:

$$<E_xE_x^*> = Z_{xx}<H_xE_x^*> + Z_{xy}<H_yE_x^*> \quad \text{----- (4.15)}$$

$$<E_xE_y^*> = Z_{xx}<H_xE_y^*> + Z_{xy}<H_yE_y^*> \quad \text{----- (4.16)}$$

$$<E_xH_x^*> = Z_{xx}<H_xH_x^*> + Z_{xy}<H_yH_x^*> \quad \text{----- (4.17)}$$

$$<E_xH_y^*> = Z_{xx}<H_xH_y^*> + Z_{xy}<H_yH_y^*> \quad \text{----- (4.18)}$$

where the terms between brackets are the auto- and cross spectra and the brackets indicate the average spectra over finite bandwidths.

By substituting (4.15) in (4.16), (4.17) and (4.18), (4.16) in (4.17) and (4.18) and (4.17) in (4.18), six estimates for the impedance tensor element Z_{xy} can be determined:

$$Z_{xy} = \frac{<E_xE_y^*><H_xE_x^*> - <E_xE_x^*><H_xE_y^*>}{<H_yE_y^*><H_xE_x^*> - <H_yE_x^*><H_xE_y^*>} \quad \text{----- (4.19)}$$

$$Z_{xy} = \frac{<E_xH_x^*><H_xE_x^*> - <E_xE_x^*><H_xH_x^*>}{<H_yH_x^*><H_xE_x^*> - <H_yE_x^*><H_xH_x^*>} \quad \text{------(4.20)}$$

$$Z_{xy} = \frac{<E_xH_y^*><H_xE_x^*> - <E_xE_x^*><H_xH_y^*>}{<H_yH_y^*><H_xE_x^*> - <H_yE_x^*><H_xH_y^*>} \quad \text{------(4.21)}$$

$$Z_{xy} = \frac{<E_xH_x^*><H_xE_y^*> - <E_xE_y^*><H_xH_x^*>}{<H_yH_x^*><H_xE_y^*> - <H_yE_y^*><H_xH_x^*>} \quad \text{----- (4.22)}$$

$$Z_{xy} = \frac{<E_xH_y^*><H_xE_y^*> - <E_xE_y^*><H_xH_y^*>}{<H_yH_y^*><H_xE_y^*> - <H_yE_y^*><H_xH_y^*>} \quad \text{----- (4.23)}$$

$$Z_{xy} = \frac{<E_xH_y^*><H_xH_x^*> - <E_xH_x^*><H_xH_y^*>}{<H_yH_y^*><H_xH_x^*> - <H_yH_x^*><H_xH_y^*>} \quad \text{----- (4.24)}$$

Six estimates for Z_{xx} can be determined in a similar way.

Following the same approach six estimates each for Z_{yx} and Z_{yy} can be determined.

4.2.4.2. Remote reference impedance calculations

The main problem in using the impedance estimates derived in the previous section is that the auto-spectra of functions that contain noise may severely bias the estimates. In order to address this problem, Gamble et al. (1979) proposed the use of a remote reference station. At this station two horizontally perpendicular magnetic components, H_{xr} and H_{yr}, are measured. The noise at this station should not correlate with the noise at the local station. Multiply the two linear relations in (3.52) with H_{xr}^* and H_{yr}^*

$$< E_x H_{xr}^* >= Z_{xx} < H_x H_{xr}^* > + Z_{xy} < H_y H_{xr}^* > \quad \text{----- (4.25)}$$

$$< E_x H_{yr}^* >= Z_{xx} < H_x H_{yr}^* > + Z_{xy} < H_y H_{yr}^* > \quad \text{----- (4.26)}$$

$$< E_y H_{xr}^* >= Z_{yx} < H_x H_{xr}^* > + Z_{yy} < H_y H_{xr}^* > \quad \text{----- (4.27)}$$

$$< E_y H_{yr}^* >= Z_{yx} < H_x H_{yr}^* > + Z_{yy} < H_y H_{yr}^* > \quad \text{----- (4.28)}$$

Solve these four equations for the impedance tensor elements:

$$Z_{xx} = \frac{< E_x H_{xr}^* >< H_y H_{yr}^* > - < E_x H_{yr}^* >< H_y H_{xr}^* >}{< H_x H_{xr}^* >< H_y H_{yr}^* > - < H_x H_{yr}^* >< H_y H_{xr}^* >} \quad \text{----- (4.29)}$$

$$Z_{xy} = \frac{< E_x H_{yr}^* >< H_x H_{xr}^* > - < E_x H_{xr}^* >< H_x H_{yr}^* >}{< H_x H_{xr}^* >< H_y H_{yr}^* > - < H_x H_{yr}^* >< H_y H_{xr}^* >} \quad \text{----- (4.30)}$$

$$Z_{yx} = \frac{< E_y H_{xr}^* >< H_y H_{yr}^* > - < E_y H_{yr}^* >< H_y H_{xr}^* >}{< H_x H_{xr}^* >< H_y H_{yr}^* > - < H_x H_{yr}^* >< H_y H_{xr}^* >} \quad \text{----- (4.31)}$$

$$Z_{yy} = \frac{< E_y H^*_{yr} >< H_x H^*_{xr} > - < E_y H^*_{xr} >< H_x H^*_{yr} >}{< H_x H^*_{xr} >< H_y H^*_{yr} > - < H_x H^*_{yr} >< H_y H^*_{xr} >} \quad \text{----- (4.32)}$$

4.2.5. Rotation of impedance tensor

The impedance estimates in the previous section were calculated for the measuring axes x, y. In a two-dimensional earth the electric field in one direction may depend on magnetic field variations both parallel and perpendicular. The ideal is for the x-axis to point north in a one dimensional case or parallel to the strike in a two dimensional case (Hobbs, 1992). In the two dimensional case this will minimise the effects of the E_xH_x and E_yH_y terms. However, the strike direction of the two-dimensional structures may vary with depth and for this reason data are measured with x directed along magnetic north. The next step in data processing is to rotate the calculated impedance elements to the principal axes (parallel and perpendicular to strike) using the following equations:

$$Z_{x'x'}(\alpha) = \tfrac{1}{2}((Z_{xx} + Z_{yy}) + (Z_{xx} - Z_{yy})\cos 2\alpha + (Z_{xy} + Z_{yx})\sin 2\alpha \quad \text{----- (4.33)}$$

$$Z_{x'y'}(\alpha) = \tfrac{1}{2}((Z_{xy} - Z_{yx}) + (Z_{xy} + Z_{yx})\cos 2\alpha + (Z_{yy} - Z_{xx})\sin 2\alpha \quad \text{----- (4.34)}$$

$$Z_{y'x'}(\alpha) = \tfrac{1}{2}((Z_{yx} - Z_{xy}) + (Z_{yx} + Z_{xy})\cos 2\alpha + (Z_{yy} - Z_{xx})\sin 2\alpha \quad \text{----- (4.35)}$$

$$Z_{y'y'}(\alpha) = \tfrac{1}{2}((Z_{xx} + Z_{yy}) - (Z_{xx} - Z_{yy})\cos 2\alpha - (Z_{xy} + Z_{yx})\sin 2\alpha \quad \text{----- (4.36)}$$

The principal axes are those which maximise $Z_{x'y'}$ and $Z_{y'x'}$ (principal impedances) or minimise $Z_{x'x'}$ and $Z_{y'y'}$ (auxiliary impedances). The impedance elements are rotated a few degrees at a time until the desired maximum or minimum is found.

Rotation of the data assuming a two dimensional earth as described above was proposed by Swift (1986). More recently various authors have given attention to the effect of three dimensional conductivity distributions on the impedance tensor (e.g. Bahr, 1988, 1991; Groom and Bailey, 1989, 1991).

The three dimensionality of the earth's electrical structure will ensure that the diagonal elements of the tensor never disappear. Several decomposition schemes for the measured impedance tensor have been proposed by these authors. Bahr (1988, 1991) chose what he called the principal superimposition model to be a local three dimensional anomaly over a regional two dimensional structure. He used certain parameters to classify different distortion types and subsequently decide whether decomposition of the impedance tensor is necessary (Bahr, 1991). Figure 4.3(a) shows a schematic summary of his distortion classification process. The equations referred to in this diagram appear in figure 4.3(b).

4.2.6. Apparent resistivity

The final processing step is the calculation of the apparent resistivity as a function of frequency using Cagnaird's (1953) formula

$$\rho_{ij} = \frac{1}{5f}\left|Z_{ij}\right|^2 \qquad i,j = x,y \qquad \text{------- (4.37)}$$

The apparent resistivities are shown on a log-log graph as a function of frequency. Spies and Eggers (1986) noted that curves calculated with equation (4.37) usually show an oscillation at low frequencies. Since these oscillations are not present in the time domain they concluded that the oscillations are artefacts of the frequency domain representation and suggested using some alternative forms of (4.37)

$$\rho_{ij} = \frac{2}{5f}\left[\mathrm{Re}(Z)\right]^2 \qquad i,j = x,y \qquad \text{------- (4.38)}$$

$$\rho_{ij} = \frac{2}{5f}\left[\mathrm{Im}(Z)\right]^2 \qquad i,j = x,y \qquad \text{------- (4.39)}$$

$$\rho_{ij} = \frac{1}{5f}\left[\mathrm{Im}(Z^2)\right] \qquad i,j = x,y \qquad \text{------- (4.40)}$$

$$\rho_{ij} = \frac{1}{5f}\left|Z^2\right| \qquad i,j = x,y \qquad \text{------- (4.41)}$$

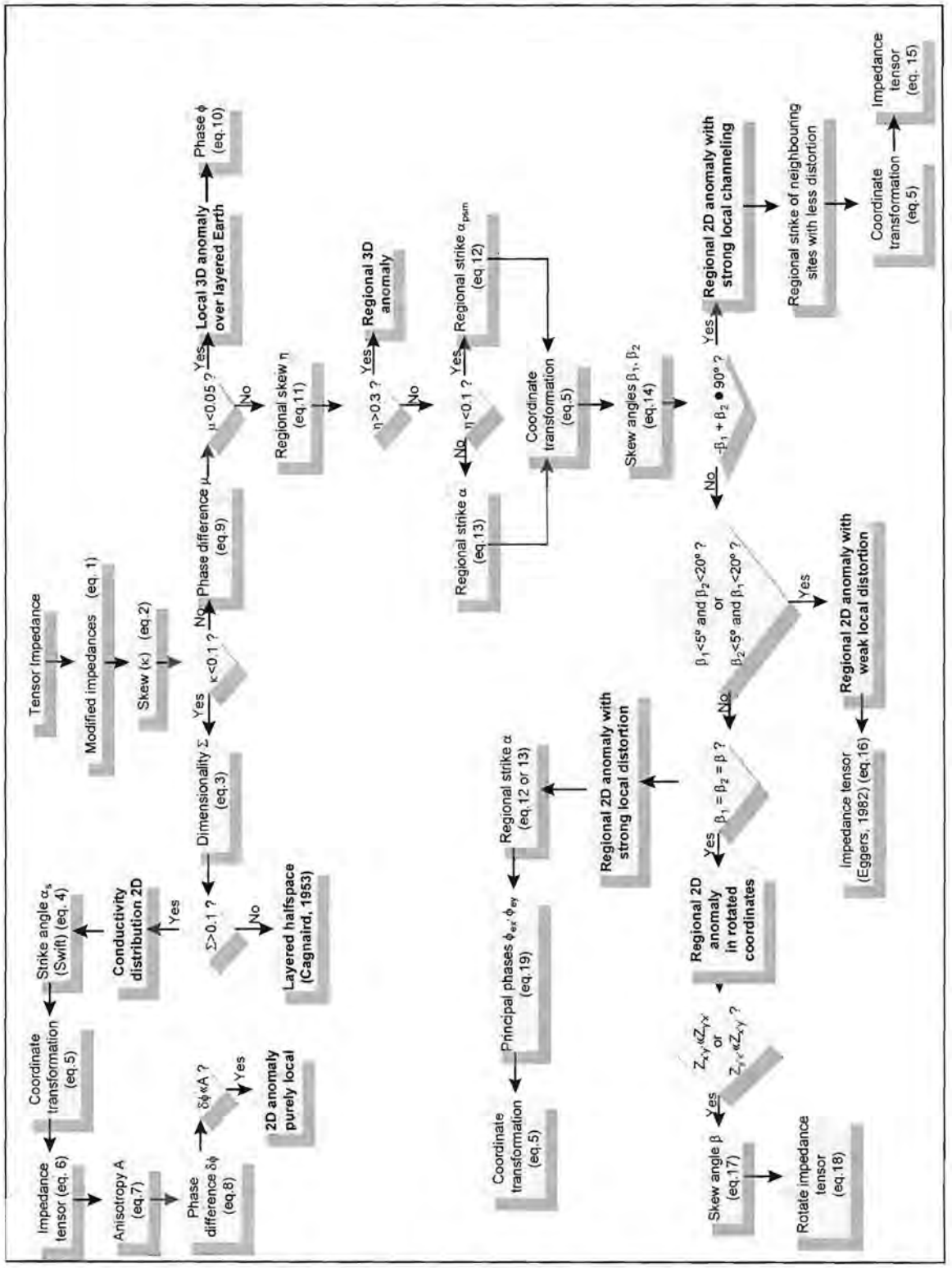

Figure 4.3(a). A flow diagram showing the calculation of distortion parameters (Bahr, 1991).

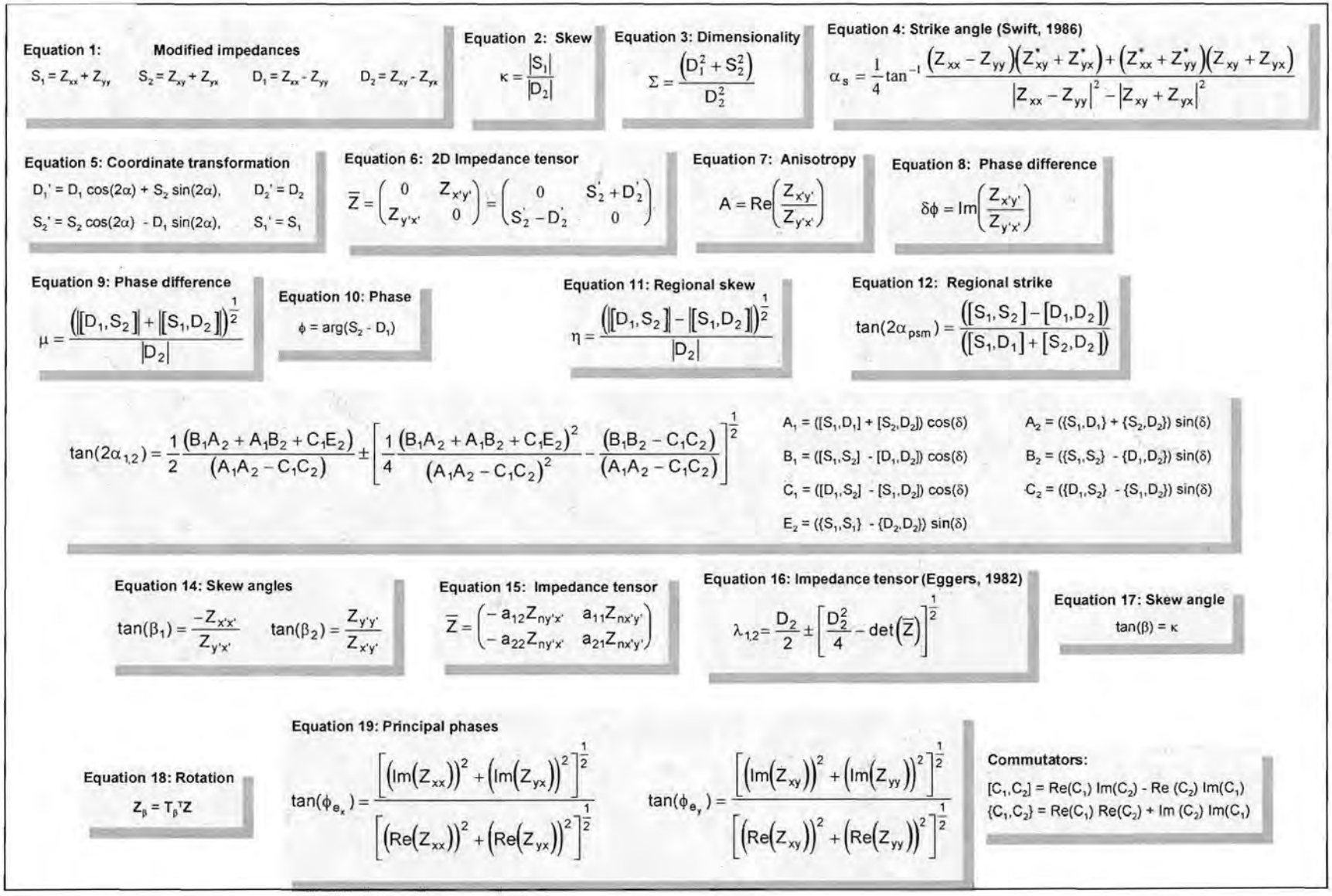

Figure 4.3(b). Equations used in Figure 4.3(a)

4.2.7. Other parameters calculated during processing

A number of additional parameters can be calculated from the impedance tensor and can assist in gaining a better understanding of the earth's electrical substructure.

4.2.7.1. Skewness

When the impedance tensor has been rotated to the principal direction, Z_{xx} and Z_{yy} will be very small if the earth is laterally uniform or two-dimensional, but larger when the earth has a three dimensional structure (Vozoff, 1972). At the same time the difference between the elements Z_{xy} and Z_{yx} is large when the earth is strongly two-dimensional and small otherwise. The ratio

$$S = \frac{|Z_{xx} + Z_{yy}|}{|Z_{xy} - Z_{yx}|} \qquad \text{------- (4.42)}$$

is known as the 'skewness' ratio. If S is large the structure of the earth appears to be three-dimensional for that specific frequency range.

4.2.7.2. Tipper

We saw in equations (3.47), (3.48) and (3.51) that the magnetic field does not have a vertical component when the electric field is directed perpendicular to the strike direction (H-polarisation). Therefore, the vertical magnetic component can be used to determine the strike direction of the two-dimensional structure (the horizontal direction in which the magnetic field is most highly coherent with H_z is perpendicular to the strike). In defining the 'Tipper' parameter we assume that H_z is linearly related to H_x and H_y (Vozoff, 1972). At each frequency

$$H_z = AH_x + BH_y \qquad \text{------- (4.43)}$$

where A and B are unknown complex coefficients. These coefficients (A,B) can be thought of as 'tipping' part of the horizontal magnetic field into the vertical and is therefore called the tipper. The tipper (T) is defined as

$$|T| = (|A|^2 + |B|^2)^{\frac{1}{2}} \qquad \text{------- (4.44)}$$

with a phase

$$\delta = \frac{(A_r^2 + A_i^2)\arctan(\frac{A_i}{A_r}) + (B_r^2 + B_i^2)\arctan(\frac{B_i}{B_r})}{T^2} \qquad \text{------- (4.45)}$$

CHAPTER 5

STATISTICAL REDUCTION OF DATA

5.1. GENERAL

In chapter 3 we derived the basic equations used in MT (eq. 3.52). In reality, in the presence of noise the equations look as follows

$$E_x = Z_{xx}H_x + Z_{xy}H_y + r \qquad \text{----- (5.1)}$$

$$E_y = Z_{xy}H_x + Z_{yy}H_y + r \qquad \text{----- (5.2)}$$

where r represents the noise component. In the field *N* data sets are collected at a specific frequency. The above equations in matrix form are

$$\begin{bmatrix} E_{x_i} \end{bmatrix} = \begin{bmatrix} H_{x_i} H_{y_i} \end{bmatrix} \begin{bmatrix} Z_{xx} \\ Z_{xy} \end{bmatrix} + \begin{bmatrix} r_i \end{bmatrix} \qquad \text{----- (5.3)}$$

$$\begin{bmatrix} E_{y_i} \end{bmatrix} = \begin{bmatrix} H_{x_i} H_{y_i} \end{bmatrix} \begin{bmatrix} Z_{yx} \\ Z_{yy} \end{bmatrix} + \begin{bmatrix} r_i \end{bmatrix} \qquad \text{----- (5.4)}$$

In general the equations are written as

$$\mathbf{x} = \mathbf{U}\beta + \mathbf{r} \qquad \text{----- (5.5)}$$

with **x** an Nx1 matrix representing the electric field components, **U** an Nx2 matrix containing the measured magnetic field components, β the 2x1 impedance matrix and **r** an Nx1 matrix containing the noise component. Since the impedance tensor is indicative of the properties of the underlying geology, there is only one tensor for *N* sets of data recordings at a particular frequency. If the data were noise free and consisted only of true natural electromagnetic events, it would be sufficient to do only one recording per frequency. In reality noise contamination is an ever-present problem in magnetotelluric data collection and consequently it is necessary to record several data sets at a specific frequency. From a statistical point of view the aim is to determine the impedance tensor that most probably represents the electrical properties of the underlying earth.

In order to determine the impedance value, it is necessary to minimise the error between observed and calculated values, for example between $E_{observed}$ and

$E_{calcualted}$ (as calculated using equation (3.52)). Figure 5.1 shows a schematic diagram of this process.

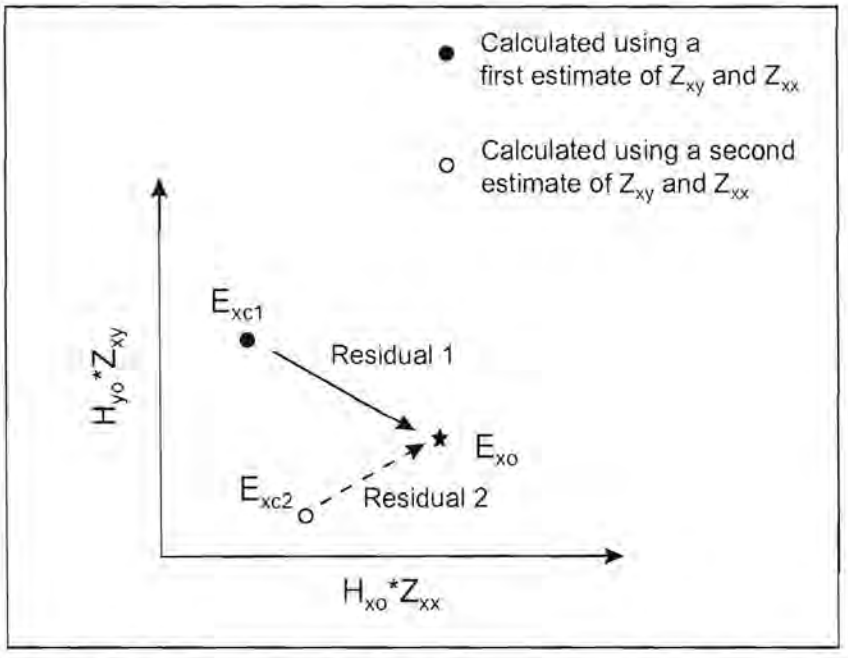

Figure 5.1 Visualisation of the minimisation of a residual

The objective is to minimise the residuals between N calculated and N observed electrical components for an estimate of Z_{xx} and Z_{xy}.

5.2. L_1 AND L_2 NORMS

A possible solution to this problem is to use the Least Squares method to determine β. The principle of least squares was outlined in section 4.2.4.1. as the most probable value of a quantity obtained from a set of measurements by choosing the value that minimises the sum of the squares of the deviations of these measurements (Young, 1962). For a set of measurements x_i the most probable value of x is that which minimises the quantity

$$\sum_{i=1}^{n}(x-x_i)^2 \qquad \text{----- (5.6)}$$

with x a variable that can be varied to obtain the minimum value of the function. For this function to be a minimum the following condition must be satisfied:

$$\frac{d}{dx}\sum_{i=1}^{N}(x-x_i)^2 = 0 \qquad \text{----- (5.7)}$$

The derivative of a sum of terms is equal to the sum of the derivatives, therefore

$$x = \frac{1}{N}\sum_{i=1}^{N} x_i \qquad \text{----- (5.8)}$$

The most probable value of x turns out to be the mean of the observations. This minimisation is called the L_2 norm. A major problem with this method is the effect of one poor observation on the mean. The technique works best if the errors are normally distributed. A first step to improve the robustness of the method is to work with the median instead of the mean. This is achieved by minimising the summed absolute values instead of the summed squared differences and is known as the L_1 norm:

$$\begin{aligned} &\frac{d}{dx}\sum_{i-1}^{N}|x - x_i| = 0 \\ &\sum_{i=1}^{N}\frac{d}{dx}|x - x_i| = 0 \qquad \text{----- (5.9)} \\ &\sum_{i=1}^{N}\text{sign}(x - x_i) = 0 \end{aligned}$$

sign is +1 when the argument is positive, -1 when the argument is negative and somewhere in between when the argument is zero (Claerbout, 1976). For N odd x is equal to the middle order statistic $x_{(\lfloor N/2 \rfloor+1)}$ where $\lfloor\ \rfloor$ denotes the integer part while for N even the median is chosen as $(x_{\lfloor N/2 \rfloor}+x_{(\lfloor N/2 \rfloor+1)})/2$ (Chave et al., 1987). Before the median can be computed the data have to be ordered in ascending order.

5.3. ROBUST M-ESTIMATION

From the discussion it is clear that the L_1 norm is not as sensitive as the L_2 norm, but it is still prone to the effect of outliers. Weighted medians go some way to improving the robustness of the impedance estimation procedure, minimising

$$\sum_{i=1}^{N}|w_i||x - x_i| \qquad \text{----- (5.10)}$$

with w_i the weight factor, but is still too vulnerable to bad data points. Furthermore, the Least Squares estimate is only really adequate when the errors in the input data have a Gaussian distribution (Egbert and Booker, 1986). It is

possible to test whether the errors are Gaussian distributed by making use of Quantile-Quantile plots (Q-Q plots)

5.3.1. Q-Q Plots

A way of examining the distribution of the error data is by drawing Q-Q plots. The Q-Q plot is achieved by plotting observed residuals against the values expected if the residuals were normally distributed (Johnson and Wichern, 1998). The observed residuals must be ordered (written in ascending order). The inverse of the Gaussian distribution function (ϕ^{-1}) gives the expected residuals.

Plot the i^{th} value of the N observed residuals r_i against $\phi^{-1}(i/N)$. If the points fall on a straight line with unit slope, the residuals have a normal (Gaussian) distribution.

To determine the residual expected from a Gaussian error, calculate (i-½)/N and consult a table that depicts the areas under a normal curve (Table A3. Walpole and Myers, 1989) for a value that corresponds to (i-½)/N.

However, impedance tensors still have to be estimated regardless of the error distribution. According to Johnson and Wichern (1998), it is possible to transform non-normal data so that it has a more Gaussian distribution. This is in effect the approach suggested by Sutarno and Vozoff (1989,1991) where they minimise a function of the residuals and not the residuals themselves.

A very important fact to realise is that in all the above we have made use of the principle of maximum likelihood, namely the assumption that the set of measurements we obtained was the most probable set of measurements (Young, 1962).

With the classical least squares approach, impedance tensor estimates can be determined by minimising the error component in equation (5.5) (Sutarno and Vozoff, 1989, 1991).

$$\sum_{i=1}^{N}(x_i - \sum_{j=1}^{2} U_{ij}\beta_j)^2 \rightarrow \min \qquad \text{----- (5.11)}$$

Find the value of β that minimises (5.11), that is, solve for the derivative equal to 0.

$$\sum_{i=1}^{N}(x_i - \sum_{j=1}^{2} U_{ij}\beta_j)U_{ij} = 0 \qquad \text{----- (5.12)}$$

In matrix form equation (5.12) becomes

$$(\tilde{x} - \tilde{U}\hat{\beta})\tilde{U} = 0$$
$$\tilde{U}^T\tilde{x} - \tilde{U}^T\tilde{U}\hat{\beta} = 0$$
$$\tilde{U}^T\tilde{U}\hat{\beta} = \tilde{U}^T\tilde{x}$$
$$\hat{\beta} = (\tilde{U}^T\tilde{U})^{-1}\tilde{U}^T\tilde{x} \qquad \text{----- (5.13)}$$

Huber (1981) solves the problem of robustness by minimising a sum of less rapidly increasing functions of the residuals instead of minimising a sum of squares:

$$\sum_{i=1}^{N}\rho(r_i) = \sum_{i=1}^{N}\rho\left(x_i - \sum_{j=1}^{2} U_{ij}\beta_j\right) = \min \qquad \text{----- (5.14)}$$

$\rho(t)$ is known as a loss function and should be chosen so that the influence function $\psi(t) = \frac{d\rho(t)}{dt}$ is continuous and bounded.

$$\sum_{i=1}^{N}\psi(r_i) = \sum_{i=1}^{N}\psi\left(x_i - \sum_{j=1}^{2} U_{ij}\beta_j\right)U_{ik} = 0, \quad k = 1,2 \qquad \text{----- (5.15)}$$

To ensure that the solution to (5.14) is scale invariant it is necessary to introduce a scaling parameter. Equations (5.14) and (5.15) are substituted by

$$\sum_{i=1}^{N}\rho\left(\frac{r_i}{s}\right) = \sum_{i=1}^{N}\rho\left(\frac{x_i - \sum_{j=1}^{2} U_{ij}\beta_j}{s}\right) \rightarrow \min \qquad \text{----- (5.16)}$$

$$\sum_{i=1}^{N}\psi\left(\frac{r_i}{s}\right)=\sum_{i=1}^{N}\psi\left(\frac{x_i-\sum_{j=1}^{2}U_{ij}\beta_j}{s}\right)U_{ik}=0,\quad k=1,2 \qquad \text{----- (5.17)}$$

Chave et al. (1987) propose two possible choices for the scaling parameter, namely

$$\hat{S}=\frac{s_{MAD}}{\sigma_{MAD}} \qquad \text{----- (5.18)}$$

$$\hat{S}=\frac{s_{IQ}}{\sigma_{IQ}} \qquad \text{----- (5.19)}$$

s_{MAD} is the median value of the absolute residuals (median absolute deviation (MAD))

$$s_{MAD} = \text{median}(|r_i - \text{median}(r)|) \qquad \text{----- (5.20)}$$

and σ_{MAD} is the expected value of the MAD for the appropriate probability density function. In equation (5.19) the subscript IQ marks the interquartile distance. s_{IQ} is the spacing between the 75% and 25% points of the sample distribution, or the centre range containing half of the probability (Chave et al., 1987)

$$s_{IQ}=r_{\left(\frac{3N}{4}\right)}-r_{\left(\frac{N}{4}\right)} \qquad \text{----- (5.21)}$$

σ_{IQ} is the corresponding theoretical value and is equal to twice the MAD for symmetric distributions.

Egbert and Booker (1986) follow a slightly different approach in determining the scale factor. They compute an initial estimate from the root mean square residual

$$\hat{s}_0=\sqrt{\frac{1}{(2N-4)}\sum_{i=1}^{2N}r_{i0}^{\,2}} \qquad \text{----- (5.22)}$$

Using the actual rms of the residuals r_{in} for the n^{th} iteration makes the estimate extremely vulnerable to the effect of outliers. By replacing sample averages by expectations, the scale estimate for the n^{th} iteration becomes

$$\hat{s}_0=\sqrt{\frac{1}{\beta(2N-4)}\sum_{i=1}^{2N}\left(E_{in}^{meas}-E_{n}^{pred}\right)^2} \qquad \text{----- (5.23)}$$

with β=0.7784.

For the loss function Huber (1981) uses a convex function that has a positive minimum at 0. It is based on a density function that has a Gaussian centre and Laplacian tails and is defined as follows:

$$\rho(t) = \begin{cases} \frac{1}{2}t^2 & |t| < t_0 \\ t_0|t| - \frac{1}{2}t_0^2 & |t| \geq t_0 \end{cases} \qquad \text{----- (5.24)}$$

t_0 is the tuning constant and value of 1.5 gives at least 95% efficiency for outlier-free normal data (Chave et al., 1987).

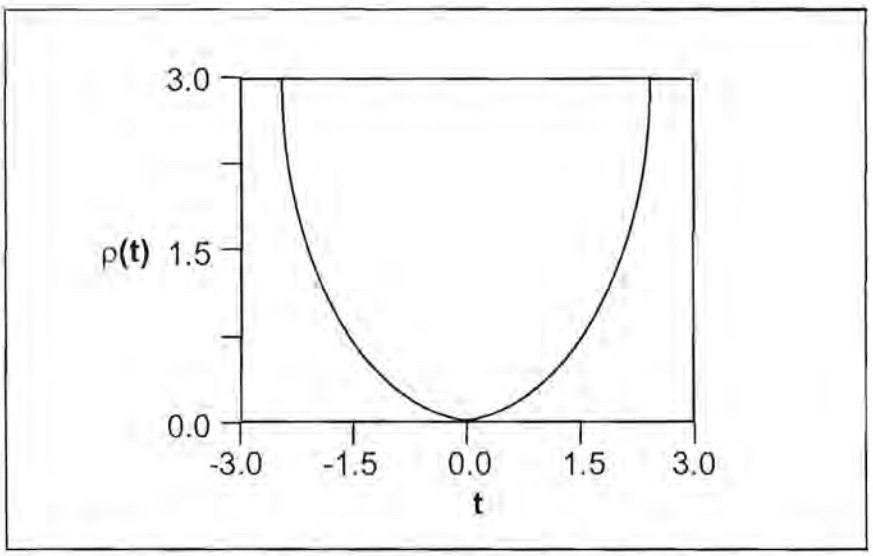

Figure 5.2. The Huber loss function (Sutarno and Vozoff,1989)

The influence function is

$$\psi(t) = \begin{cases} t & -t_0 < t < t_0 \\ t_0 & t \geq t_0 \\ -t_0 & t \leq -t_0 \end{cases} \qquad \text{----- (5.25)}$$

In order to achieve the best possible solution for the impedance tensor, the robust linear regression problem can be converted into a weighted least squares problem. Division of the influence function by the scaled residuals produces the weight function. Through substituting the influence function in equation (5.15) with the

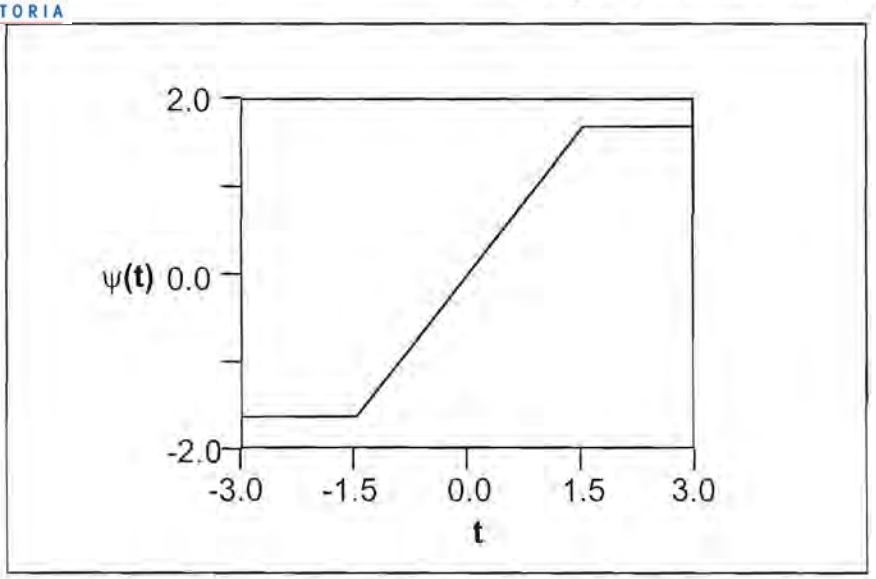

Figure 5.3. The Huber influence function (Sutarno and Vozoff, 1989)

weighted function and writing it in matrix form, the problem reduces to solving the following equation iteratively:

$$\tilde{U}^T\tilde{W}\tilde{r} = 0$$
$$\tilde{U}^T\tilde{W}(\tilde{x} - \tilde{U}\hat{\beta}) = 0$$
$$\tilde{U}^T\tilde{W}\tilde{U}\hat{\beta} = \tilde{U}^T\tilde{W}\tilde{x}$$
$$\hat{\beta} = (\tilde{U}^T\tilde{W}\tilde{U})^{-1}\tilde{U}^T\tilde{W}\tilde{x} \qquad \text{----- (5.26)}$$

For the loss function in (5.24), the Huber weight function reduces to

$$W(t) = \begin{cases} 1 & |t| < t \\ \dfrac{t_0}{|t|} & |t| \geq t_0 \end{cases} \qquad \text{----- (5.27)}$$

Equation (5.26) is solved iteratively, choosing the least squares estimate as an initial solution. From this the predicted outputs and residuals are calculated using equations (5.1 and 2) and (5.28) respectively.

$$r_i = x_i^{meas} - x_i^{pred} \qquad i = 1,\ldots,N \qquad \text{----- (5.28)}$$

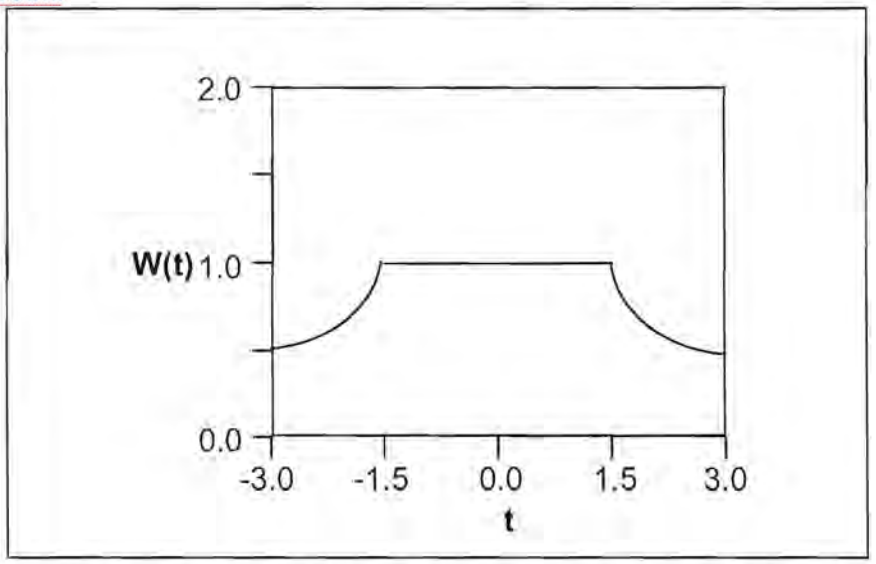

Figure 5.4. The Huber weight function (Sutarno and Vozoff, 1989)

Next, the scale parameter and Huber weights are determined and used to solve (5.26). The new impedance tensor estimate is then used to calculate the predicted outputs and the process is repeated until the estimates converge.

Sutarno and Vozoff (1991) states that "the Huber weights fall off slowly for large residuals and provide inadequate protection against severe residuals". They suggest the use of Thomson weights for a few iterations after convergence with the Huber weights. Thomson weights are described by the function

$$W(t) = e^{-e^{\alpha(|t|-\alpha)}} \qquad \text{------ (5.29)}$$

α determines the scale at which down weighting begins. Egbert and Booker (1986) use a value of 2.8 for α. Chave et al. (1987) describes the N^{th} quantile of the appropriate probability distribution as an excellent choice for α. Furthermore, if outliers have been eliminated, the residuals are χ^2 distributed. This distribution with two degrees of freedom is equivalent to the exponential distribution and thus has the pdf

$$f(t) = \frac{1}{2} e^{\frac{-t}{2}} \qquad t \geq 0 \qquad \text{----- (5.30)}$$

with $\sigma_{MAD} = 2\sinh^{-1}(0.5) \approx 0.9624$ and $\square_{IQ} = 2 \log 3 \approx 2.1972$ (Chave et al., 1987). The quantiles of the exponential distribution are given by

$$Q_j = 2\log\left(\frac{N}{N-j+0.5}\right) \qquad j = 1,\ldots,N. \qquad \text{----- (5.31)}$$

According to Sutarno and Vozoff (1991), if outliers have been eliminated the magnitudes of the residuals are Rayleigh-distributed with pdf

$$f(t) = te^{\frac{-t^2}{2}} \qquad t \geq 0 \qquad \text{----- (5.32)}$$

and $\sigma_{MAD} = 0.44845$. The quantiles are given by

$$Q_j = \sqrt{2\log\left(\frac{N}{N-j+0.5}\right)} \qquad j = 1,\ldots,N. \qquad \text{----- (5.33)}$$

With magnetotelluric data, equations (5.1) and (5.2) consists of complex numbers. Sutarno and Vozoff (1989) suggest two ways of handling complex data:

- regard the data as having independent Gaussian real and imaginary parts and apply separate weights to them,
- use the magnitude of the complex numbers and apply identical weights to the real and imaginary parts.

The second method is preferable since it is rotationally invariant (Sutarno and Vozoff, 1991). Equation (5.26) then becomes

$$\hat{\beta} = (\tilde{U}^*\tilde{W}\tilde{U})^{-1}\tilde{U}^*\tilde{W}\tilde{x} \qquad \text{----- (5.34)}$$

where * denotes the Hermitian conjugate.

5.4. ADAPTIVE L_p NORM

An alternative approach has been developed to deal with the problem of non-Gaussian distributed errors. Kijko (1994) proposes that it is not always necessary to use the L_1 or L_2 norm to minimise residuals, but that one can use the L_p norm where p can be a real value not necessarily equal to 1 or 2. He goes further to develop an adaptive procedure whereby the value of p is automatically determined from the quality of the data. The technique was developed for use with seismological data but can easily be applied to magnetotelluric data.

Instead of minimising equation (5.6), the following misfit function is minimised

$$\sum_{i=1}^{n} |x - x_i|^p \qquad \text{------ (5.35)}$$

where $1 \leq p < \infty$. The value of p depends on the distribution of the residuals and is therefore related to the kurtosis of the residual distribution. Press et al. (1992) define the kurtosis as a measurement of the peakedness or flatness of a distribution relative to the normal distribution. A distribution with a sharp peak is known as 'leptokurtic' and the term 'platykurtic' describes a flat distribution. The kurtosis (β_2) is given by

$$\beta_2 = \frac{\mu_4}{\mu_2^2} \qquad \text{------ (5.36)}$$

where μ_2 and μ_4 are the second- and fourth order central moments.

Several authors suggested different ways to determine the value of p using the kurtosis. Money et al. (1982) used the equation

$$\hat{p} = \frac{9}{\hat{\beta}_2^2} + 1 \qquad \text{------ (5.37)}$$

where $1 \leq \hat{p} < \infty$. Sposito et al. (1983) developed a different equation

$$\hat{p} = \frac{6}{\hat{\beta}_2^2} \qquad \text{------ (5.38)}$$

with $1 \leq \hat{p} \leq 2$.

Therefore, when data are severely contaminated, the error distribution will have long tails, resulting in a large kurtosis and subsequently a small value for p.

Kijko (1994) developed an adaptive algorithm for determining an estimate for the p-value.

5.5. APPLICATION OF STATISTICAL REDUCTION TECHNIQUES TO SYNTHETIC DATA

The statistical reduction methods discussed in the previous sections will first be applied to synthetic data. Hattingh (1989) describes the construction of a unit apparent resistivity curve. He generates electric field data by multiplying real

magnetic field data with unit impedance (equation (3.52)). The resultant apparent resistivity versus frequency curve will plot as a straight line on double logarithmic paper.

5.5.1. Synthetic data with Gaussian distributed random errors

For the first test, noise with a Gaussian distribution was added to the data. Figure 5.4 shows the apparent resistivity and phase versus frequency curves. Noise added to the two curves both had a zero mean, but different standard deviations.

The Q-Q plots for these data sets (Figure 5.6) plot on roughly straight lines, confirming that the noise is normally distributed. The correlation coefficients between the observed and expected residuals are 0.89516 and 0.896132 for noise with standard deviations of 0.0001 and 0.2 respectively.

Figures 5.7 to 5.12 show the curves fitted to the data using the L_1 norm, L_2 norm, adaptive L_p norm and robust M-estimation techniques. In the calculation of the L_1, L_2 and adaptive L_p norms, an algorithm for the downhill simplex method taken from Press et al. (1992) was used to minimise the impedance variables. Nelder and Mead (1965) introduced this method of minimising multidimensional functions.

The L_1 and L_2 norm methods yield very similar results (Figures 5.7 and 5.8). Curves estimated by these two techniques approximate the original data displayed in Figure 5.5 very well.

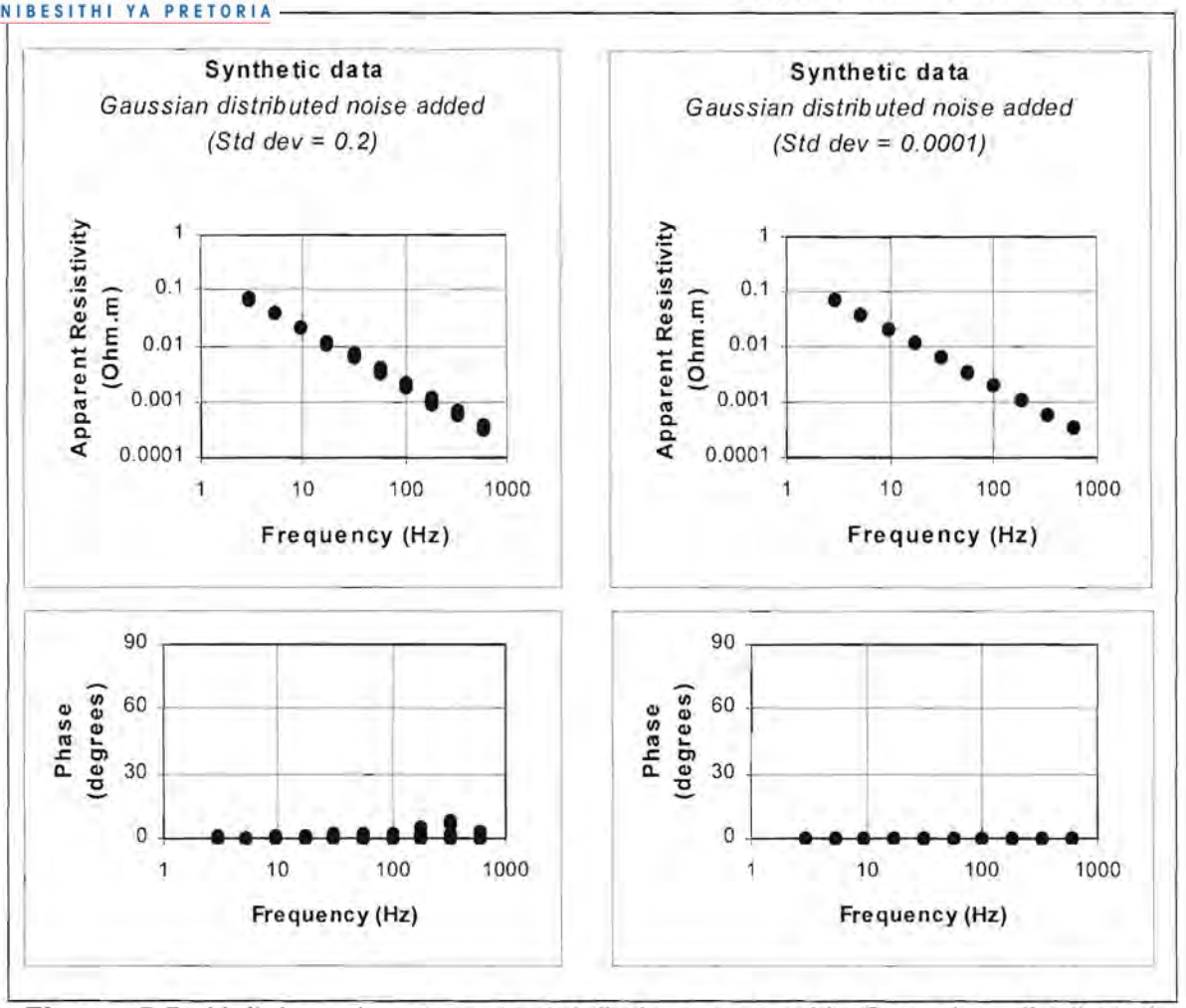

Figure 5.5. Unit impedance magnetotelluric curves with Gaussian distributed noise added.

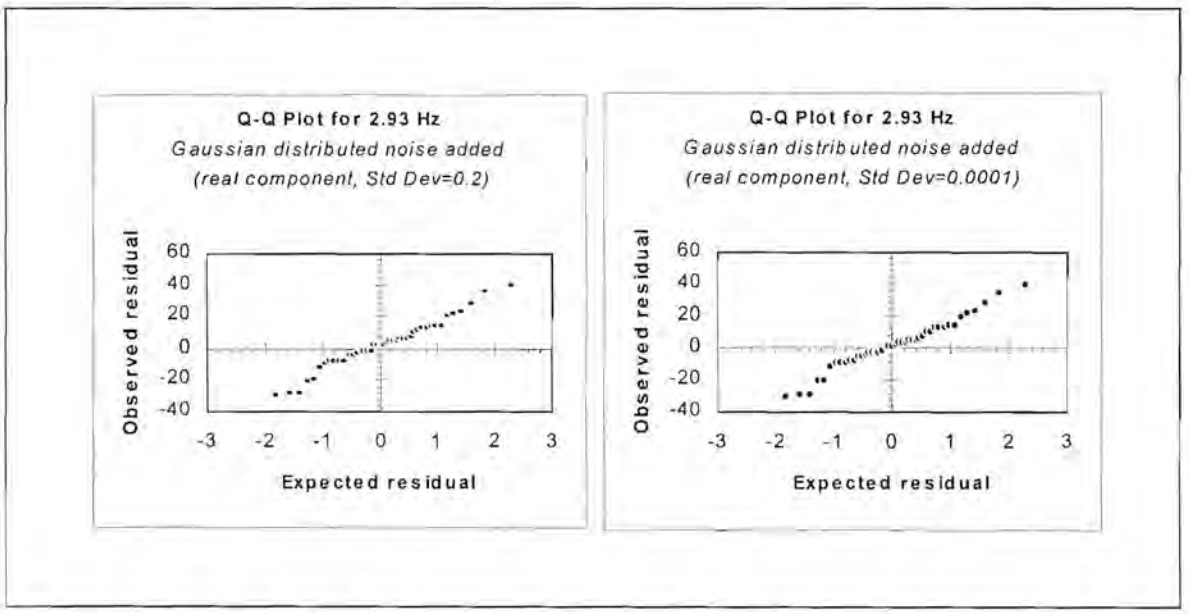

Figure 5.6. Q-Q plots of the synthetic data with Gaussian distribution noise added

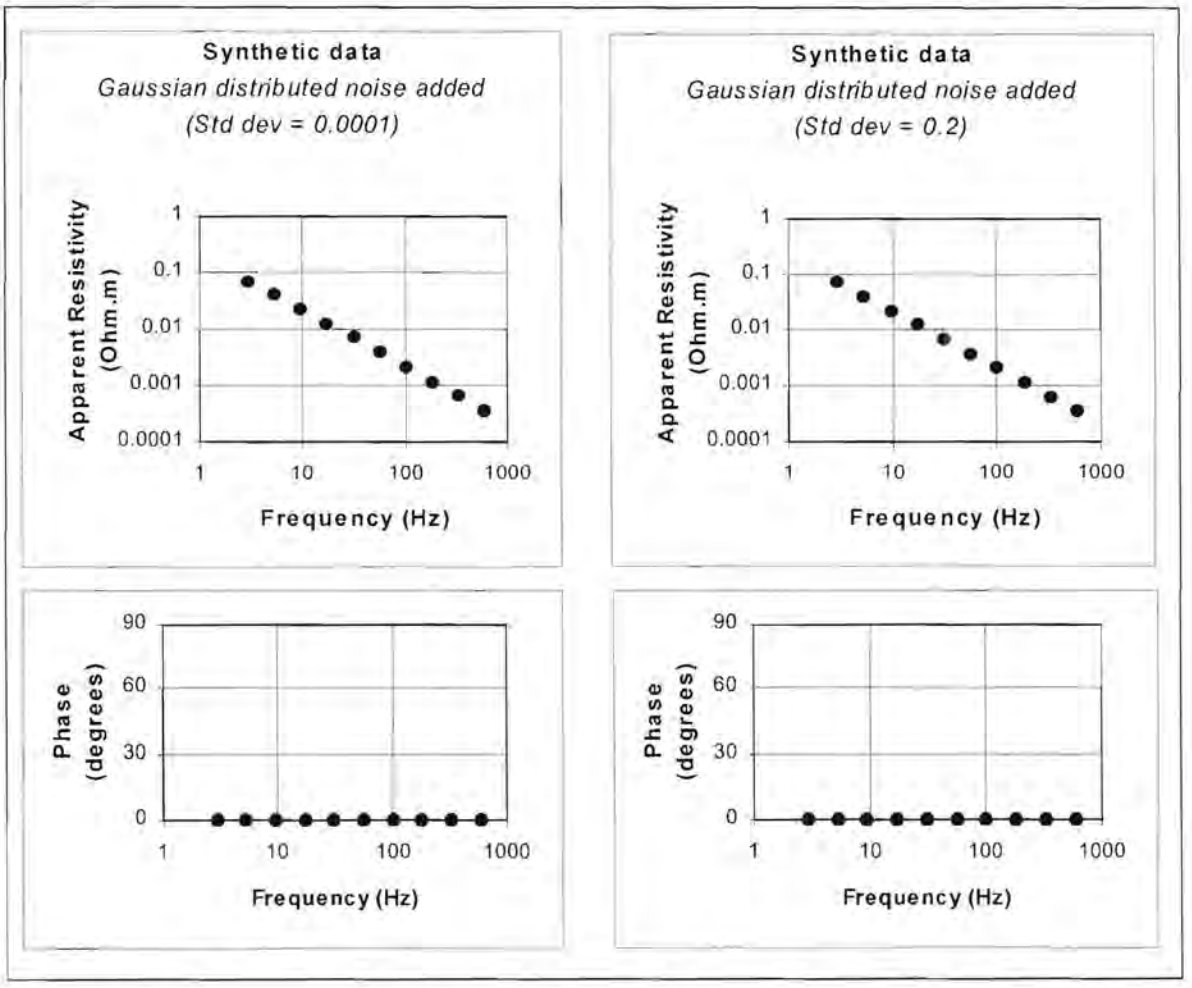

Figure 5.7. Apparent resistivity versus frequency curves produced by the L_1 norm estimation technique for the synthetic data (with Gaussian distributed noise) displayed in Figure 5.5.

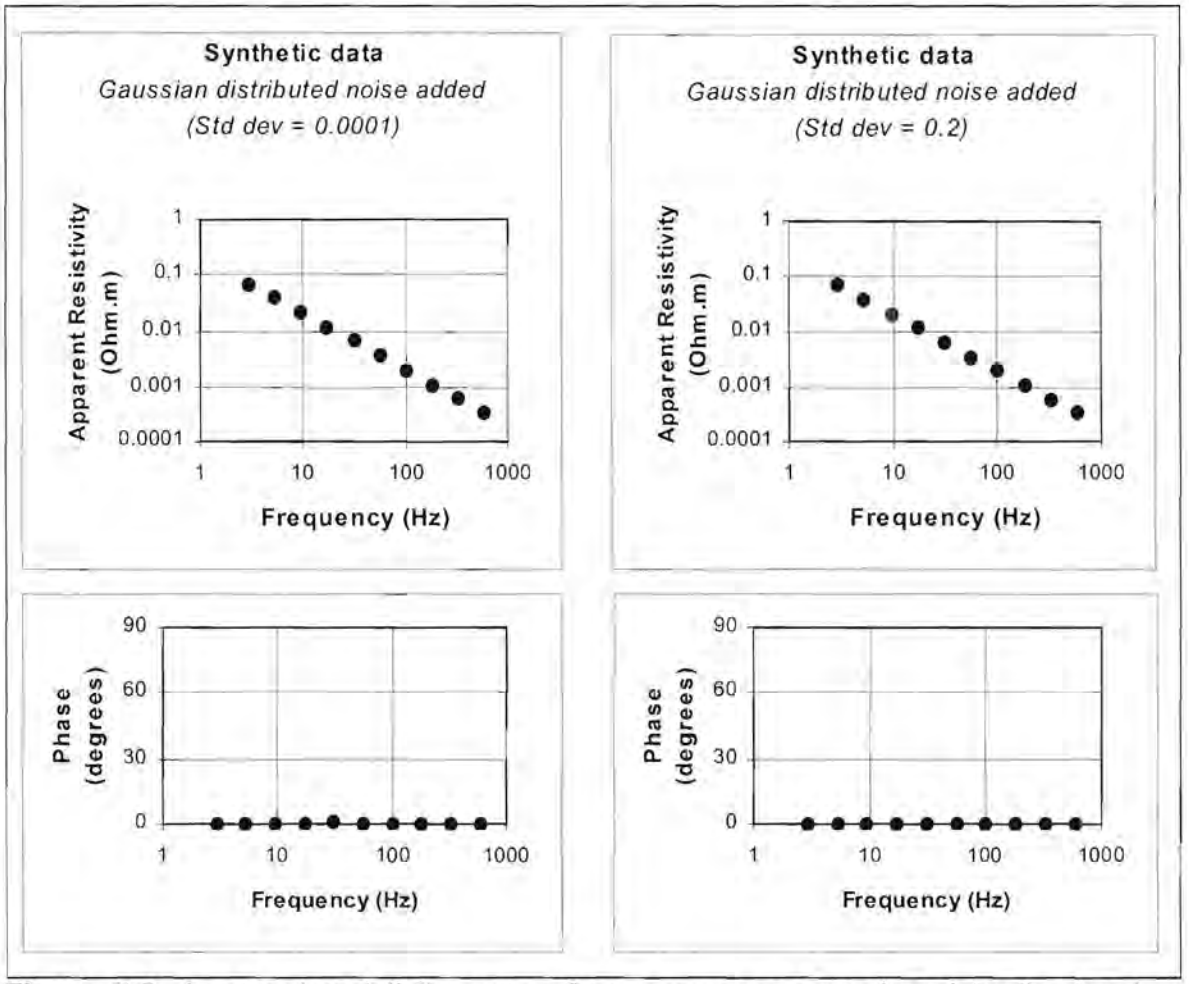

Figure 5.8. Apparent resistivity versus frequency curves produced by the least squares (L_2) estimation technique for the synthetic data (with Gaussian distributed noise) displayed in Figure 5.5.

The adaptive L_p norm technique yielded similar results to the L_1 and L_2 norms. The curves in Figure 5.9 were calculated using the formula of Money et al. (1982) to calculate exponent p. Figures 5.10.1 to 5.10.10 show the values of p calculated for each frequency during the estimation of the apparent resistivity and phase versus frequency curves.

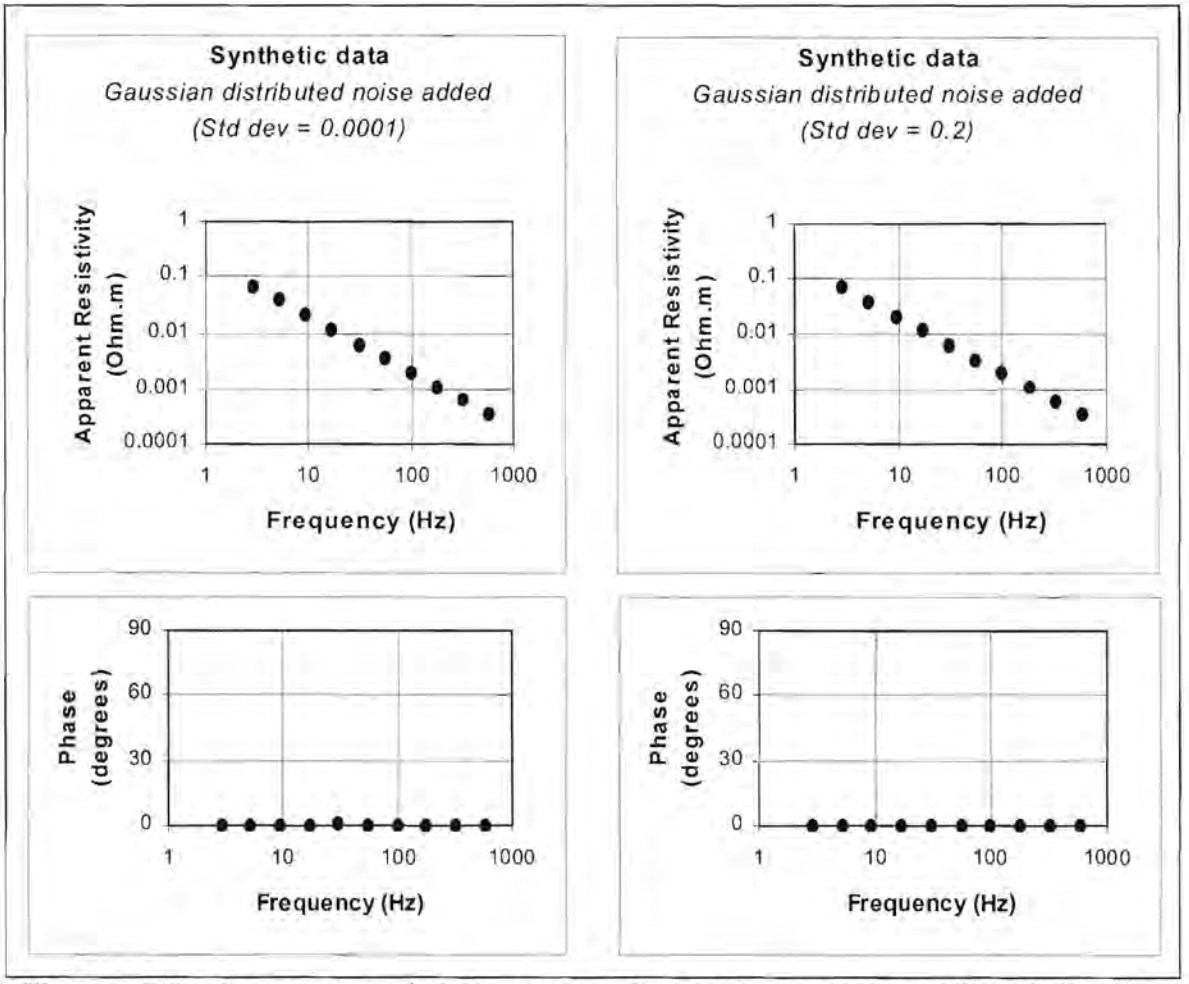

Figure 5.9. Apparent resistivity versus frequency curves produced by the adaptive L_p norm technique for the synthetic data (with Gaussian distributed noise) displayed in Figure 5.5. The formula suggested by Money et al. (1982) was used to calculate the exponent p.

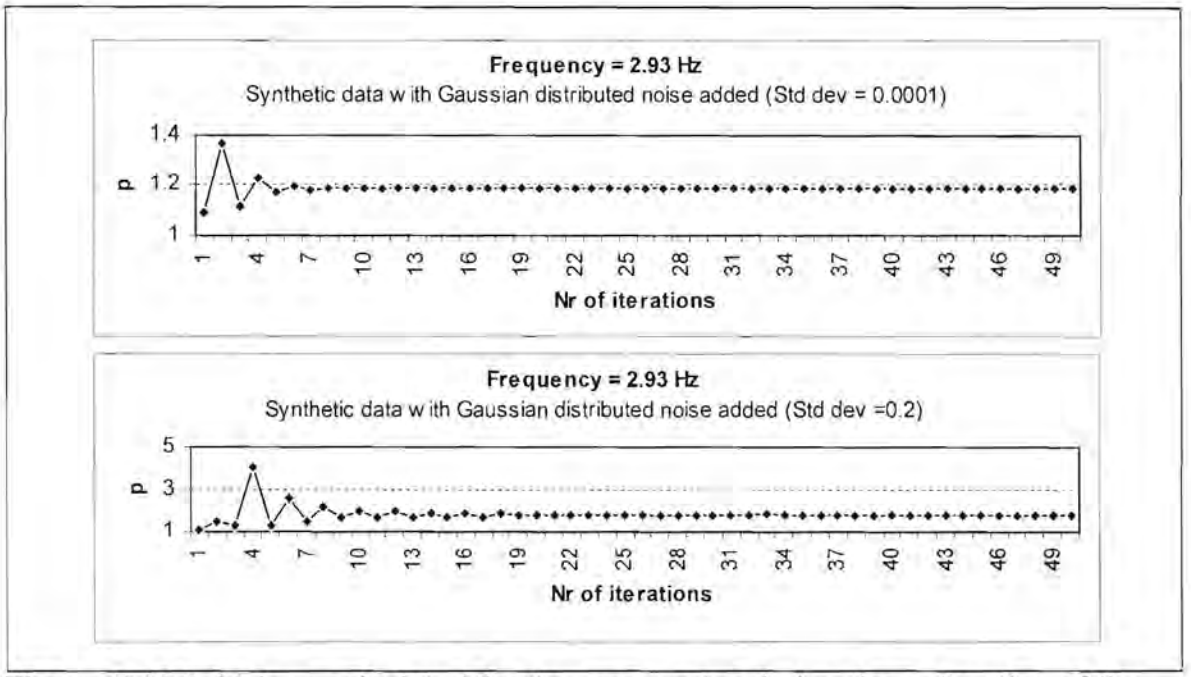

Figure 5.10.1. Values calculated for the exponent p during the estimation of the apparent resistivity values displayed in Figure 5.9 at 2.93 Hz

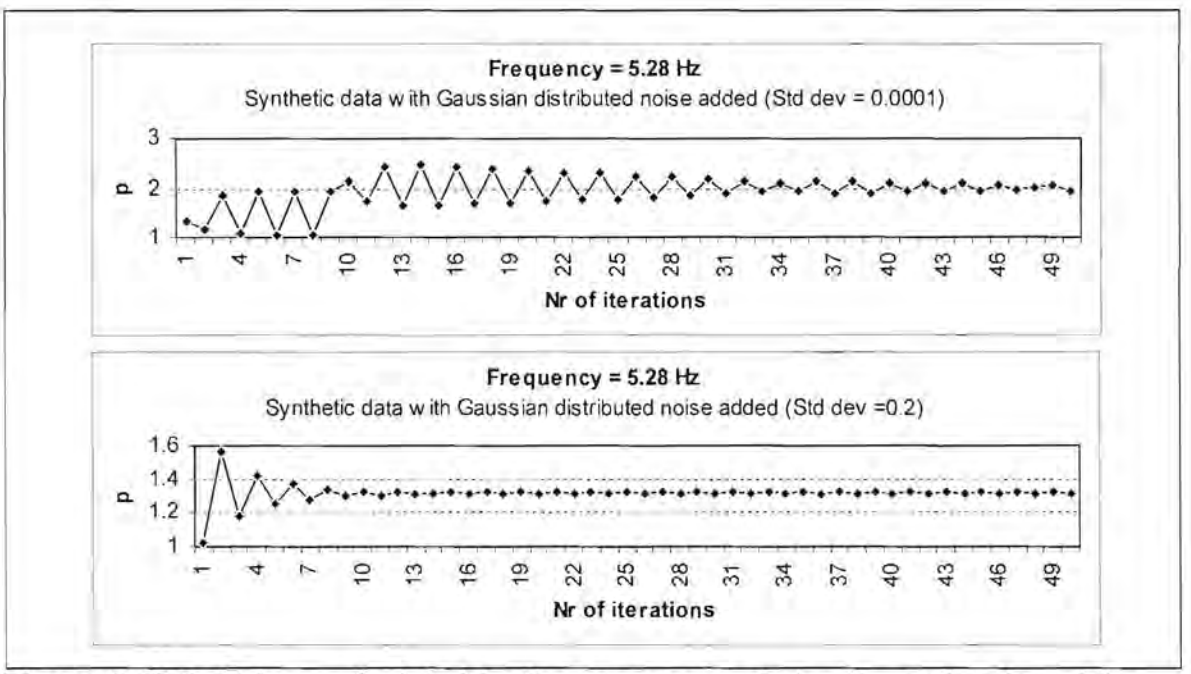

Figure 5.10.2. Values calculated for the exponent p during the estimation of the apparent resistivity values displayed in Figure 5.9 at 5.28 Hz

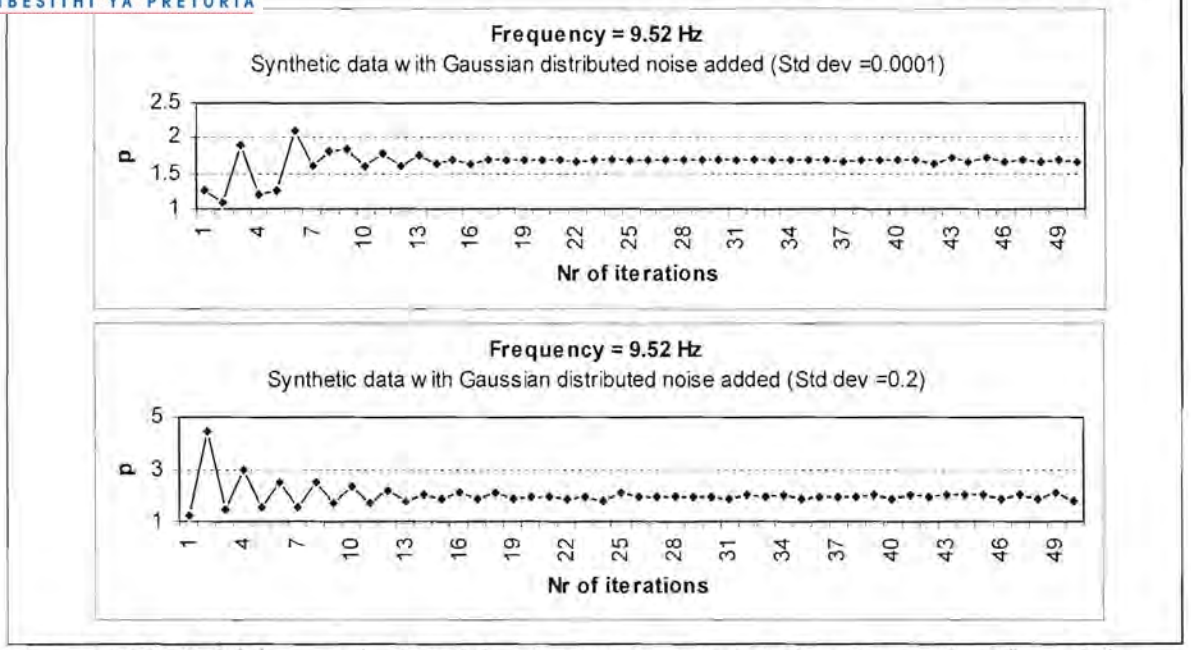

Figure 5.10.3. Values calculated for the exponent p during the estimation of the apparent resistivity values displayed in Figure 5.9 at 9.52 Hz

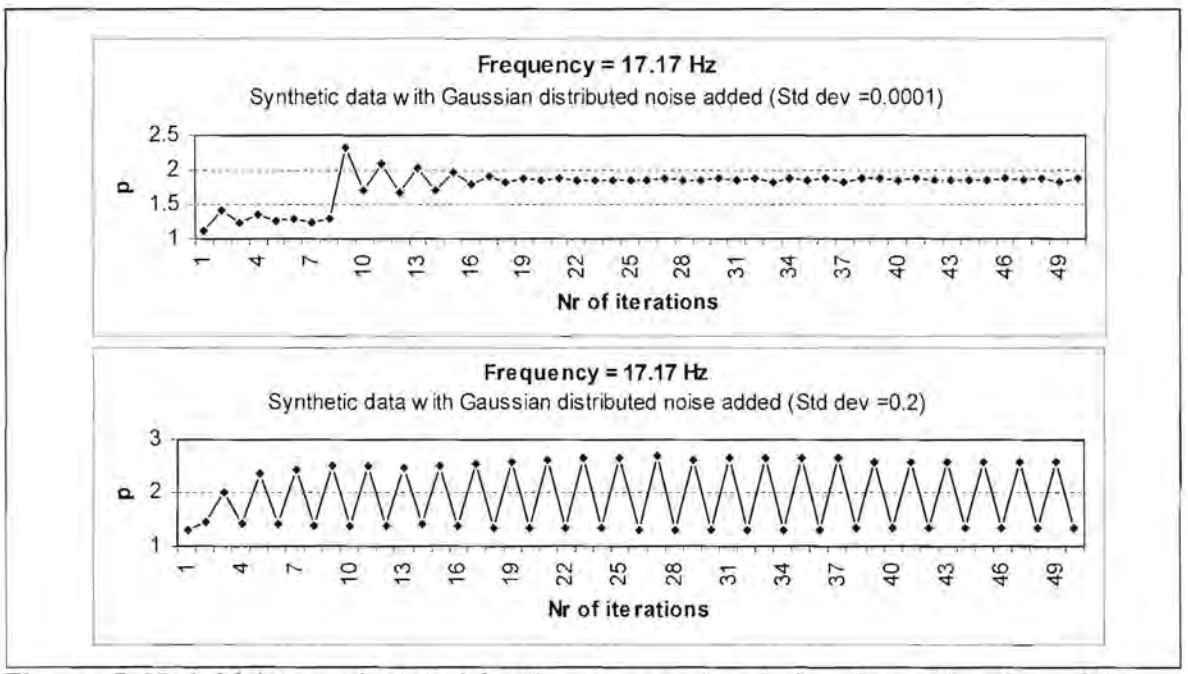

Figure 5.10.4. Values calculated for the exponent p during the estimation of the apparent resistivity values displayed in Figure 5.9 at 17.17 Hz

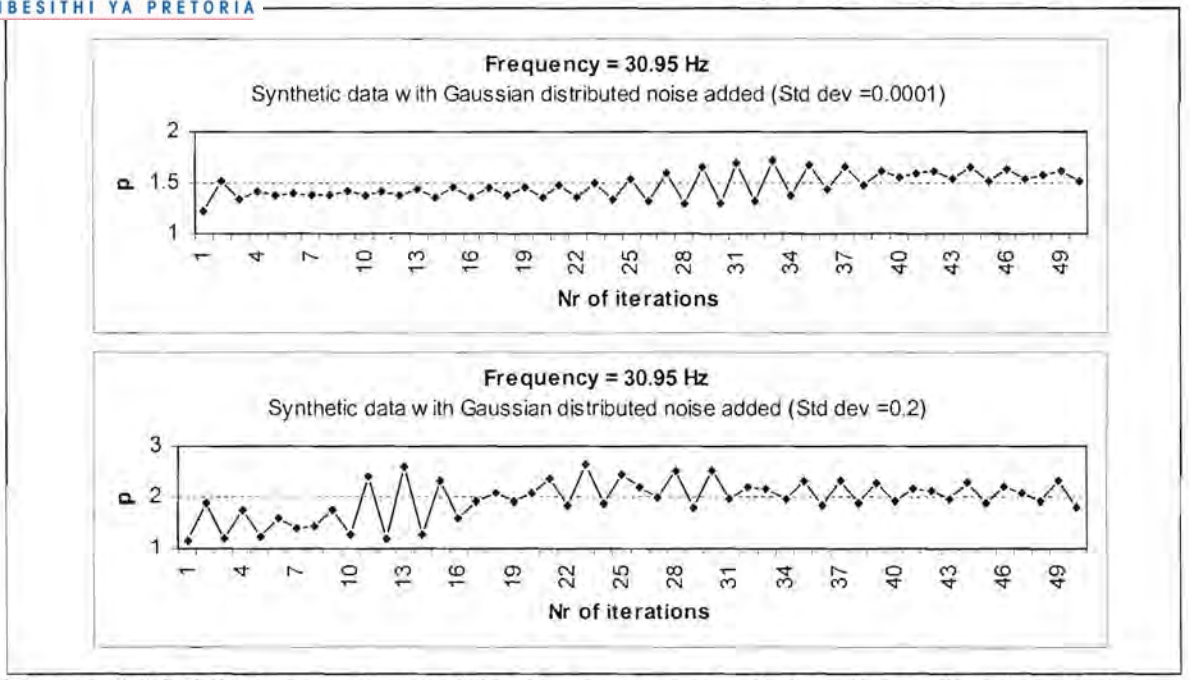

Figure 5.10.5. Values calculated for the exponent p during the estimation of the apparent resistivity values displayed in Figure 5.9 at 30.95 Hz

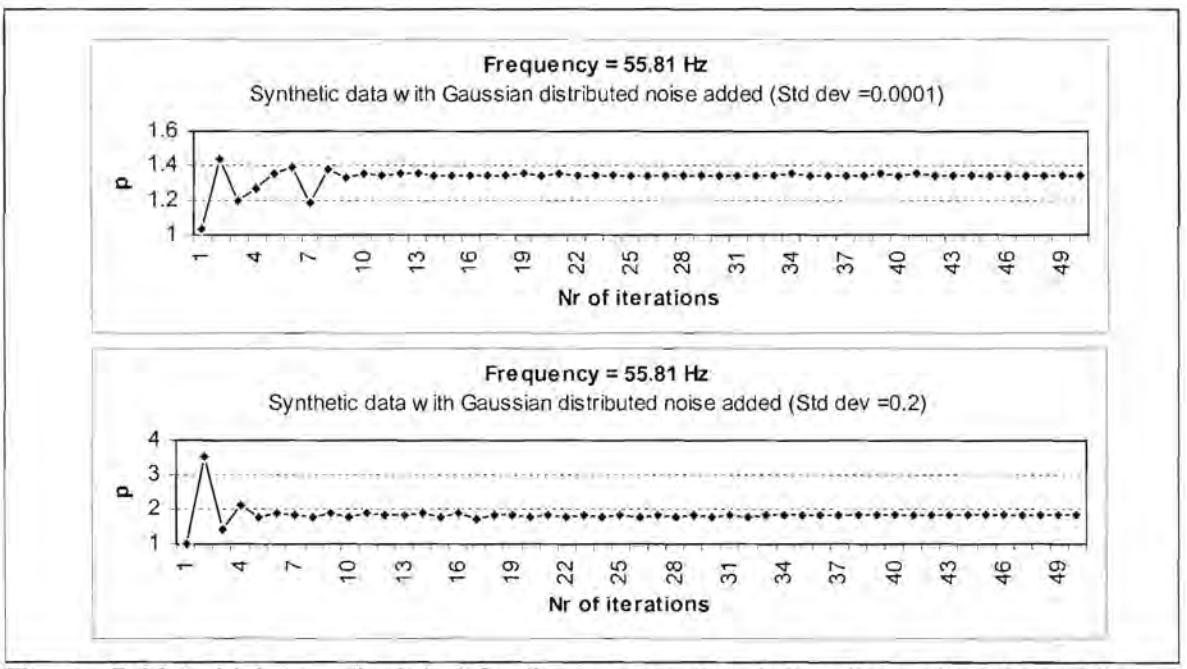

Figure 5.10.6. Values calculated for the exponent p during the estimation of the apparent resistivity values displayed in Figure 5.9 at 55.81Hz

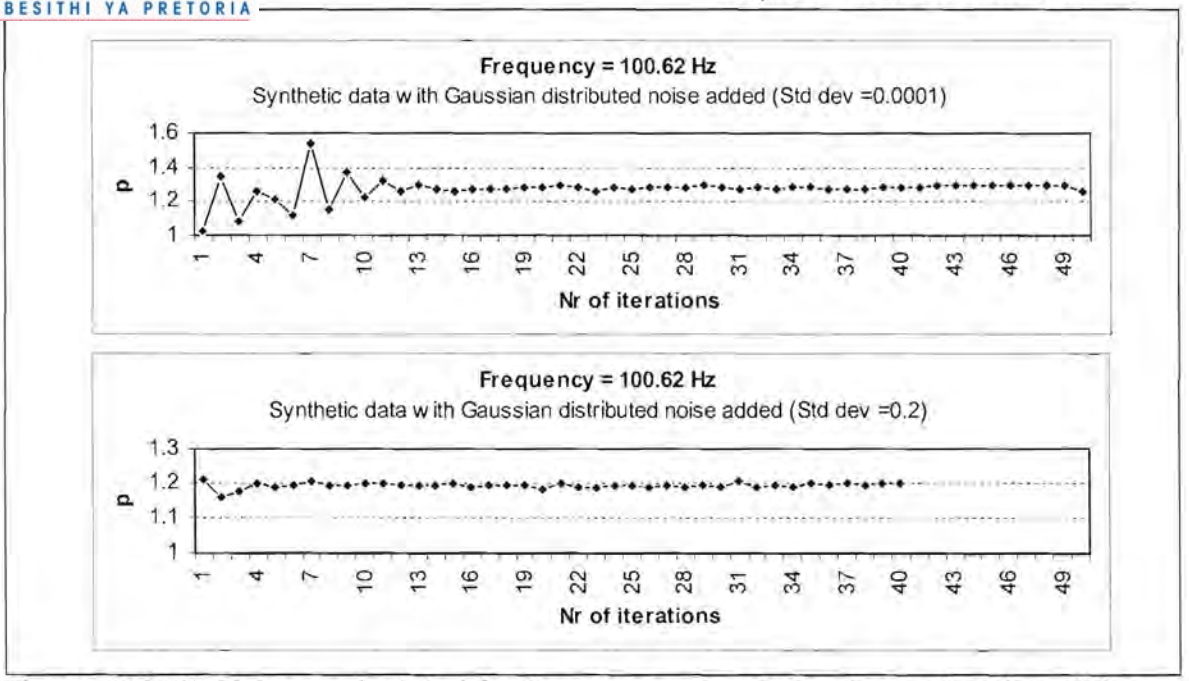

Figure 5.10.7. Values calculated for the exponent p during the estimation of the apparent resistivity values displayed in Figure 5.9 at 100.62 Hz

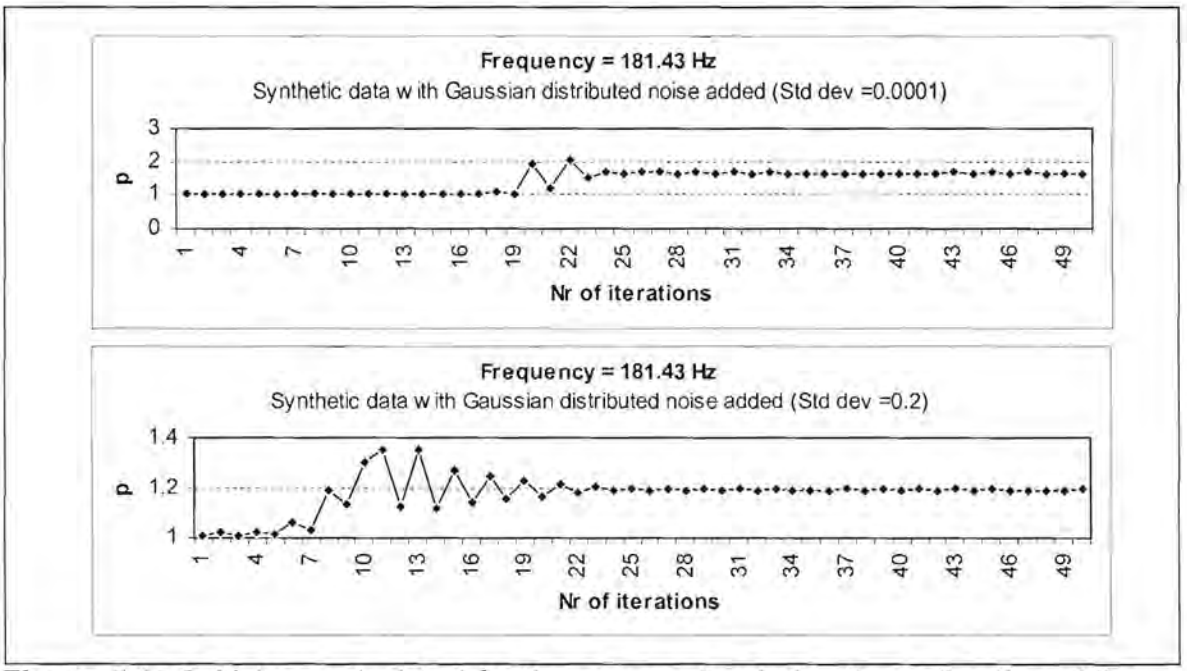

Figure 5.10.8. Values calculated for the exponent p during the estimation of the apparent resistivity values displayed in Figure 5.9 at 181.43 Hz

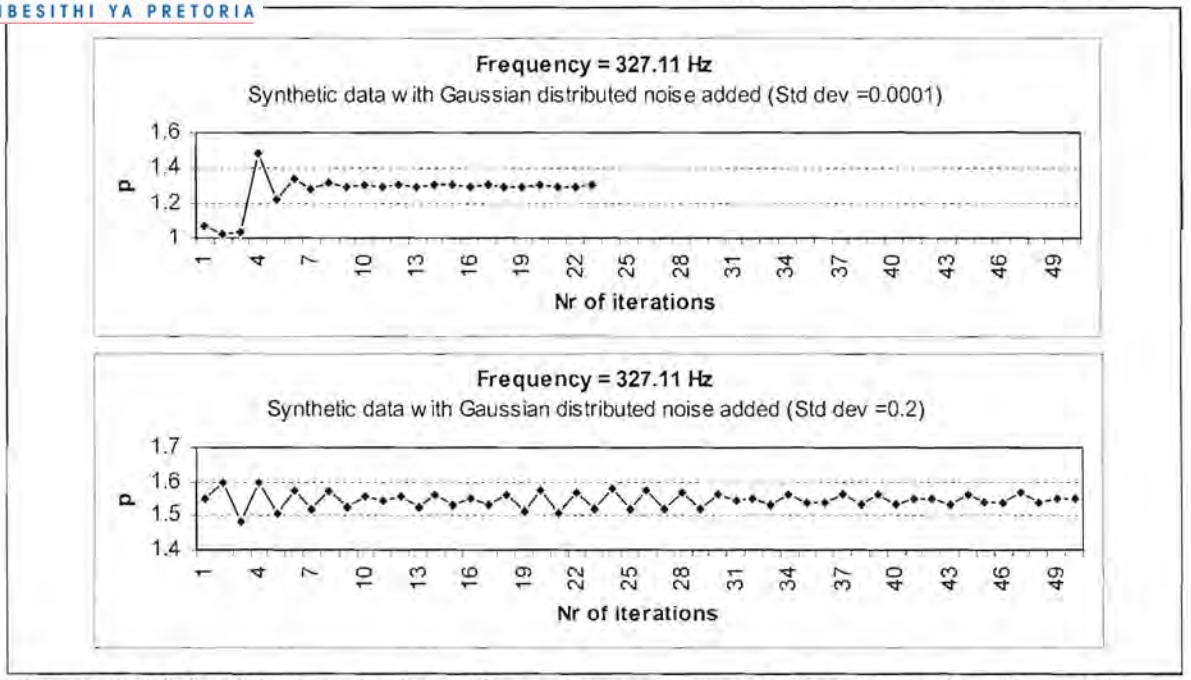

Figure 5.10.9. Values calculated for the exponent p during the estimation of the apparent resistivity values displayed in Figure 5.9 at 327.11 Hz

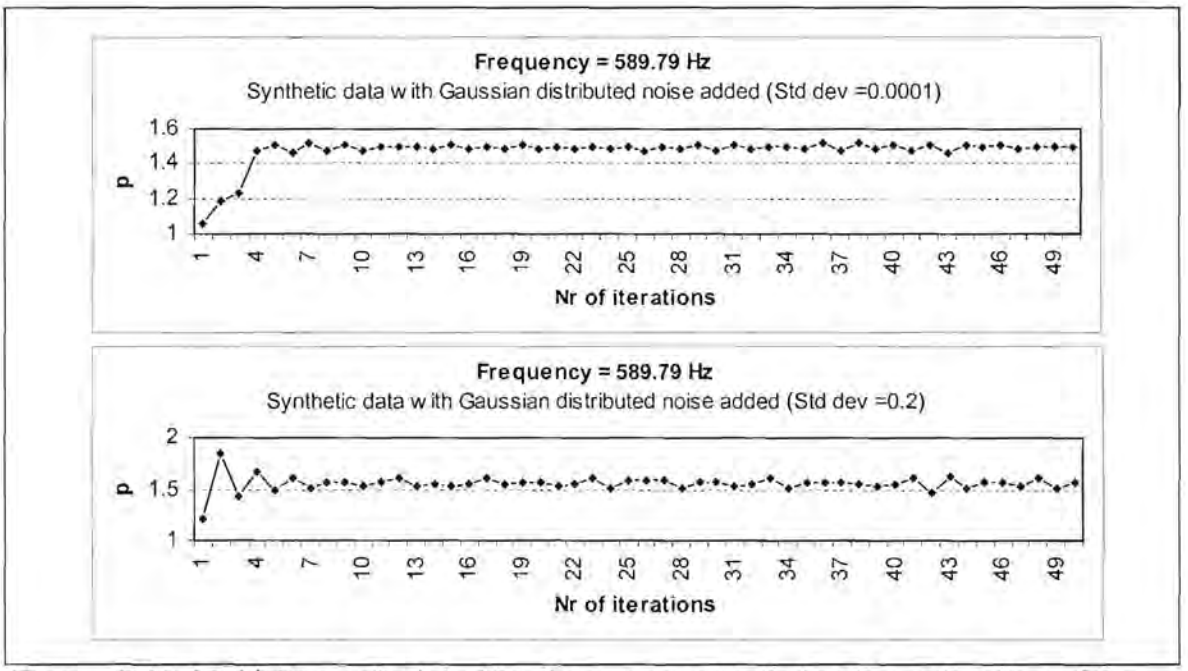

Figure 5.10.10. Values calculated for the exponent p during the estimation of the apparent resistivity values displayed in Figure 5.9 at 589.79 Hz

Using the formula suggested by Sposito et al. (1983) in equation (5.38) to calculate the exponent p, yield the apparent resistivity versus frequency curves shown in Figure 5.11. The results are again of high quality as would be expected for noise with a normal distribution. Figures 5.12.1 to 5.12.10 show the values of p calculated during the adaptive L_p norm process.

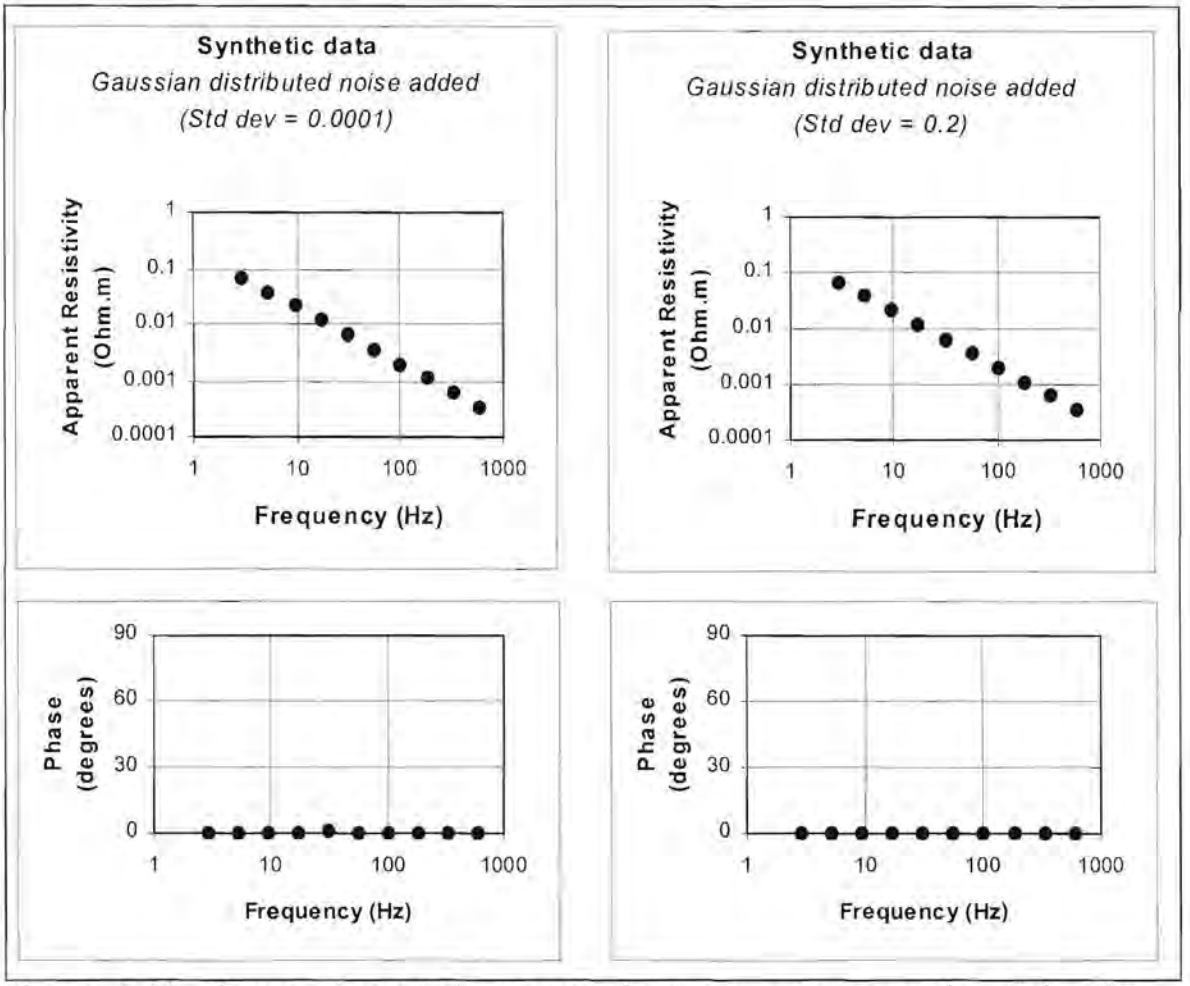

Figure 5.11. Apparent resistivity versus frequency curves produced by the adaptive L_p norm technique for the synthetic data (with Gaussian distributed noise) displayed in Figure 5.5. The formula suggested by Sposito et al. (1983) was used to calculate the exponent p.

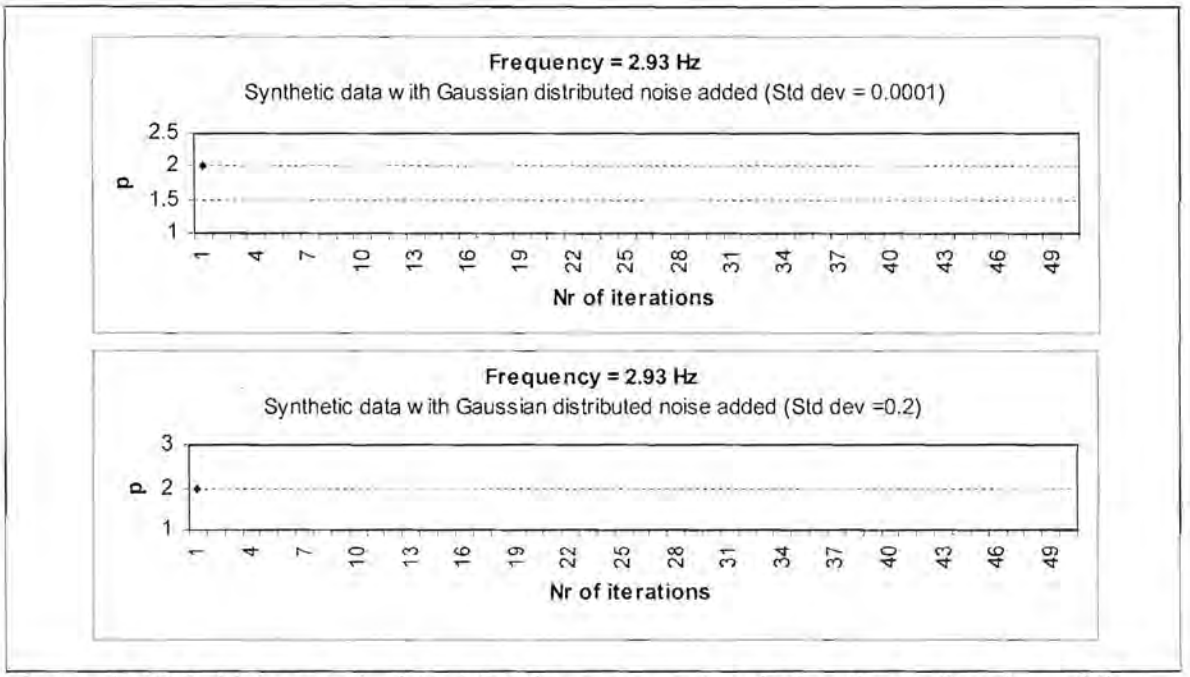

Figure 5.12.1. Values calculated for the exponent p during the estimation of the apparent resistivity values displayed in Figure 5.11 at 2.93 Hz

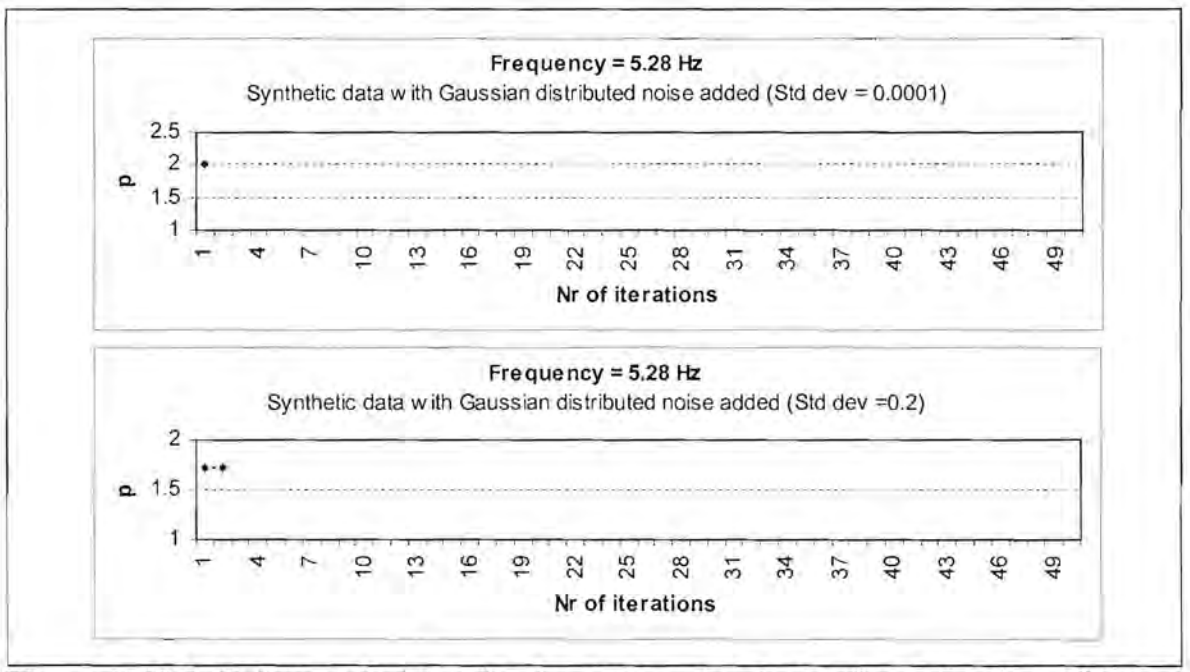

Figure 5.12.2. Values calculated for the exponent p during the estimation of the apparent resistivity values displayed in Figure 5.11 at 5.28 Hz

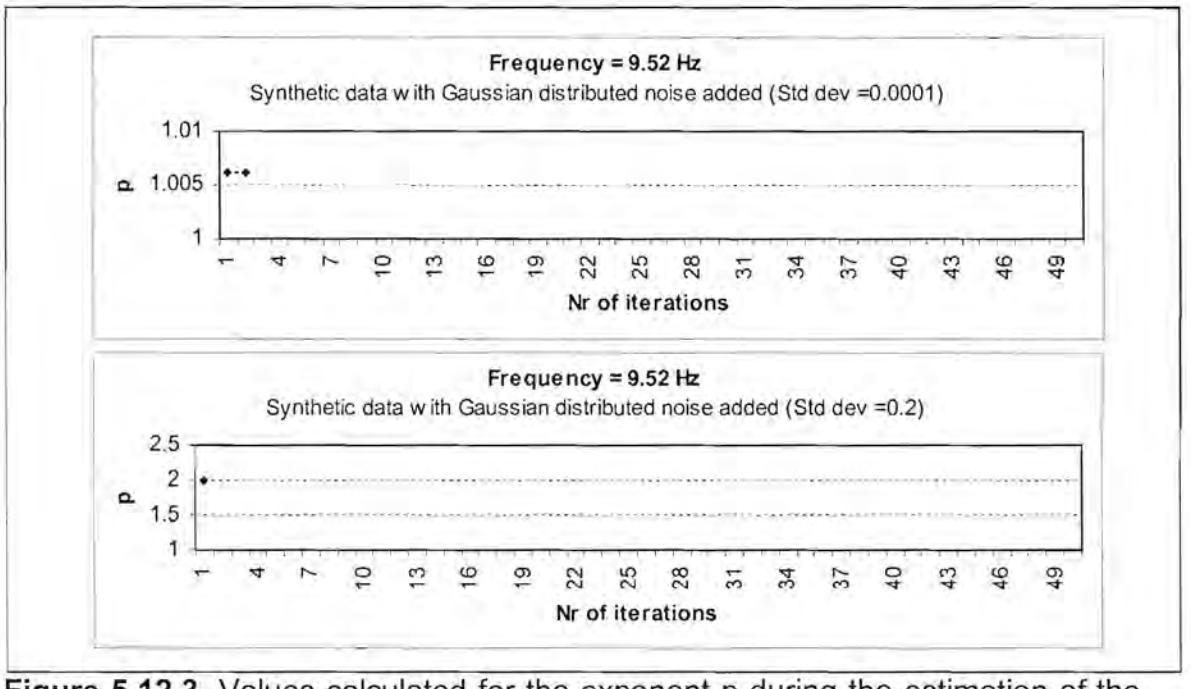

Figure 5.12.3. Values calculated for the exponent p during the estimation of the apparent resistivity values displayed in Figure 5.11 at 9.52 Hz

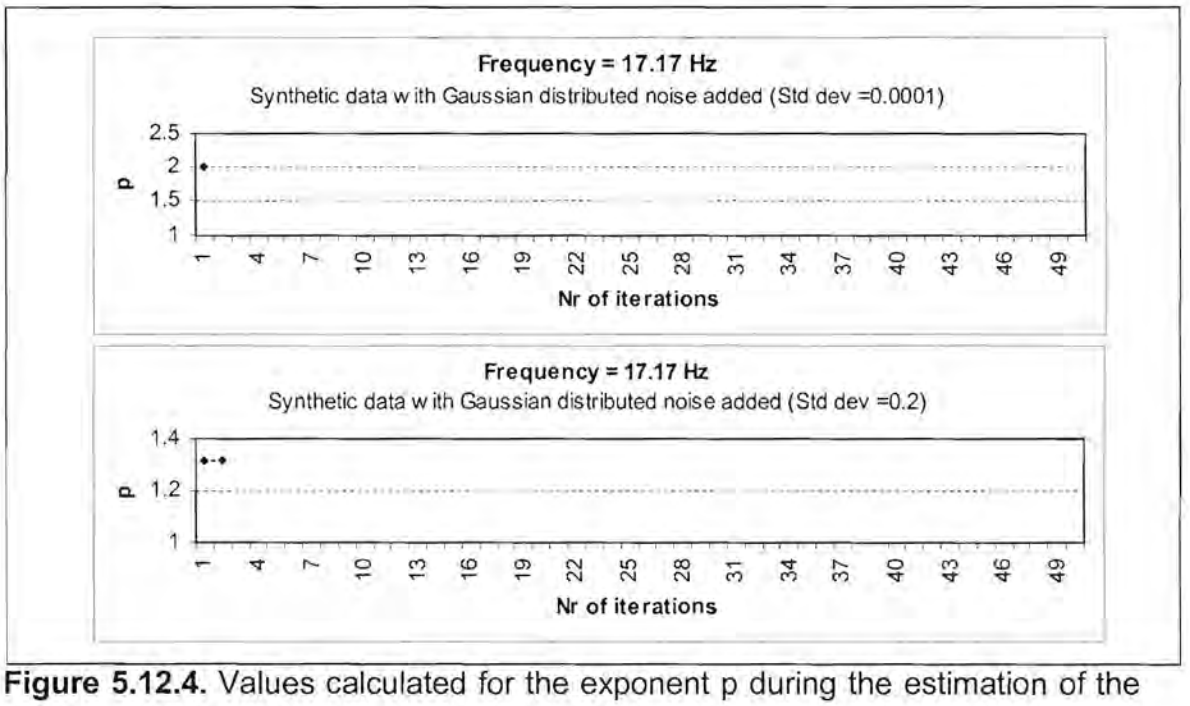

Figure 5.12.4. Values calculated for the exponent p during the estimation of the apparent resistivity values displayed in Figure 5.11 at 17.17 Hz

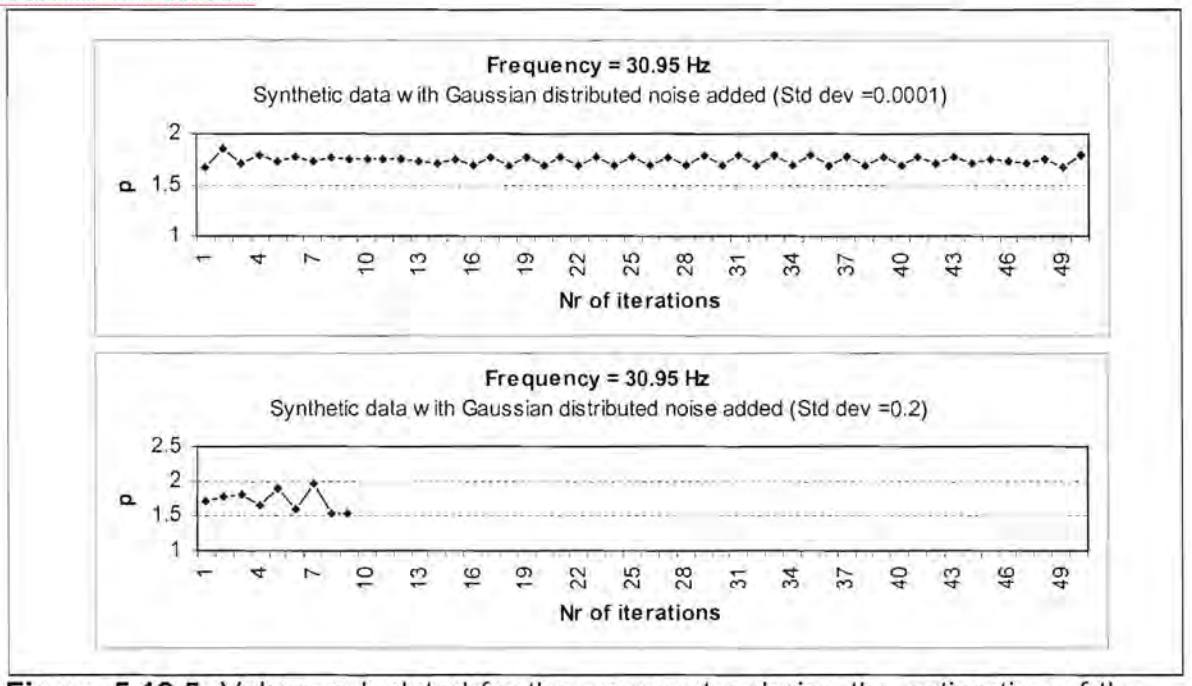

Figure 5.12.5. Values calculated for the exponent p during the estimation of the apparent resistivity values displayed in Figure 5.11 at 30.95 Hz

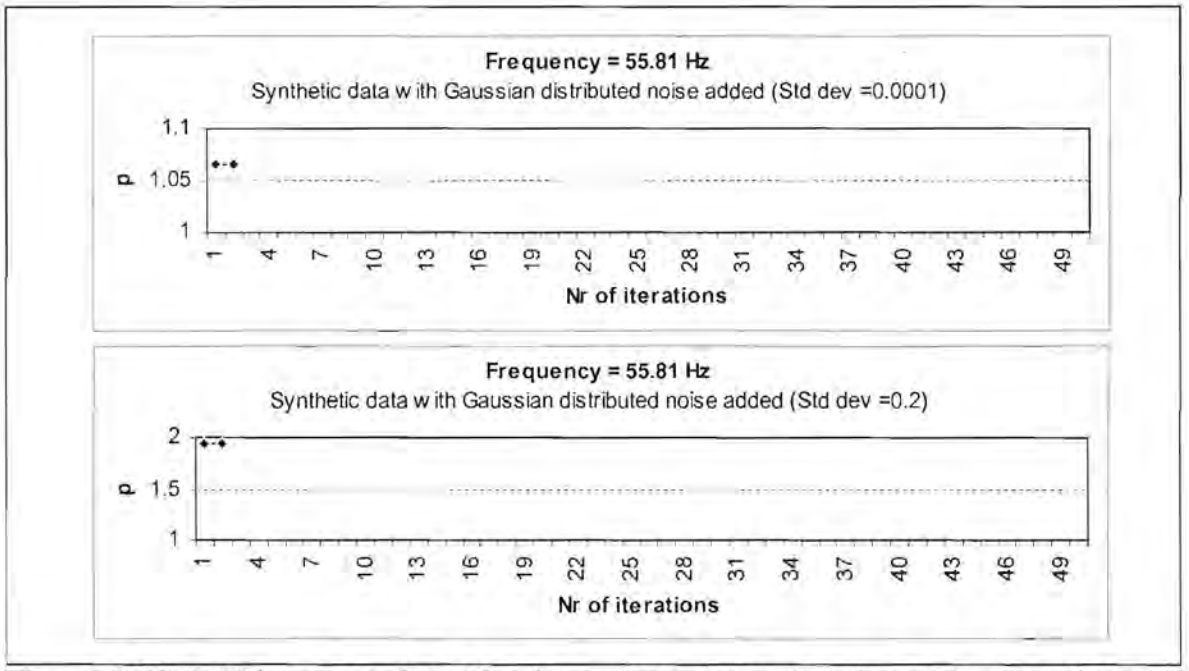

Figure 5.12.6. Values calculated for the exponent p during the estimation of the apparent resistivity values displayed in Figure 5.11 at 55.81 Hz

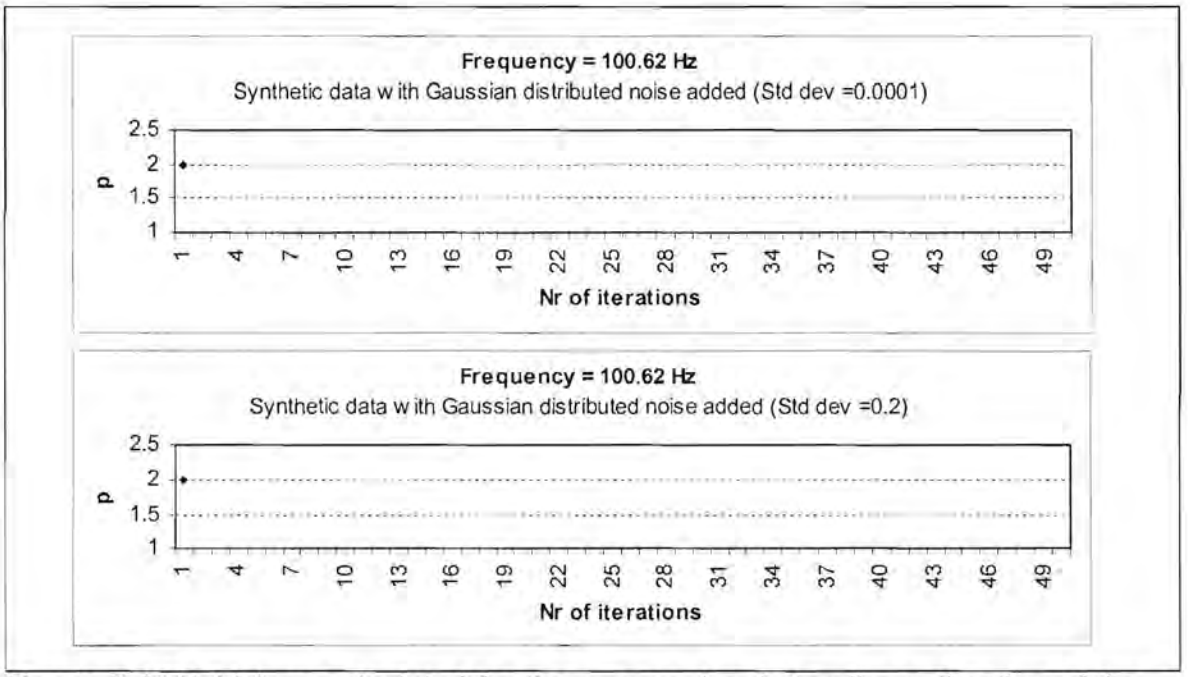

Figure 5.12.7. Values calculated for the exponent p during the estimation of the apparent resistivity values displayed in Figure 5.11 at 100.62 Hz

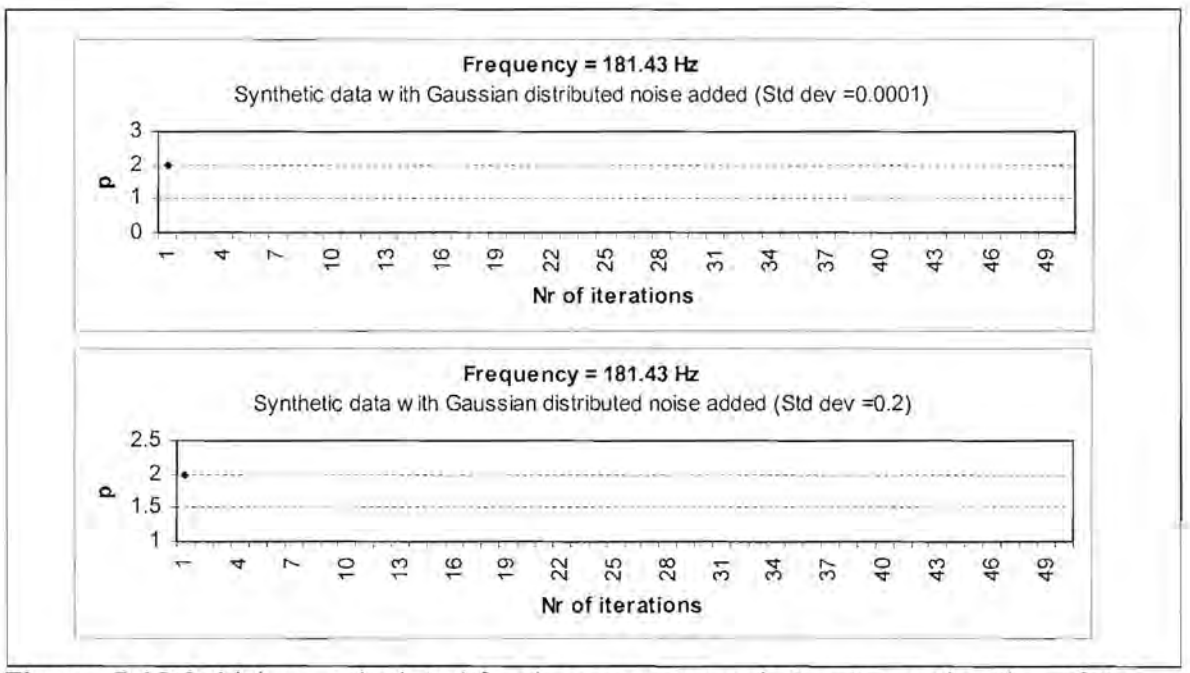

Figure 5.12.8. Values calculated for the exponent p during the estimation of the apparent resistivity values displayed in Figure 5.11 at 181.43 Hz

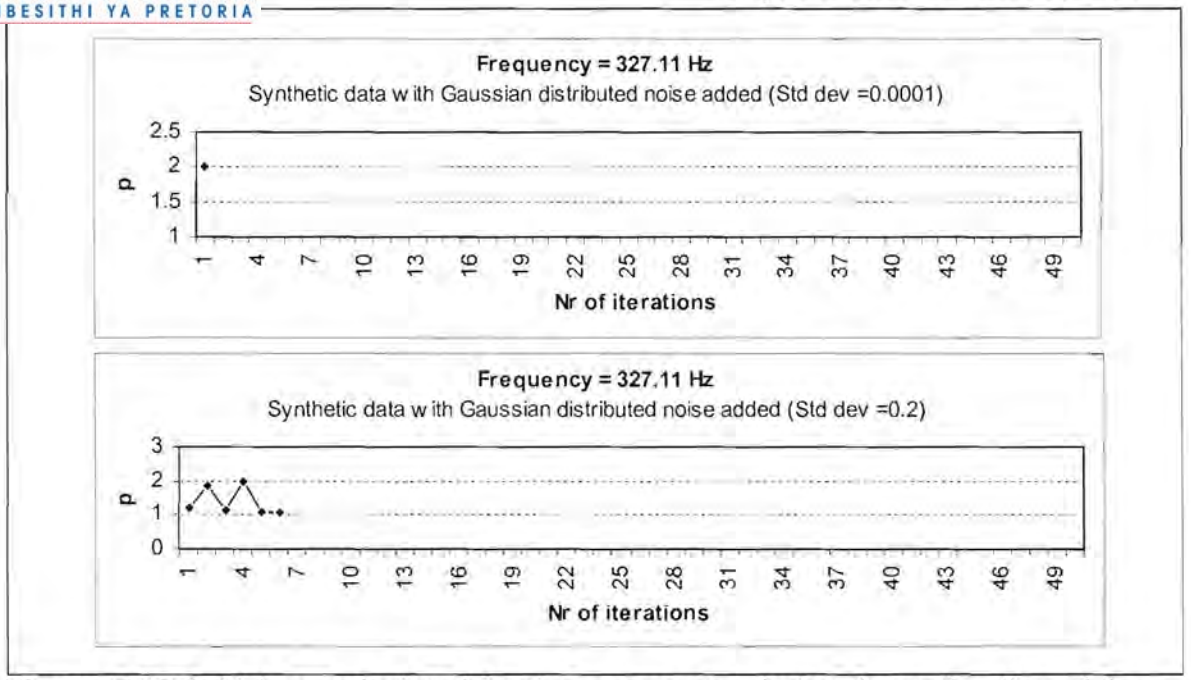

Figure 5.12.9. Values calculated for the exponent p during the estimation of the apparent resistivity values displayed in Figure 5.11 at 327.11 Hz

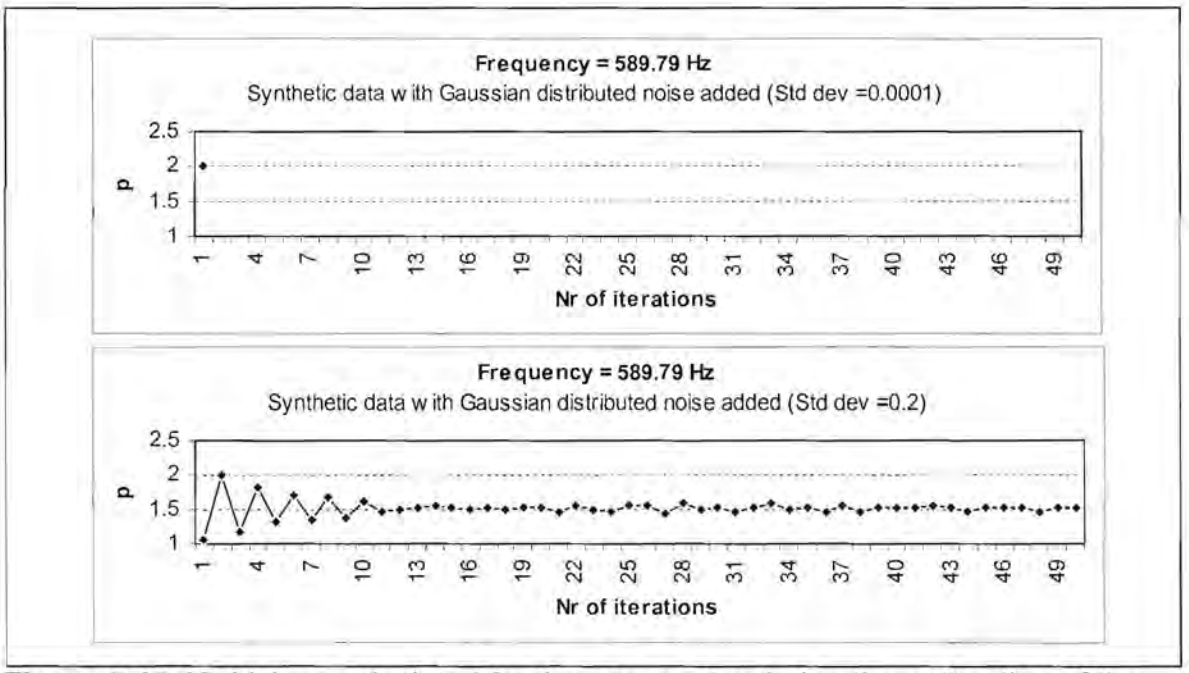

Figure 5.12.10. Values calculated for the exponent p during the estimation of the apparent resistivity values displayed in Figure 5.11 at 589.79 Hz

The amount of iterations is markedly less when Sposito's formula is used in the estimation of p. A main reason for this is that equation (5.38) does not allow p to be greater than two. The adaptive procedure is terminated when p becomes too large.

The minimisation using the Robust M estimation technique also yielded very good results (Figure 5.13), similar to the L_1, L_2 and adaptive L_p norm methods.

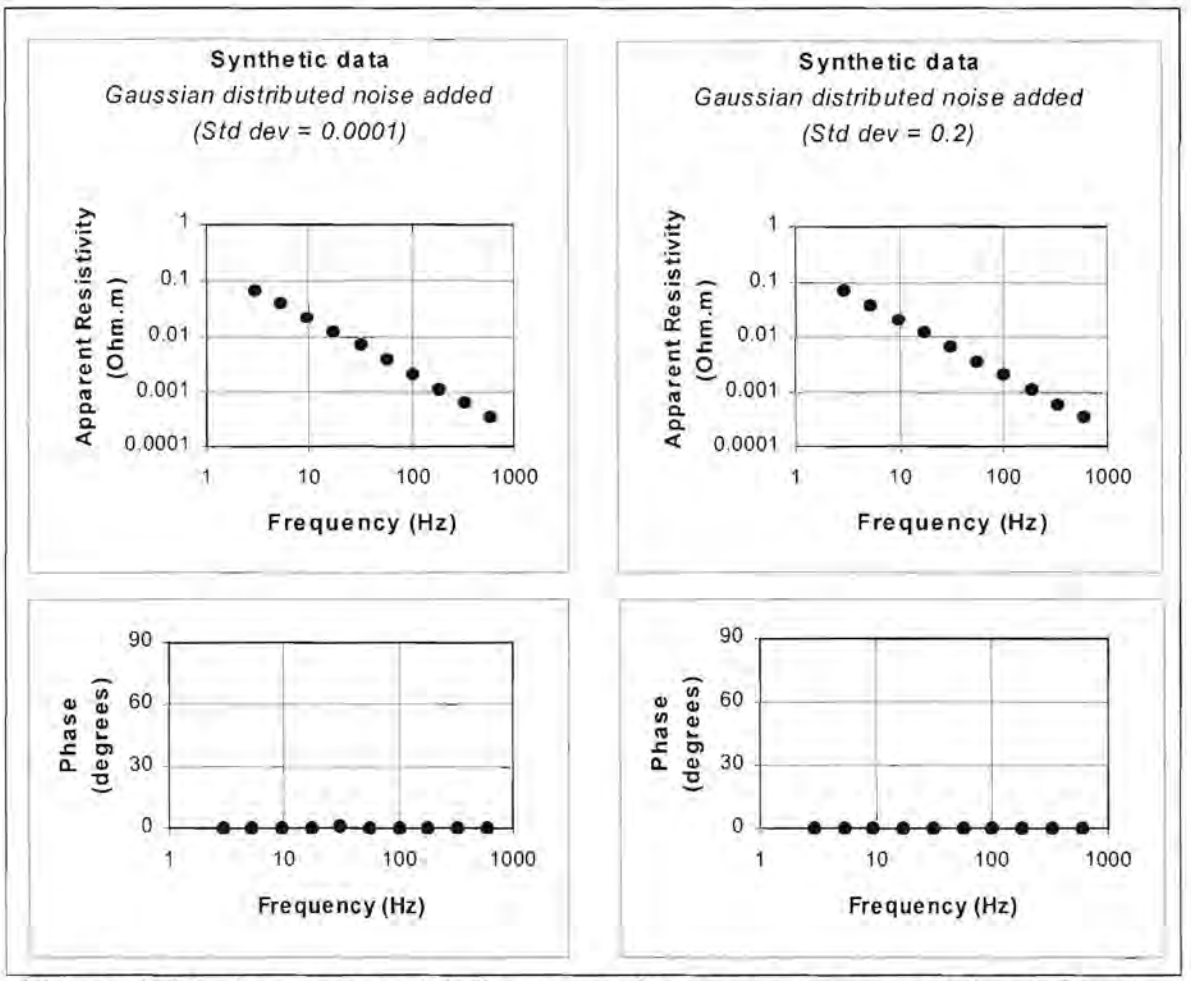

Figure 5.13. Apparent resistivity versus frequency curves produced by the Robust M estimation technique for the synthetic data (with Gaussian distributed noise) displayed in Figure 5.5.

All of the tested statistical reduction methods yielded good results for data containing normally distributed errors, as would be expected. An increase in standard deviation of the noise did not affect the quality of the estimated curves.

5.5.2. Synthetic data with non-Gaussian distributed random errors

Figure 5.14 shows two curves, both with Gaussian distributed random noise added. In this case the mean is 0.0 and the standard deviation is 1.0 for both

curves. Random noise without a specific distribution was added to the data in the first curve. This introduced outliers to the data.

Figure 5.14. Apparent resistivity versus frequency curves using the unit impedance with Gaussian and randomly distributed noise added.

The Q-Q plots for these two data sets calculated at a frequency where outliers are clearly visible (Figure 5.15) confirm that the noise in the first curve does not have a perfect normal distribution. The correlation coefficients between the observed and expected residuals are 0.771726 for the curve with the randomly distributed errors, and 0.984253 for the data containing only normally distributed errors.

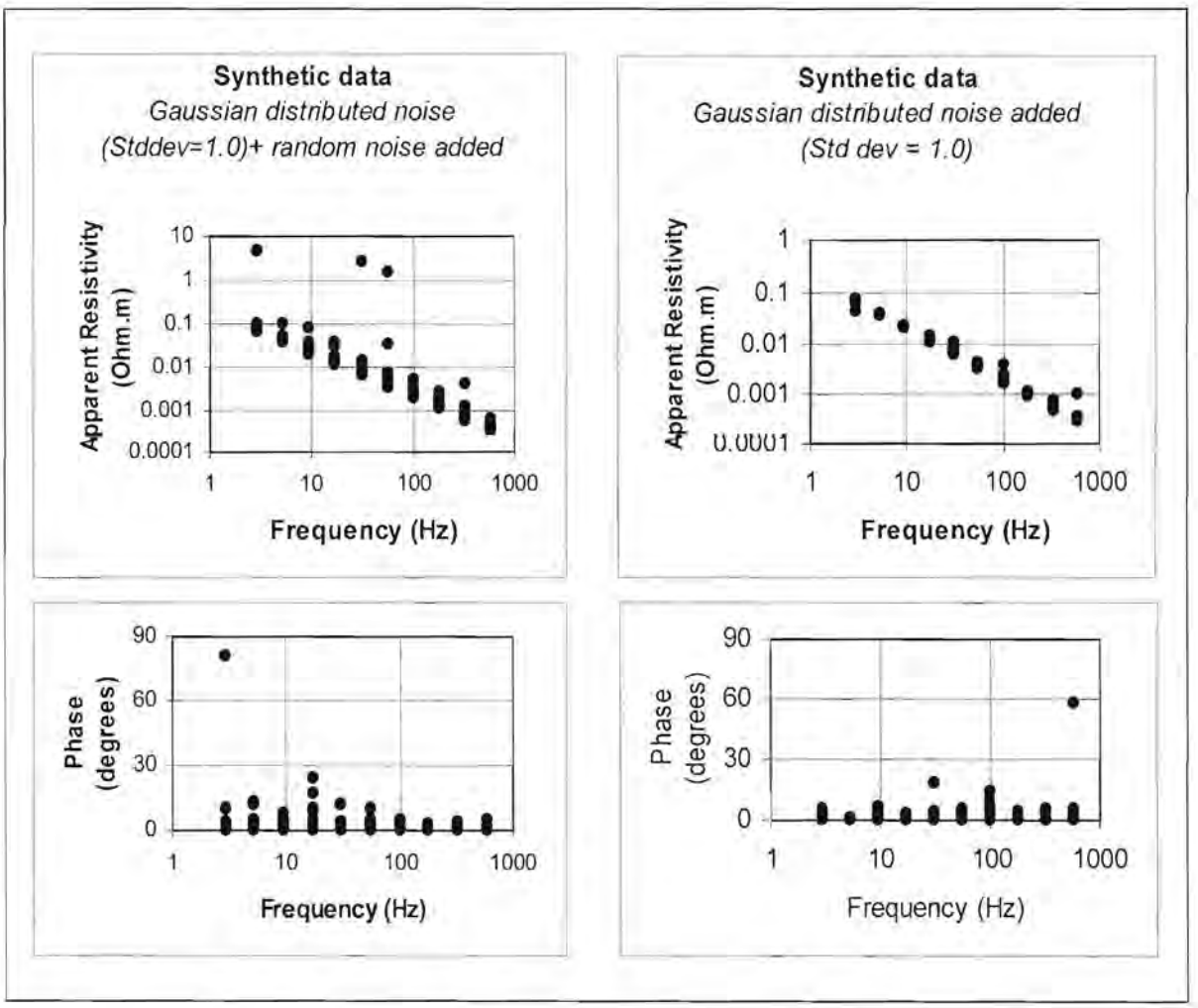

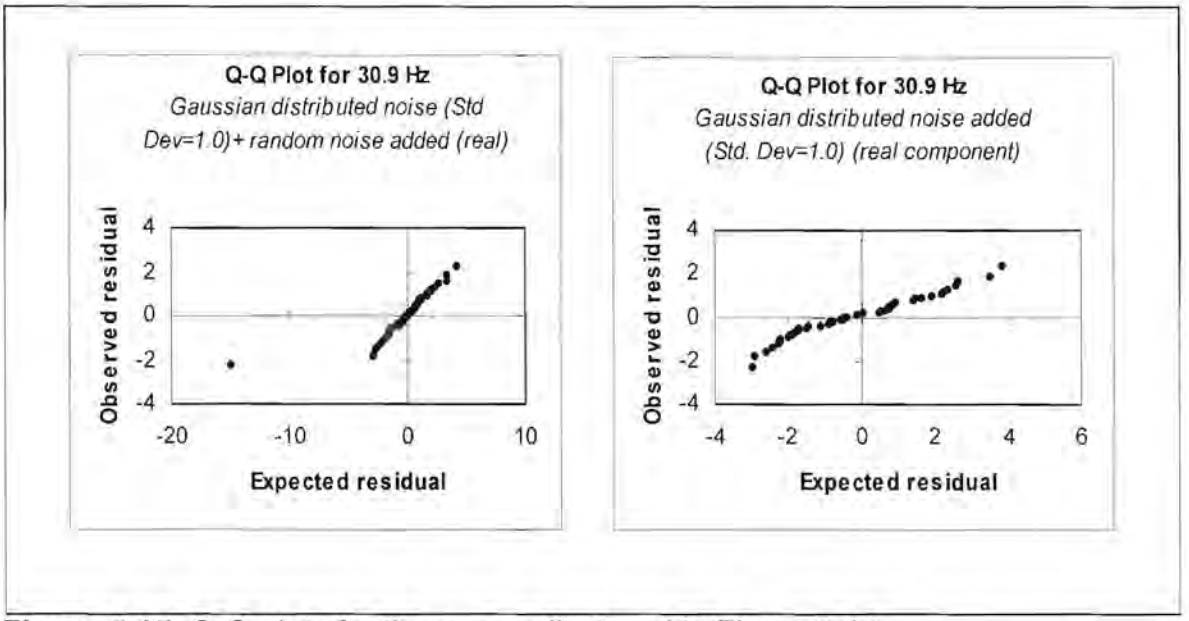

Figure 5.15. Q-Q plots for the curves displayed in Figure 5.14.

The curves fitted to the data using the L_1 and L_2 norms yield very different results (Figures 5.16 and 5.17). The L_1 norm produces a good fit for the apparent resistivity curve and a mediocre fit for the phase curve. In contrast with this the L_2 norm results in a very bad fit for both apparent resistivities and phases compared to the L_1 norm. Phases calculated for the data containing only Gaussian distributed noise also show larger misfits at higher frequencies.

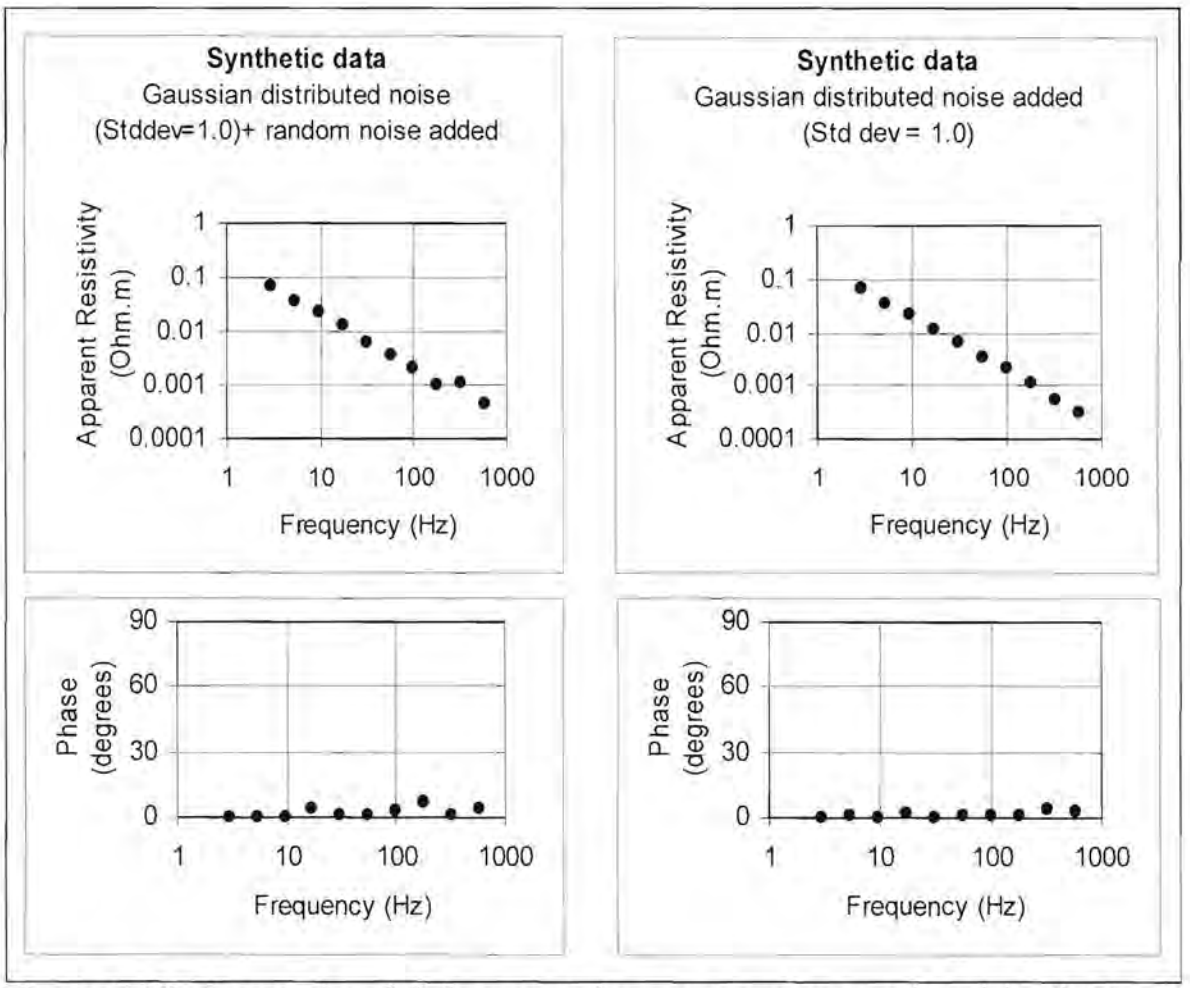

Figure 5.16. Apparent resistivity versus frequency curves produced by the L_1 norm estimation technique for the synthetic data displayed in Figure 5.14.

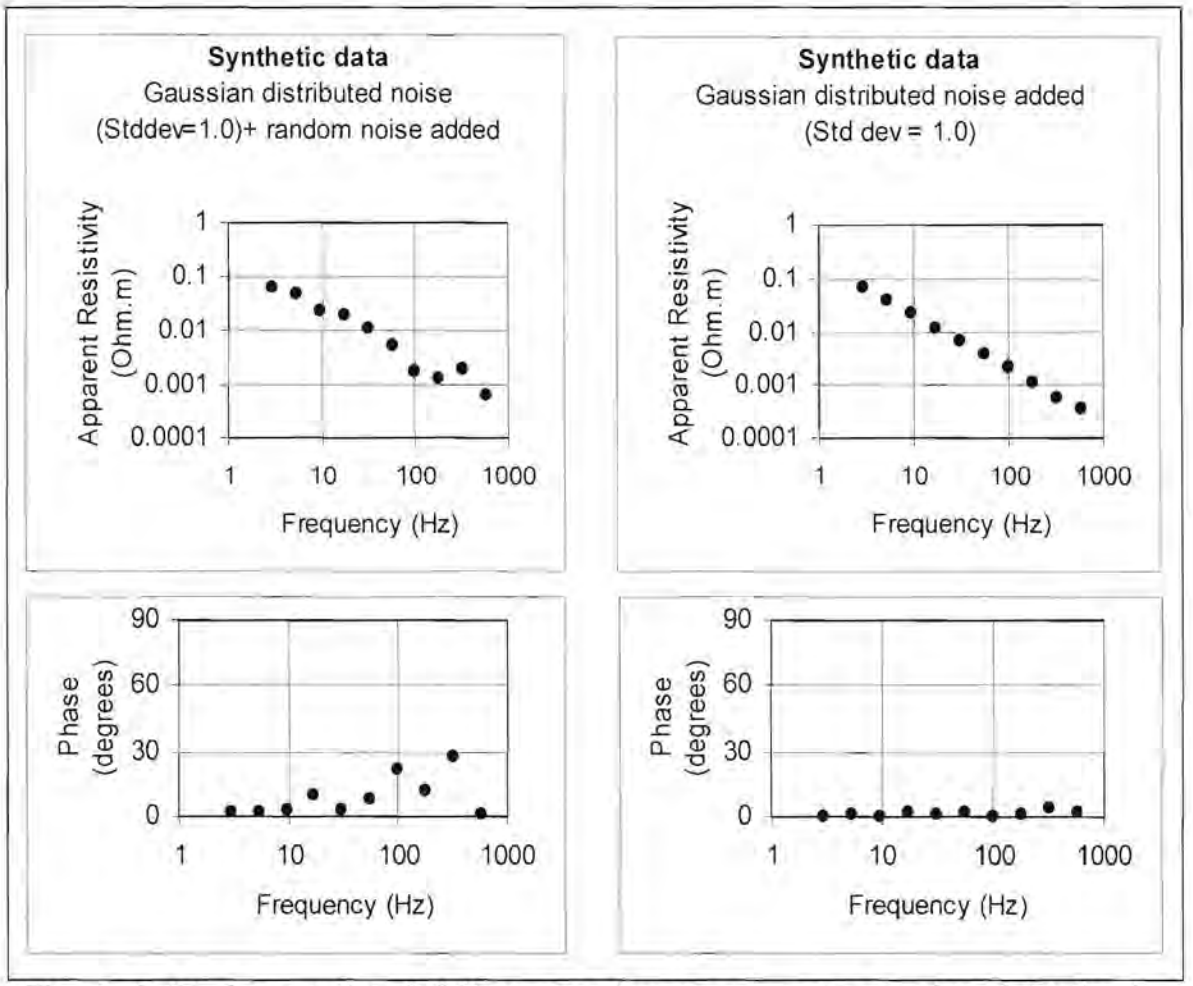

Figure 5.17. Apparent resistivity versus frequency curves produced by the L_2 norm estimation technique for the synthetic data displayed in Figure 5.14.

Results obtained with the adaptive L_p norm procedure and using Money et al.'s method of calculating p (equation 5.37) are depicted in Figure 5.18. The apparent resistivity curve is very similar to the curve estimated with the L_1 norm. The phase data again yield better results than the L_2 norm but worse results than the L_1 norm. Figures 5.19.1 to 5.19.10 show the value for p calculated during each iteration.

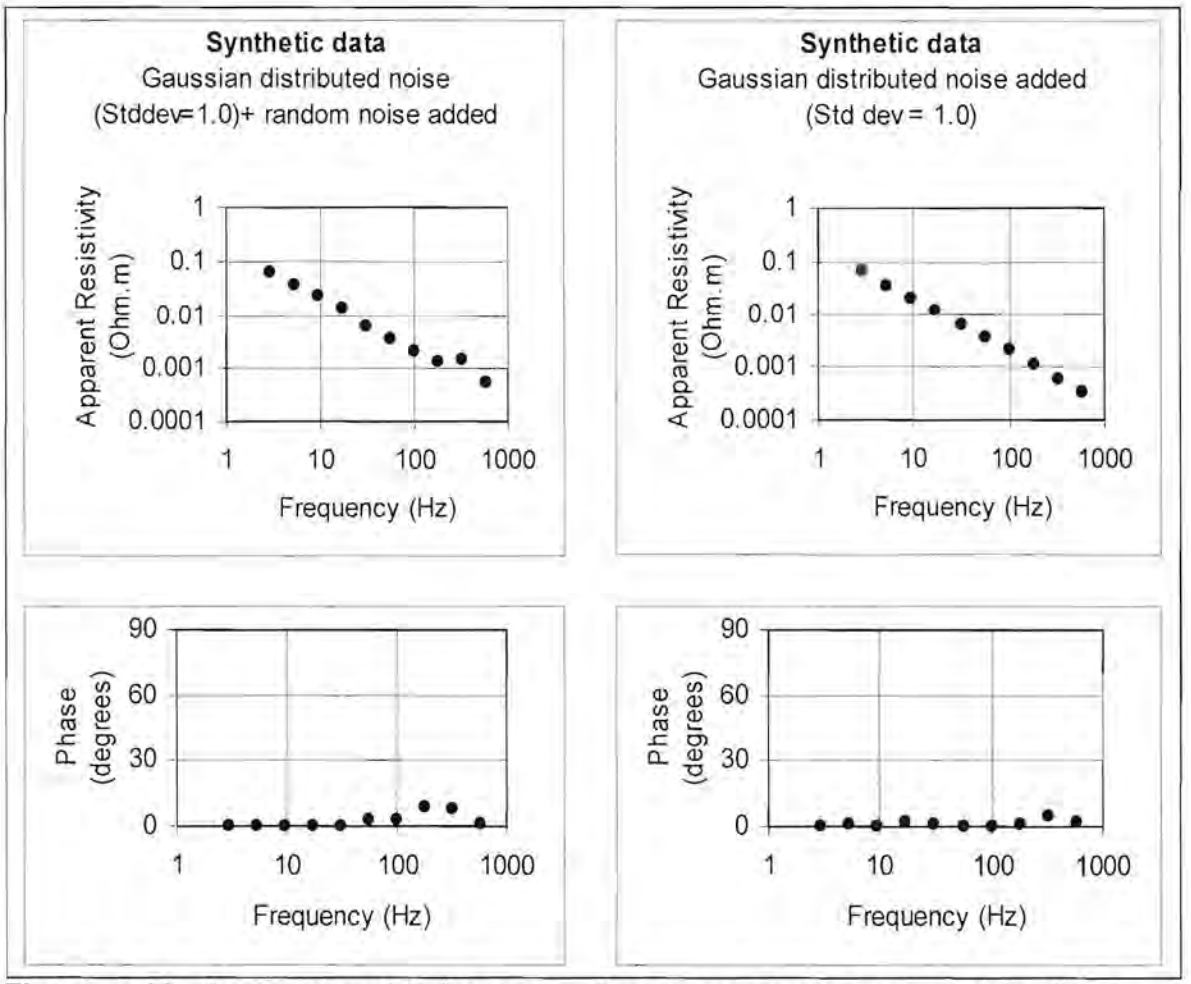

Figure 5.18. Apparent resistivity versus frequency curves produced by the L_p norm estimation technique for the synthetic data displayed in Figure 5.14. Money et al.'s (1982) equation was used to calculate p.

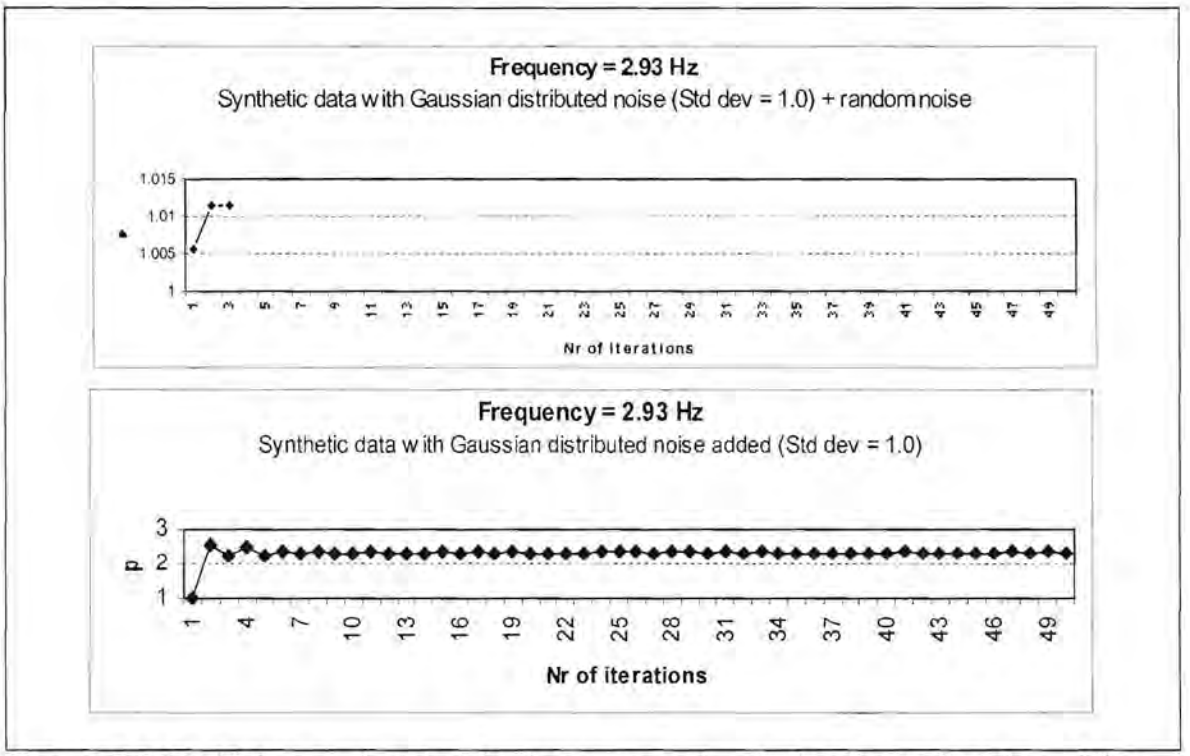

Figure 5.19.1. Values calculated for the exponent p during the estimation of the apparent resistivity values displayed in Figure 5.18 at 2.93 Hz

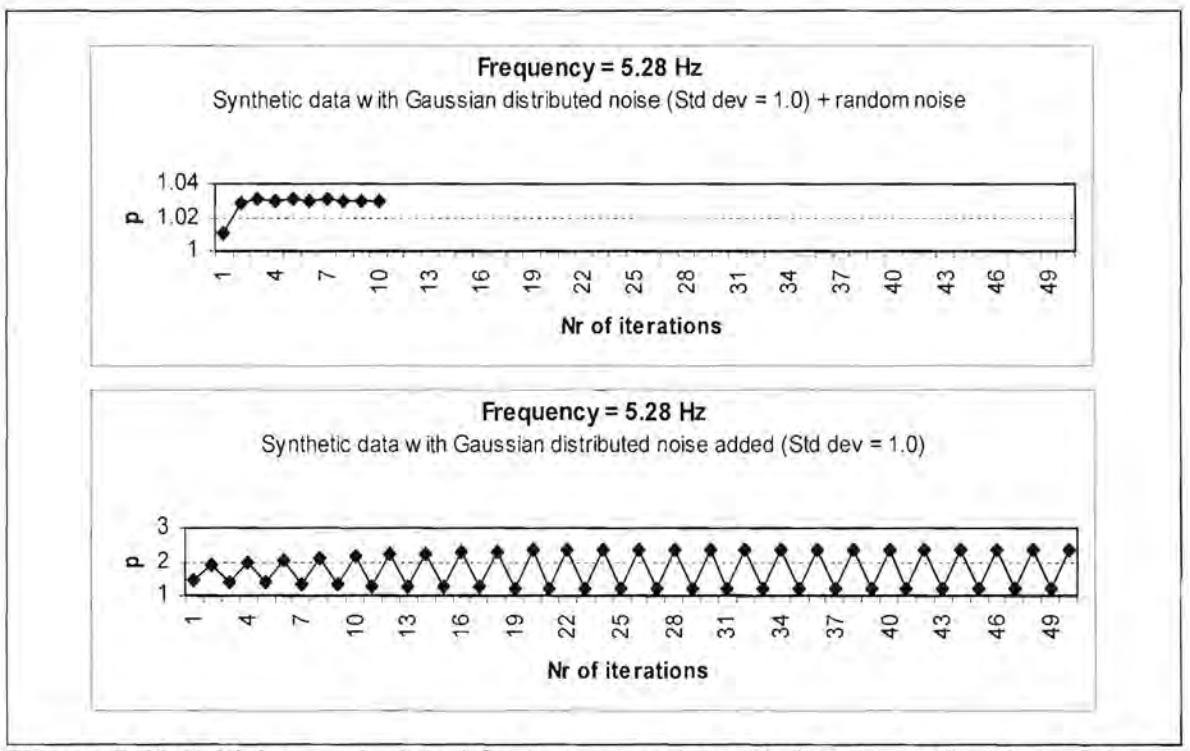

Figure 5.19.2. Values calculated for the exponent p during the estimation of the apparent resistivity values displayed in Figure 5.18 at 5.28 Hz

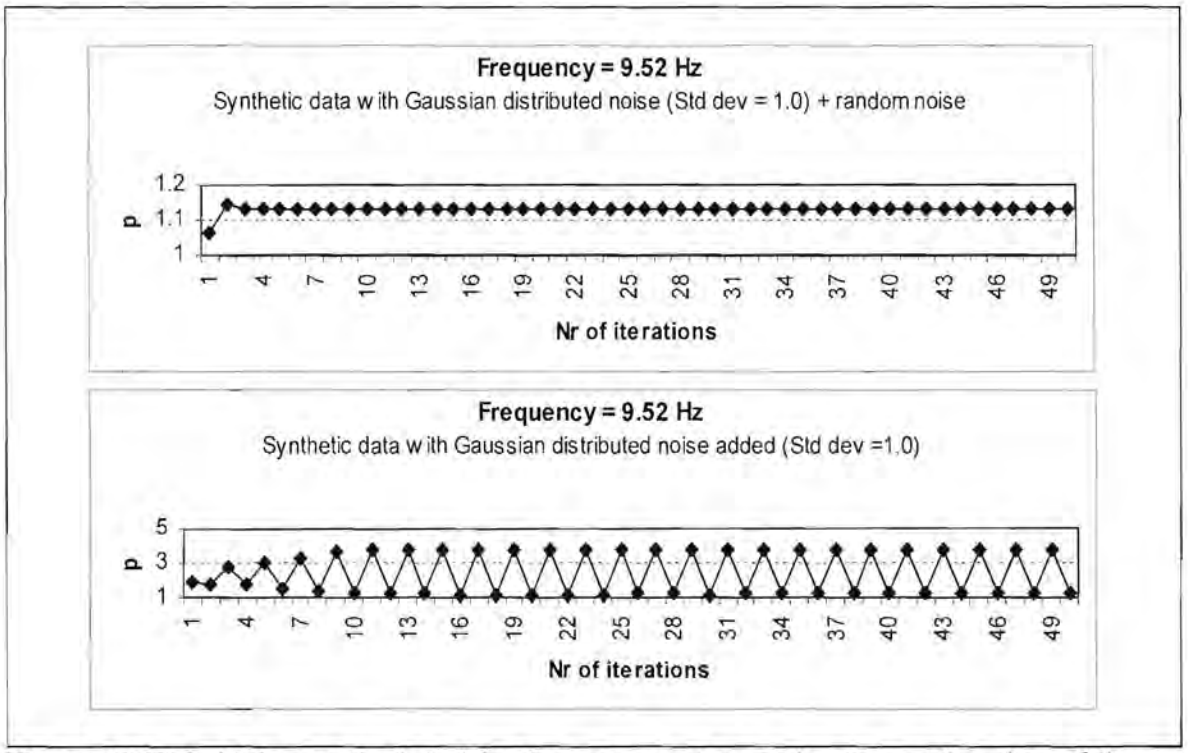

Figure 5.19.3. Values calculated for the exponent p during the estimation of the apparent resistivity values displayed in Figure 5.18 at 9.52 Hz

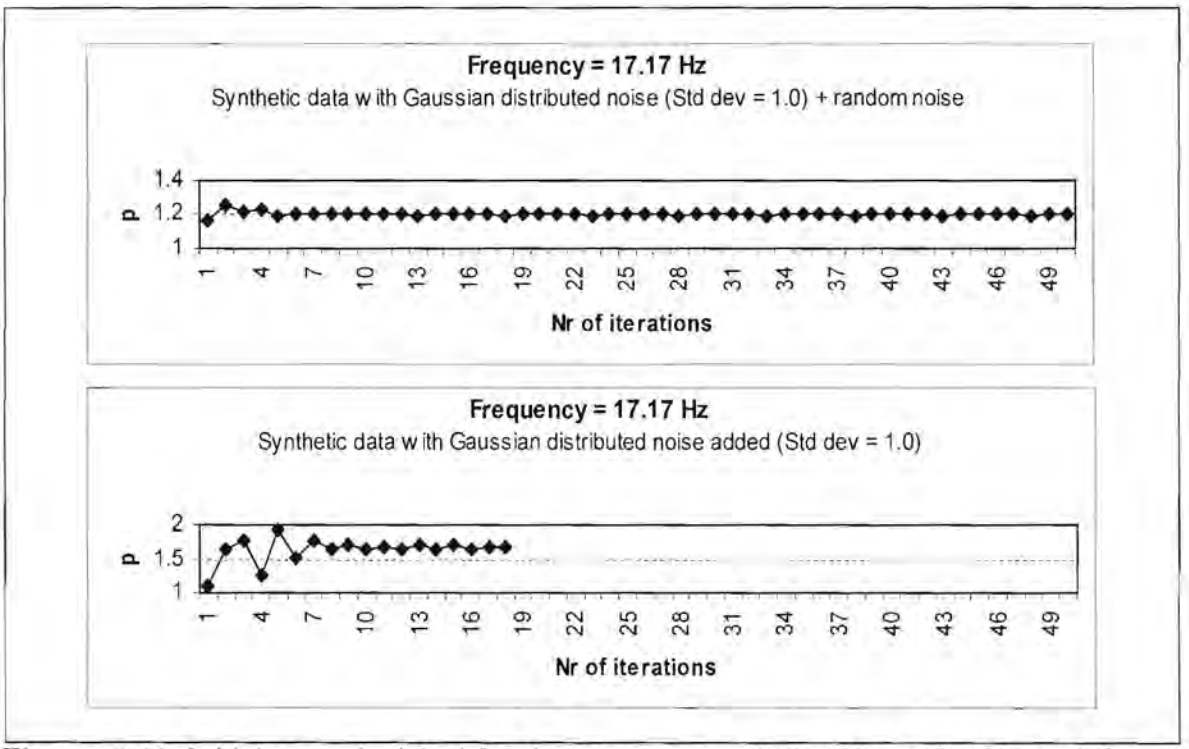

Figure 5.19.4. Values calculated for the exponent p during the estimation of the apparent resistivity values displayed in Figure 5.18 at 17.17 Hz

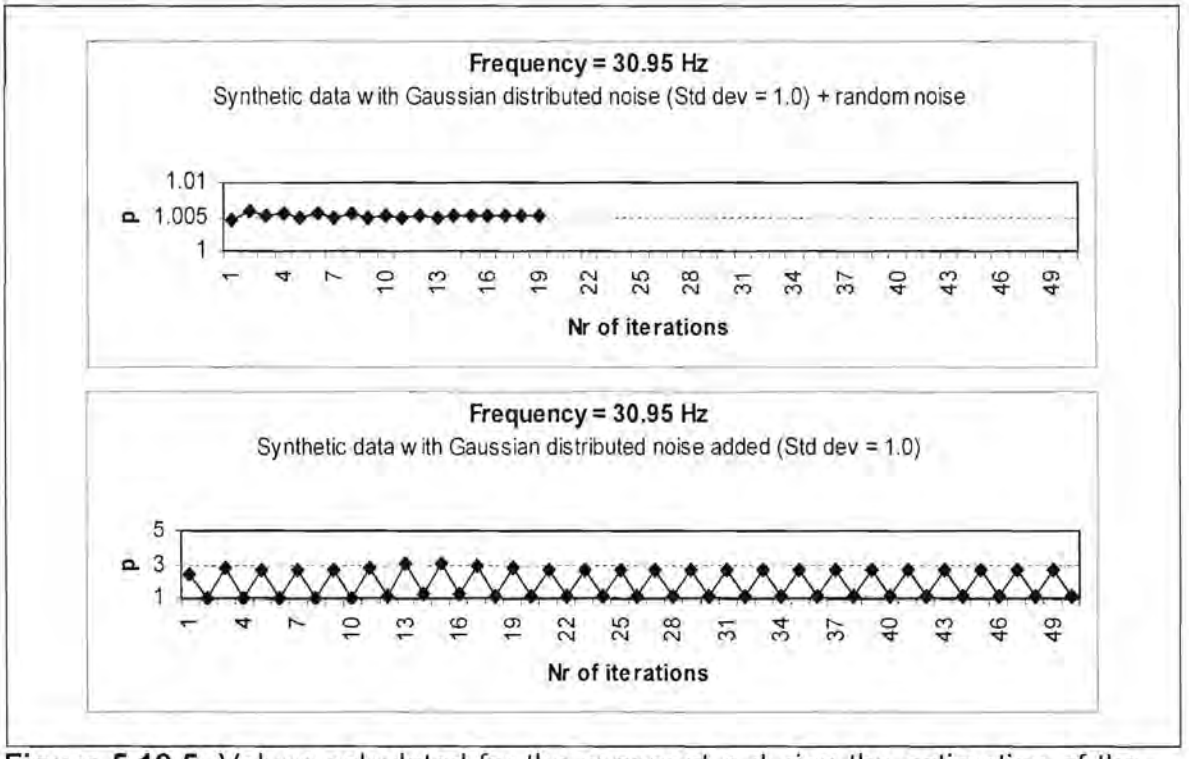

Figure 5.19.5. Values calculated for the exponent p during the estimation of the apparent resistivity values displayed in Figure 5.18 at 30.95 Hz

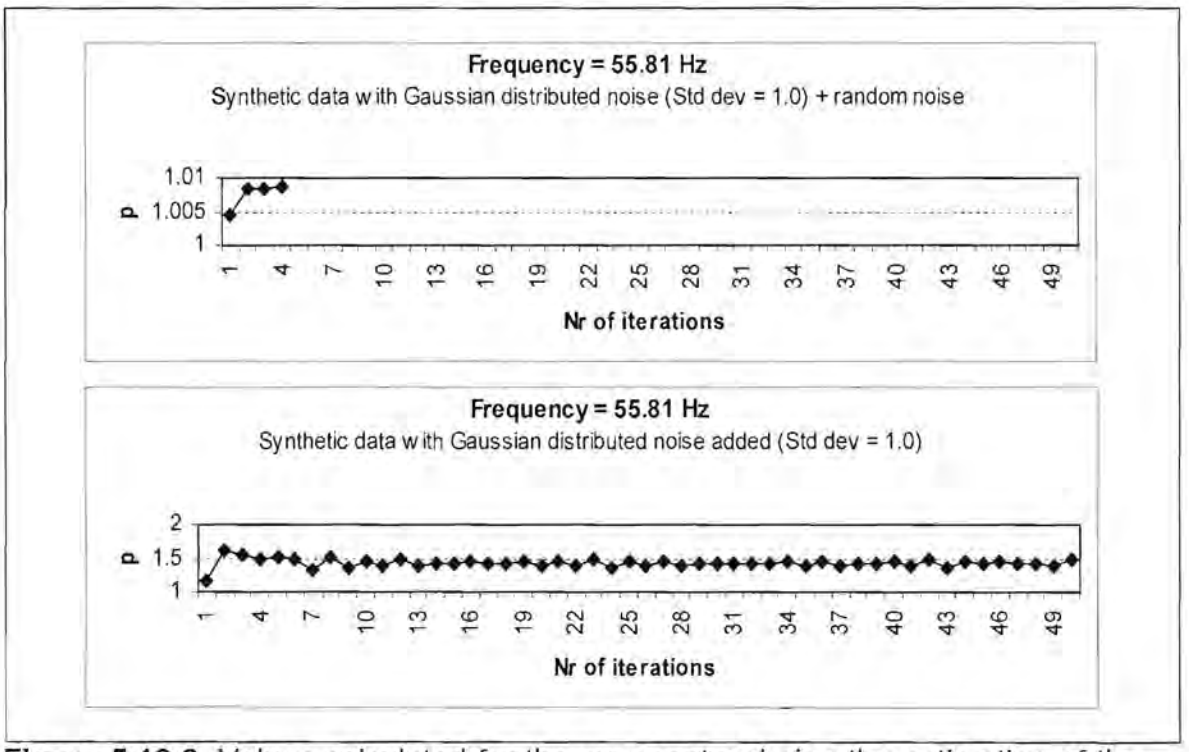

Figure 5.19.6. Values calculated for the exponent p during the estimation of the apparent resistivity values displayed in Figure 5.18 at 55.81 Hz

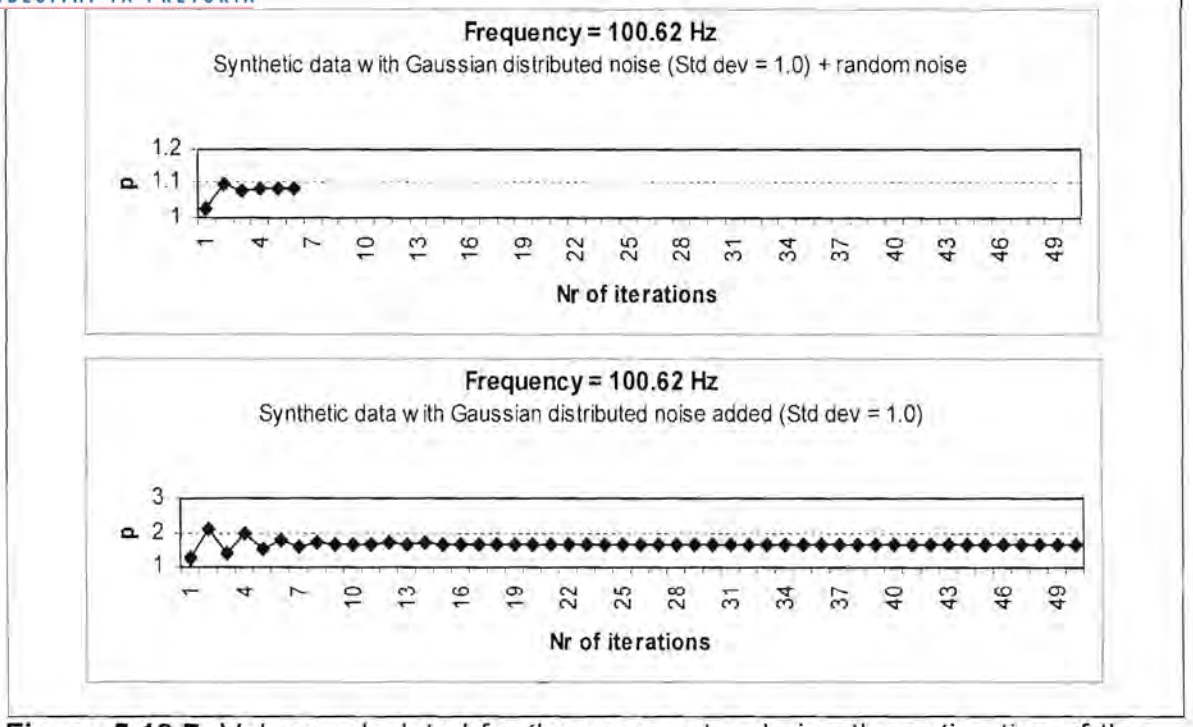

Figure 5.19.7. Values calculated for the exponent p during the estimation of the apparent resistivity values displayed in Figure 5.18 at 100.62 Hz

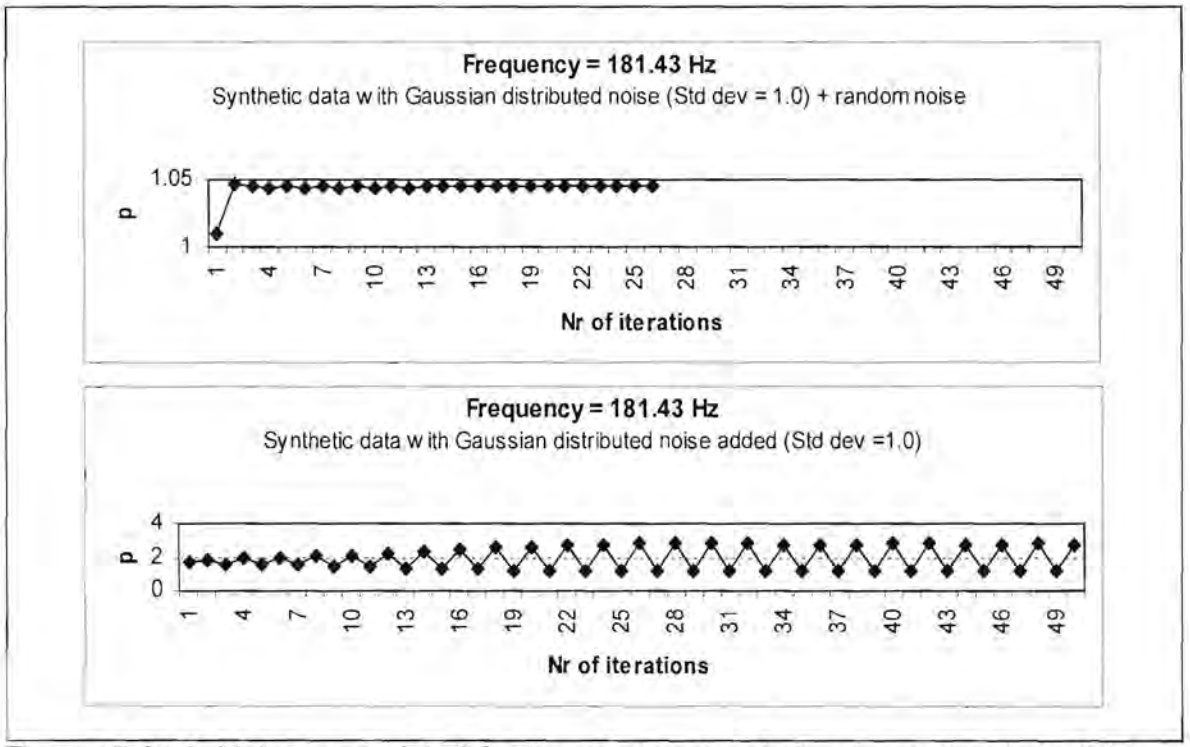

Figure 5.19.8. Values calculated for the exponent p during the estimation of the apparent resistivity values displayed in Figure 5.18 at 181.43 Hz

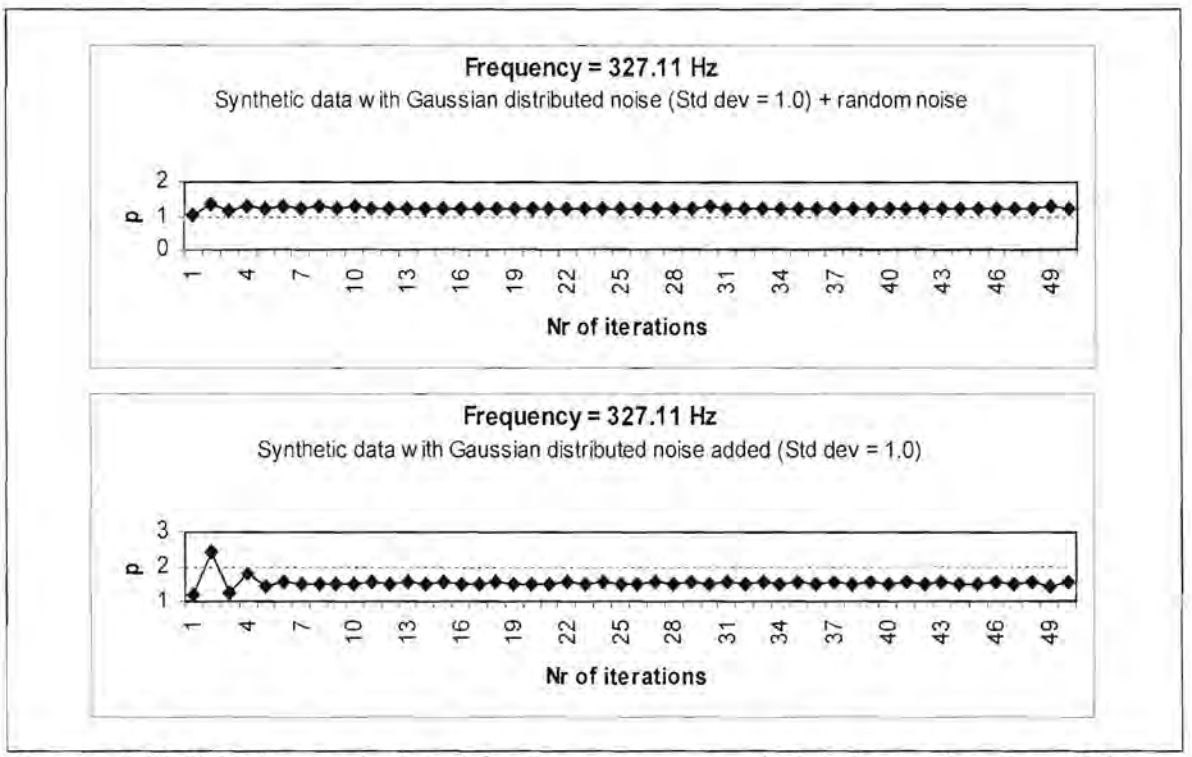

Figure 5.19.9. Values calculated for the exponent p during the estimation of the apparent resistivity values displayed in Figure 5.18 at 327.11 Hz

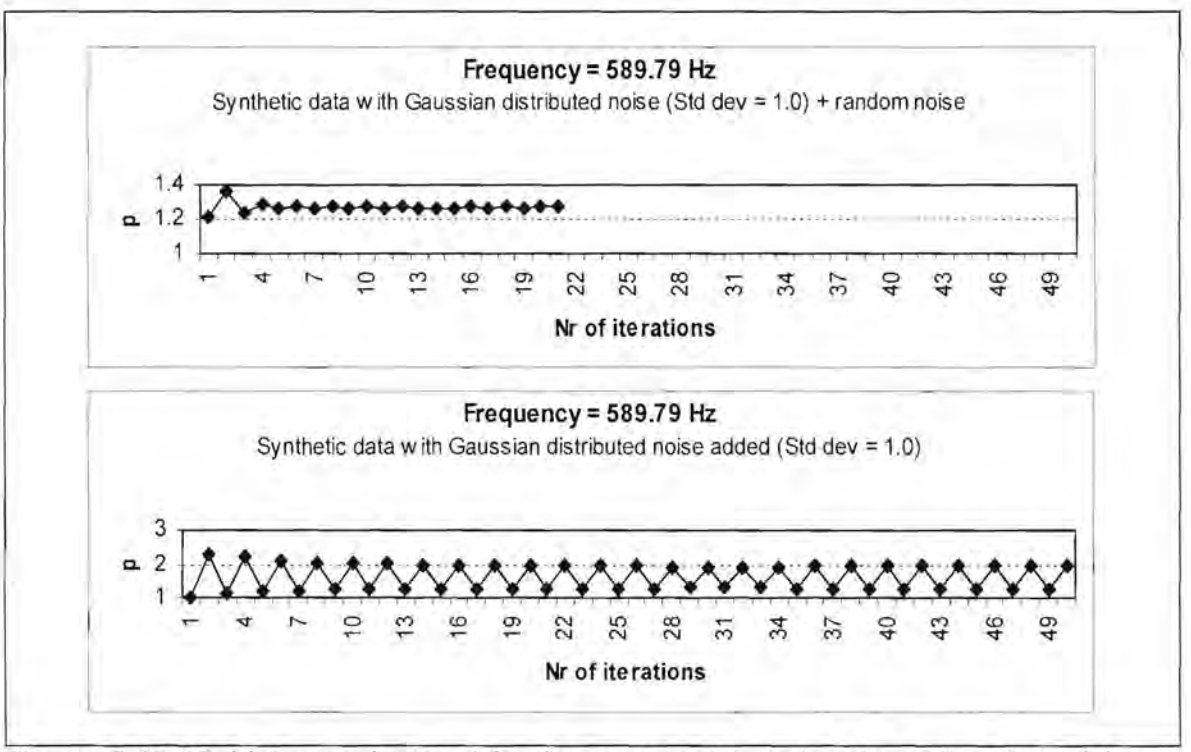

Figure 5.19.10. Values calculated for the exponent p during the estimation of the apparent resistivity values displayed in Figure 5.18 at 589.79 Hz

Figure 5.20 shows the results of using the adaptive L_p norm estimation technique and Sposito et al.'s (1983) formula (Equation 5.38) to calculate p.

Where non-Gaussian distributed noise was added, the results are very poor and correlate very well with the curves obtained from the least squares method. The reason for this becomes clear when one looks at the values of p calculated for each iteration in Figures 5.21.1 to 5.21.10. At most frequencies the adaptation procedure was terminated after only a few iterations because the values calculated for p were greater than 2, and this is not allowed when using equation (5.38).

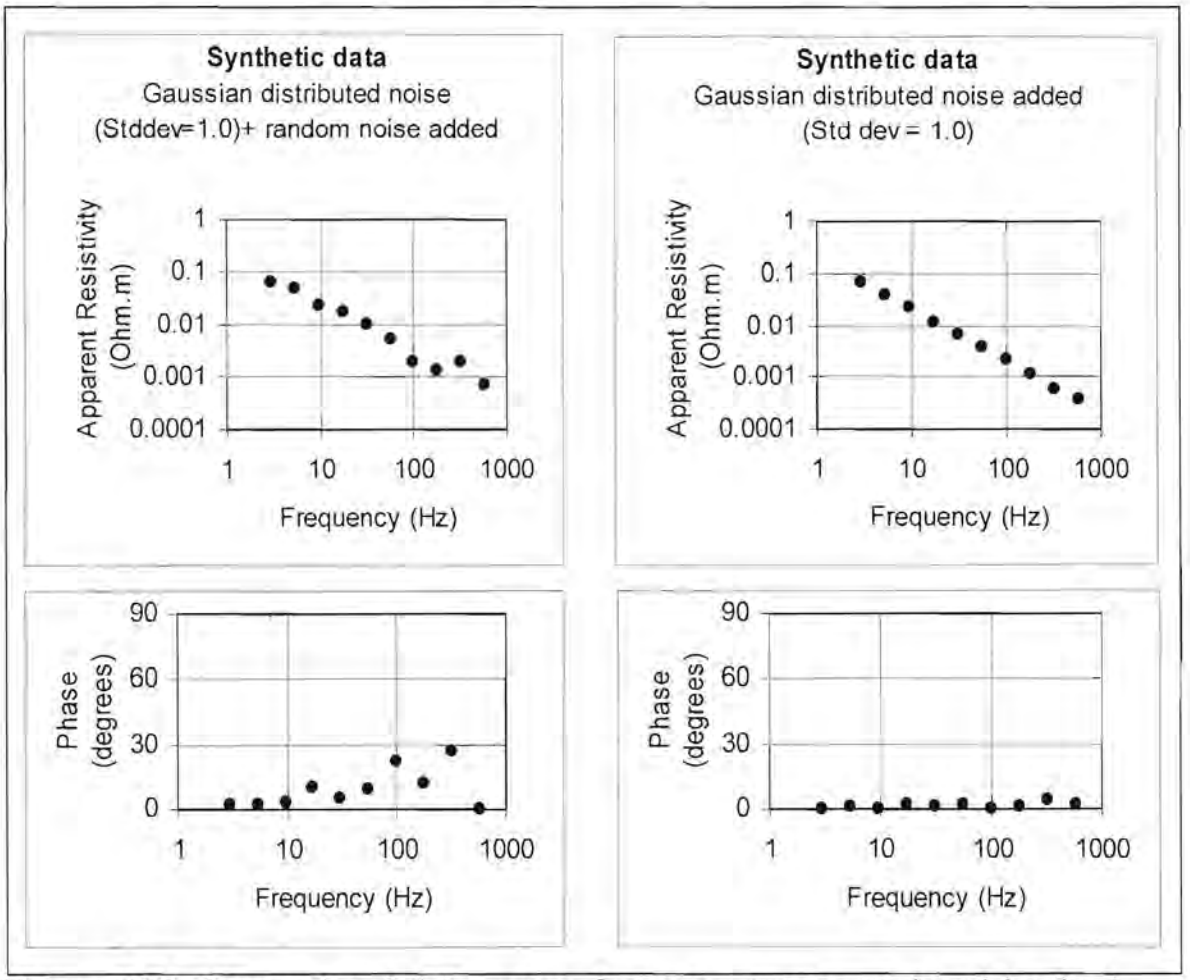

Figure 5.20. Apparent resistivity versus frequency curves produced by the L_p norm estimation technique for the synthetic data displayed in Figure 5.14. Sposito's (1983) equation was used to calculate p.

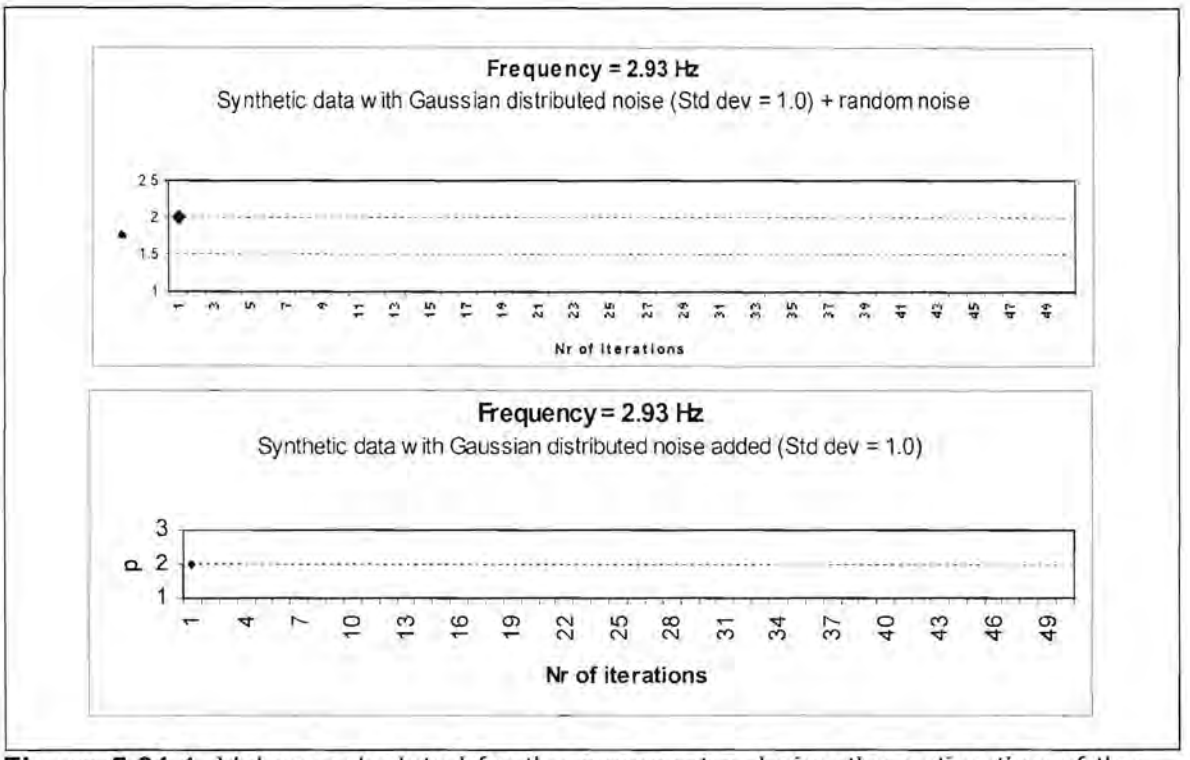

Figure 5.21.1. Values calculated for the exponent p during the estimation of the apparent resistivity values displayed in Figure 5.20 at 2.93 Hz

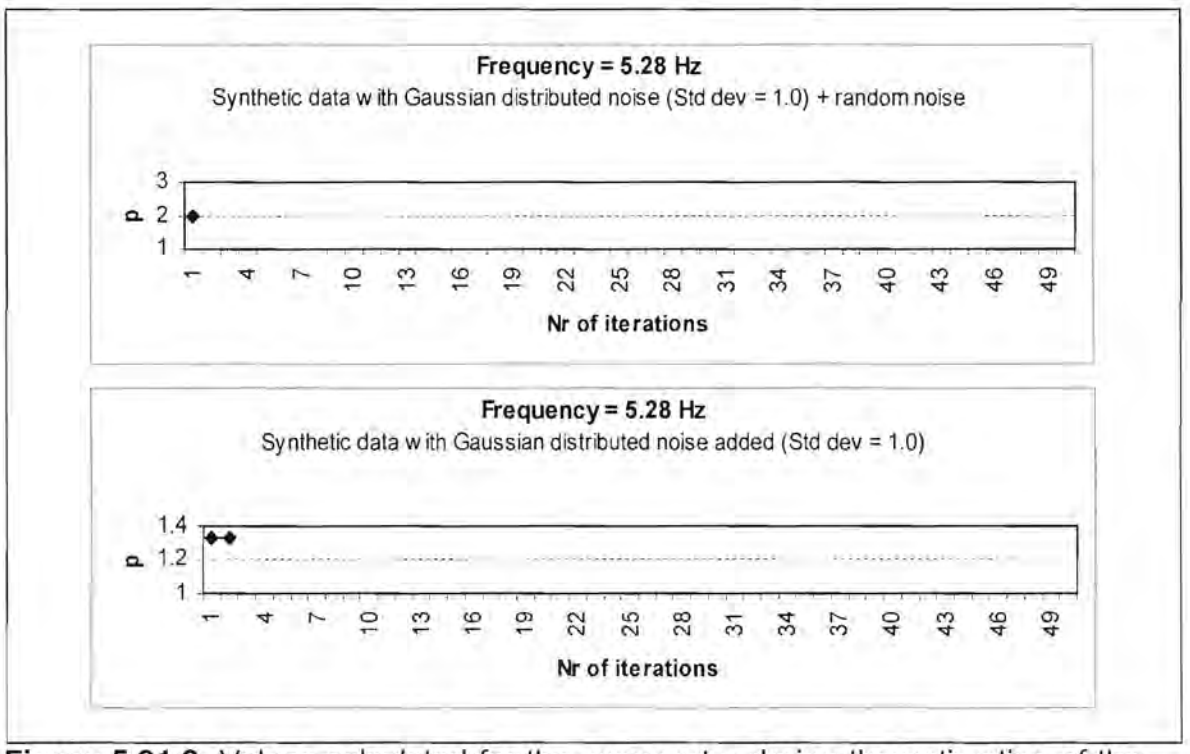

Figure 5.21.2. Values calculated for the exponent p during the estimation of the apparent resistivity values displayed in Figure 5.20 at 5.28 Hz

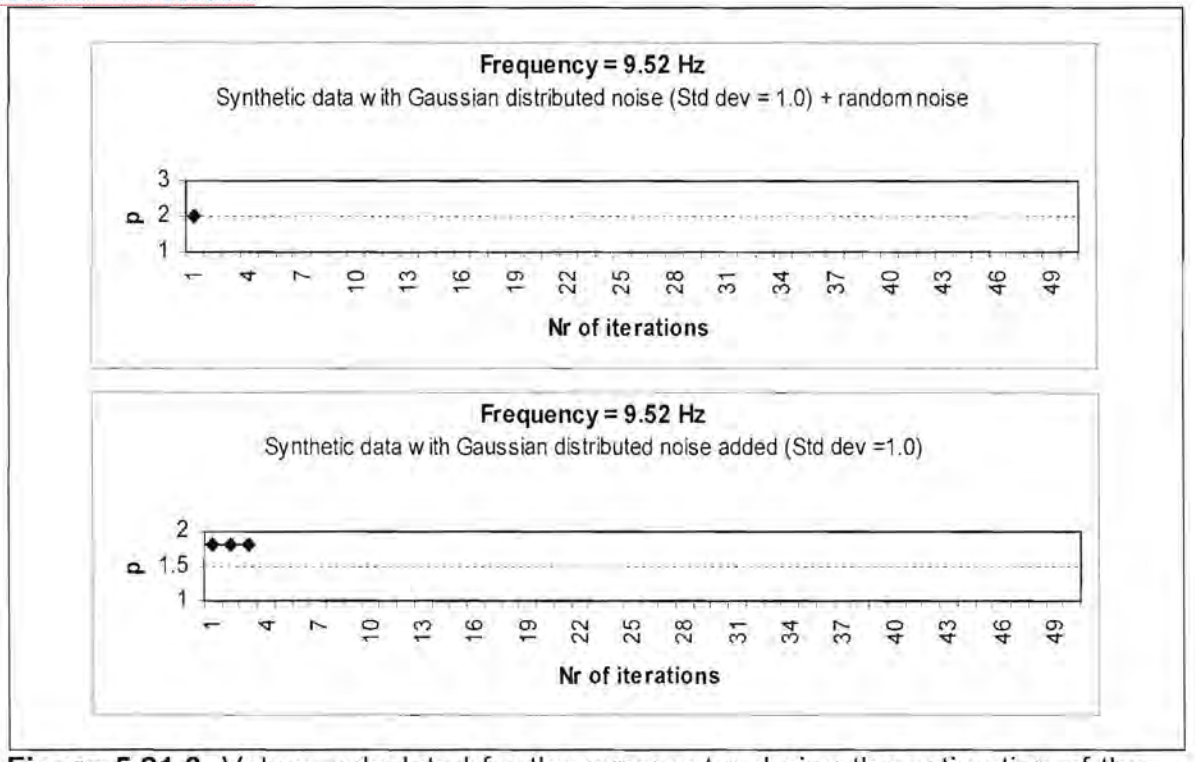

Figure 5.21.3. Values calculated for the exponent p during the estimation of the apparent resistivity values displayed in Figure 5.20 at 9.52 Hz

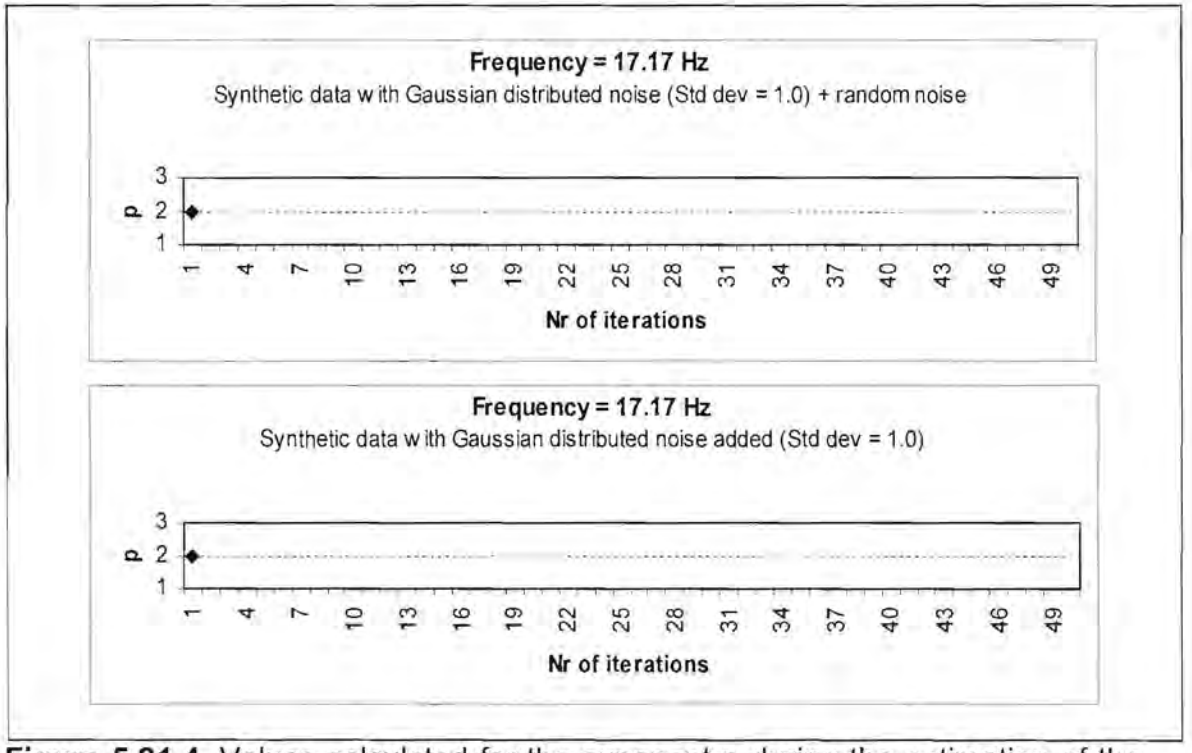

Figure 5.21.4. Values calculated for the exponent p during the estimation of the apparent resistivity values displayed in Figure 5.20 at 17.17 Hz

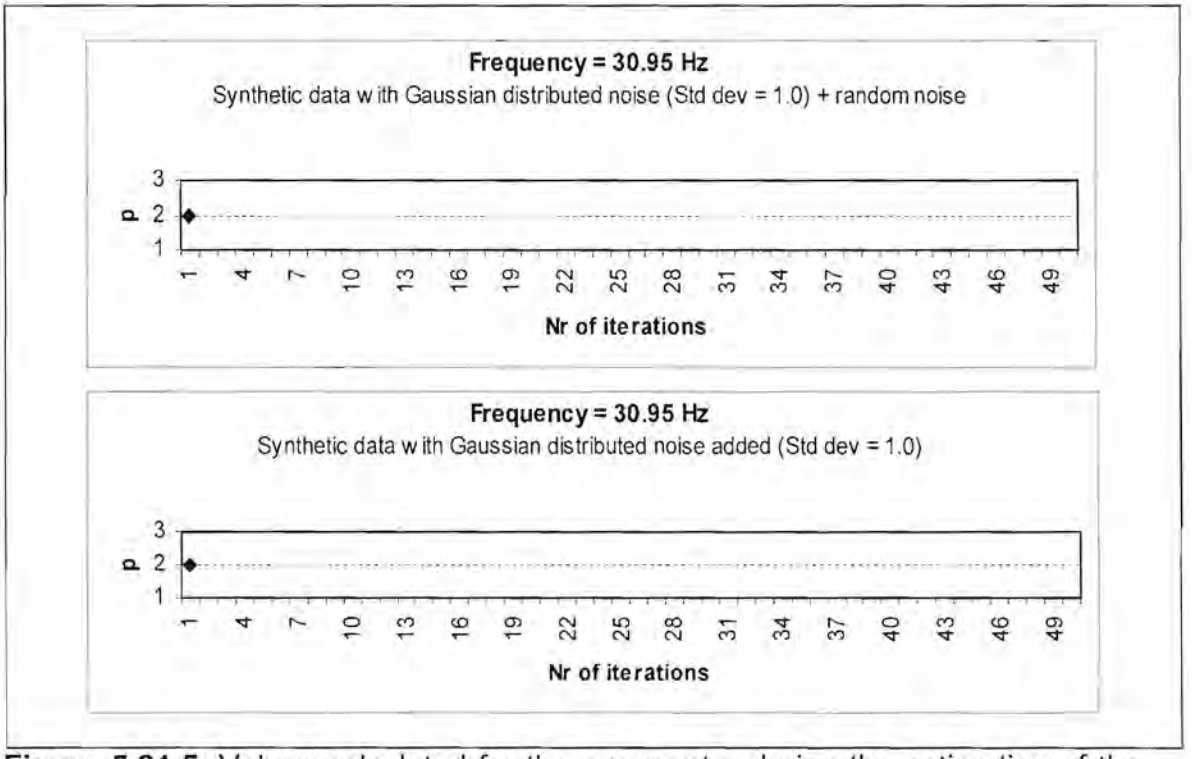

Figure 5.21.5. Values calculated for the exponent p during the estimation of the apparent resistivity values displayed in Figure 5.20 at 30.95 Hz

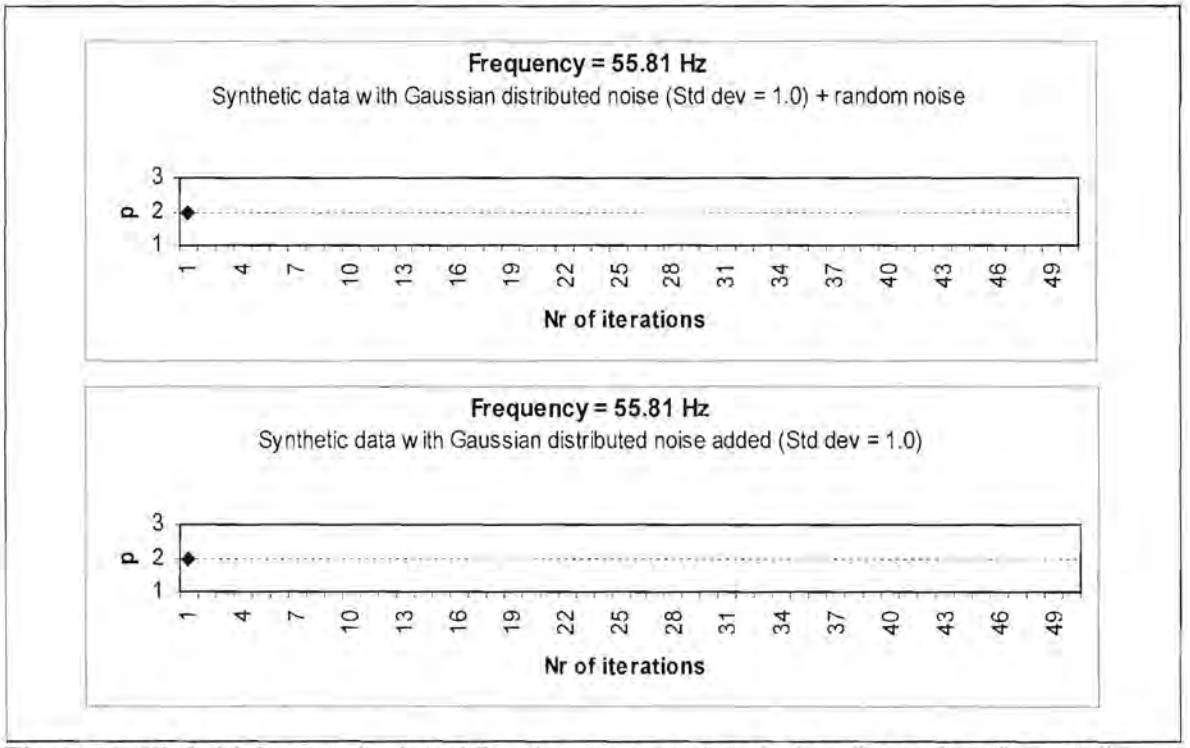

Figure 5.21.6. Values calculated for the exponent p during the estimation of the apparent resistivity values displayed in Figure 5.20 at 55.81 Hz

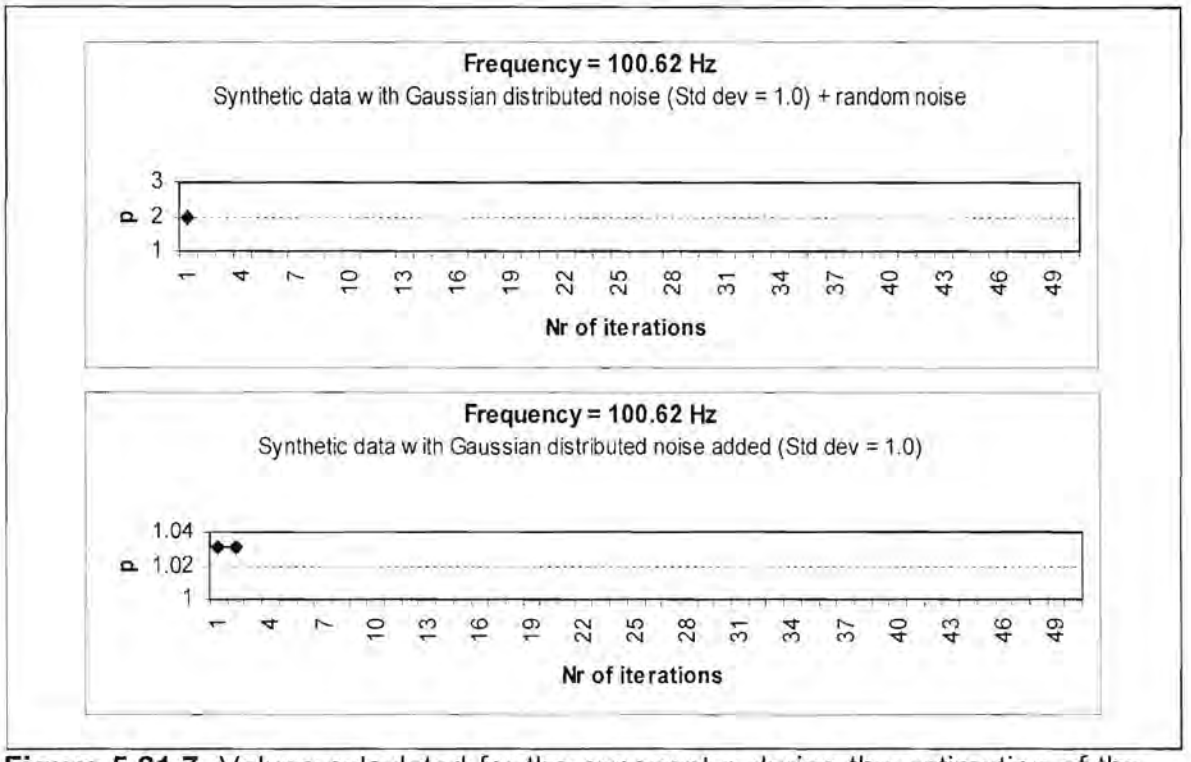

Figure 5.21.7. Values calculated for the exponent p during the estimation of the apparent resistivity values displayed in Figure 5.20 at 100.62 Hz

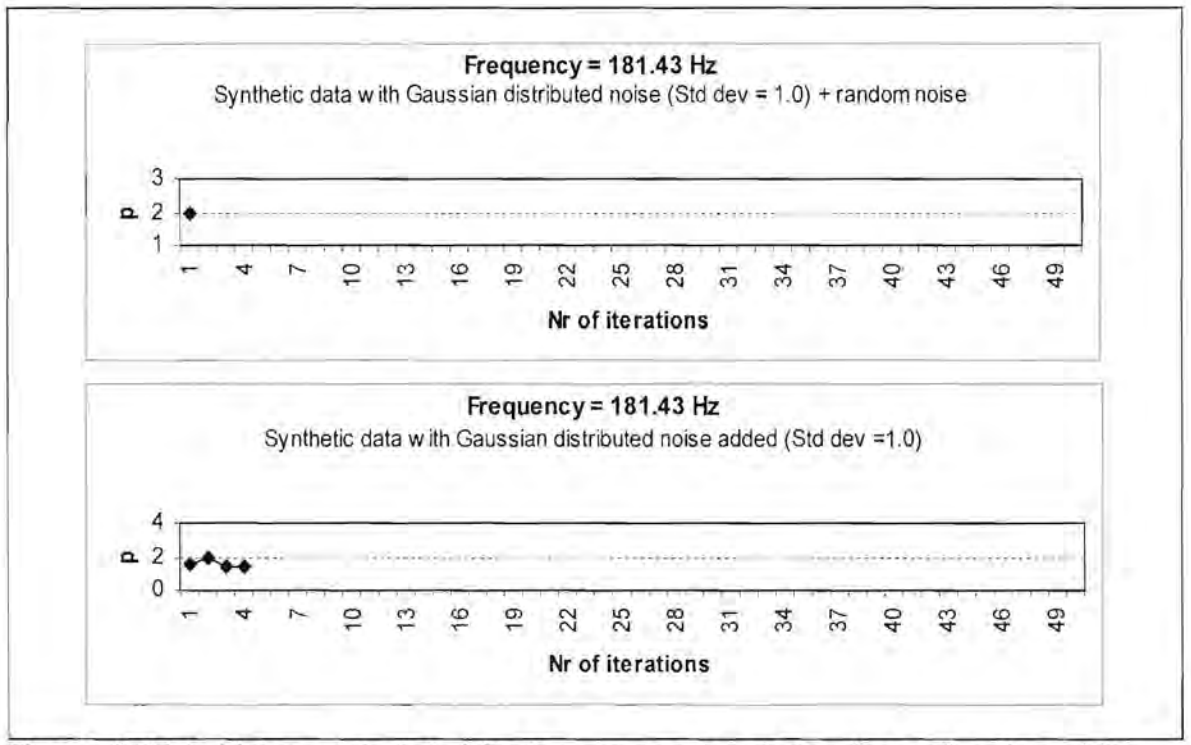

Figure 5.21.8. Values calculated for the exponent p during the estimation of the apparent resistivity values displayed in Figure 5.20 at 181.43 Hz

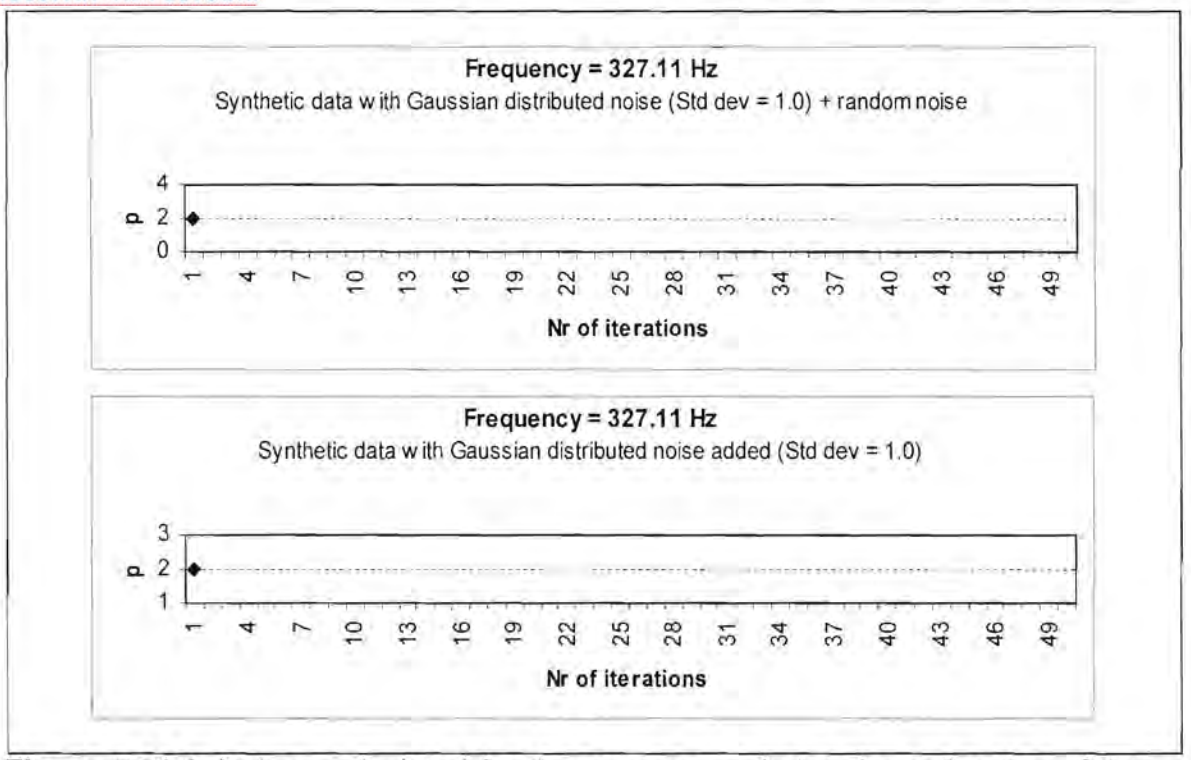

Figure 5.21.9. Values calculated for the exponent p during the estimation of the apparent resistivity values displayed in Figure 5.20 at 327.11 Hz

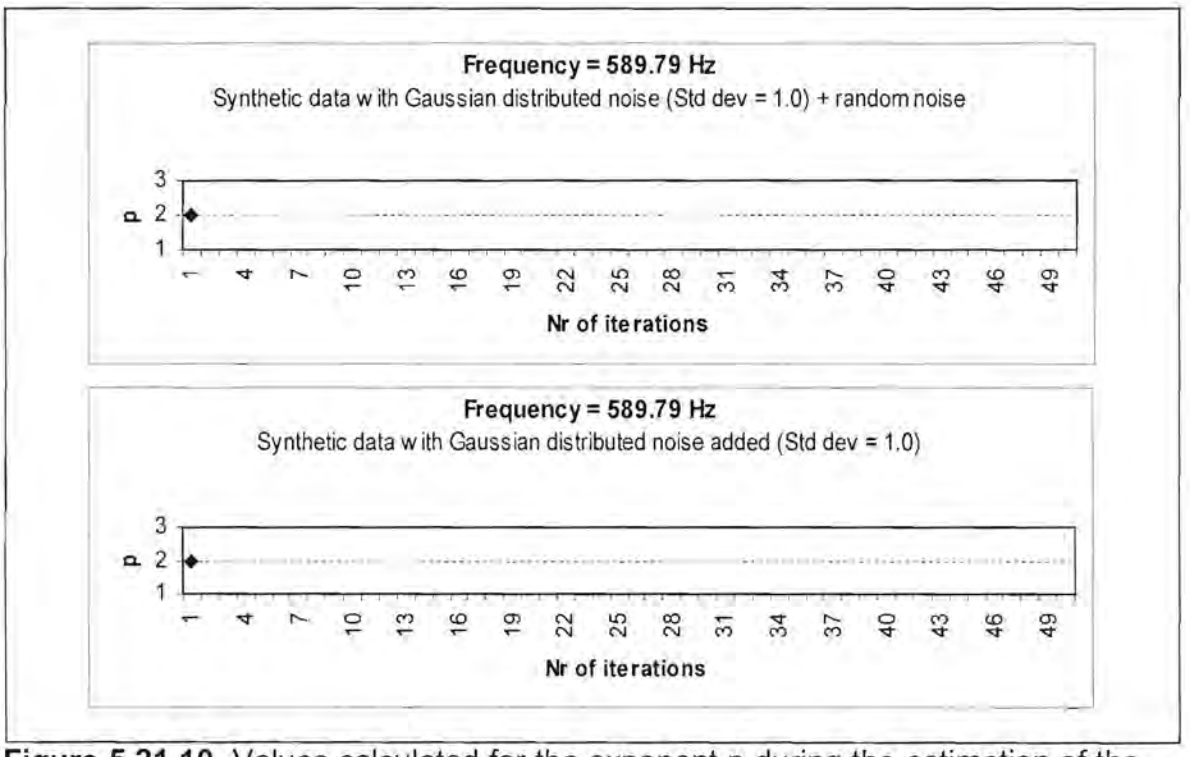

Figure 5.21.10. Values calculated for the exponent p during the estimation of the apparent resistivity values displayed in Figure 5.20 at 589.79 Hz

The Robust M estimation method yields very good results for the apparent resistivity curve at most frequencies (Figure 5.22), even though it starts with the least squares estimate of the impedance tensor as an initial estimate.

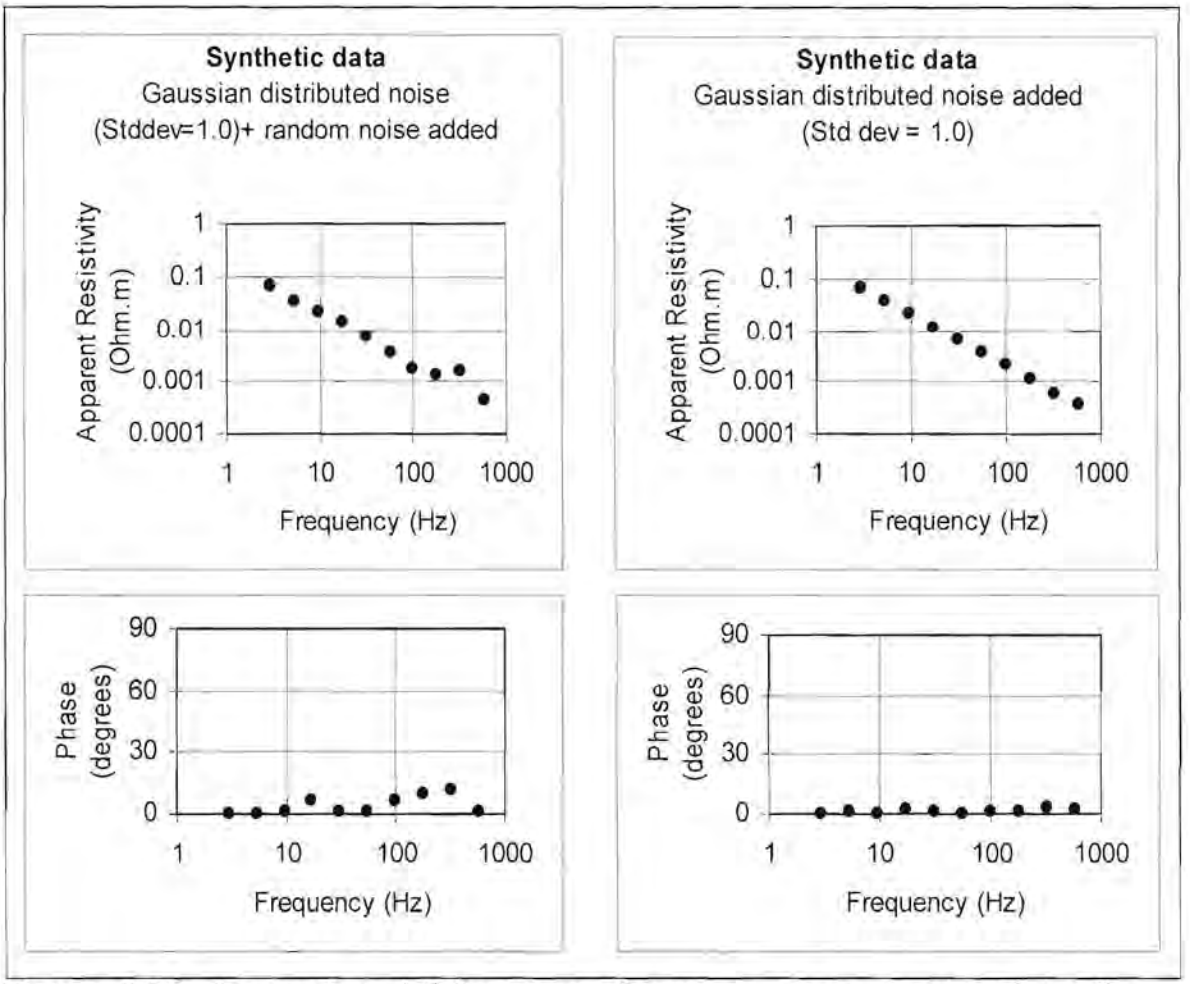

Figure 5.22. Apparent resistivity versus frequency curves produced by the Robust M estimation technique for the synthetic data displayed in Figure 5.14.

Where random noise without any specific distribution was introduced to the impedance tensor, the L_1 norm, Robust M estimation and L_p norm (using equation (5.37) to calculate p) techniques yielded satisfactory results for the apparent resistivity curves. The least squares technique and L_p norm with equation (5.38) yielded bad results. All of the estimation methods used resulted in bad fits for the phase curves.

5.5.3. Conclusions drawn from synthetic data tests

In the case where only Gaussian distributed noise are introduced to the impedance tensor, all the tested statistical reduction techniques yielded very good results. An increase in the standard deviation of the distribution of the noise causes a slight deterioration in the quality of the curve fitted to the phase data.

Completely random noise added to the impedance tensor caused a marked decrease in the success of some of the minimisation techniques. The least squares method did not produce good results at all. The same is true for the adaptive L_p technique where equation (5.38) was used to determine the value of p. Estimated values of p greater than 2 caused the adaptive process to be terminated and therefore at most frequencies L_2 minimisation occurred.

The L_1 norm, robust M estimation method and L_p norm using equation (5.37) all yielded good results, with the best fit produced by the L_1 norm. From the above examples it is concluded that the adaptive L_p-norm method is more susceptible to the starting impedance values than the robust M-estimation technique.

From the examples studied in this chapter it is clear that none of the minimisation techniques yielded perfect results. It is therefore critical that the curves obtained should be studied very carefully, keeping in mind the amount of artificial noise present near the sounding station. Additionally calculated parameters that can provide more information on the presence of noise, such as the Tipper, must be taken into account.

CHAPTER 6

CASE STUDY

A magnetotelluric (MT) survey was conducted along the road between Sishen and Keimoes in the Northern Cape Province of South Africa. It followed the route of a deep seismic reflection survey that was carried out during 1989 on behalf of the Geological Survey and the National Geophysics Programme by Geoseis (Pty) Ltd. of South Africa. The aim of the MT survey was twofold:

- Compare the results obtained by the two methods to determine whether it would be beneficial to do a magnetotelluric survey prior to a deep reflection seismic survey in order to locate areas of interest. This would be of economic interest since a deep reflection seismic survey costs considerably more than a magnetotelluric survey.
- Shed light on a number of interesting features that is visible on the reflection data.

The statistical techniques discussed in the previous chapter were applied to the data.

6.1. SURVEY LOCATION

Eleven sounding stations were positioned along the Sishen - Keimoes road at roughly 20km intervals. Figure 6.1 shows the location of the survey area in South Africa.

CHAPTER 6

CASE STUDY

A magnetotelluric (MT) survey was conducted along the road between Sishen and Keimoes in the Northern Cape Province of South Africa. It followed the route of a deep seismic reflection survey that was carried out during 1989 on behalf of the Geological Survey and the National Geophysics Programme by Geoseis (Pty) Ltd. of South Africa. The aim of the MT survey was twofold:

- Compare the results obtained by the two methods to determine whether it would be beneficial to do a magnetotelluric survey prior to a deep reflection seismic survey in order to locate areas of interest. This would be of economic interest since a deep reflection seismic survey costs considerably more than a magnetotelluric survey.
- Shed light on a number of interesting features that is visible on the reflection data.

The statistical techniques discussed in the previous chapter were applied to the data.

6.1. SURVEY LOCATION

Eleven sounding stations were positioned along the Sishen - Keimoes road at roughly 20km intervals. Figure 6.1 shows the location of the survey area in South Africa.

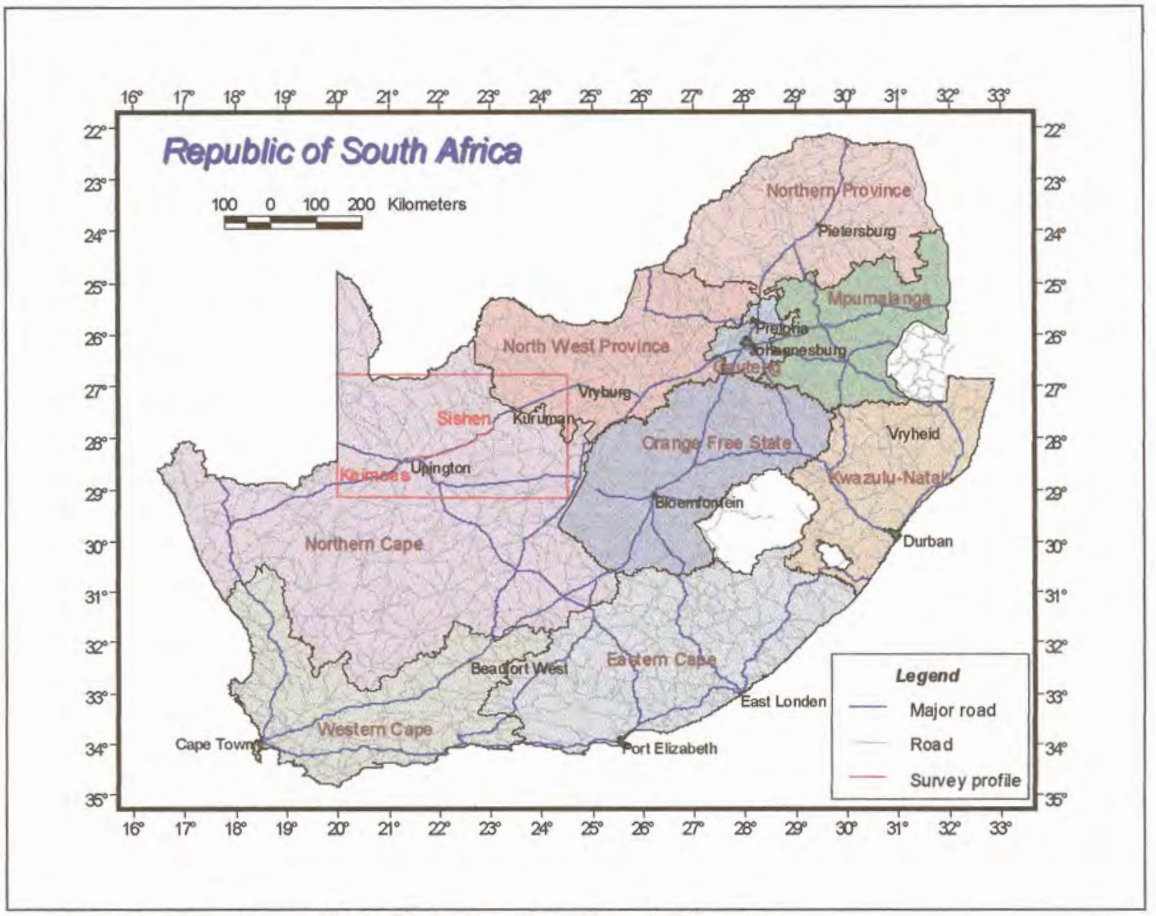

Figure 6.1. Location of the Sishen - Keimoes MT profile.

The Northern Cape Province is an arid region inhabited mainly by farming communities. Many of the farms near Upington and Keimoes are cultivated by vineyards and use electricity as power source for their irrigation systems. This acts as a source of artificial noise on the magnetotelluric data. A large open cast iron ore mine located at Sishen ships ore to Saldanha on the west coast via an electrical railway line. The railway line produces noise with a frequency of 15.6 Hz.

6.2. GENERAL GEOLOGY OF THE STUDY AREA

Figure 6.2 shows the general geology of the study area extracted from the 1:1 000 000 geological map (Keyser, 1997).

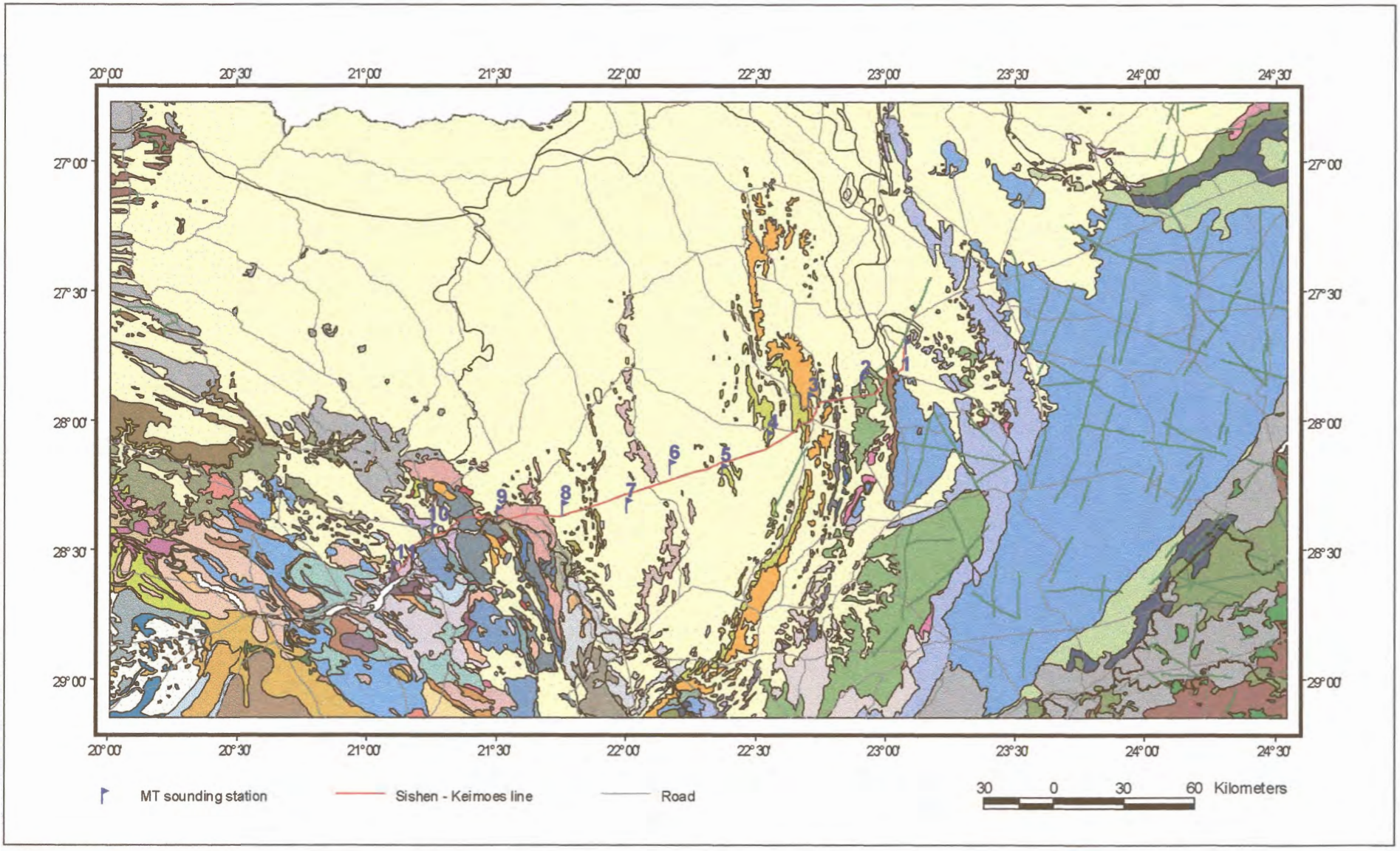

Figure 6.2. Geology of the study area from the 1:1 000 000 geological map (Keyser, 1997) with the location of the MT sounding stations indicated.

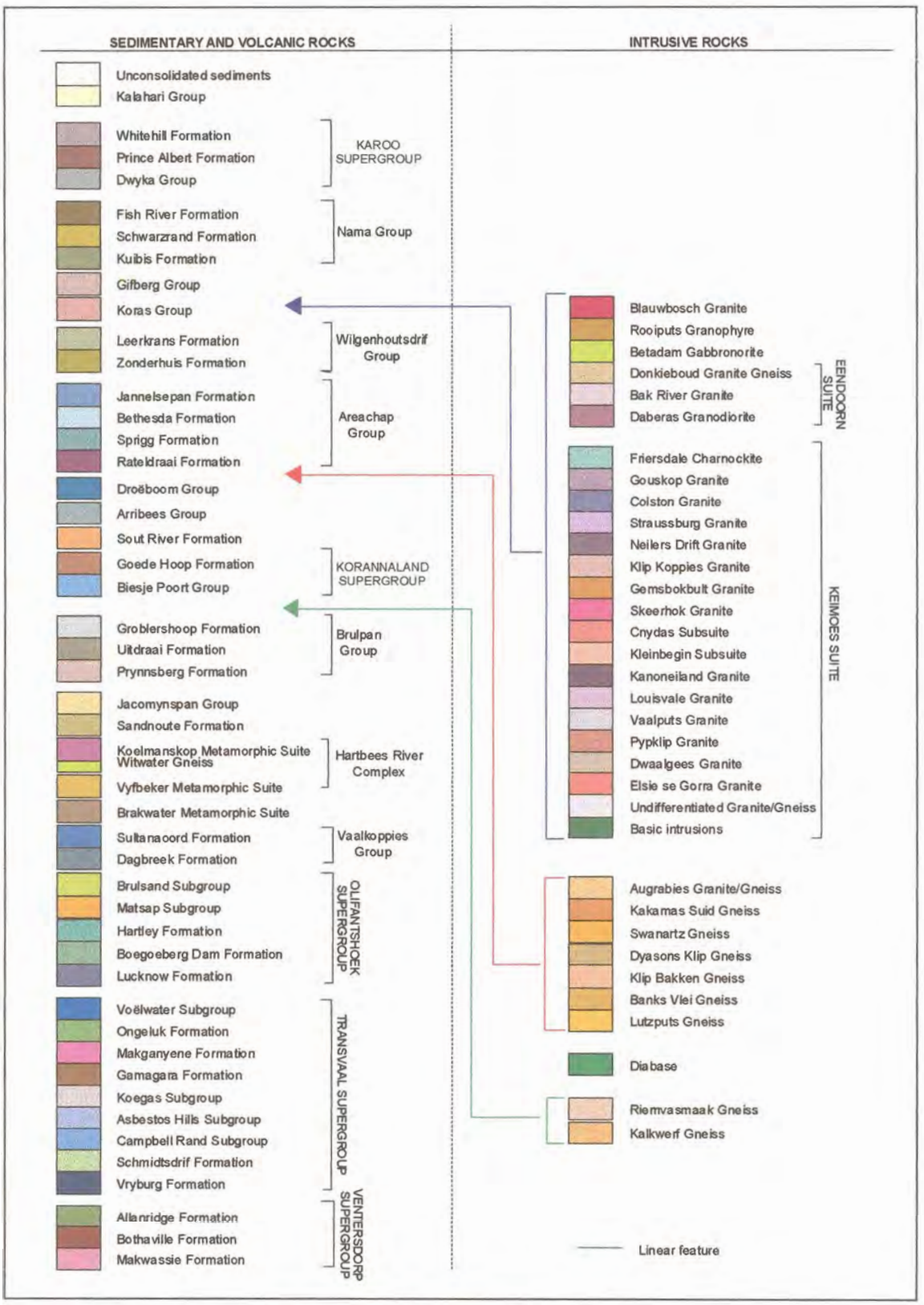

Figure 6.2 (continued). Legend for the geological map.

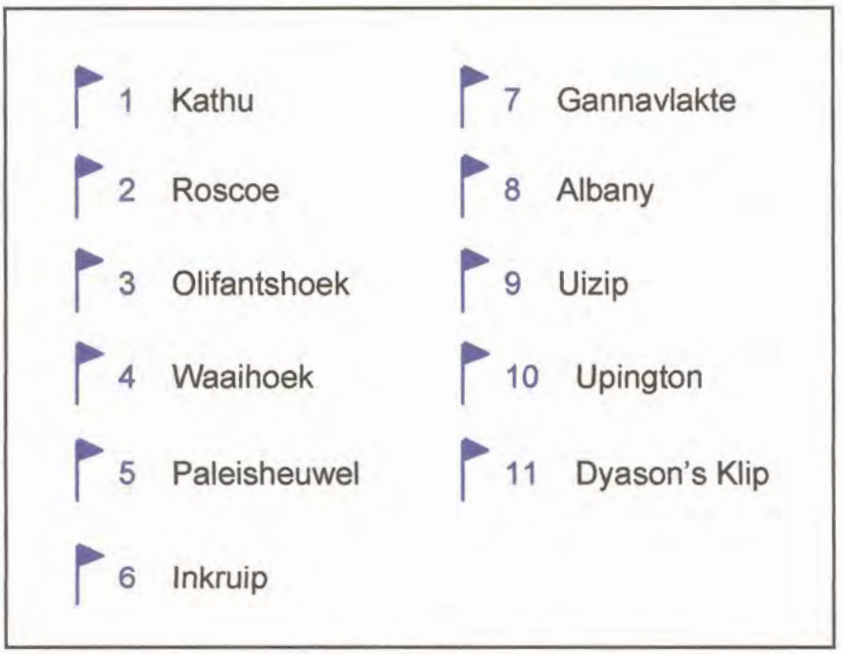

Figure 6.2 (continued). MT stations depicted on the geological map.

The study area (Figure 6.2) has a very complex tectonic history. At least three different terranes constitute the basement material on which geological formations were deposited.

The stations gradually move from Transvaal Supergroup material in the east, across Olifantshoek-, Brulpan- and Vaalkoppies sediments onto mainly intrusive granitic rocks in the west.

6.2.1. Transvaal Supergroup

The Transvaal Supergroup rocks in Griqualand West were deposited in a basin on the western edge of the Kaapvaal Craton. Extensive faulting and folding deformed the western edge of the basin. Beukes (1986) identifies a chemical sedimentary unit (the Ghaap Group) unconformably overlain by a mixed volcanic-chemical rock unit. Beukes and Smit (1987) report the following thicknesses for the different subgroups and formations (from top to bottom):

- Schmidtsdrif Formation (dolomite, shale, limestone, sandstone) : 10 – 250m

- Campbellrand Subgroup (mainly carbonaceous rocks) : 1500 – 1700m
- Asbestos Hills Subgroup : Kuruman Formation (banded ironstone, crocidolite, jaspilite, chert) 150 – 750m; Griquatown Formation (jaspilite with crocidolite, amphibolite, shale) 200 – 300m
- Koegas Subgroup (mudstone, amphibolite, quartzite, jaspilite and conglomerate at the base, jaspilite, quartzite, dolomite and banded ironstone at the top) : 240 – 600m
- Gamagara Formation (shale, quartzite, conglomerate) : 290m
- Makganyene Formation (diamictite with subordinate sandstone, conglomerate, limestone and mudstone) : 40 – 150m
- Ongeluk Formation (andesitic lava with zones of red jasper and agglomerate) : 900m
- Voëlwater Subgroup (dolomite, jaspilite, lava) : 250m

A deep borehole drilled at Kathu penetrated the Campbellrand Subgroup at a depth of 325m and was sunk to a depth of 3672m without reaching the base of the Schmidtsdrif Subgroup (Altermann and Siegfried, 1997). Altermann and Siegfried (1997) give the fact that the borehole was located on the northern flank of the Maremane Dome as a possible reason for the apparently increased thickness of the strata at the drill site.

Beukes (1986) states that the deposition of the lower part of the Transvaal Supergroup in the Griqualand West area was controlled by three tectono-sedimentary elements, namely a shallow water platform, a platform edge and a deeper basin to the west and southwest of the continent. He envisions the following scenario: sediments of the Schmidtsdrif Formation were derived from the Kaapvaal Craton and were fluvially deposited; carbonates of the Schmitsdrif Formation and Campbell Rand Subgroup were deposited in a carbonate platform sequence on a platform edge; transgression put an end to shallow water carbonate deposition; banded iron formation making up the Asbestos Hills Subgroup was deposited in deeper water and the Koegas Subgroup was deposited in a fresh water lake. The presence of stromatolites lead

Altermann and Herbig (1991) to believe that the Campbell Rand Subgroup was deposited in a shallow marine environment rather than on a platform edge.

De Villiers and Visser (1977) propose that there can be no doubt about the glacial origin of the diamictite of the Makganyene Formation. They suggest a sequence of events that started with glaciation in the north and transportation of glacial debris from the north towards the south into a water body, resulting in glaciomarine/glaciolacustrine deposits. Periodic retreats of the ice caused build-up of sedimentary piles along the basin margin that subsequently slumped into the basin, forming sandstone and subgraywacke deposits. Volcanism started during the waning stages of the ice period and clastic sedimentation stopped completely when the Ongeluk lava covered the area. Pillow lava indicates outpouring before the basin was filled with sediment.

6.2.2. Olifantshoek Supergroup

This Supergroup comprises mainly clastic sediments and volcanic rocks. The Mapedi Formation (included with the Lucknow Formation on the 1:1 000 000 map) follows disconcordantly on the Voëlwater Formation. It consists of quartzite and conglomerate at the base followed by phyllitic shale and a few layers of lava. Quartzite with a few layers of dolomitic limestone makes up the Lucknow Formation. This formation forms the foothills of the Langeberg east of Olifantshoek (Visser, 1989). The Hartley Formation, that is almost completely composed of andesitic lava, follows paraconcordantly on the Lucknow Formation.

The Matsap and Brulsand Subgroups constitute the Volop Group that follows on the Hartley Formation. Quartzite, conglomerate, greywacke and sandstone of this group strike roughly north-south and dip 30°-60° to the west (Visser, 1989).

6.2.3. Vaalkoppies Group

The Vaalkoppies Group comprises the Dagbreek and Sultanaoord Formations. The Dagbreek Formation consists of quartz-sericite schist, quartzite and amphibolite. It is characterised by a layer of quartzose schist with high aluminium content at the top (Visser, 1989). The Sultanaoord Formation follows concordantly on this Formation and consists mainly of quartzite.

6.2.4. Brulpan Group

This Group contains the Uitdraai and Groblershoop Formations. Banded and massive quartzite make up the Uitdraai Formation. The Groblershoop Formation is composed of quartz-sericite schist, with lenticular layers of greenstones and quartzite.

6.3. MAGNETOTELLURIC SOUNDING STATIONS

In this section the data at each of the sounding stations will be discussed individually. These discussions will include comparisons between apparent resistivity and phase curves obtained from the different statistical reduction techniques.

6.3.1. Katu

For this sounding station data were only obtained in the limited frequency range of 0.01 Hz to 1 Hz due to a lack of natural electromagnetic energy. The electrode spacing was 80m.

Results of statistical reduction

Figures 6.3 (a) to (f) show the data curves obtained for this station with the statistically estimated results overlain. The quality of the ρ_{yx} data is especially bad and the curves fitted through them are equally poor. Curves estimated for the ρ_{xy} with the different statistical techniques are

very similar, but it seems as though the adaptive L_p – norm using Sposito's equation (Figure 6.3e) yields the best results for both the ρ_{xy} and ρ_{yx} data. The phase data are of very poor quality. As a result the fitted curves are not realistic at all. This can be attributed to a low signal to noise ratio.

Interpretation

The apparent resistivity increases with depth, starting at approximately 10 Ωm at the highest frequency and increasing to 1000 Ωm at the lowest frequency. Since the curves obtained for both directions are very similar, it can be assumed that the underlying electrical structure is one-dimensional. Figure 6.4 shows a one-dimensional model for this sounding.

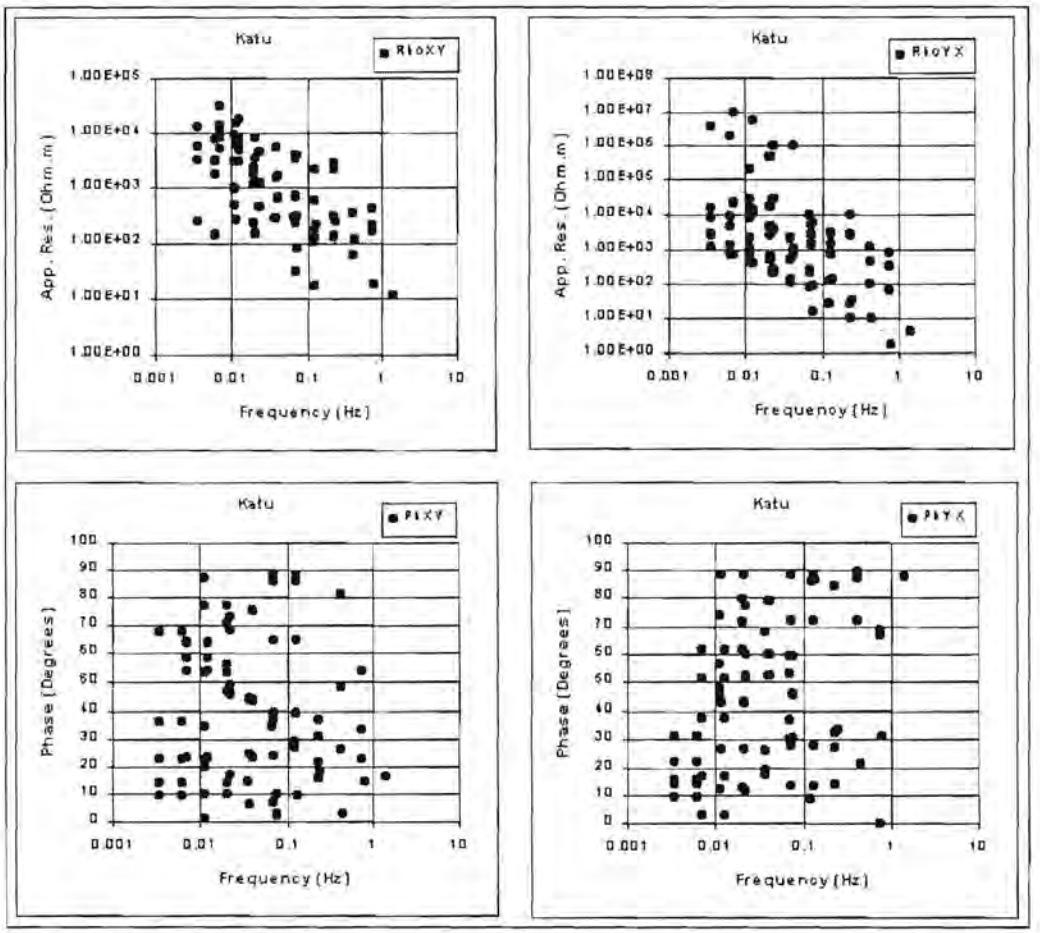

Figure 6.3(a). Apparent resistivity and impedance phase versus frequency curves for Katu.

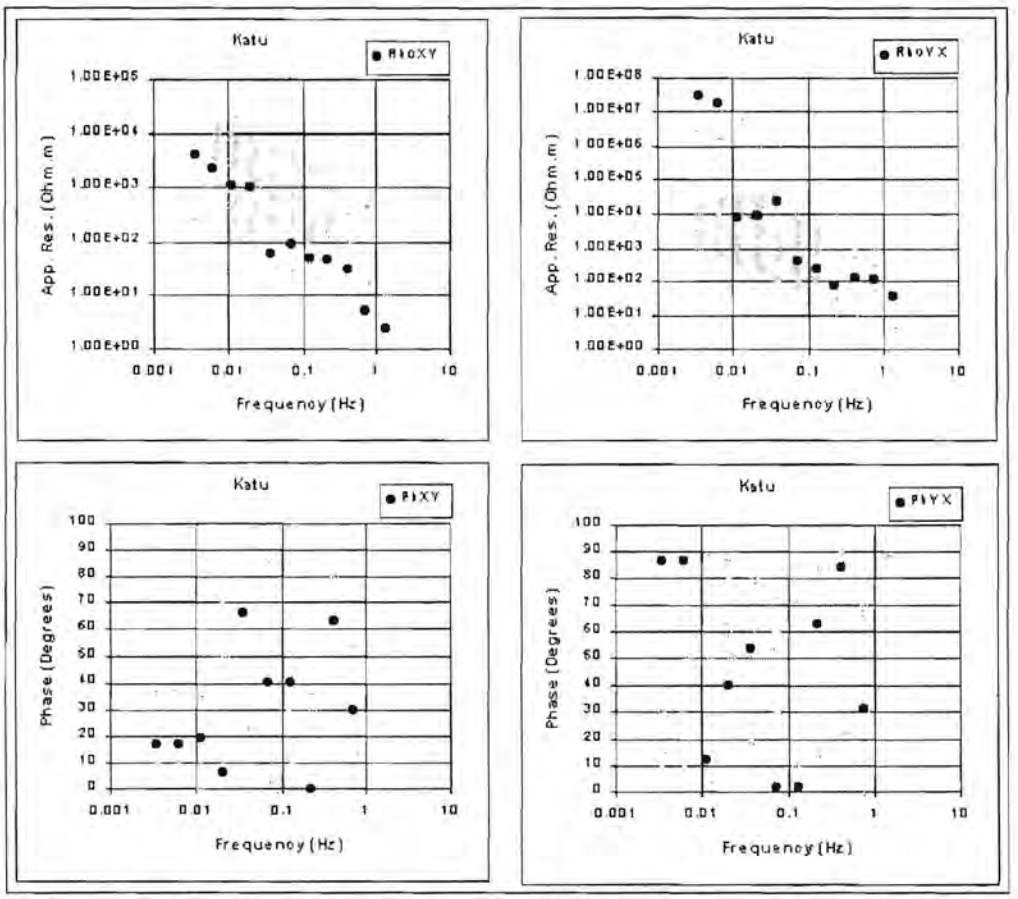

Figure 6.3(b). Curves estimated for Katu using L_1 -norm reduction.

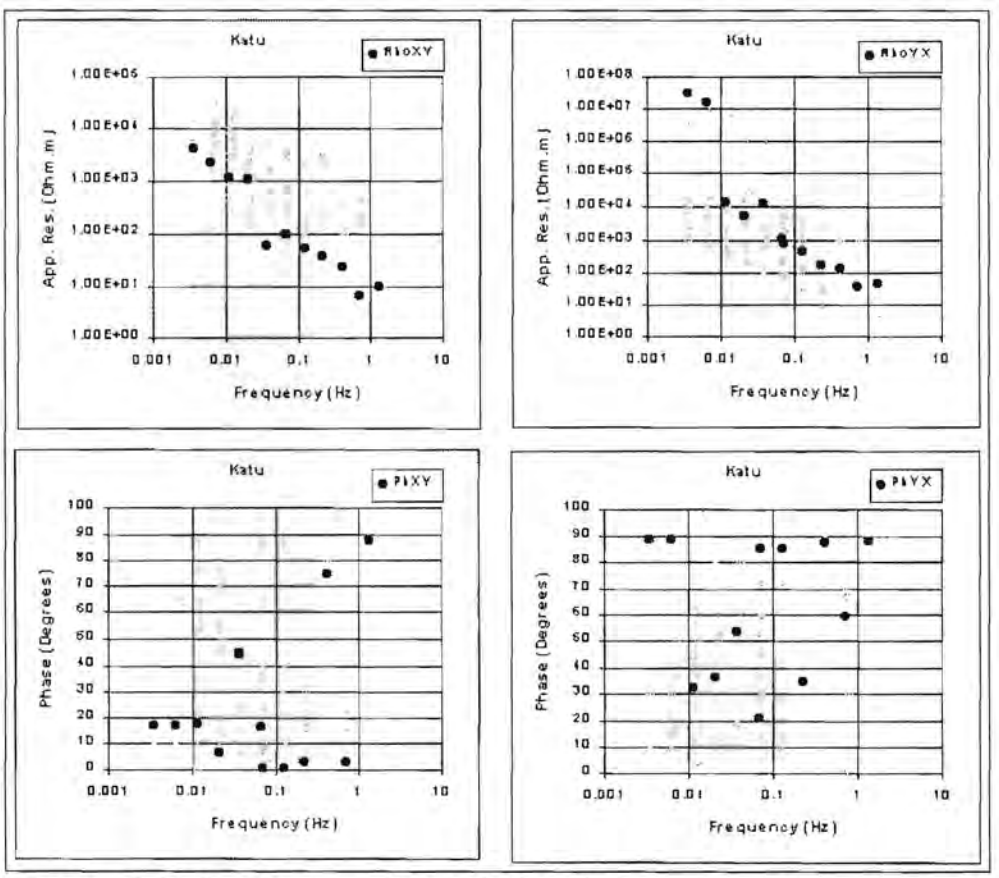

Figure 6.3(c). Curve estimated for Katu using least squares reduction.

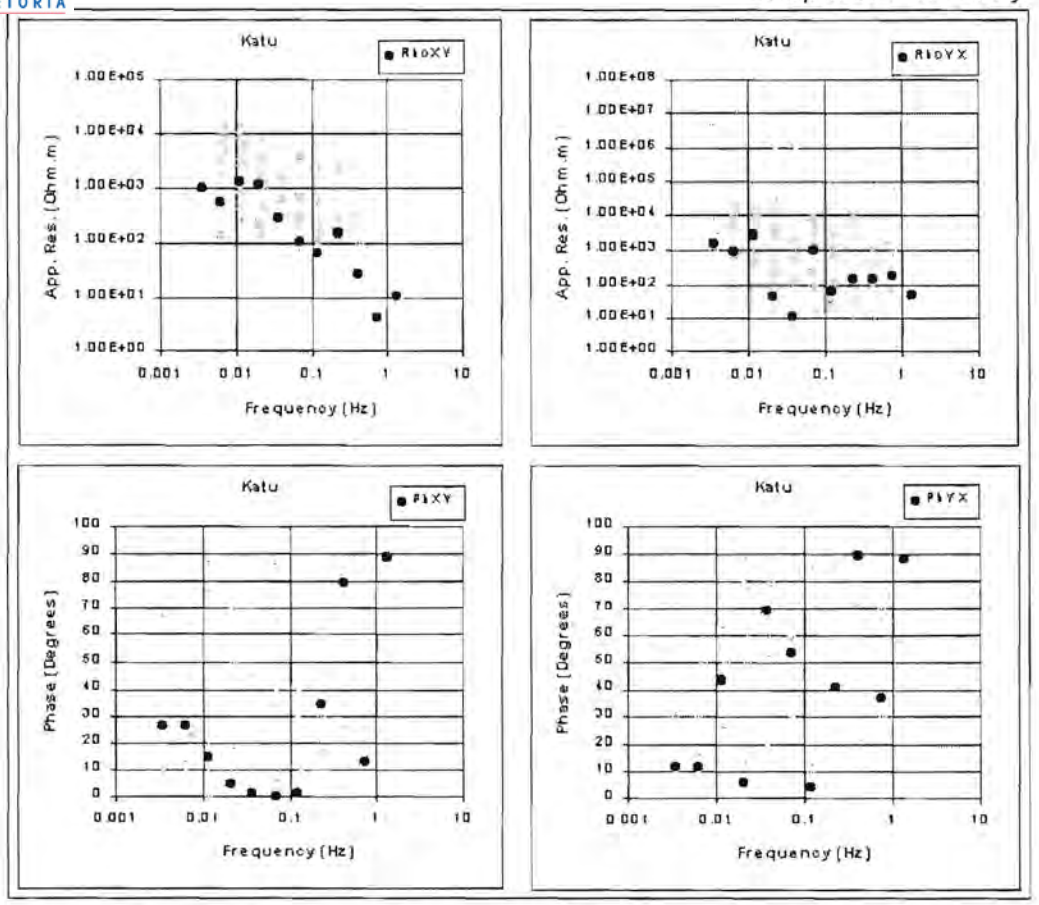

Figure 6.3(d). Curves estimated for Katu using robust M-estimation.

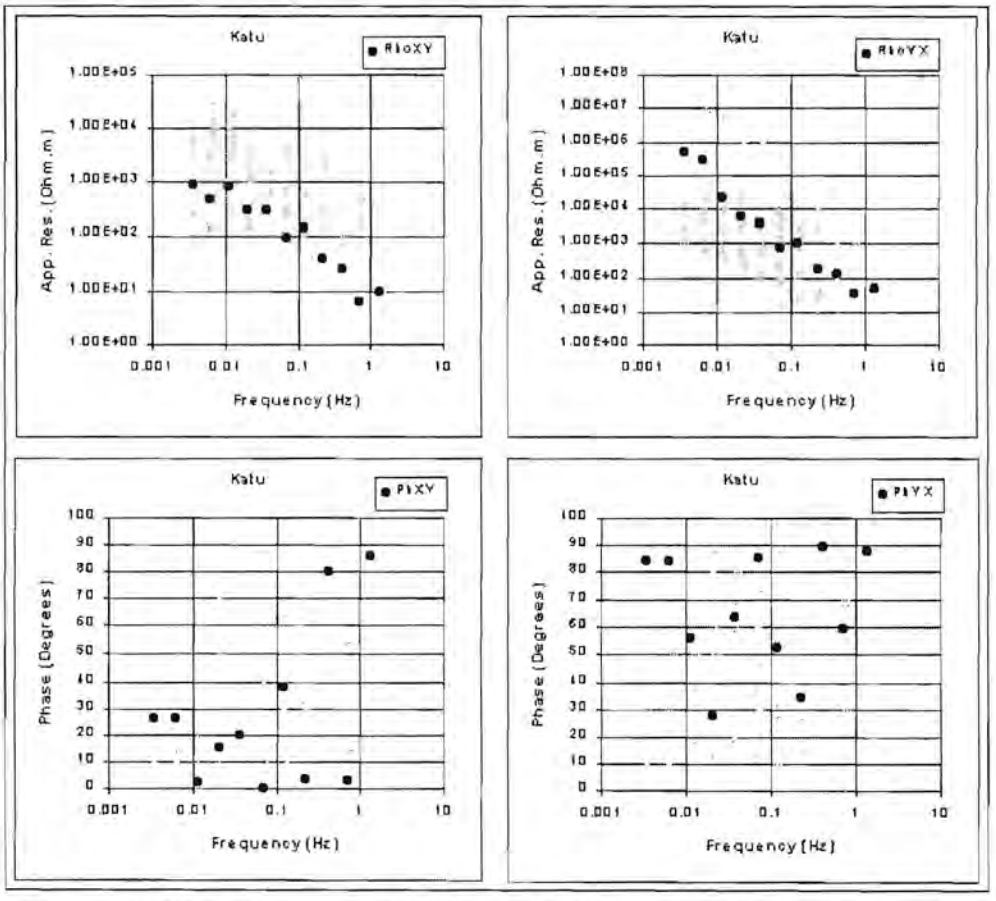

Figure 6.3(e). Curves estimated for Katu using adaptive L_p norm reduction (Sposito et al., 1983).

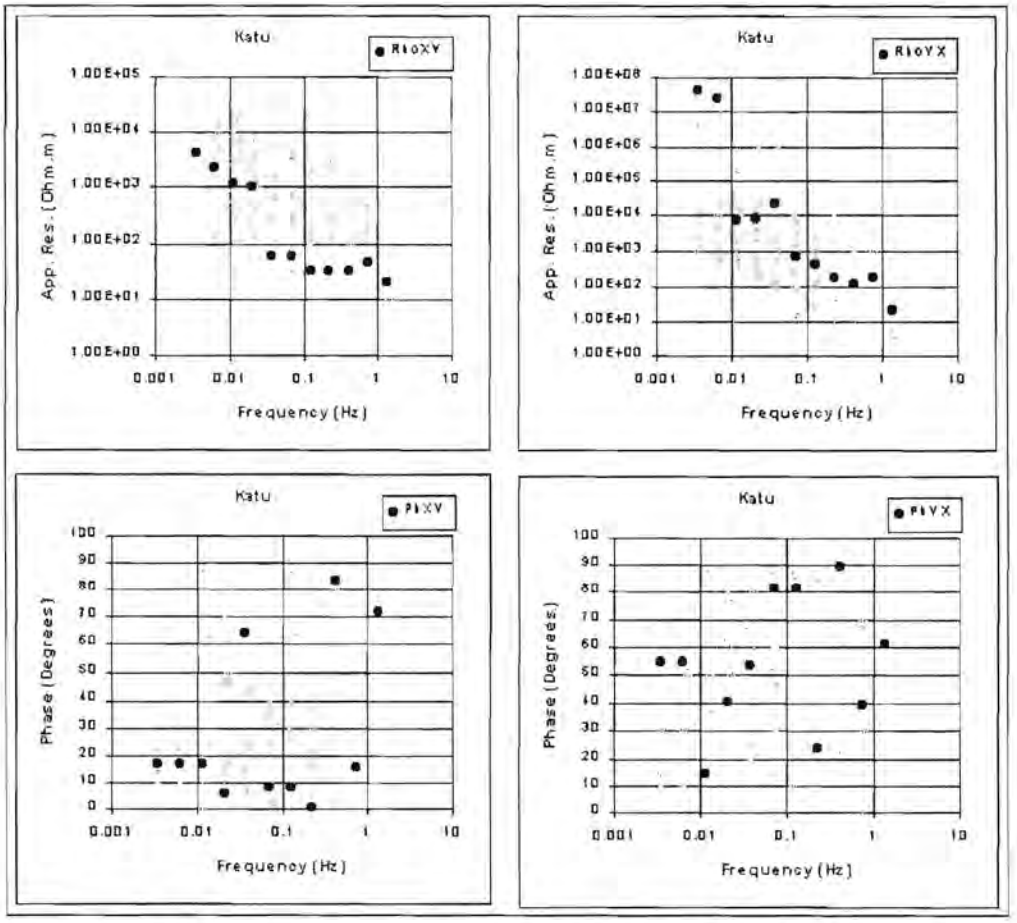

Figure 6.3(f). Curves estimated for Katu using adaptive L_p norm reduction (Money et al., 1982).

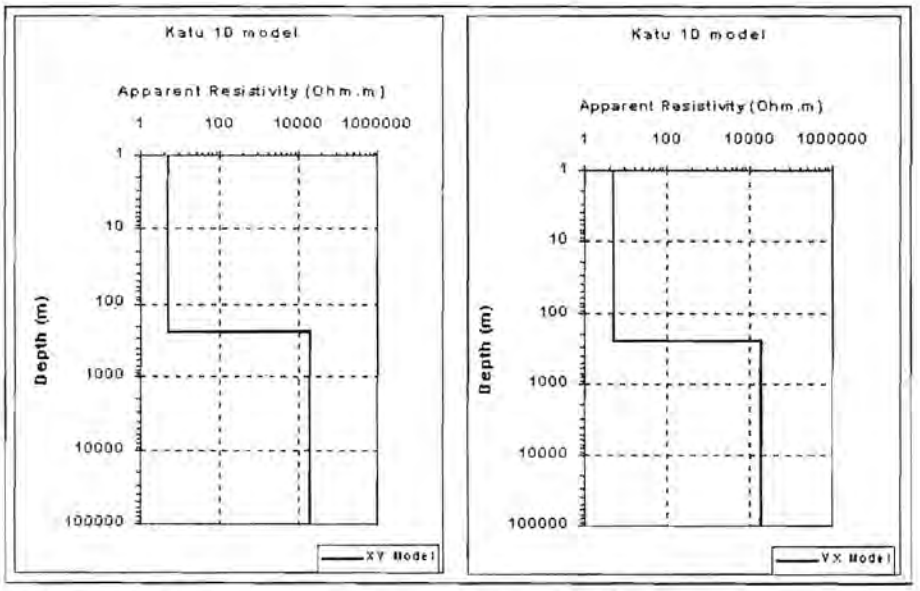

Figure 6.4. One dimensional models for Katu.

6.3.2. Roscoe

At Roscoe data were collected between 0.01 Hz and 2000 Hz. The quality of the apparent resistivity and phase data in the xy-direction is quite good, although there is a jump in the ρ_{xy} curve at 0.3 Hz (Figure 6.5(a)). The reason for this jump is unclear. It is not visible in the yx-direction and is therefore probably not caused by calibration errors.

A number of outliers appear on the ρ_{yx} data. The phase data in this direction is severely scattered indicating serious noise problems.

Results of statistical reduction

Figures 6.5(b) to (f) show the fitted curves overlain on the data. In this case, the robust M-estimation technique yields the best result for the data in both directions. The adaptive L_p-norm and least squares methods (Figure 6.5(c), (e) and (f)) were severely affected by outliers for the yx-direction data. Results obtained with the L1 norm (Figure 6.5(b)) compares quite well with the robust M-estimation curves.

Interpretation

For the xy-direction the apparent resistivity increases with decreasing frequency until roughly 0.3 Hz where the curve turns. This turn is very suspect since it coincides with the sudden jump in the data at this specific frequency.

The ρ_{yx} curve is more complex than the ρ_{xy} curve. At high frequencies the Earth is very conductive. The apparent resistivity increases with depth, but at approximately 20 Hz the curve flattens, pointing to the possible presence of a conductor. As the frequency decreases, the apparent resistivity increases to roughly 400 Ωm. At 0.3 Hz the curve flattens and starts to turn downwards.

The apparent resistivity curves in the xy- and yx-directions differ quite substantially. This indicates that the underlying geology is becoming more complex than at Katu and two- and three-dimensional structures are playing a role. Figure 6.6 depicts the layered earth one-dimensional models for each of the apparent resistivity curves.

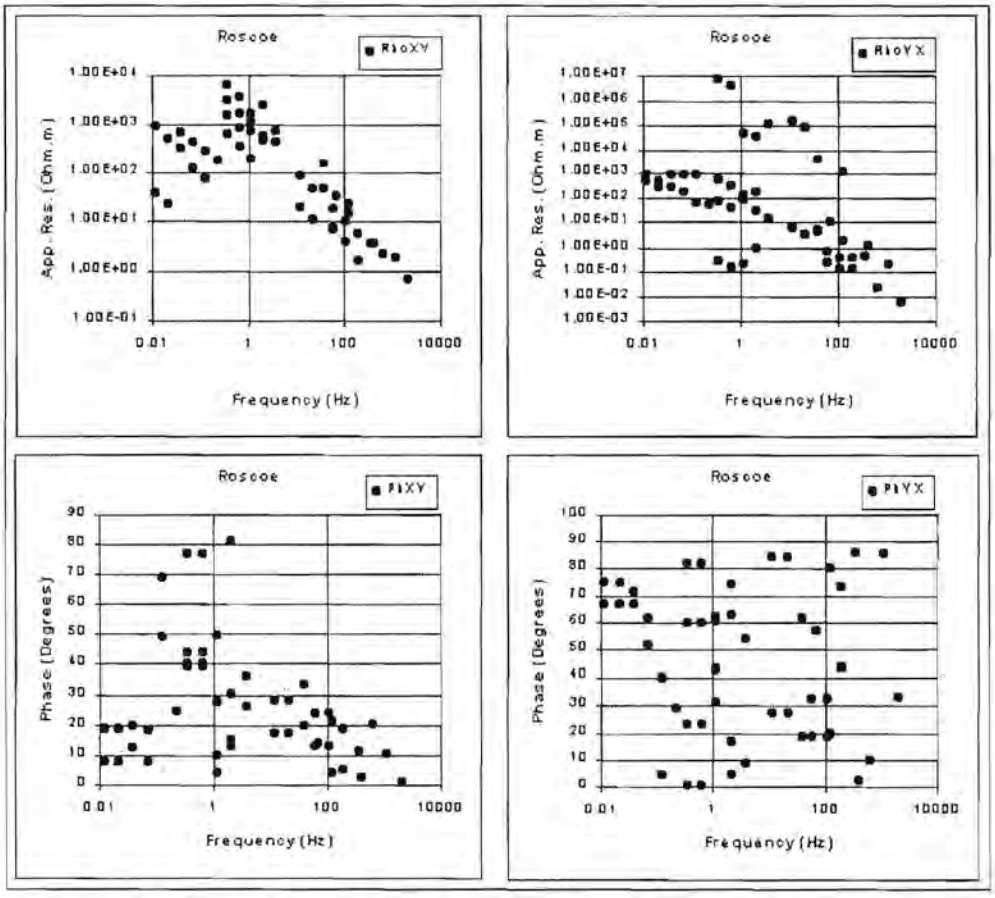

Figure 6.5(a). Apparent resistivity and impedance phase versus frequency curves for Roscoe.

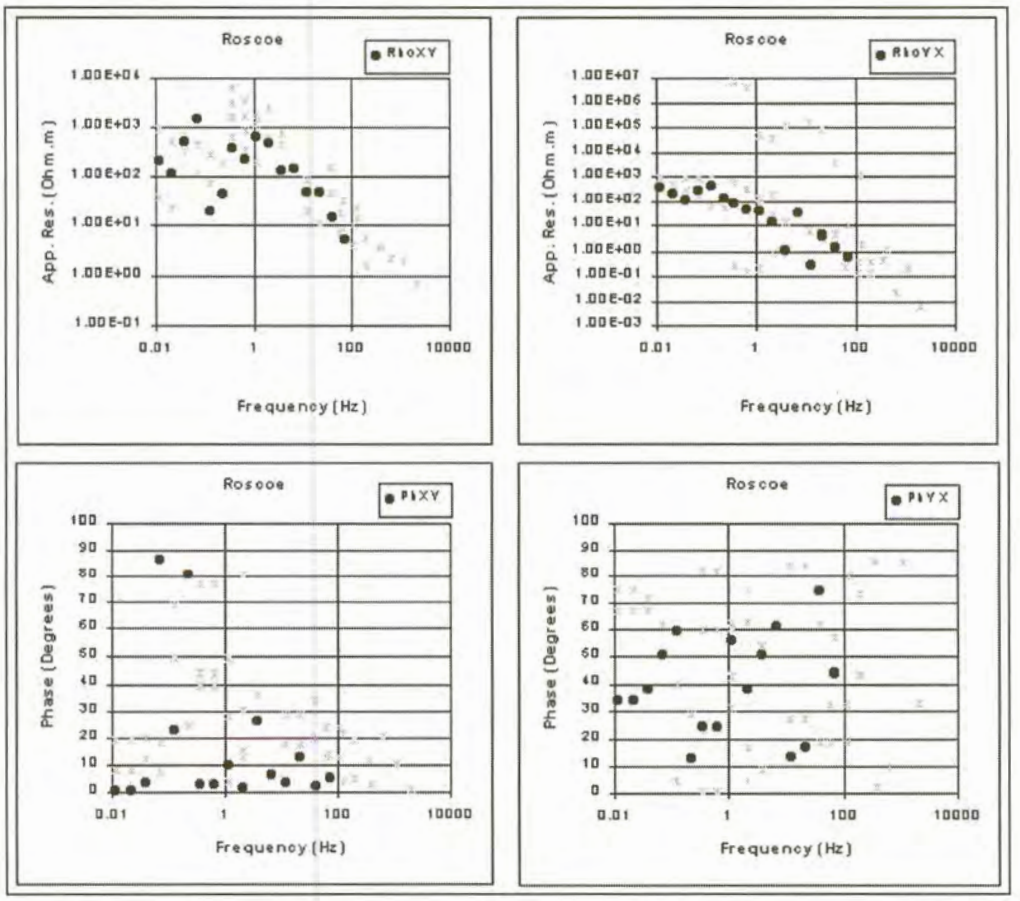

Figure 6.5(b). Curves estimated for Roscoe using L_1 norm reduction.

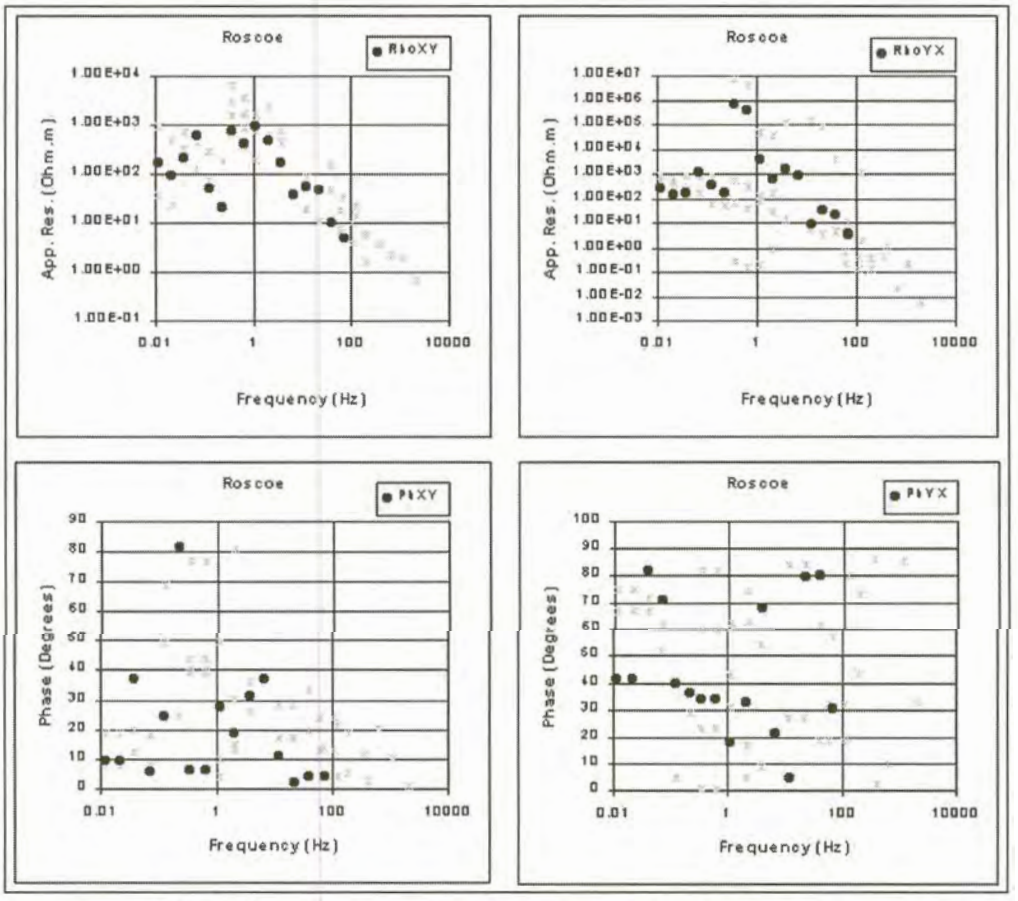

Figure 6.5(c). Curves estimated for Roscoe using least squares reduction.

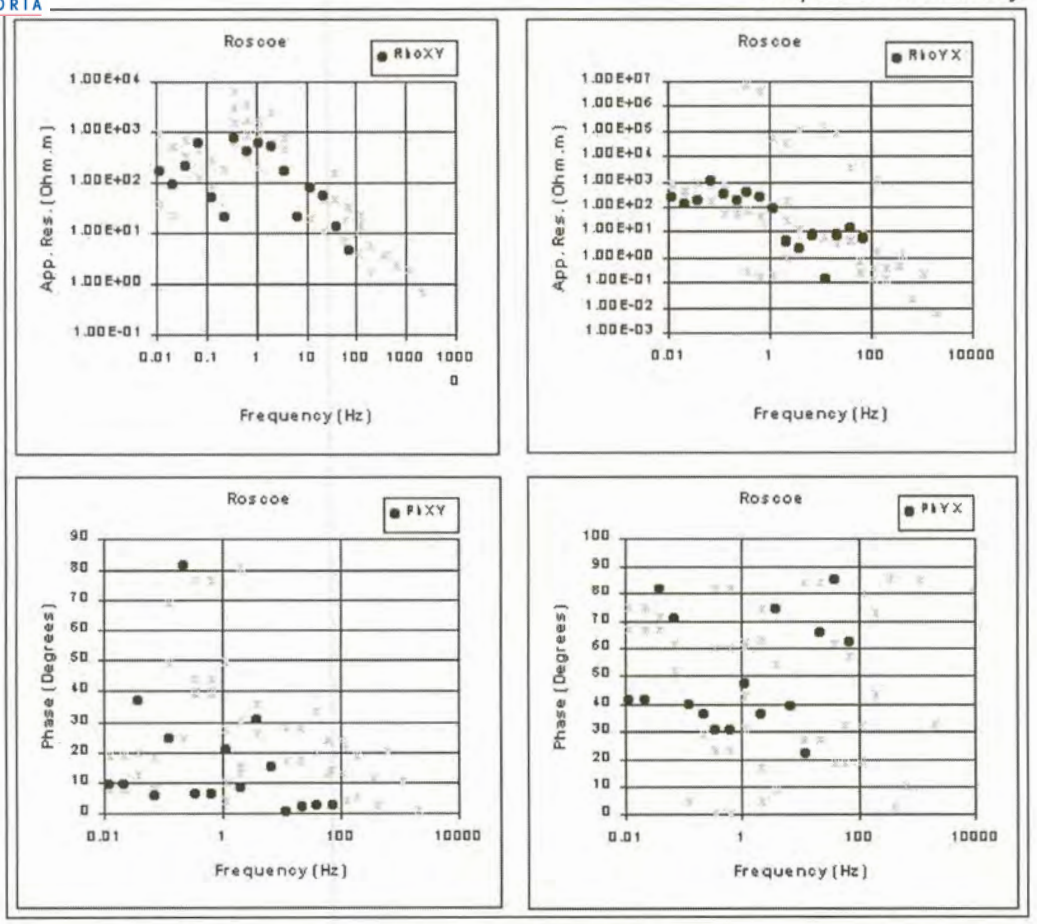

Figure 6.5(d). Curves estimated for Roscoe using robust M-estimation.

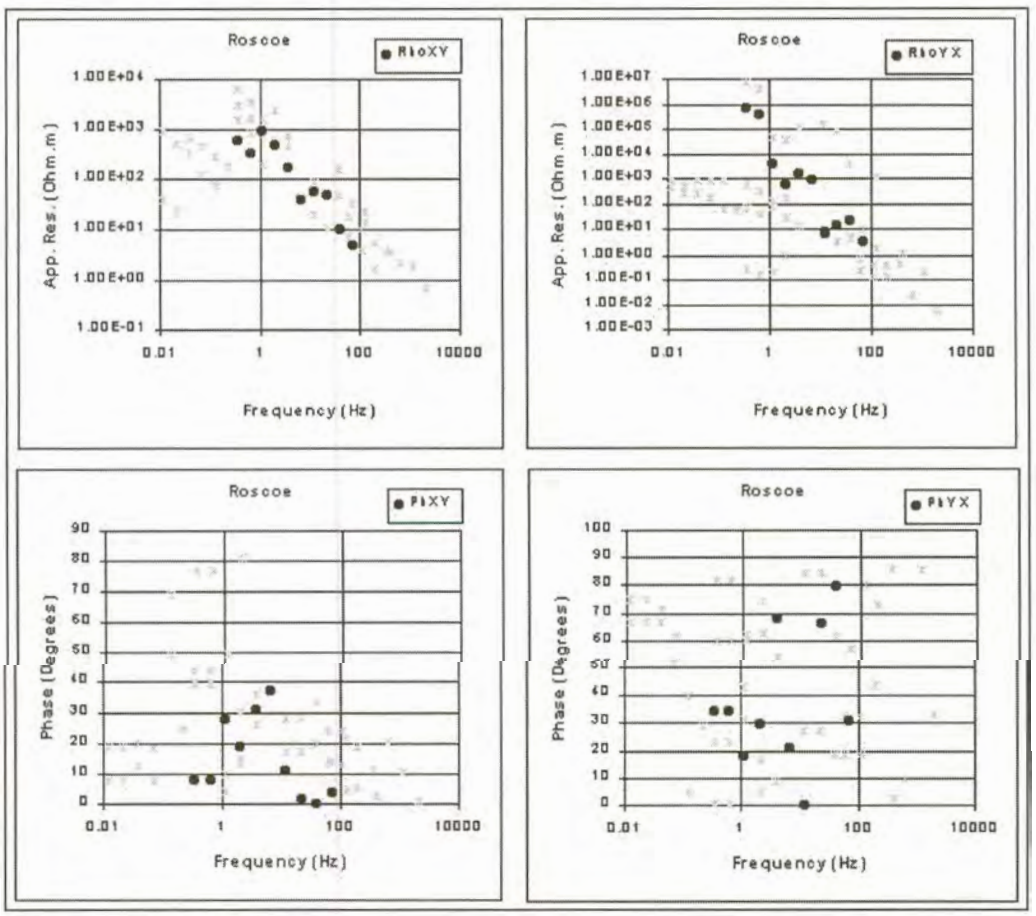

Figure 6.5(e). Curves estimated for Roscoe using adaptive L_p norm reduction (Sposito et al., 1983).

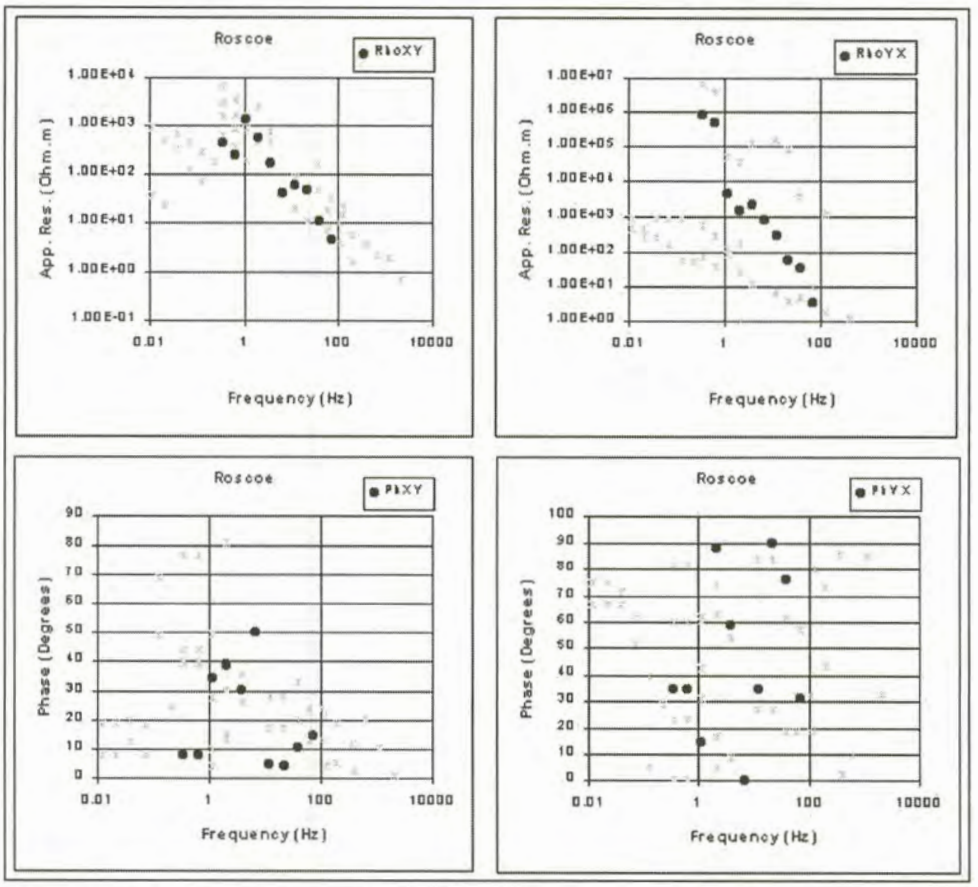

Figure 6.5(f). Curves estimated for Roscoe using adaptive L_p norm reduction (Money et al., 1982).

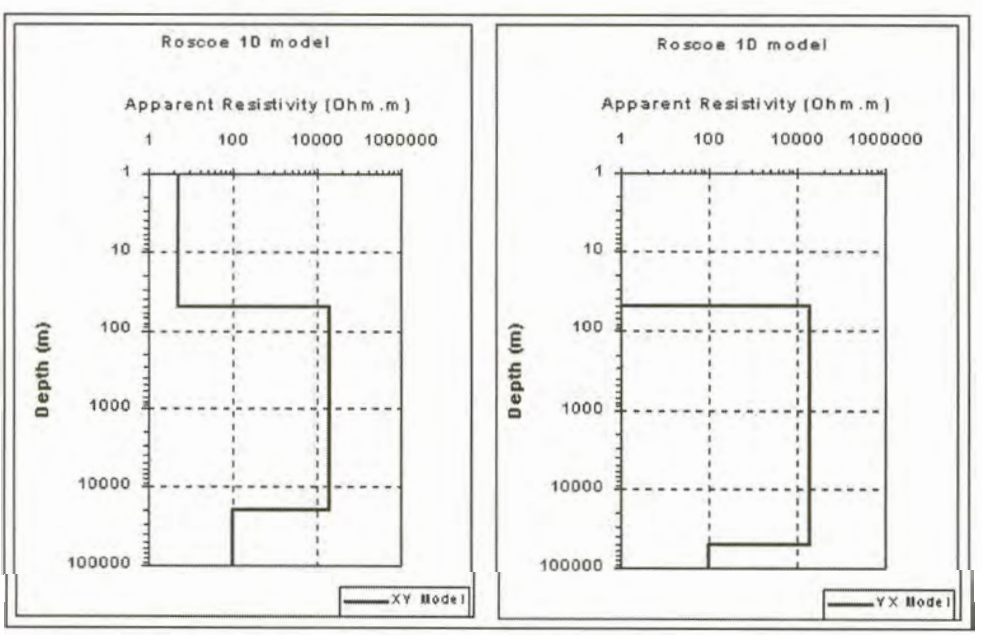

Figure 6.6. One dimensional models for Roscoe.

6.3.3. Olifantshoek

Data at this station were obtained between 0.01Hz and 10000Hz, with a gap between 0.1Hz and 2Hz where no data were collected (Figure 6.7(a)). The phase data are once again of very poor quality. On the xy-direction apparent resistivity data, some values fall on a straight line at higher frequencies. This is definitely caused by noise.

Results of statistical reduction

All of the statistical reduction techniques were severely biased by the noise that appears in the high frequency range of the xy-direction apparent resistivity data. None of the curves estimated for the apparent resistivity data in the yx direction yields a good fit.

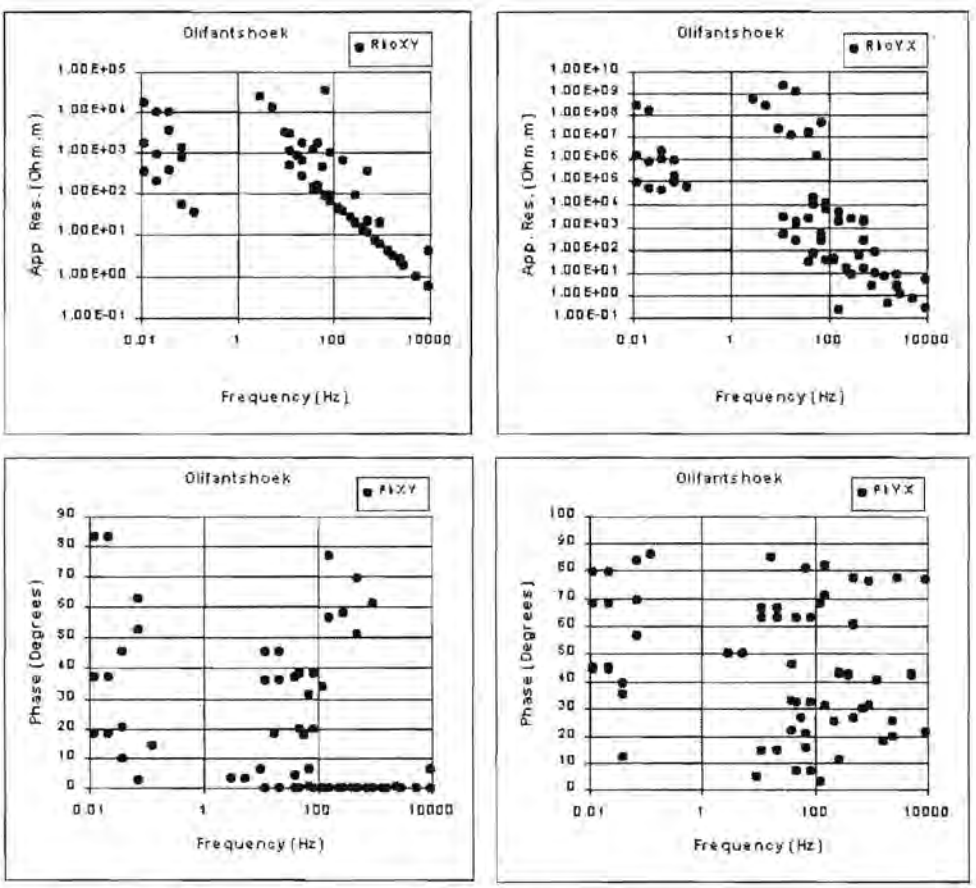

Figure 6.7(a). Apparent resistivity and impedance phase versus frequency curves for Olifantshoek.

Interpretation

The one-dimensional model calculated for the xy-direction shows an increase in resistivity as frequencies change from 1000 Hz to 10 Hz (Figure 6.8). Indications are that the curve turns somewhere between 10 Hz and 0.1 Hz and flattens to roughly 1000 ohm.m at 0.01 Hz. The data in the yx-direction increase steadily with decreasing frequency. The difference between the two curves suggest that the earth is probably anisotropic beneath this station.

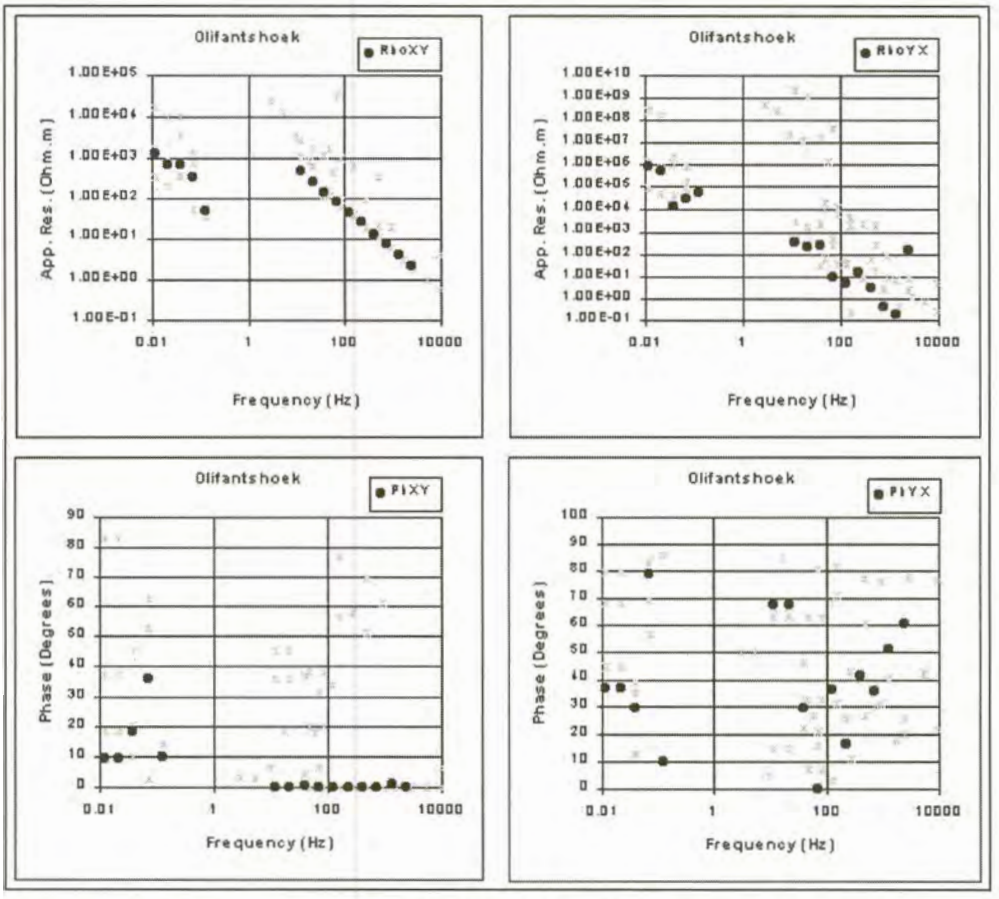

Figure 6.7(b). Curves estimated for Olifantshoek using L_1 norm reduction.

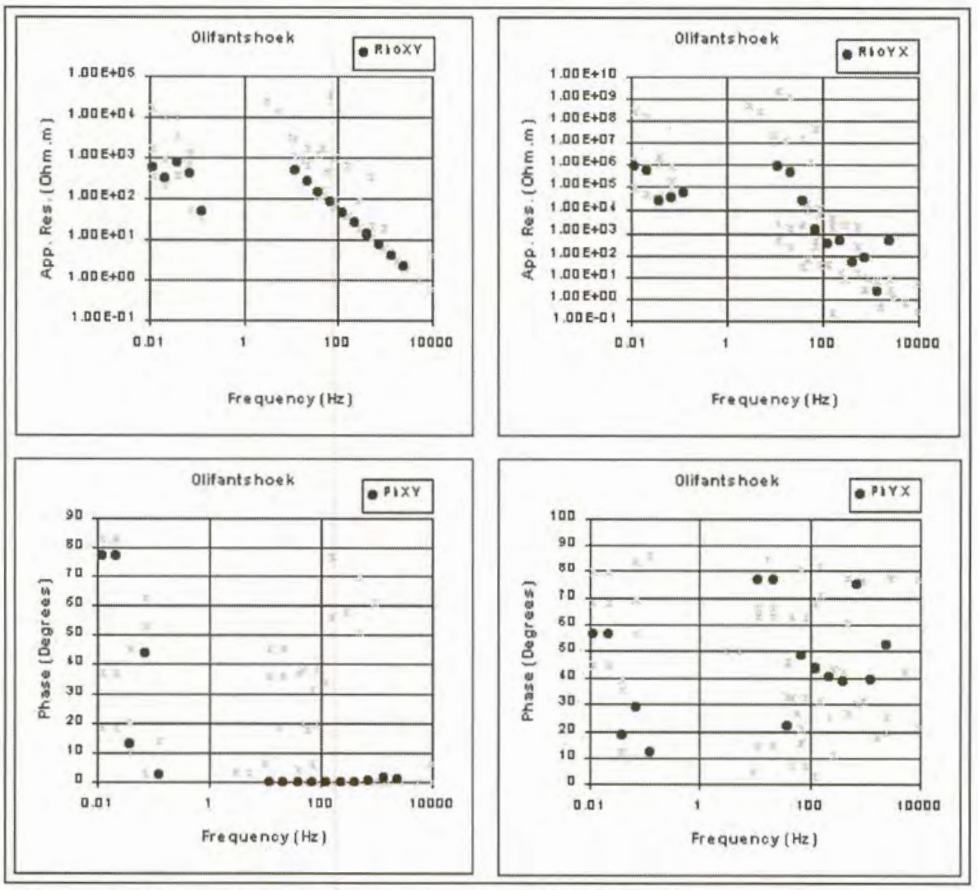

Figure 6.7(c). Curves estimated for Olifantshoek using least squares reduction.

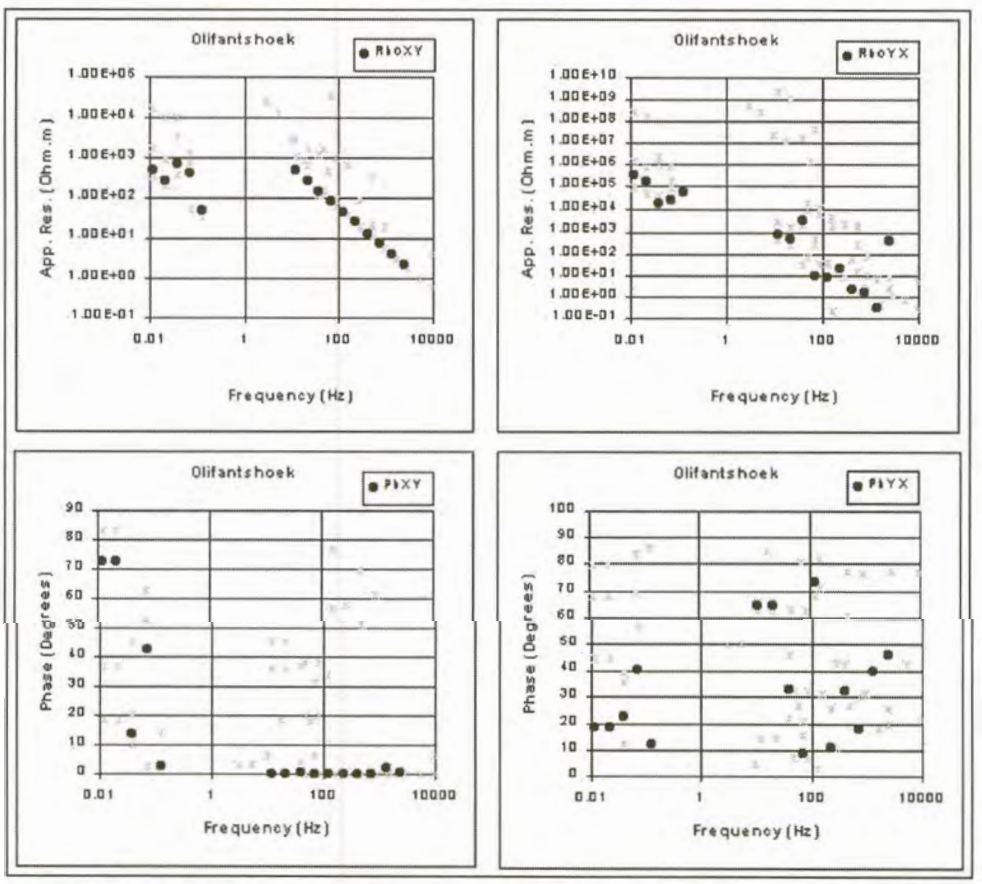

Figure 6.7(d). Curves estimated for Olifantshoek using robust M-estimation.

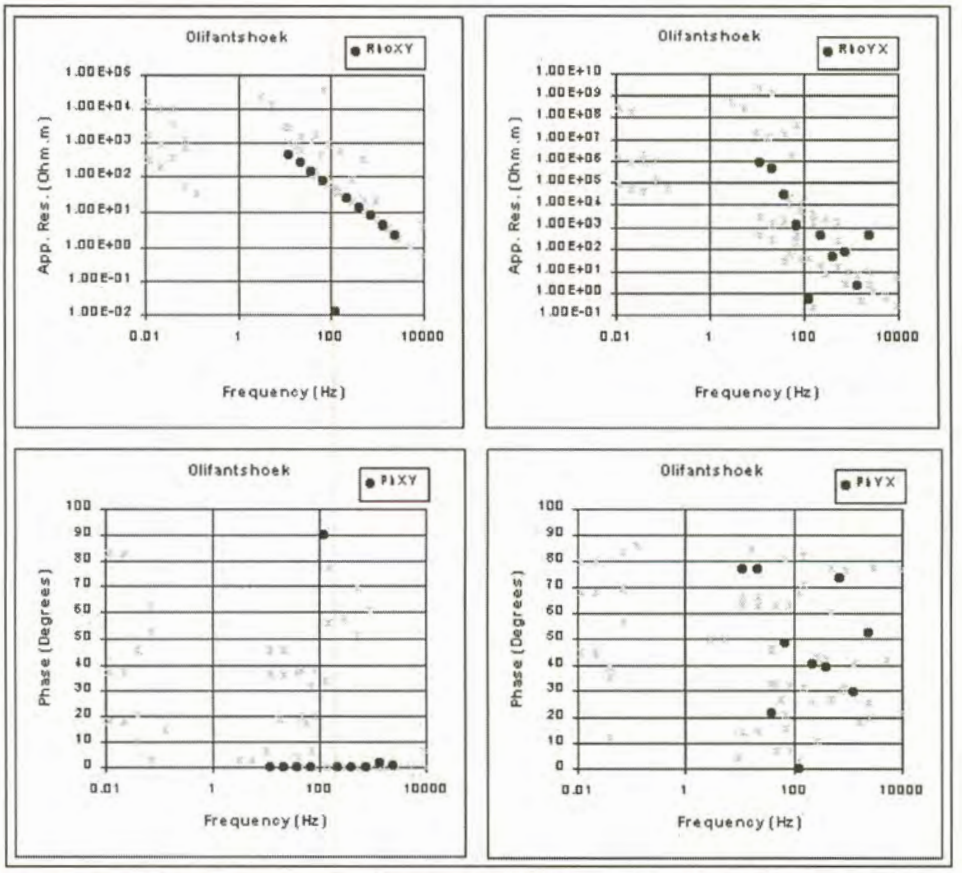

Figure 6.7(e). Curves estimated for Olifantshoek estimated using adaptive L_p norm reduction (Sposito et al., 1983).

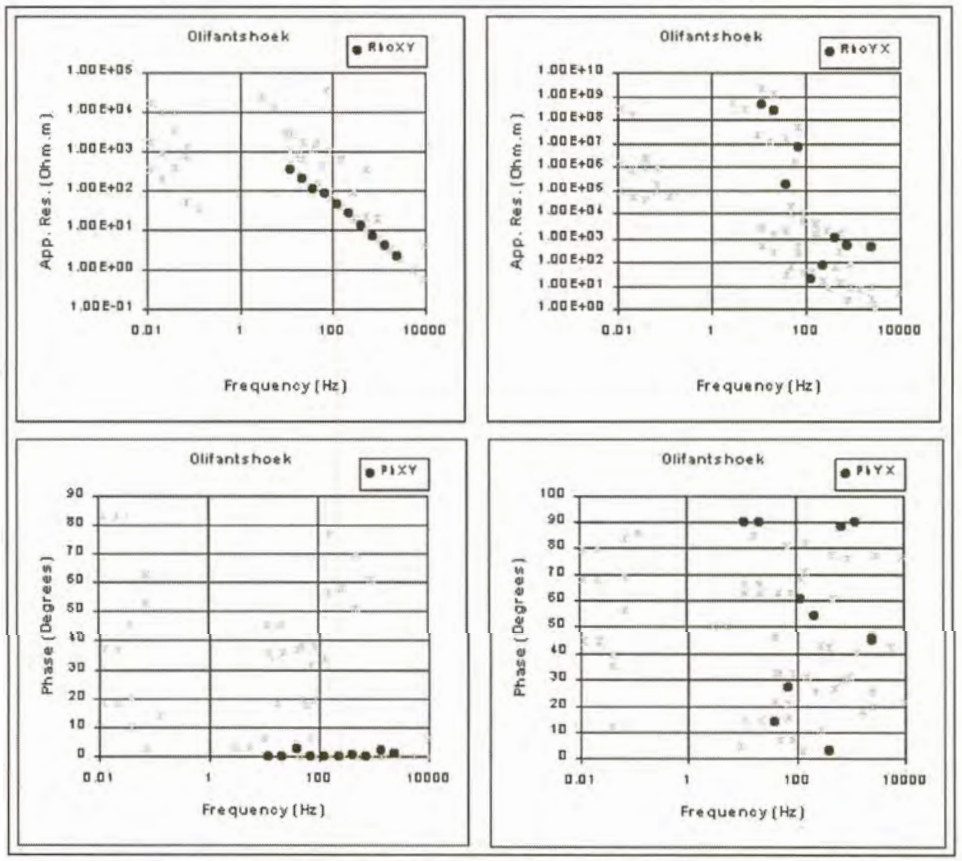

Figure 6.7(f). Curves estimated for Olifantshoek using adaptive L_p norm reduction (Money et al., 1982).

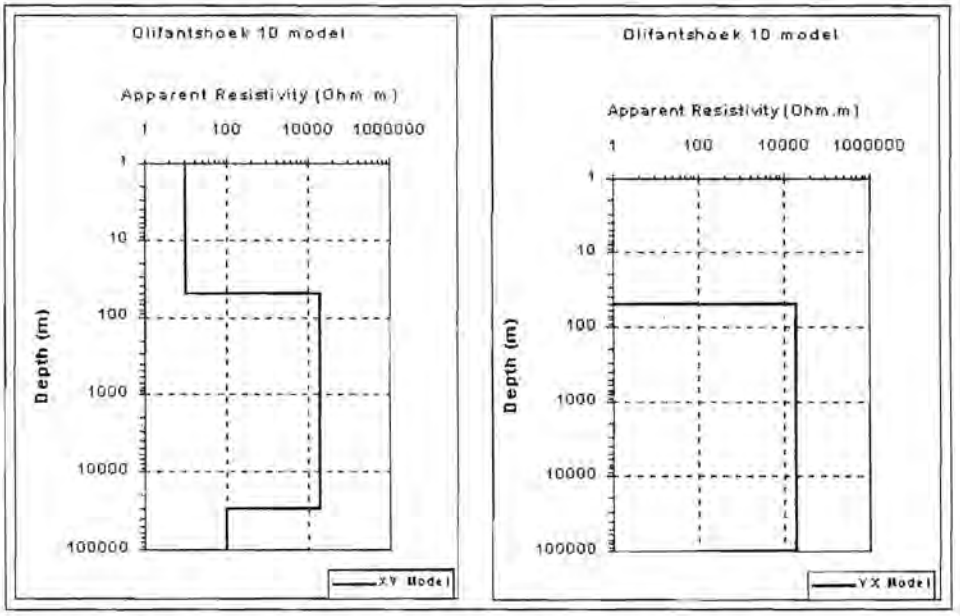

Figure 6.8. One dimensional models for Olifantshoek.

6.3.4. Waaihoek

Figure 6.9(a) shows data collected at this station. The quality of the data is much better for the xy-direction data than for the yx-direction data. Even the phase data in the xy-direction have a higher quality than at any of the previous stations.

Results of statistical reduction

All the statistical techniques, with the exception of the L1 norm (Figure 6.9(b)), yield good results for the data in the xy-direction. The curve determined by the adaptive L_p norm technique using Money's equation (Figure 6.9(f)) shows some deterioration at 55 Hz. The best results for the phase data are obtained by the L2-norm and robust M-estimation methods (Figures 6.9(c) and (d)).

More outliers are present in the yx-direction. This causes a marked deterioration in the quality of the fitted curves, especially at higher frequencies. The curve calculated using the L_p-norm method and Money's equation gives the best result in the higher frequency range.

Interpretation

The apparent resistivity curves are nearly identical in the two measurement directions. This suggests a lack of two- and three-dimensional structures at this station.

The curves start at approximately 10 Ωm at high frequencies and increases to roughly 1000 Ωm at 11 Hz. It then flattens and remains at this for lower frequencies. There is a subtle increase in apparent resistivity at the lowest frequencies. Figure 6.10 shows the one-dimensional model deduced from these curves.

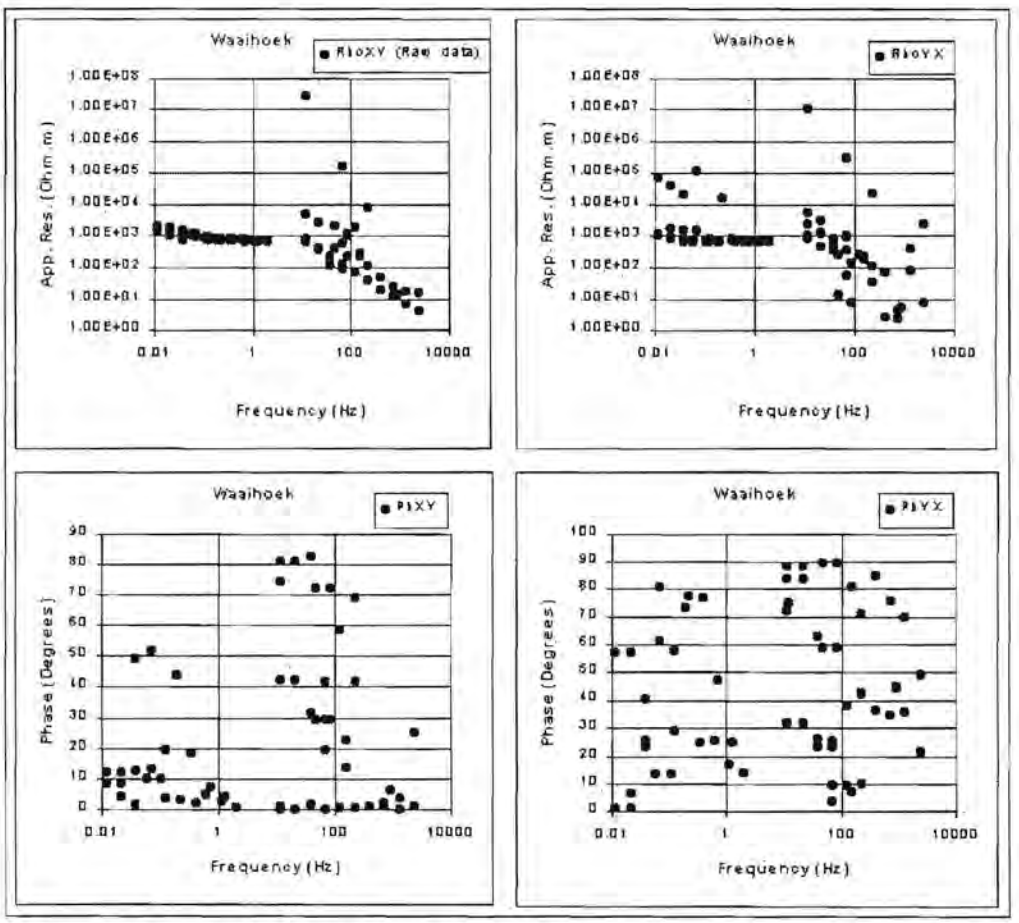

Figure 6.9(a). Apparent resistivity and impedance phase versus frequency curves for Waaihoek.

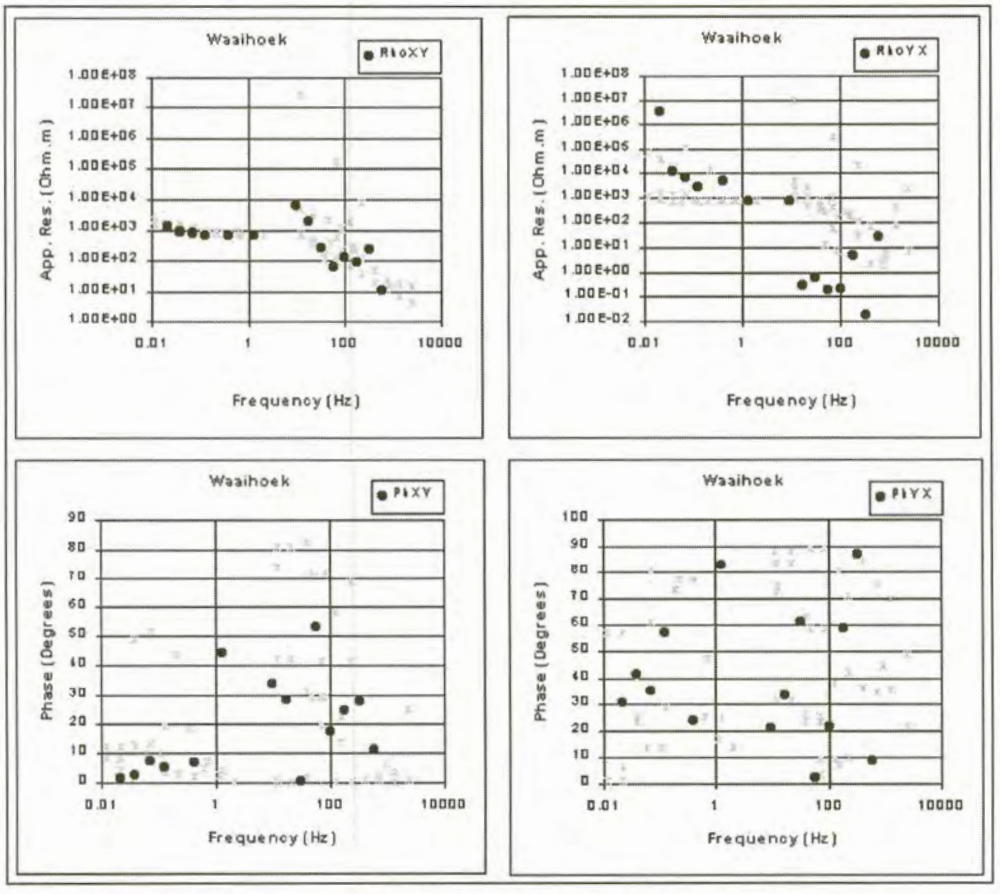

Figure 6.9(b). Curves estimated for Waaihoek using L_1 norm.

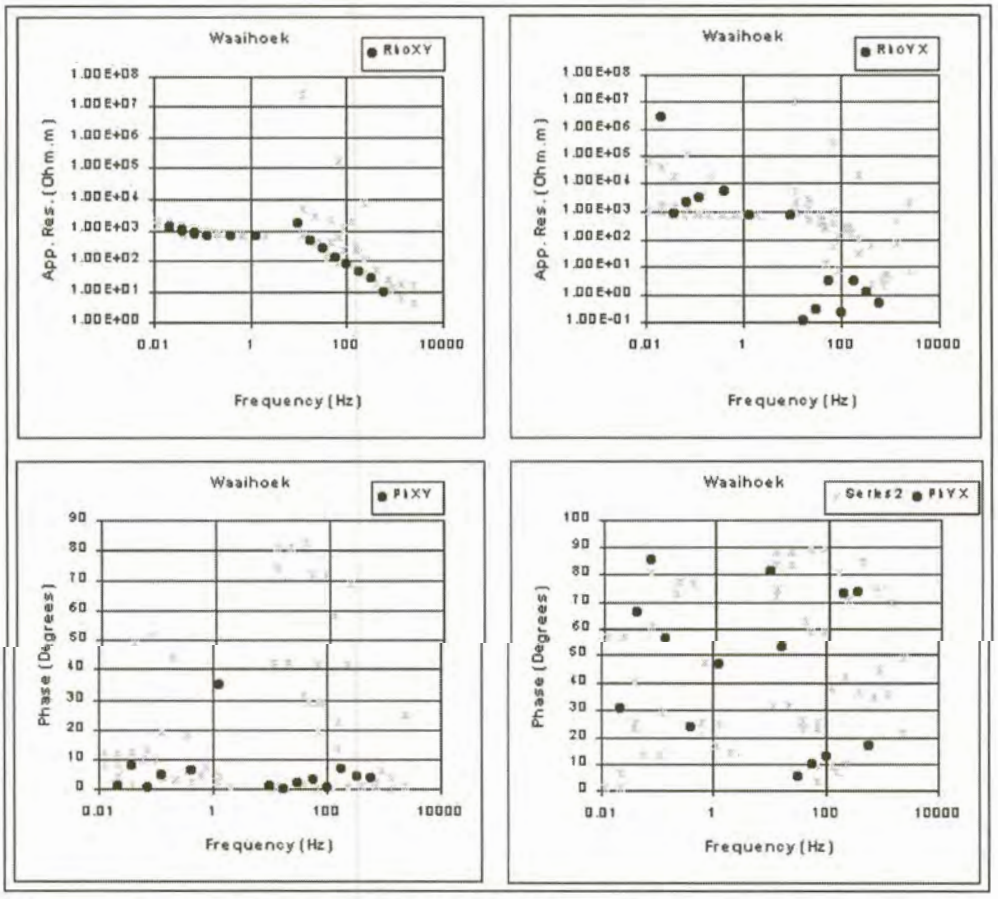

Figure 6.9(c). Curves estimated for Waaihoek using least squares reduction.

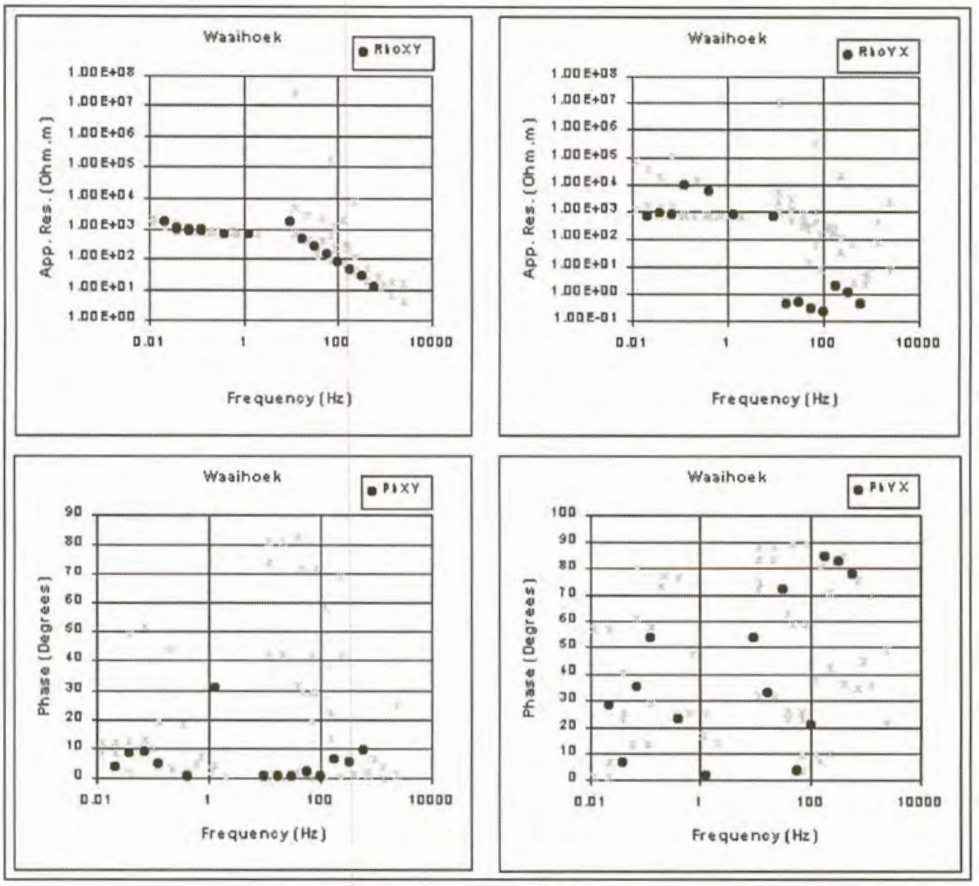

Figure 6.9(d). Curves calculated for Waaihoek using robust M-estimation.

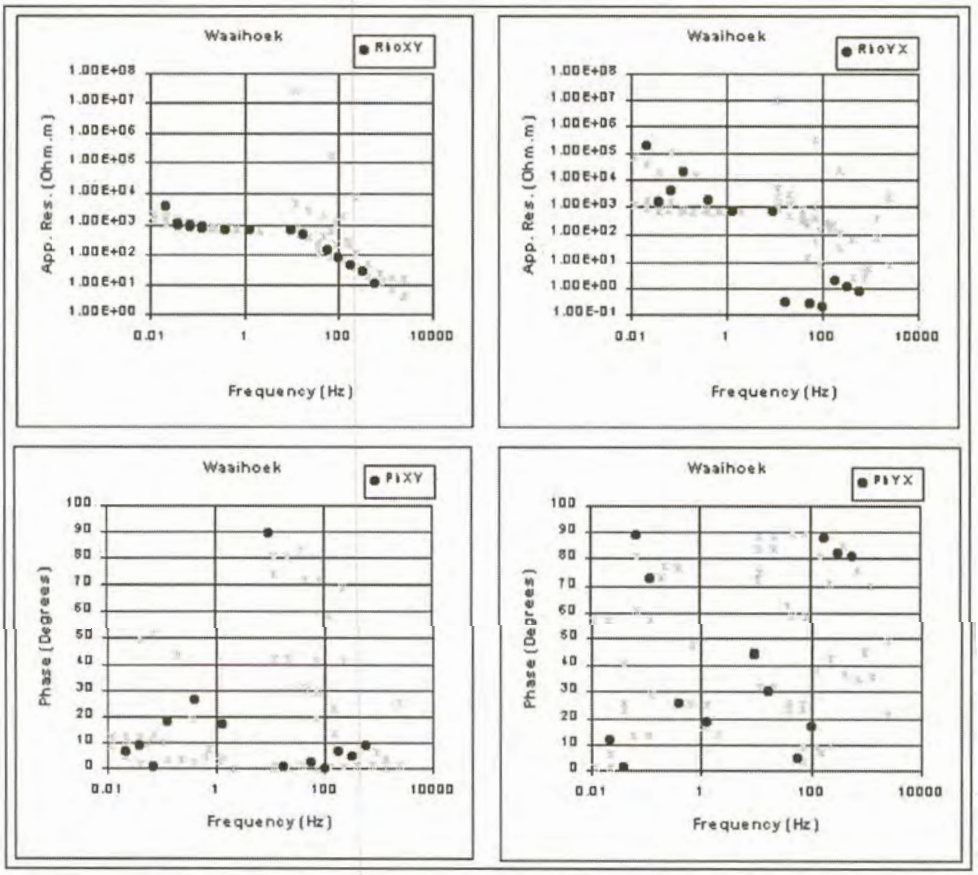

Figure 6.9(e). Curves calculated for Waaihoek using adaptive L_p norm reduction (Sposito et al., 1983).

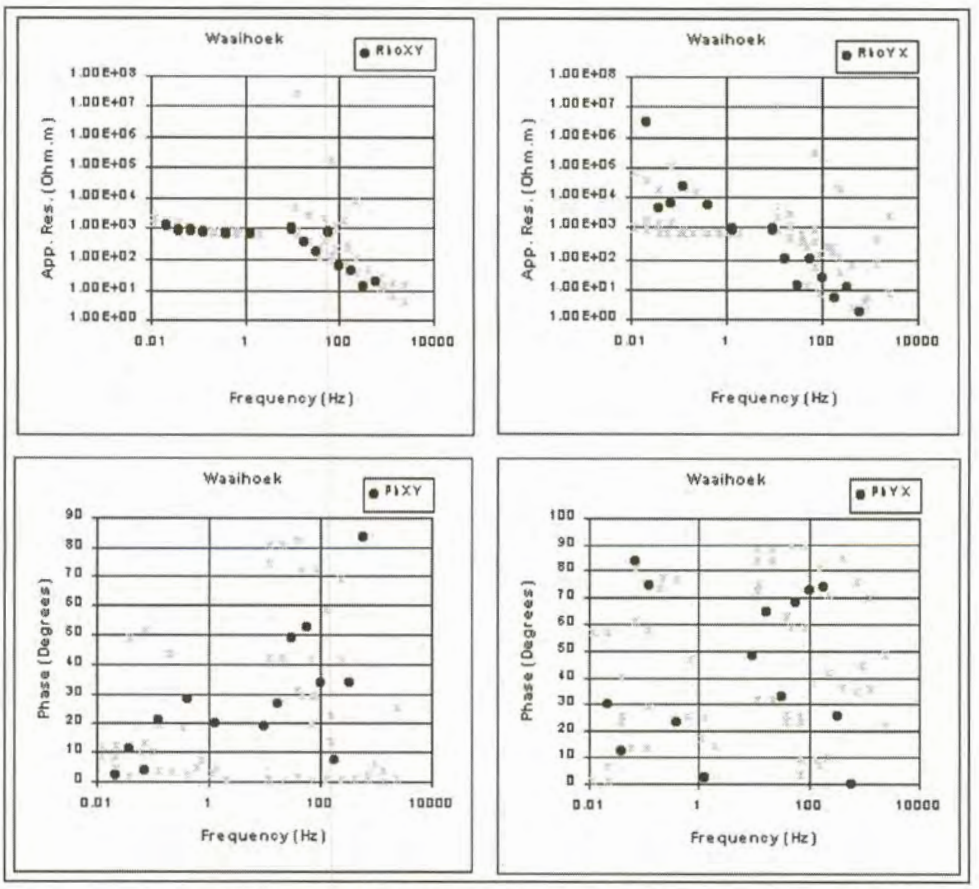

Figure 6.9(f). Curves calculated for Waaihoek using adaptive L_p norm reduction (Money et al., 1982).

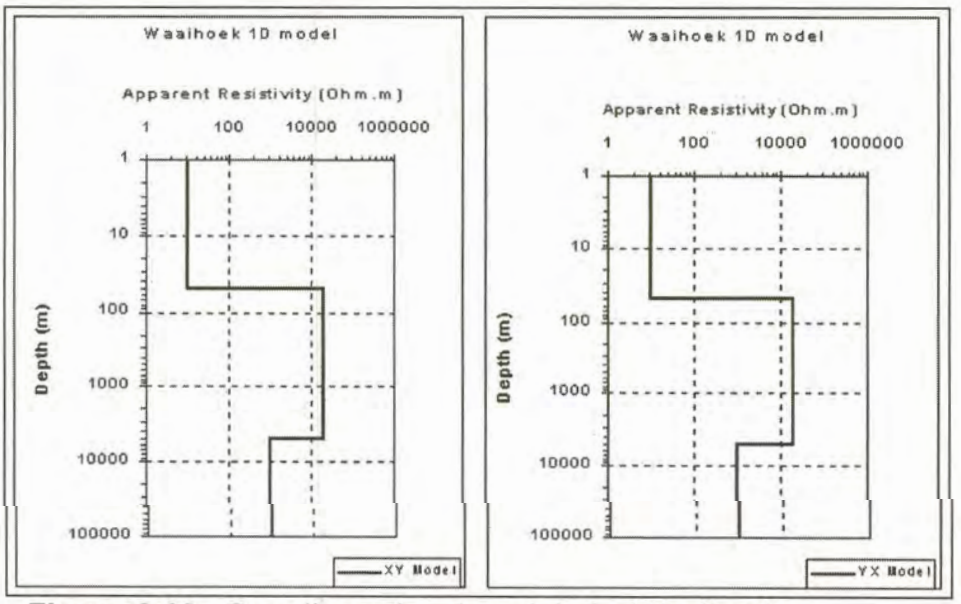

Figure 6.10. One dimensional models for Waaihoek.

6.3.5. Paleisheuwel

The data curves for this station are very scattered, although it is possible to see some trend in the apparent resistivity curves (Figure 6.11(a)). Data were only obtained up to 115 Hz. Although data in both directions are scattered, a number of outliers occur on the ρ_{yx} curve.

Results of statistical reduction

All the statistical reduction methods yield very poor results for this data set. The curves estimated for the yx-direction data yield better results than for the xy-direction. The adaptive L_p norm technique using Sposito's equation produces the best fit to the data (Figure 6.11(e)). Curves obtained for the xy-direction vary quite significantly depending on the statistical method used.

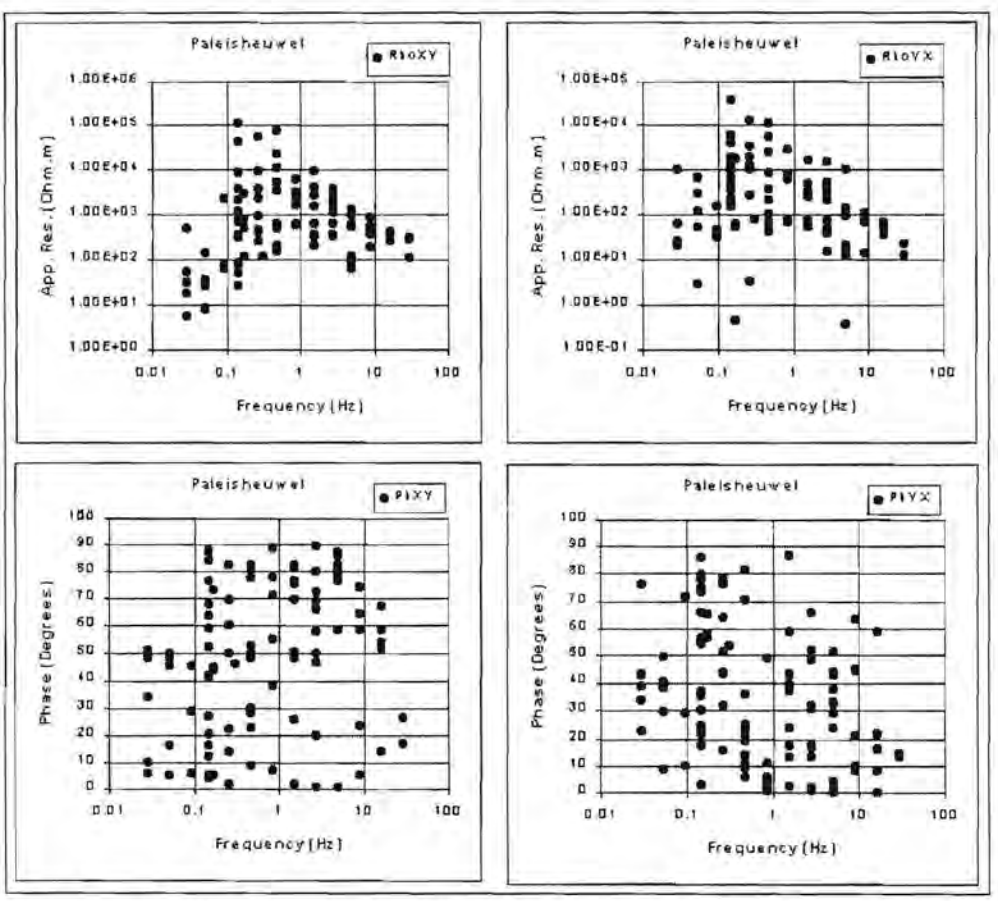

Figure 6.11(a). Apparent resistivity and impedance phase versus frequency curves for Paleisheuwel.

Interpretation

The apparent resistivity curves in both directions have basically the same trend, but values for the ρ_{xy} curve are almost an order of magnitude larger than those for the yx-direction. Both curves start with low resistivities at high frequencies, increasing with a decrease in frequency. At approximately 0.25 Hz the resistivities start to decrease. The one-dimensional models for this station are shown in Figure 6.12.

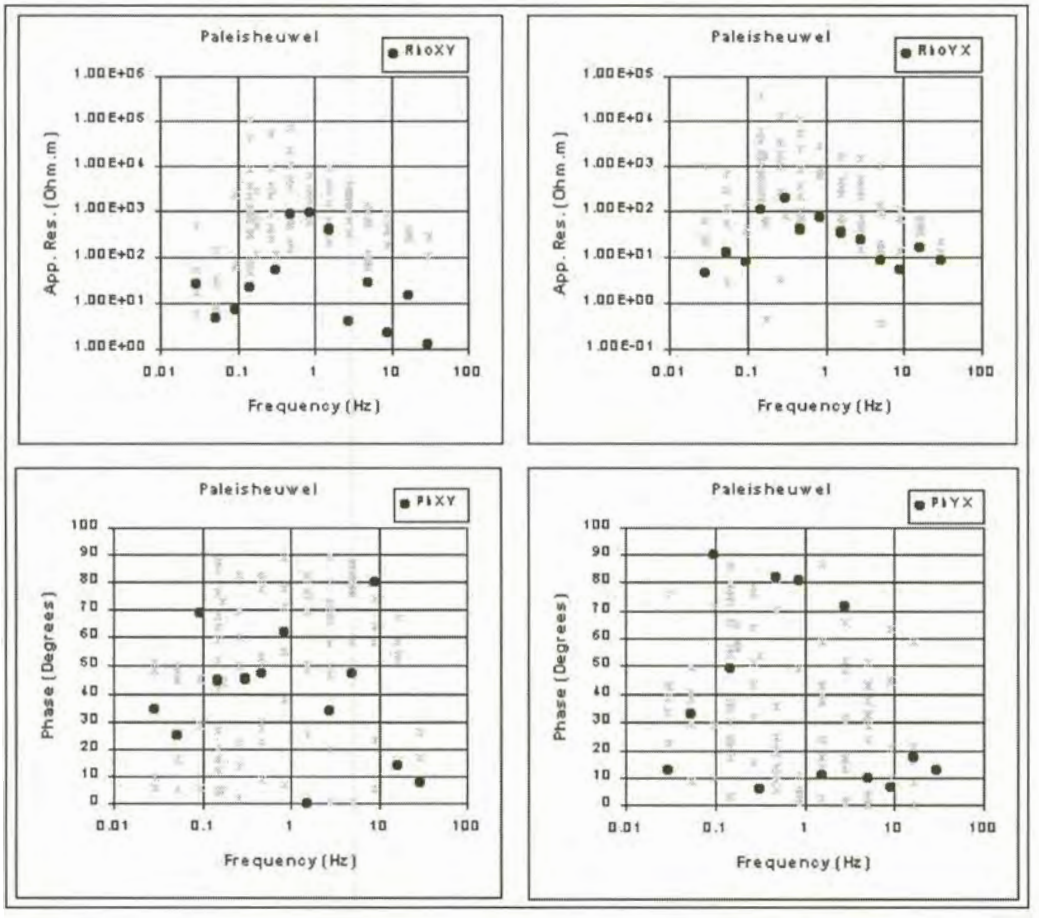

Figure 6.11(b). Curves estimated for Paleisheuwel using L_1 norm reduction.

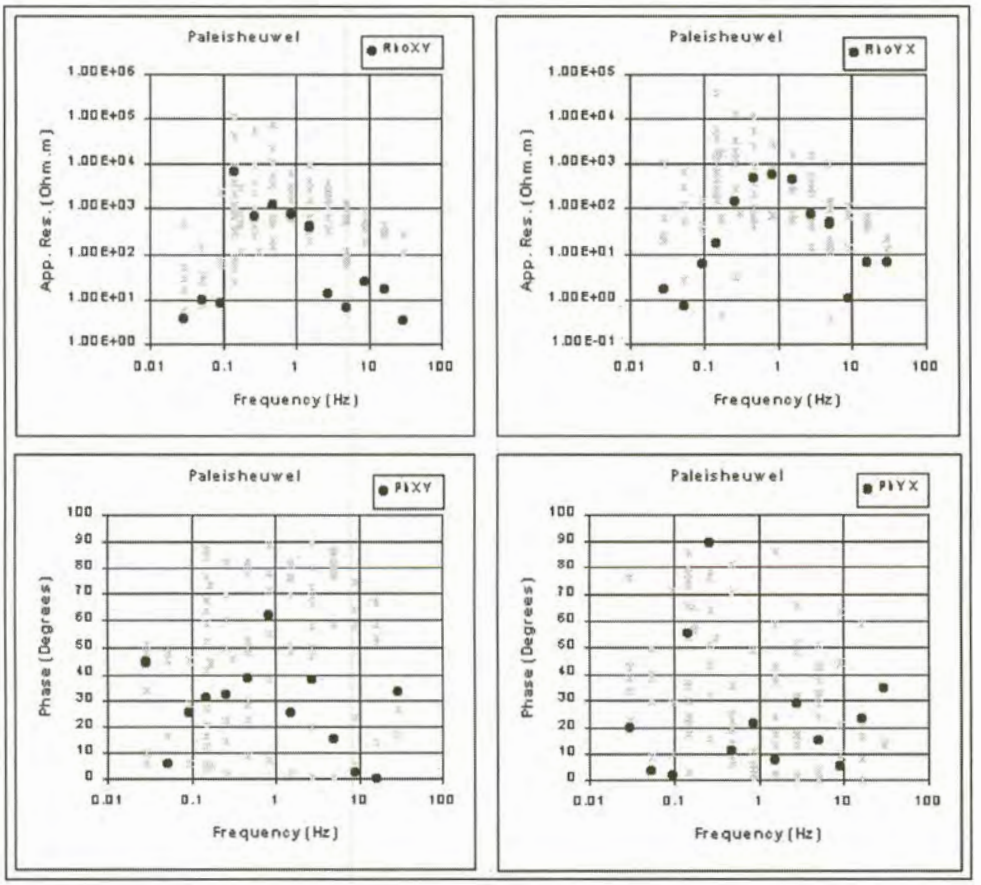

Figure 6.11(c). Curves estimated for Paleisheuwel using least squares reduction.

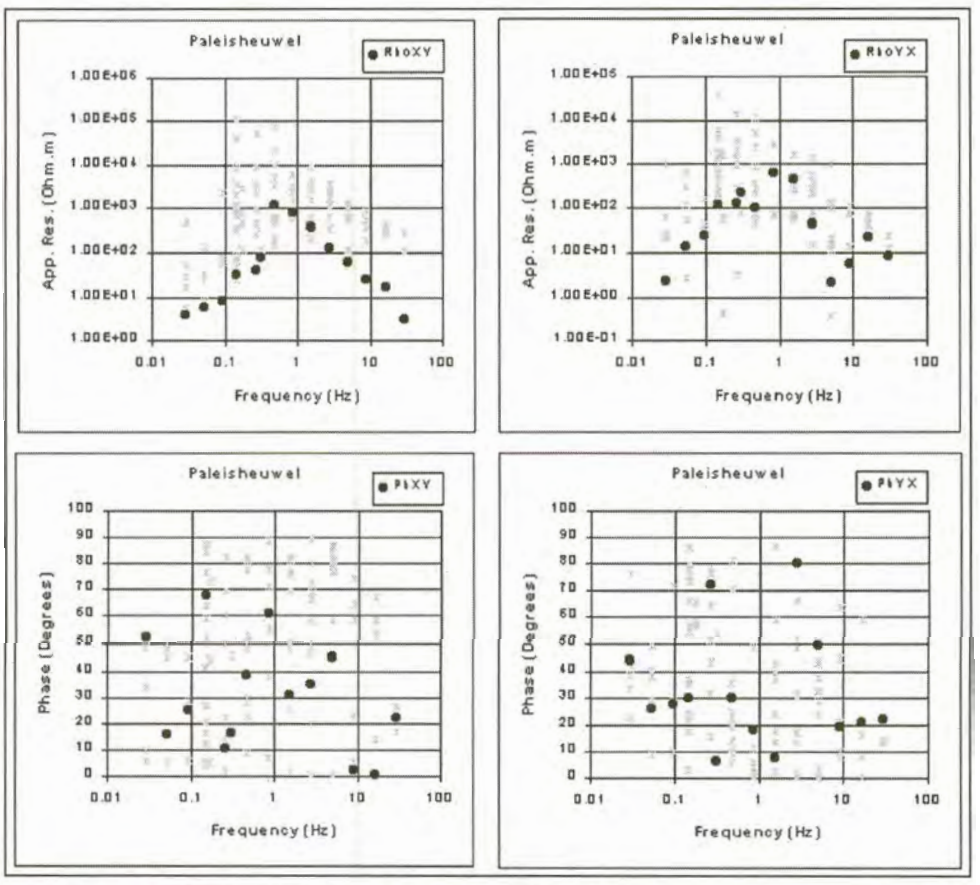

Figure 6.11(d). Curves calculated for Paleisheuwel using robust M-estimation.

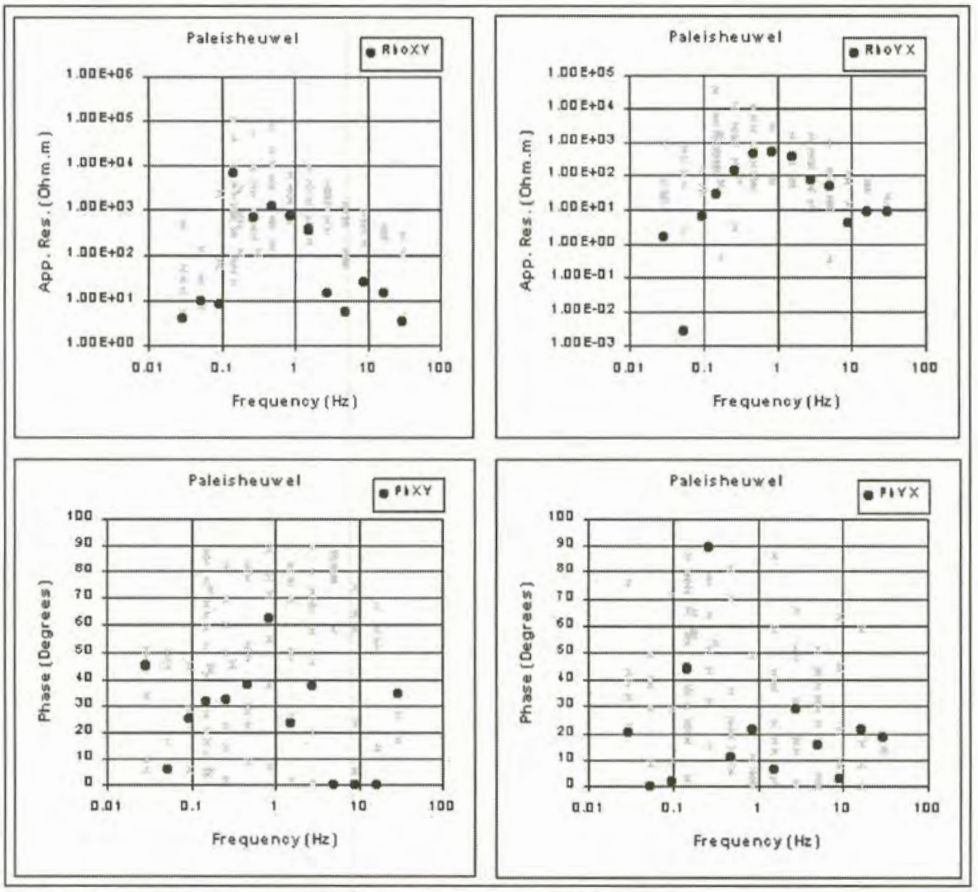

Figure 6.11(e). Curves estimated for Paleisheuwel using adaptive L_p norm reduction (Sposito et al., 1983).

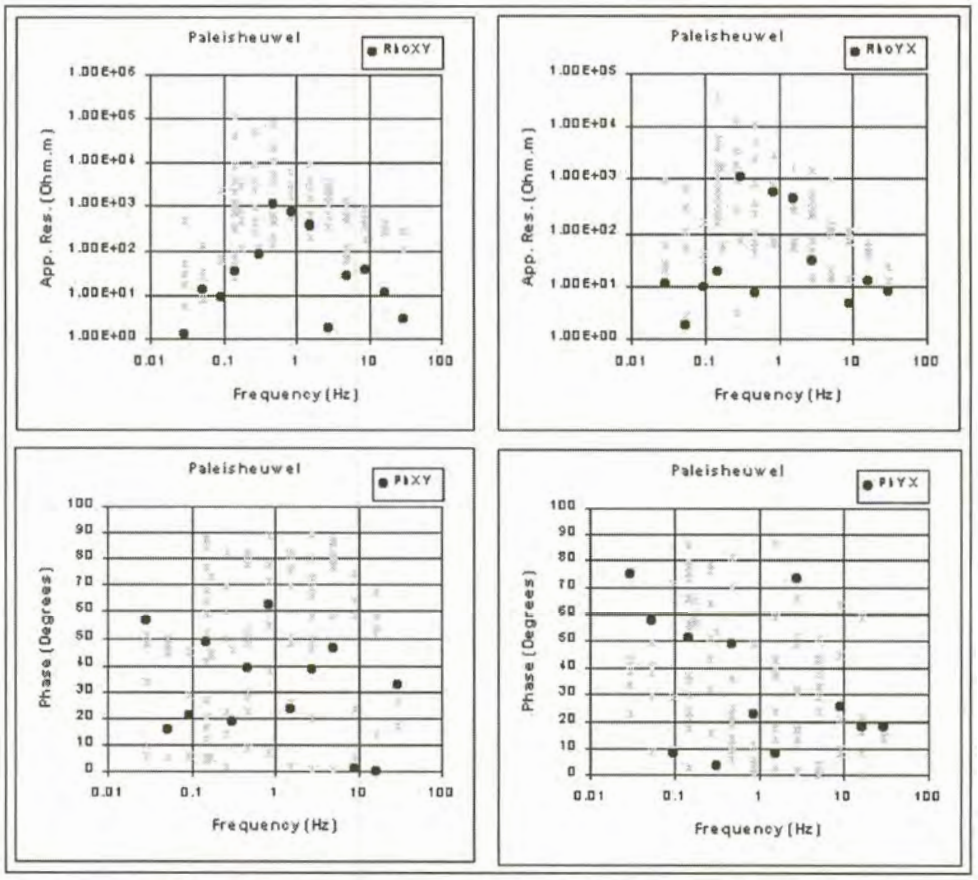

Figure 6.11(f). Curves estimated for Paleisheuwel using adaptive L_p norm reduction (Money et al., 1982).

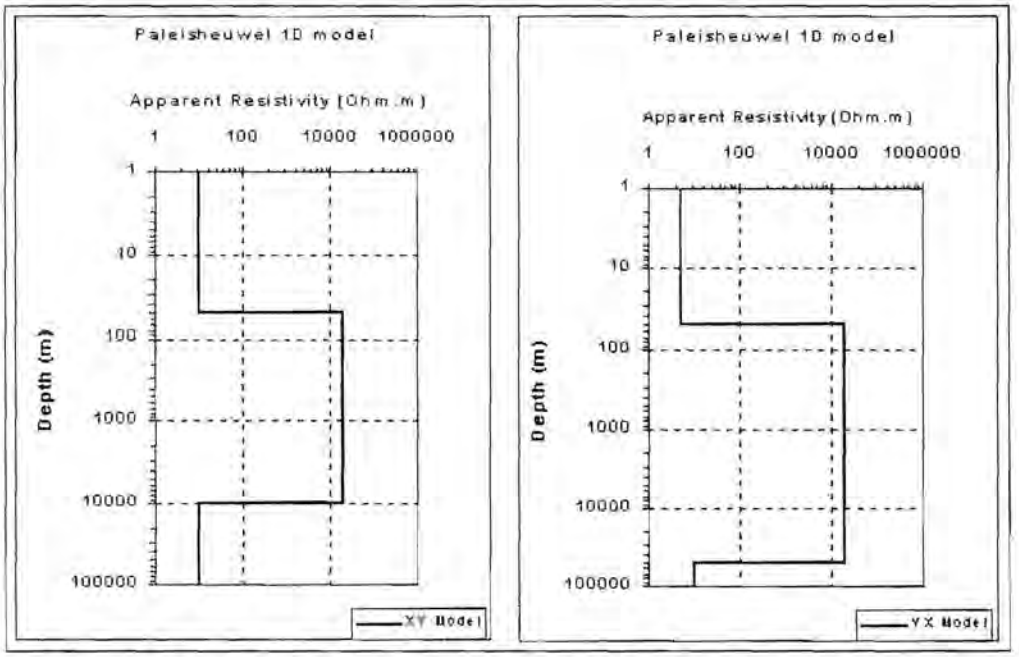

Figure 6.12. One dimensional models for Paleisheuwel.

6.3.6. Inkruip

The data for this station are scattered, but it is possible to distinguish a trend for both the ρ_{xy} and ρ_{yx} data sets (Figure 6.13(a)). Data were obtained between 0.15 Hz and 167 Hz.

Results of statistical reduction

Curves fitted through the data with the different statistical reduction methods are all of quite good quality (Figure 6.13(b) to (f)). Better results are obtained at frequencies where more data could be obtained. At the lowest freqeuncies where only a few data points occur the quality of the curves deteriorates drastically.

For data in both directions the least squares technique yields the poorest results (Figure 6.13(c)). Curves calculated by the robust M-estimation- and adaptive L_p norm methods are very similar.

Interpretation

The apparent resistivity curves in the two directions differ quite substantially. In the xy-direction the apparent resistivity increases with

decreasing frequency. The curve flattens out a little in the vicinity of 5 Hz, but from about 2 Hz it increases again. At high frequencies the ρ_{yx} curve increases with decreasing frequency, but at roughly 20 Hz it turns and the apparent resistivity steadily decreases with decreasing frequency.

The large difference between the two curves indicates a very anisotropic electrical substructure at this station. One dimensional models for this station (Figure 6.14) are very different for the two measurement directions.

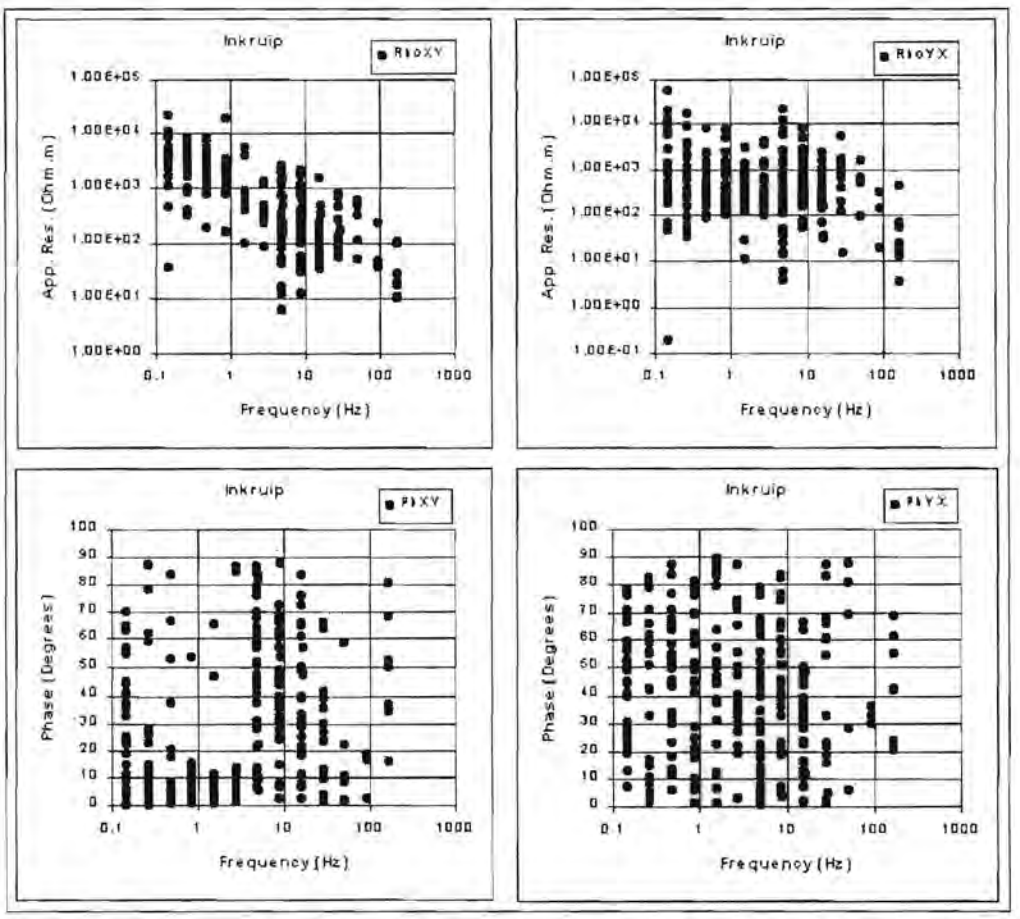

Figure 6.13(a). Apparent resistivity and impedance phase versus frequency curves for Inkruip.

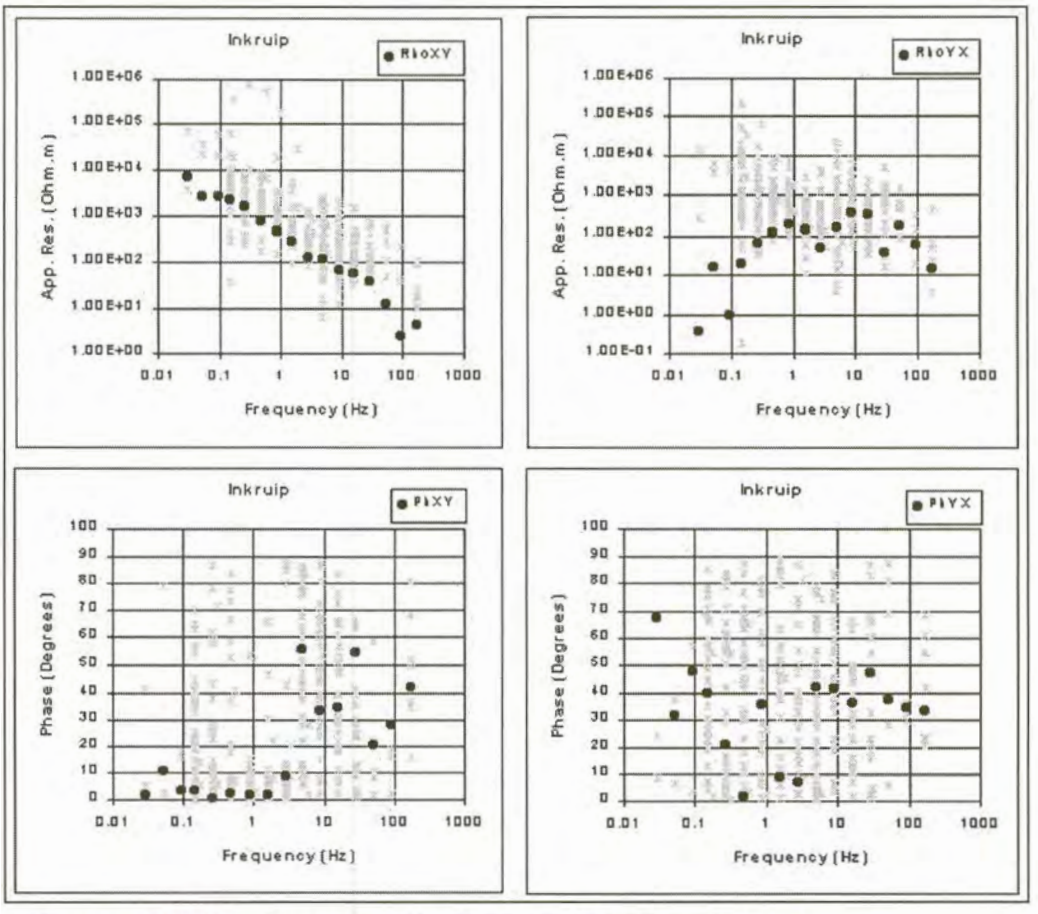

Figure 6.13(b). Curves estimated for Inkruip using L_1 norm reduction.

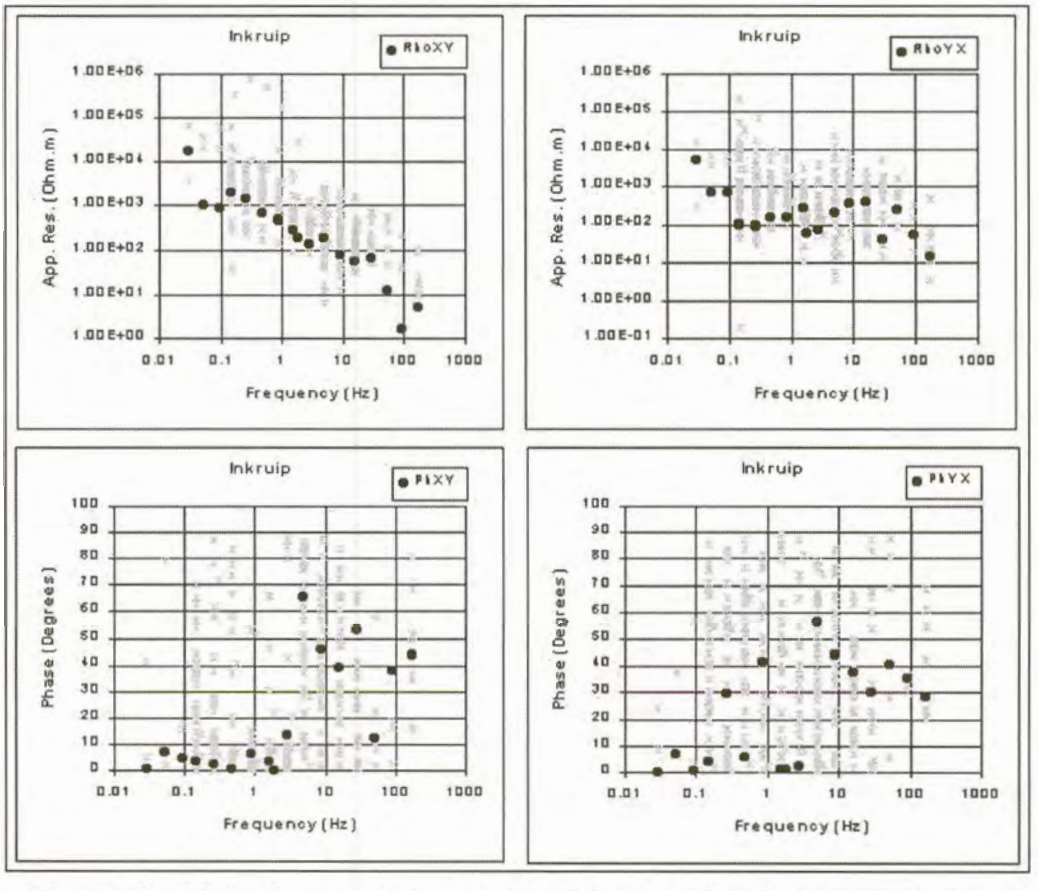

Figure 6.13(c). Curves estimated for Inkruip using least squares reduction.

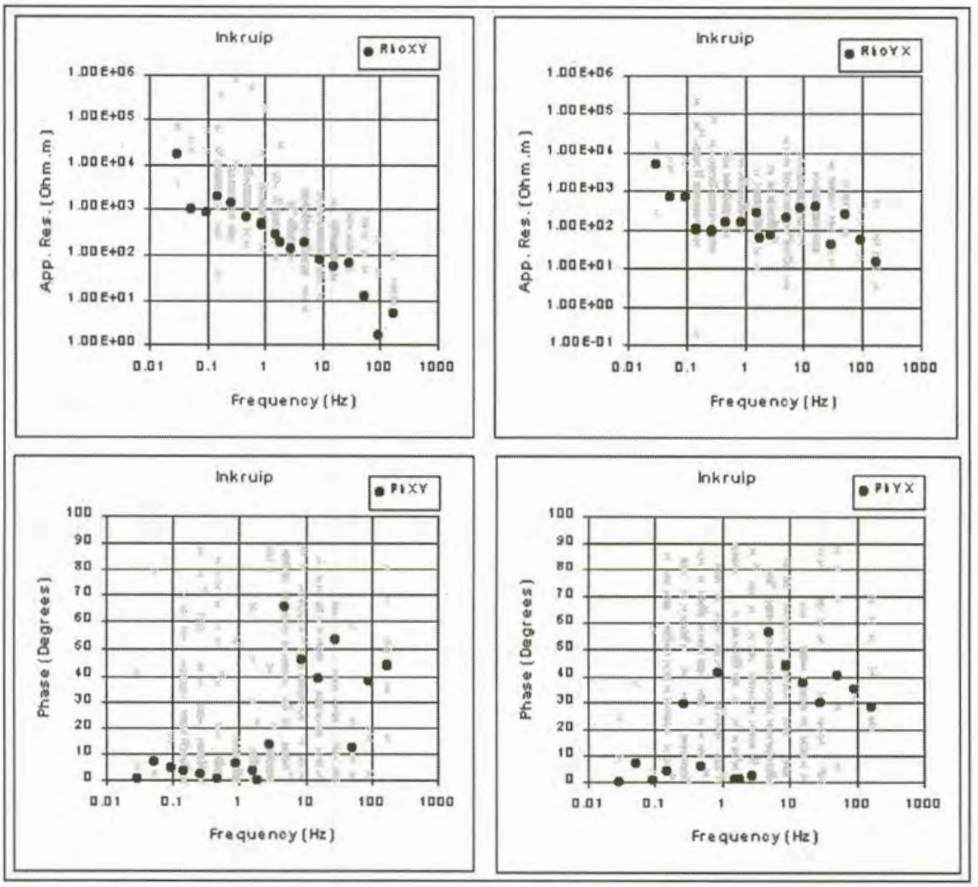

Figure 6.13(d). Curves estimated for Inkruip using robust M-estimation.

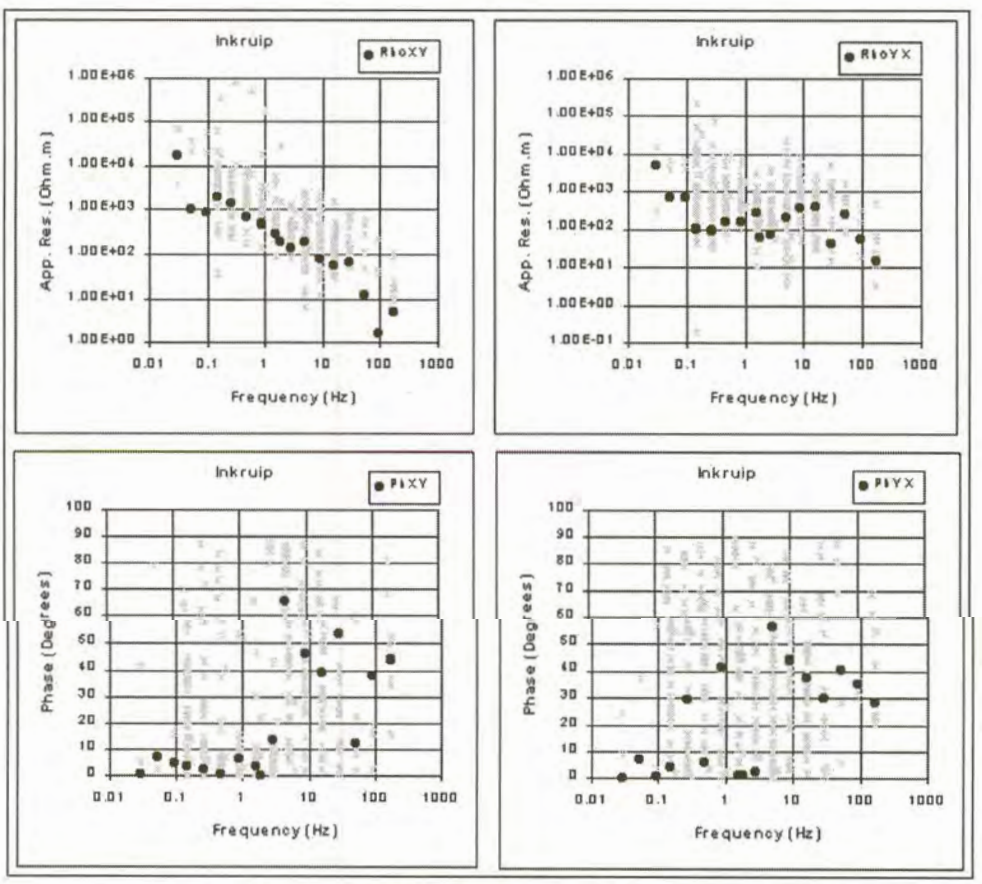

Figure 6.13(e). Curves estimated for Inkruip using adaptive L_p norm reduction (Sposito et al., 1983).

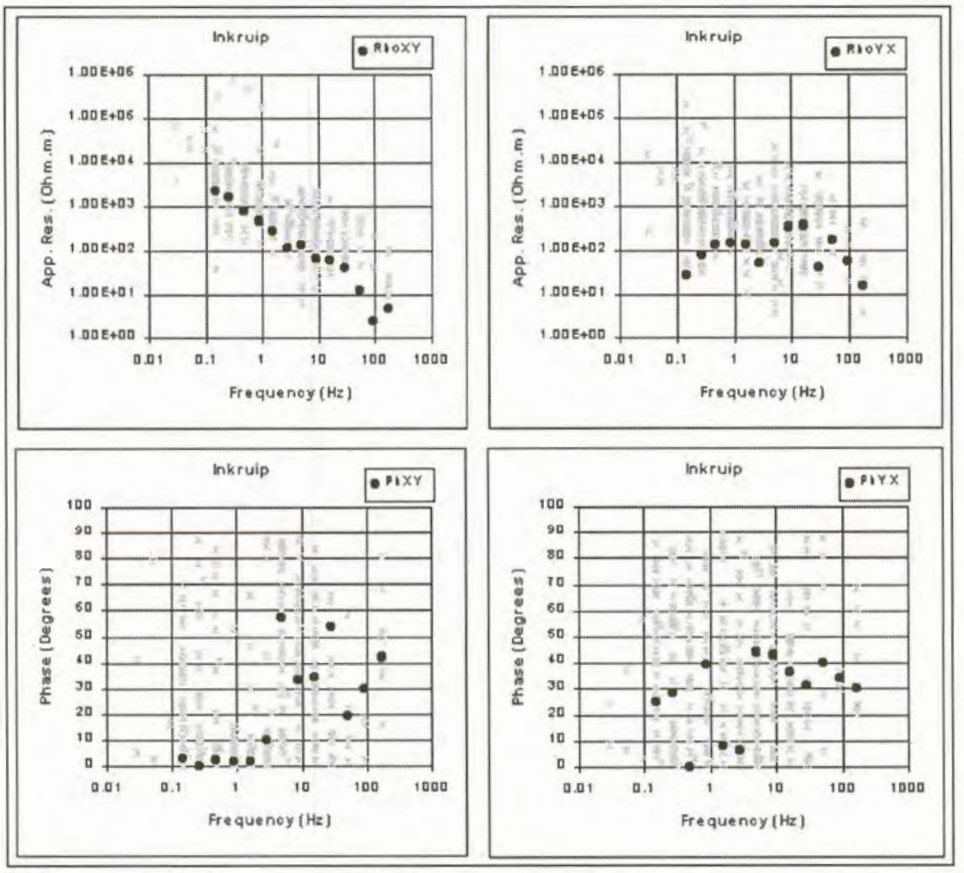

Figure 6.13(f). Curves estimated for Inkruip using adaptive L_p norm reduction (Money et al., 1982).

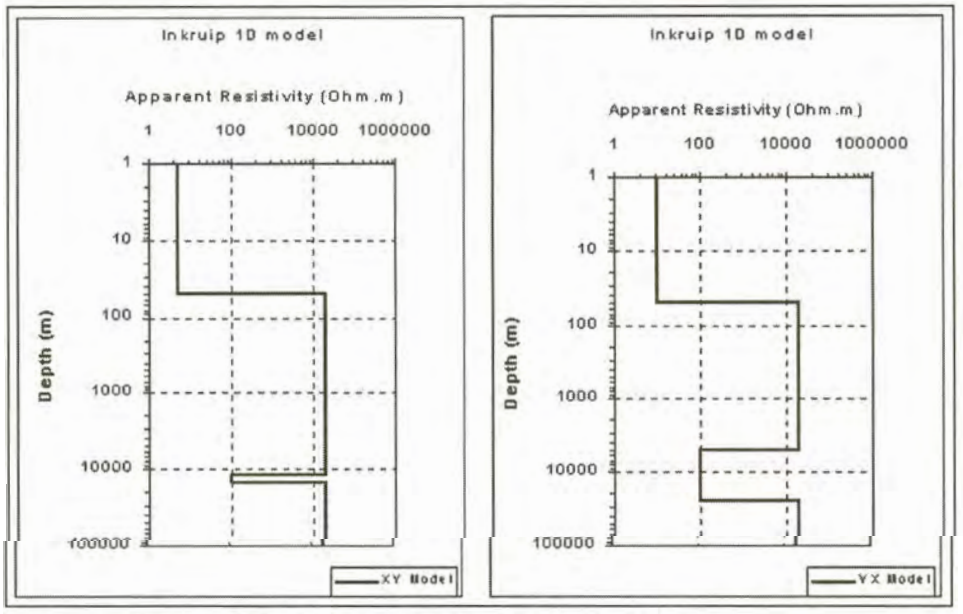

Figure 6.14. One dimensional models for Inkruip.

6.3.7. Gannavlakte

Data were collected between 0.1 Hz and 1000 Hz at this station (Figure 6.15(a)). The quality of the data is very low for both measurement directions.

Results of statistical reduction

None of the statistical methods yielded good fits (Figures 6.15(b) to (f)).

Interpretation

The data at this station follow the same trend as for Inkruip. Apparent resistivity values in the xy-direction increase with decreasing frequencies, with a possible conductor present at 10 Hz. In the yx-direction the resistivity values also increase with decreasing frequency at higher frequencies. At 10 Hz the curve flattens out. From 1 Hz and lower the resistivies start to increase again. Figure 6.16 shows the one-dimensional models for this station.

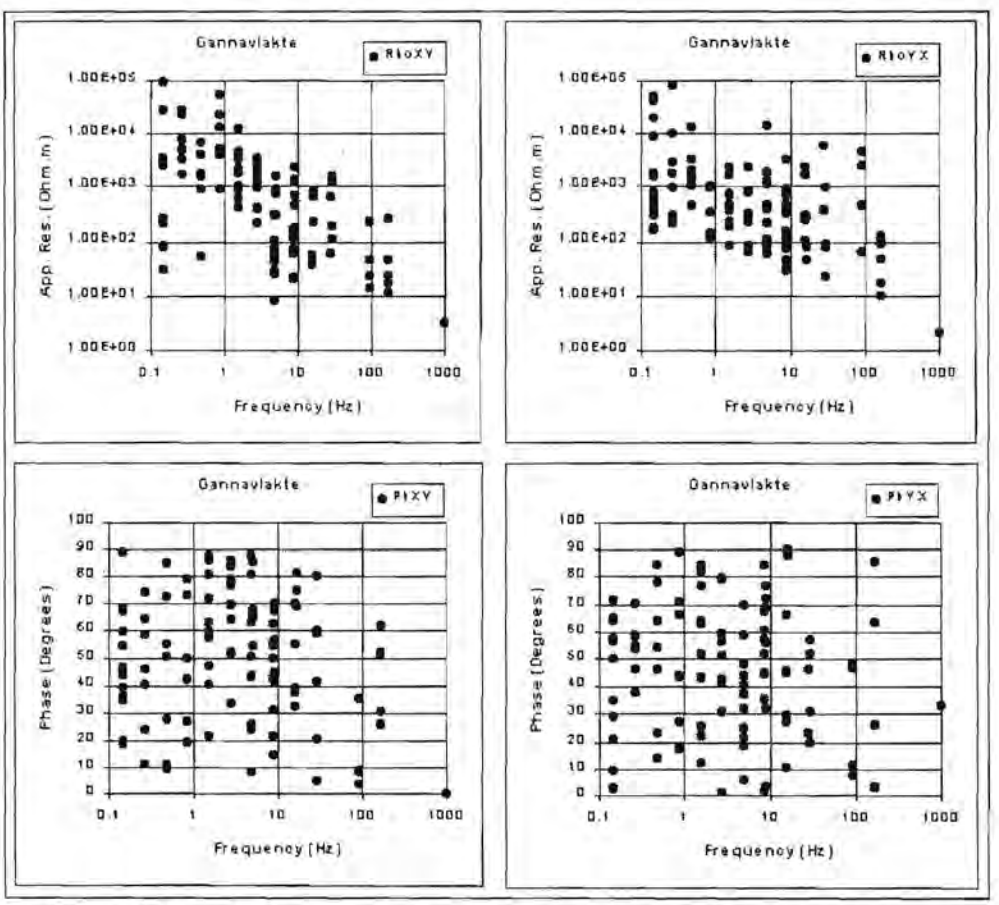

Figure 6.15(a). Apparent resistivity and impedance phase versus frequency curves for Gannavlakte.

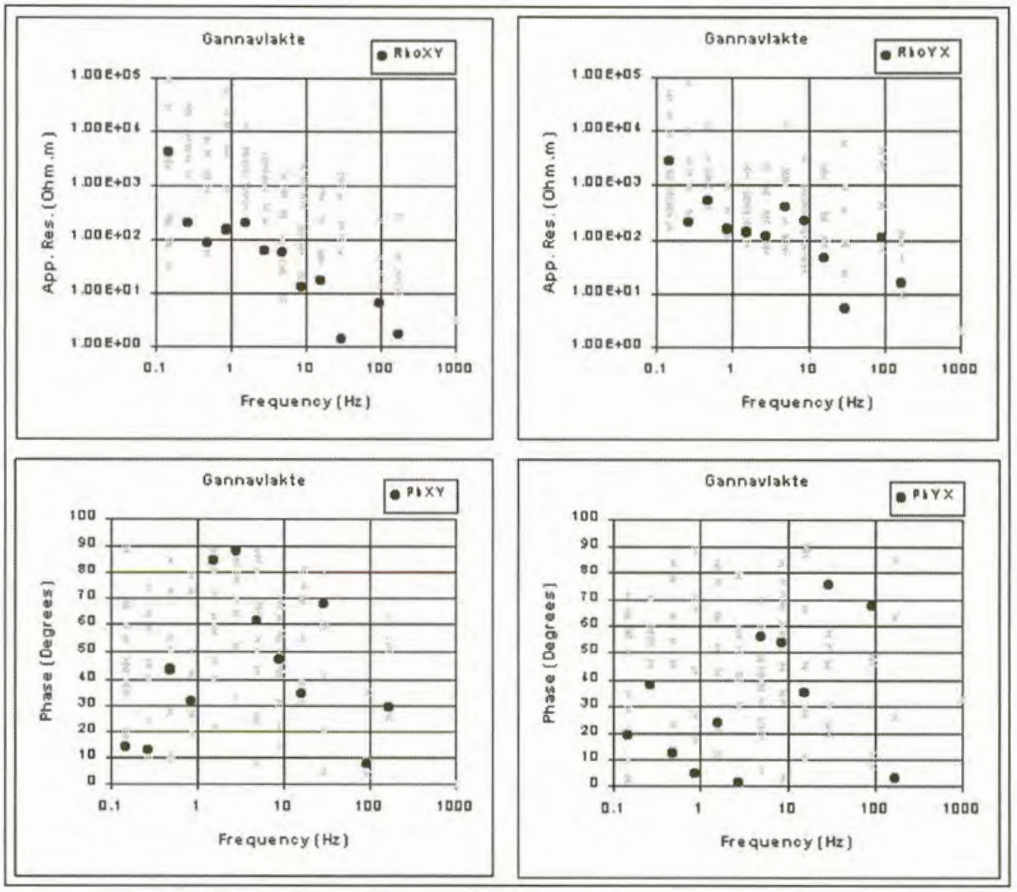

Figure 6.15(b). Curves estimated for Gannavlakte using L_1 norm reduction.

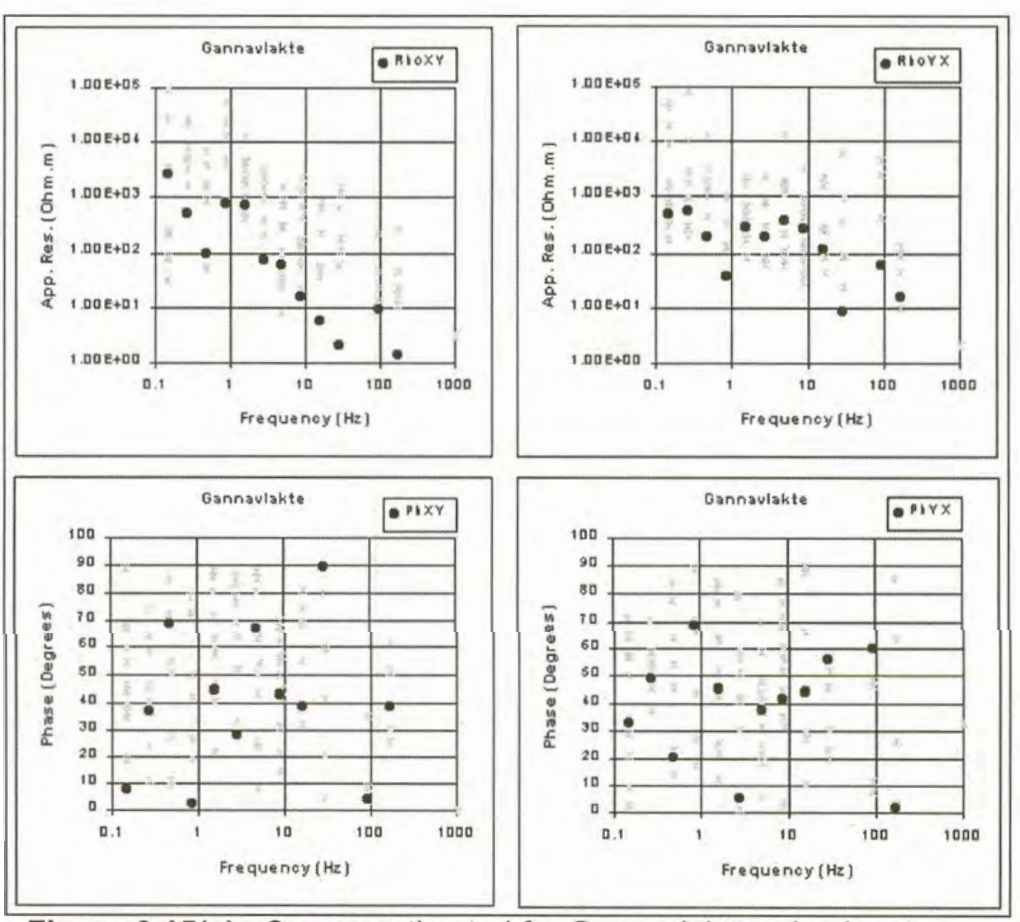

Figure 6.15(c). Curves estimated for Gannavlakte using least squares reduction.

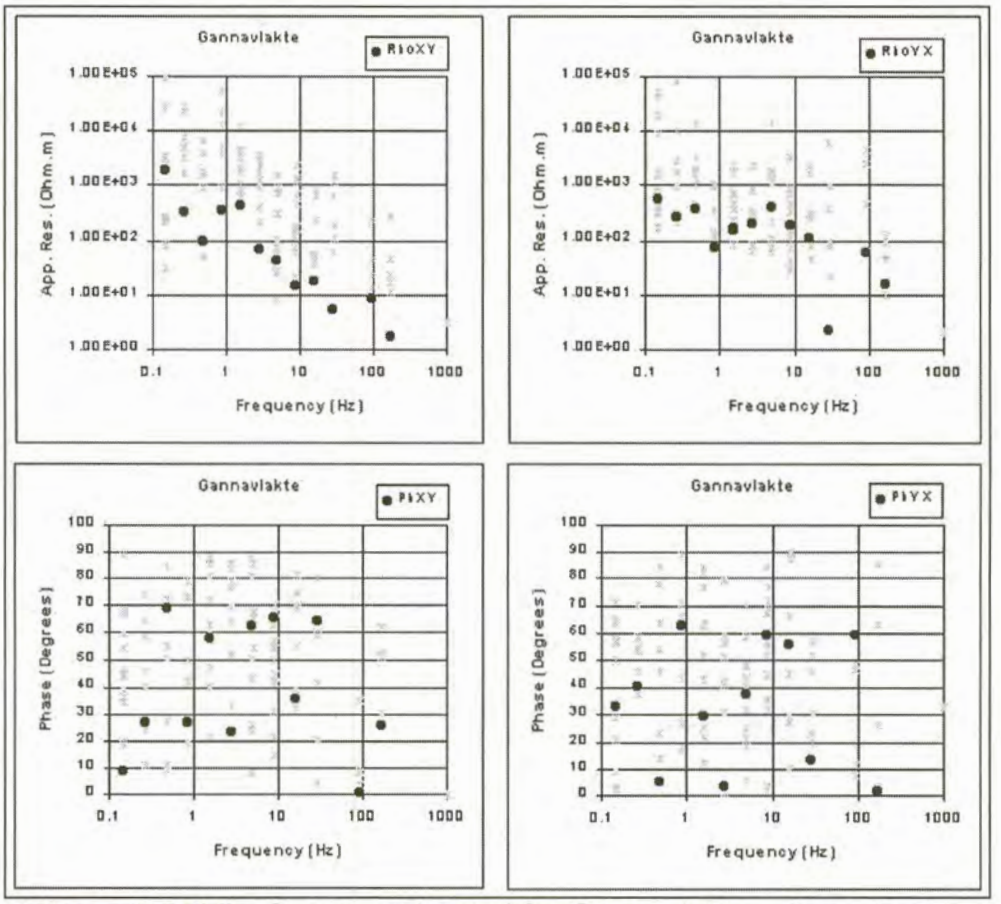

Figure 6.15(d). Curves estimated for Gannavlakte using robust M-estimation.

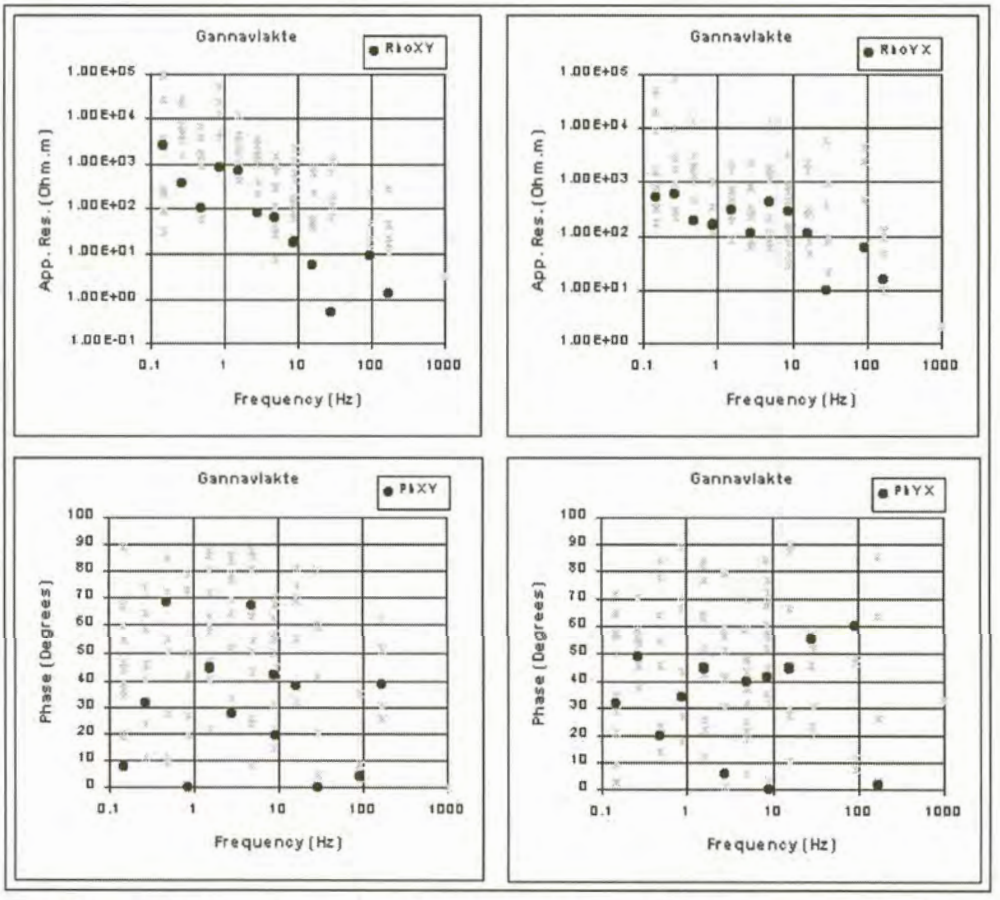

Figure 6.15(e). Curves estimated for Gannavlakte using adaptive L_p norm reduction (Sposito et al., 1983).

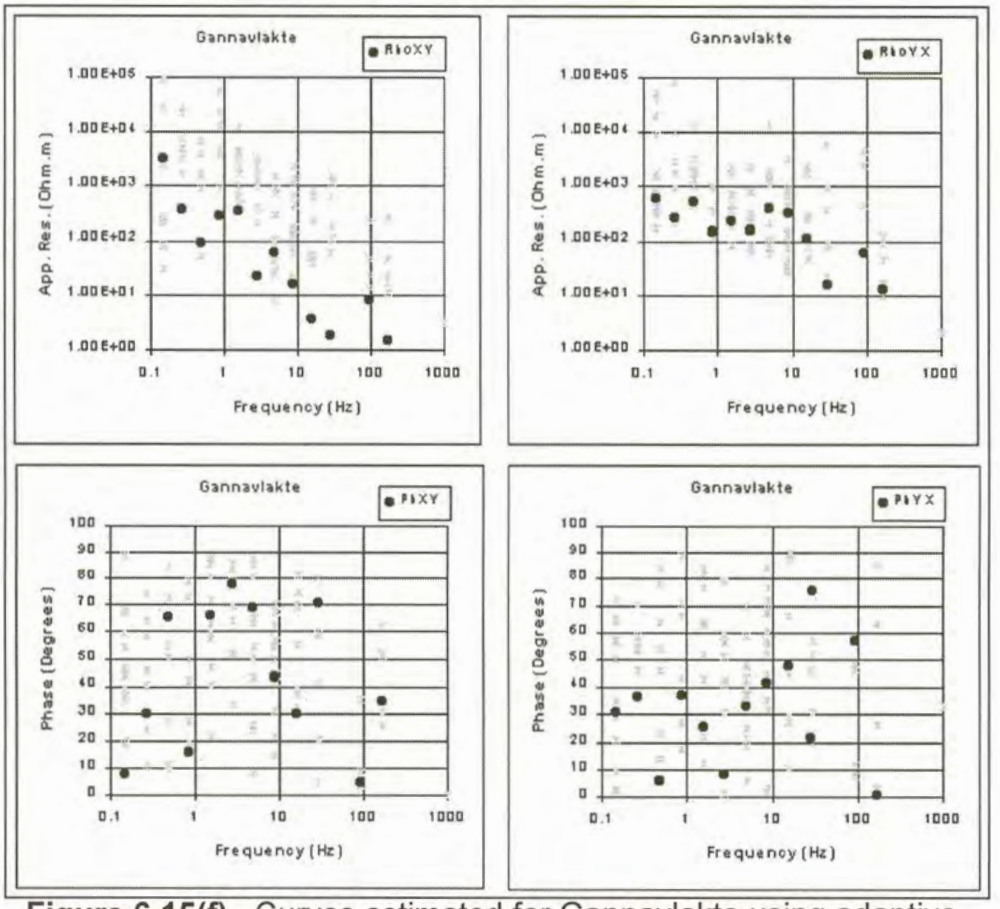

Figure 6.15(f). Curves estimated for Gannavlakte using adaptive L_p norm reduction (Money et al., 1982).

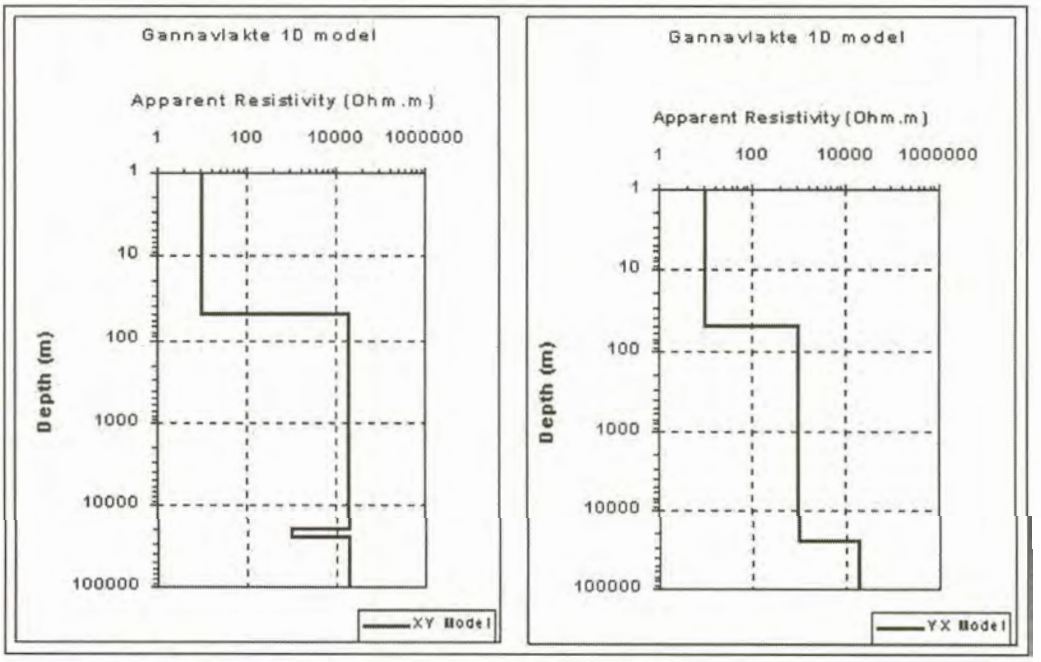

Figure 6.16. One dimensional models for Gannavlakte.

6.3.8. Albany

Figure 6.17(a) shows the data obtained at his station. Data were collected at a large range of frequencies, from 0.01 Hz to 1000 Hz. Although the quality of the apparent resistivity data are very good, the impedance phases are extremely scattered.

Results of statistical reduction

For data in the xy-direction the robust M-estimation technique yields the best results. In general curves fitted for this direction are of lower quality than for the yx-direction. The adaptive L_p norm using Sposito's equation gives the best curve for the ρ_{yx} data (Figure 6.17(e)). The L1 norm gives the worst results, especially at low frequencies (Figure 6.17(b)).

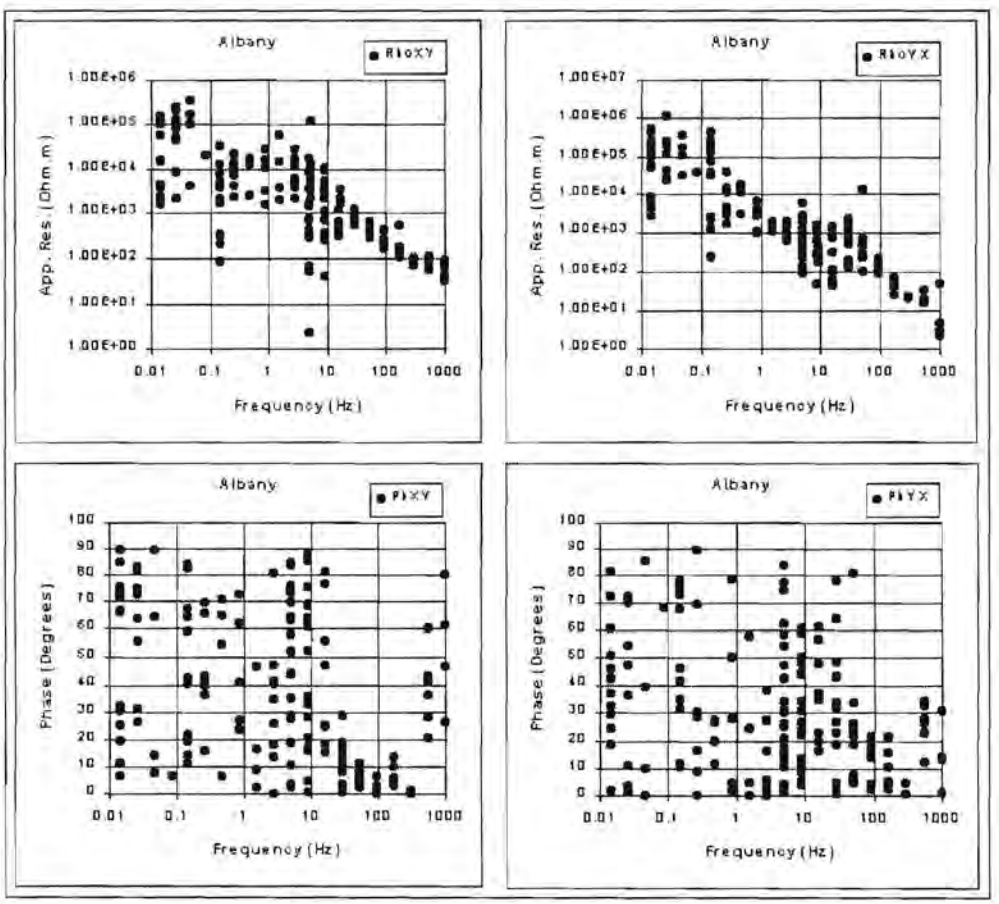

Figure 6.17(a). Apparent resistivity and impedance phase versus frequency curves for Albany.

Interpretation

In the xy-direction the apparent resistivity increases with decreasing frequency. At approximately 2 Hz the curve turns and the resistivities start to decrease, but below 0.1 Hz it increases again. The curve for the yx-direction starts out similar to the ρ_{xy} curve, but between 30 Hz and 1 Hz it flattens out. Below 1 Hz it increases again with decreasing frequency. Figure 6.18 shows the one-dimensional models calculated for these curves.

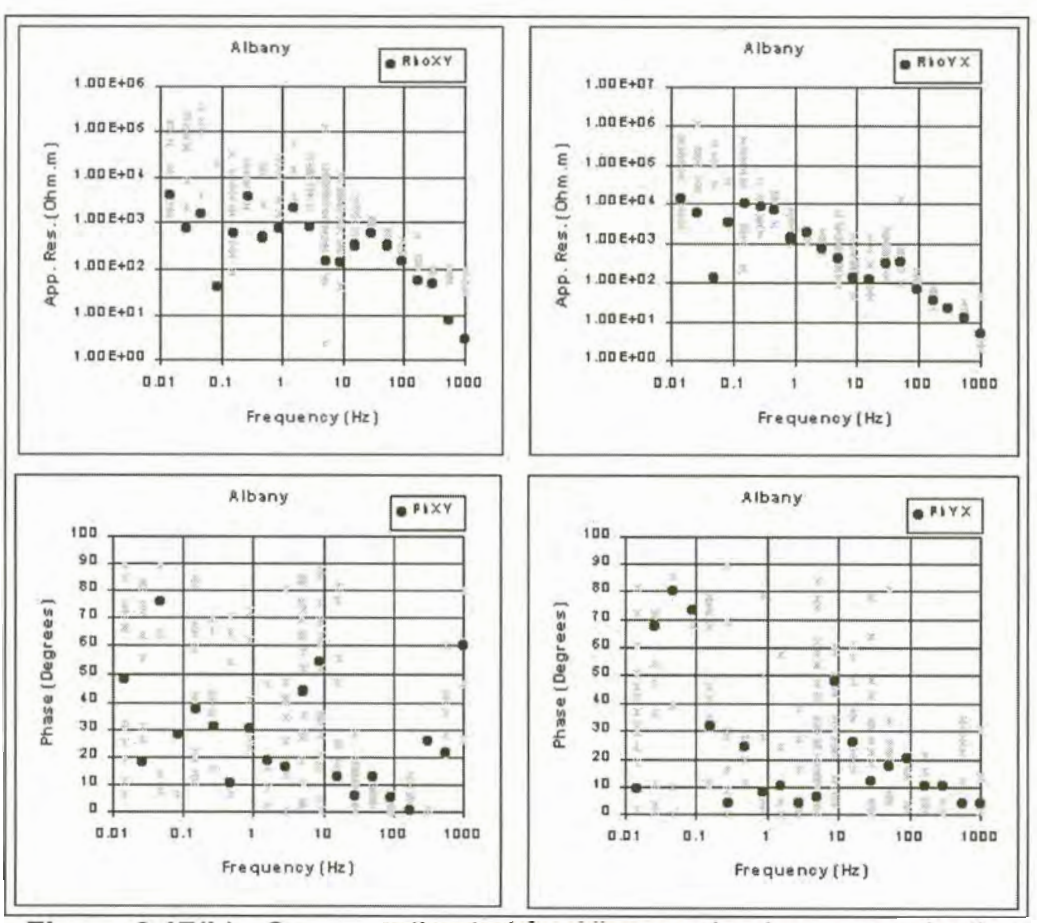

Figure 6.17(b). Curves estimated for Albany using L_1 norm reduction.

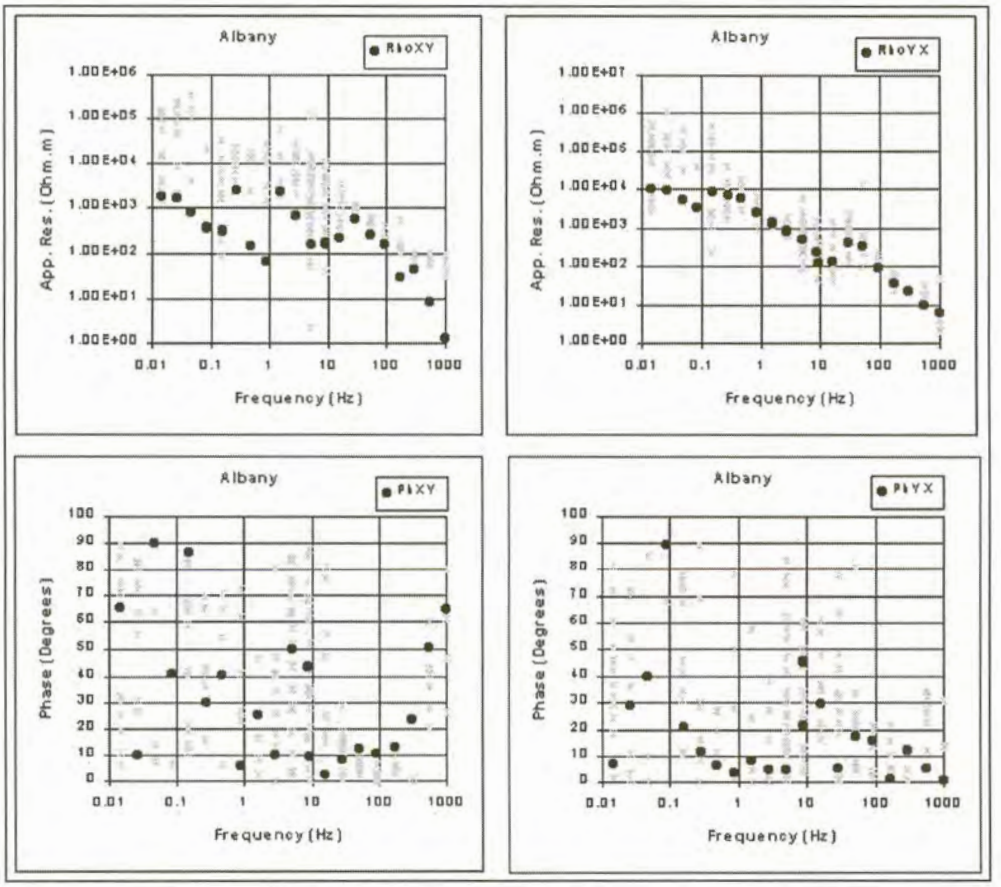

Figure 6.17(c). Curves estimated for Albany using least squares reduction.

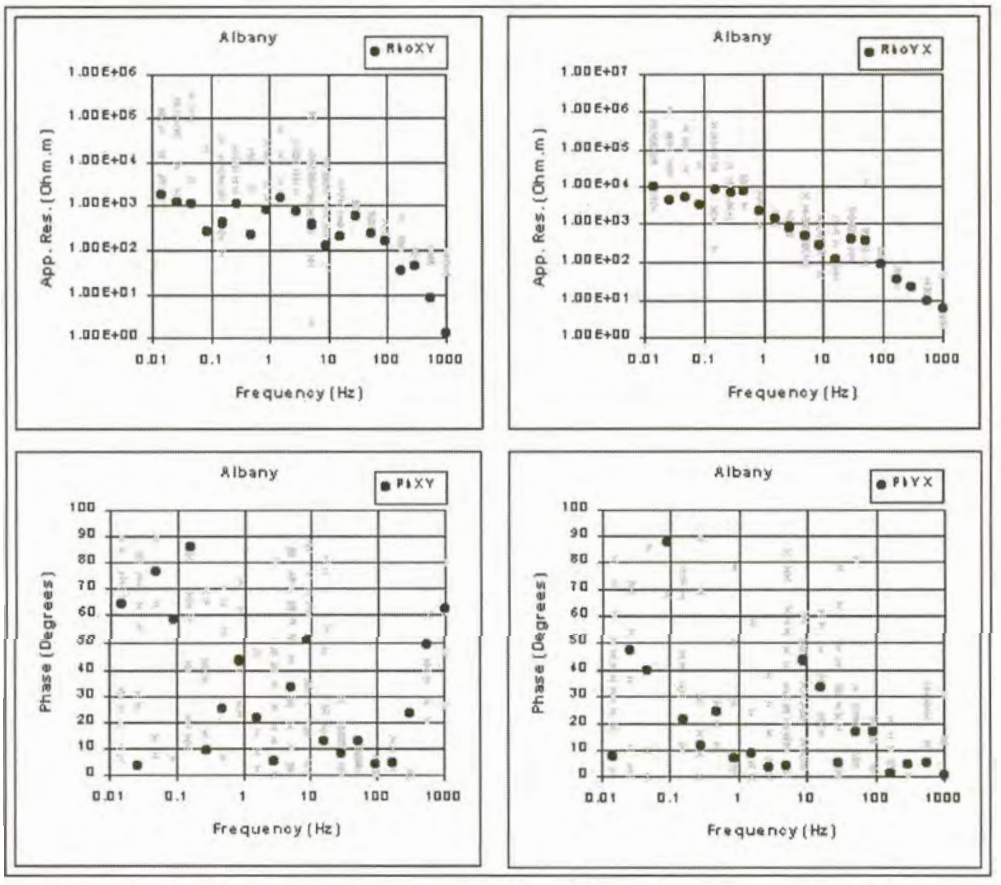

Figure 6.17(d). Curves estimated for Albany using robust M-estimation.

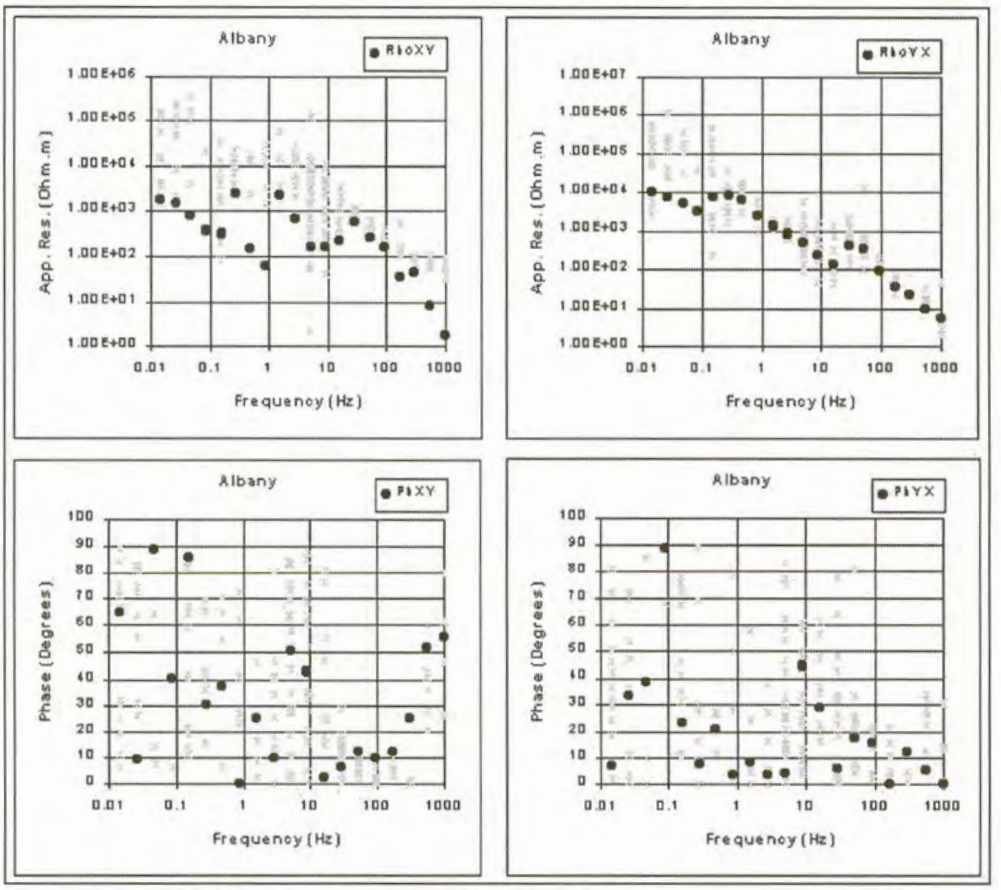

Figure 6.17(e). Curves estimated for Albany using adaptive L_p norm reduction (Sposito et al., 1983).

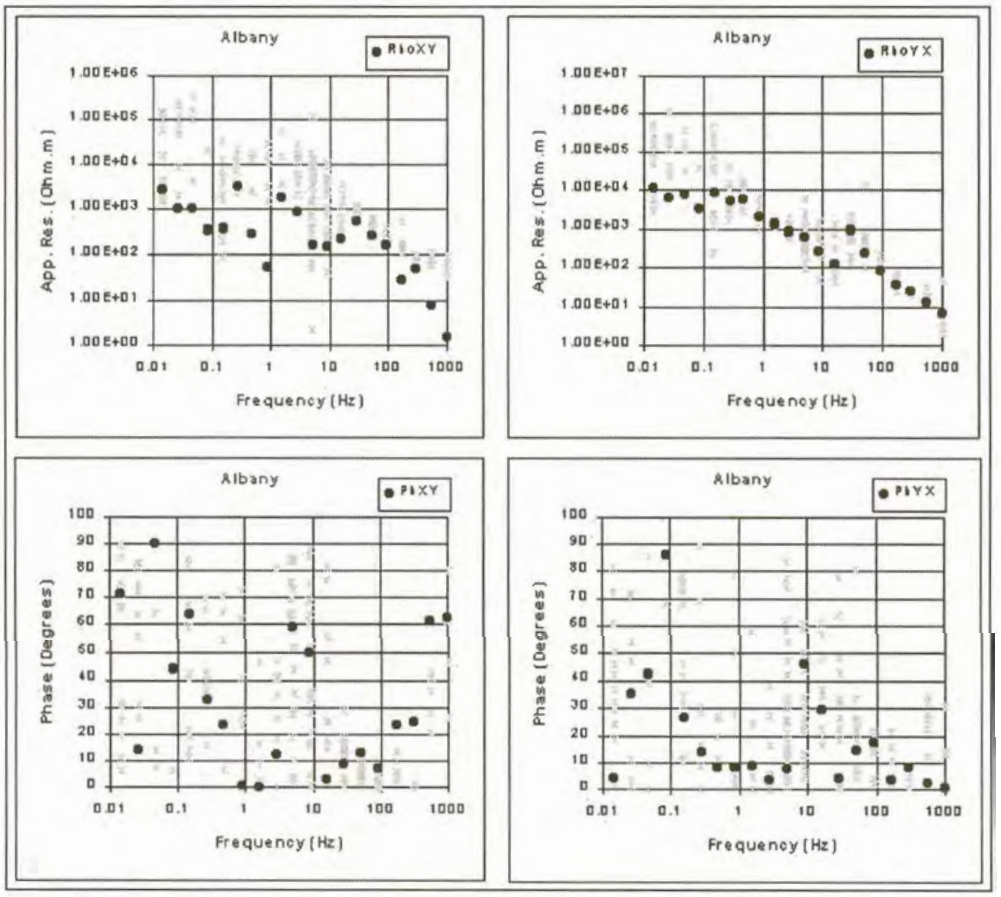

Figure 6.17(f). Curves estimated for Albany using adaptive L_p norm reduction (Money et al., 1982).

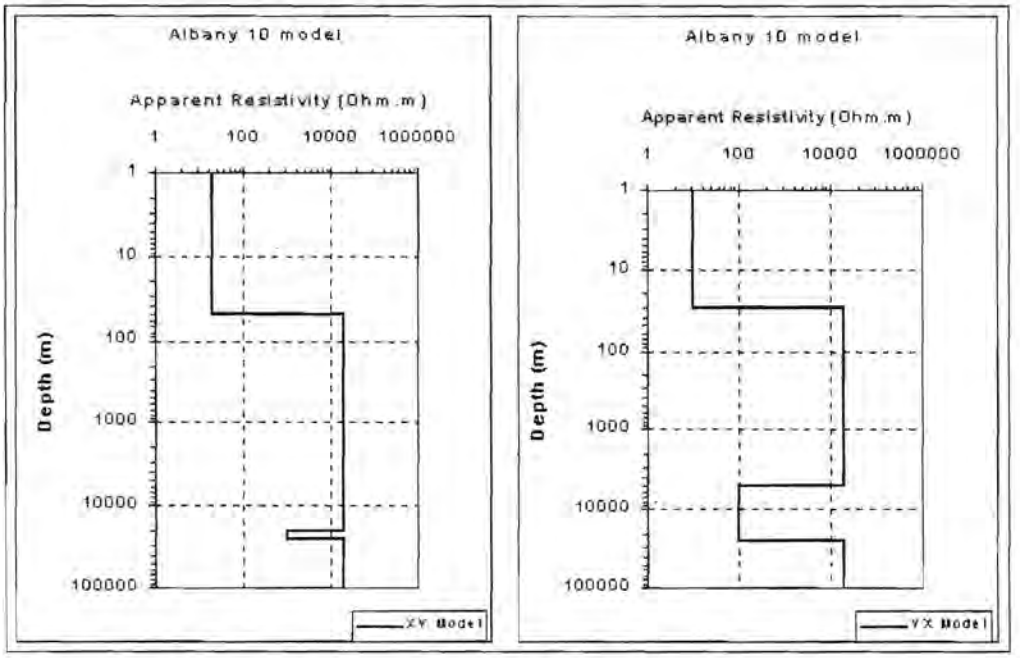

Figure 6.18. One dimensional models for Albany.

6.3.9. Uizip

Only a small amount of data were gathered at this station. Data were obtained between 0.01 Hz and 100 Hz (Figure 6.19). Impedance phase data in the xy-direction are of moderate quality.

Results of statistical reduction

The robust M-estimation technique yields the best results for both the xy- and yx-direction data (Figure 6.19(d)). The adaptive L_p norm methods failed to converge at most of the frequencies (Figures 6.19 (e) and (f)).

Interpretation

Data in the two directions are very similar at lower frequencies. Resistivities decrease with increasing frequency. The ρ_{xy} curve starts to turn just below 10 Hz while the ρ_{yx} curve turns at 1 Hz. The difference in the one-dimensional models (Figure 6.20) shows that the underlying geology is anisotropic.

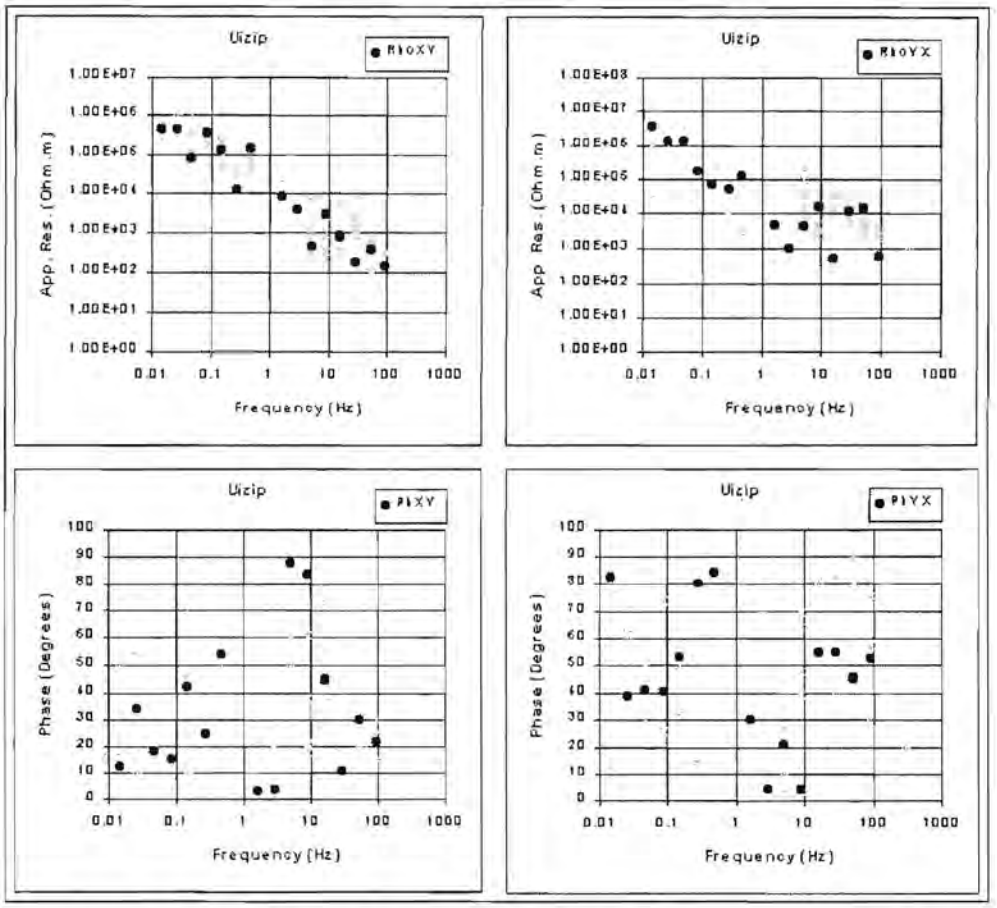

Figure 6.19(c). Curves estimated for Uizip using least squares reduction.

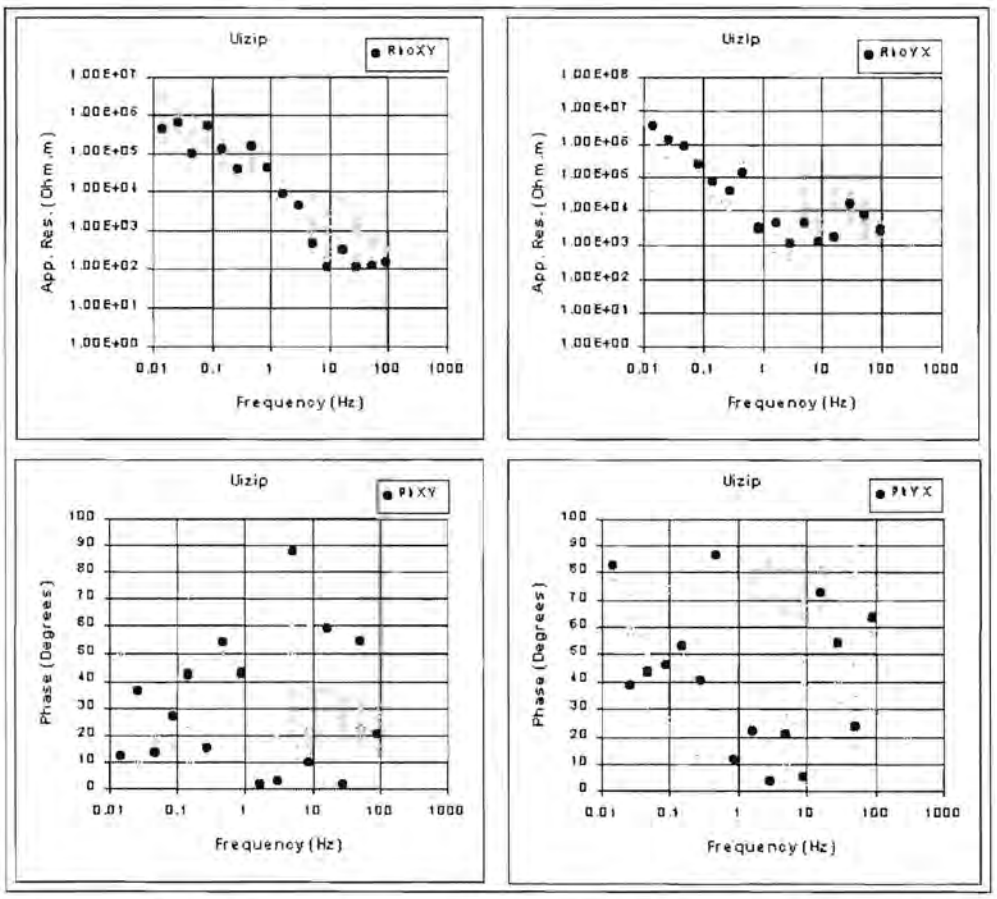

Figure 6.19(d). Curves estimated for Uizip using robust M-estimation.

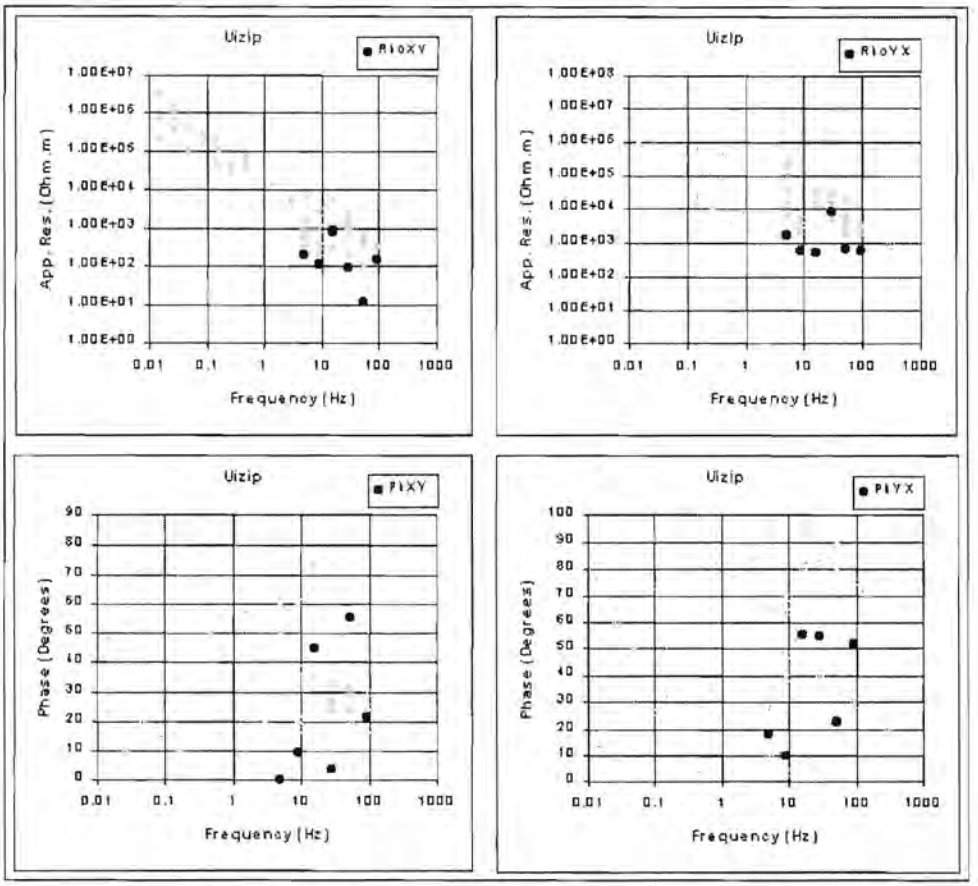

Figure 6.19(e). Curves estimated for Uizip using adaptive L_p norm reduction (Sposito et al., 1983).

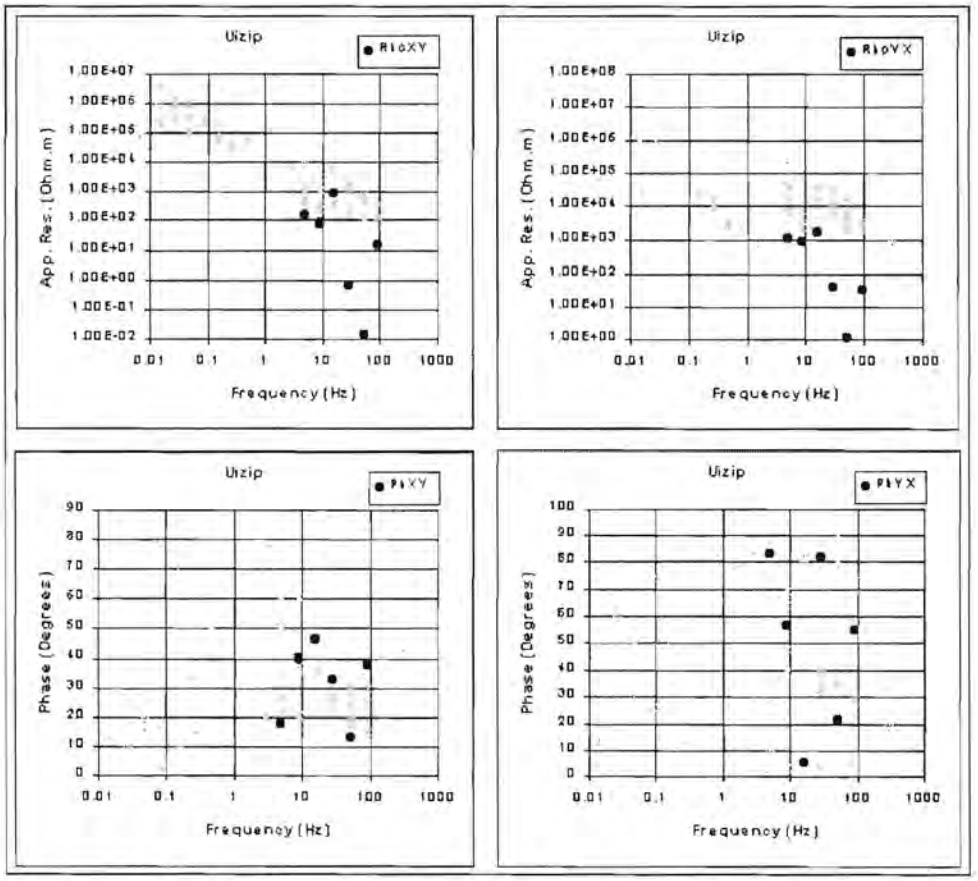

Figure 6.19(f). Curves estimated for Uizip using adaptive L_p norm reduction (Money et al., 1982).

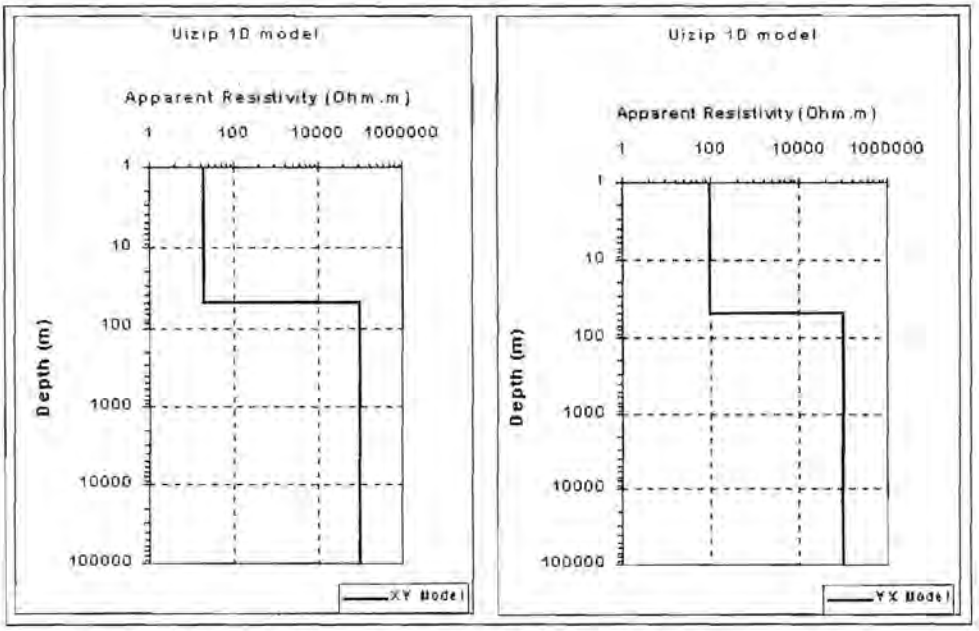

Figure 6.20. One dimensional models for Uizip.

6.3.10. Upington

Most of the data collected at this station fall in the higher frequency range. Below 5 Hz the amount of data drastically decreases (Figure 6.21(a)). Data in the yx-direction are more scattered than in the xy-direction.

Results of statistical reduction

The L1-, L2 norms and robust M-estimation methods give good results in the xy-direction. At lower frequencies the adaptive L_p norm techniques failed to converge, probably as a result of the lack of data at these frequencies. The quality of the curves fitted through the ρ_{yx} data is not very good. The robust M-estimation technique resulted in the best curve.

Interpretation

For both directions, the data result in high resistivity values at high frequencies. The resistivity curves increase a little before starting to turn at 5 Hz. In the xy-direction the curve stays flat until roughly 0.3 Hz where

the resistivities start to increase again. For the yx-direction the values already start to increase at 1Hz.

One dimensional models for this station are shown in Figure 6.22.

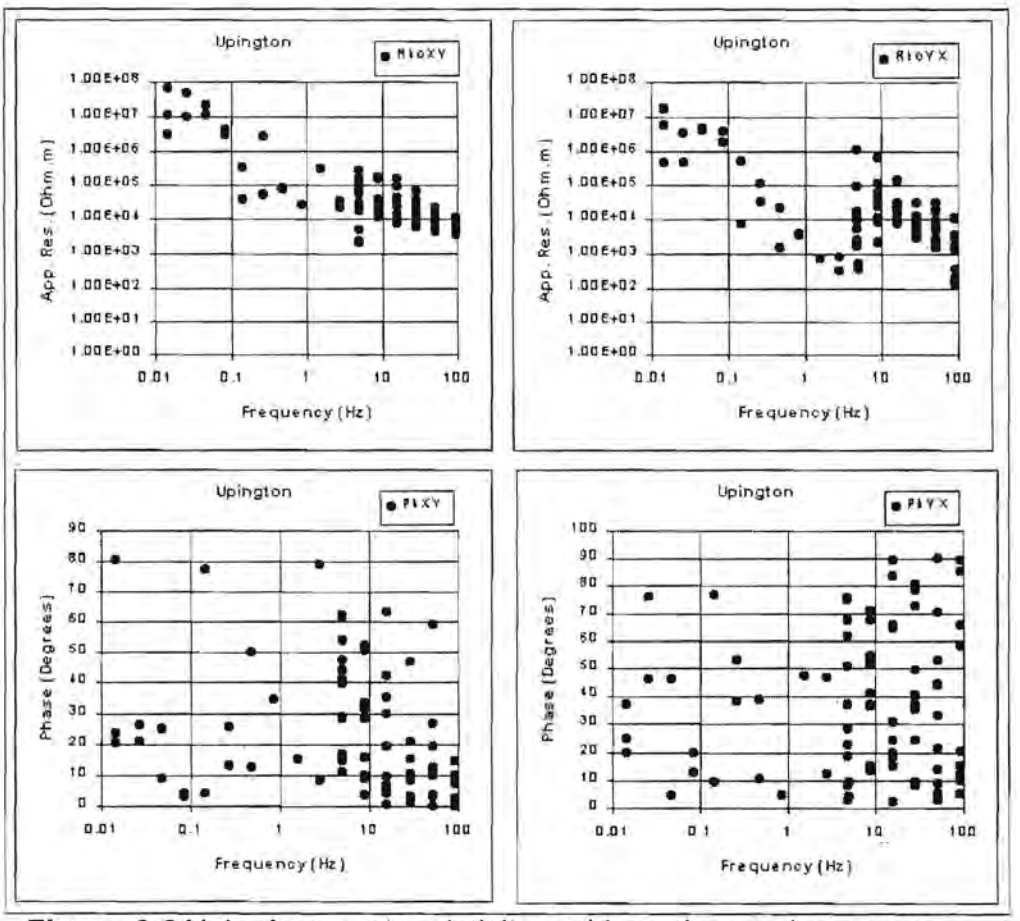

Figure 6.21(a). Apparent resistivity and impedance phase versus frequency curves for the Upington station.

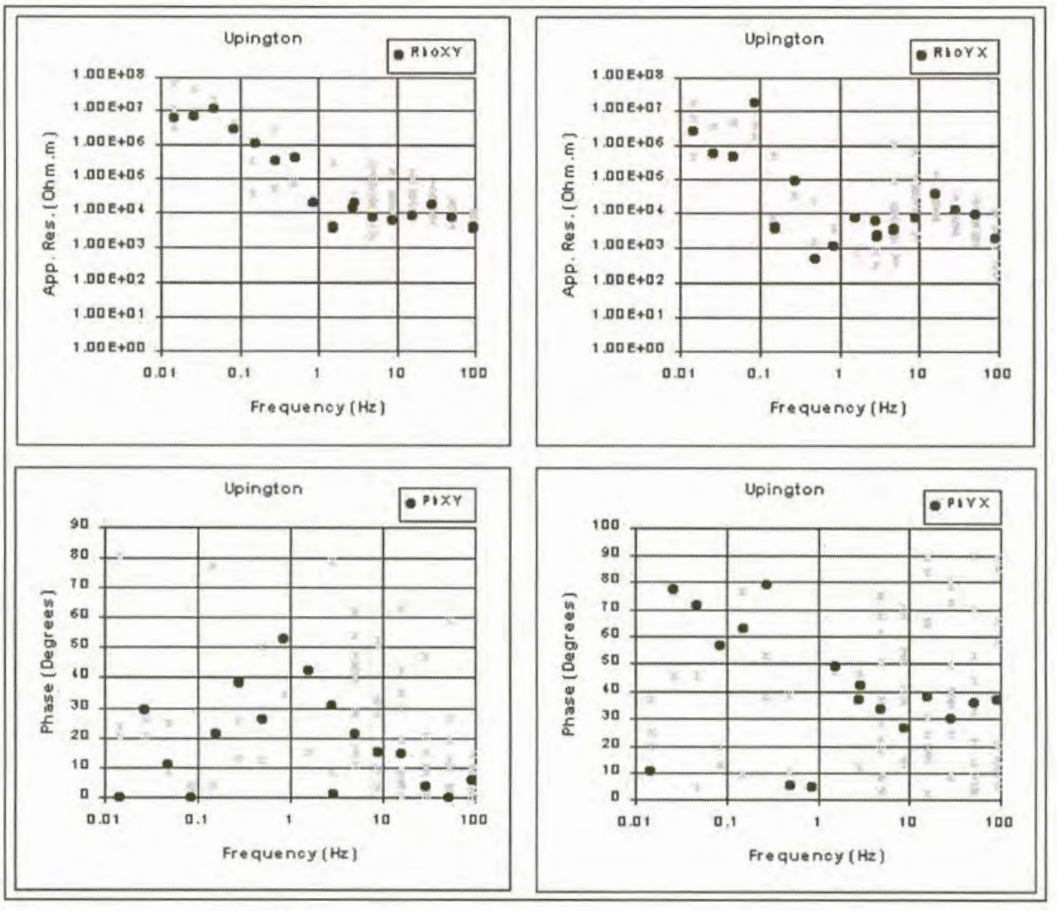

Figure 6.21(b). Curves estimated for Upington using L_1 norm reduction.

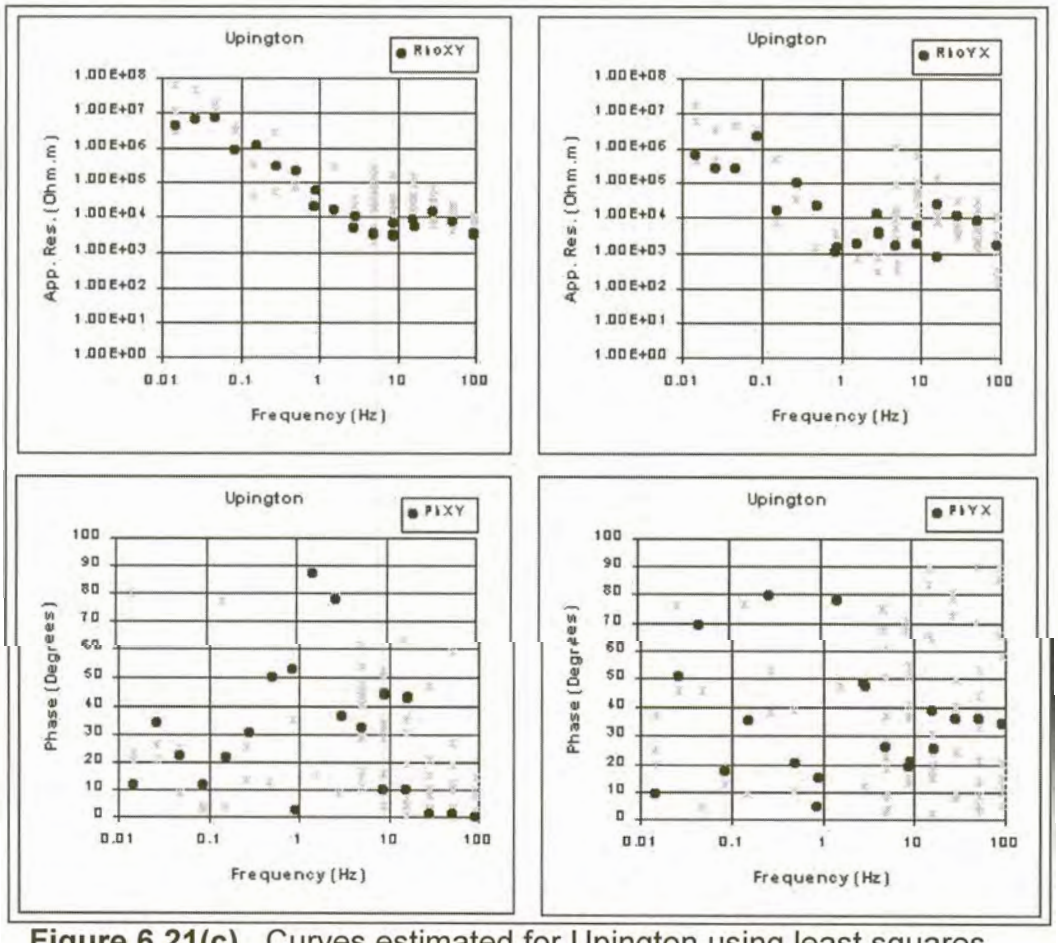

Figure 6.21(c). Curves estimated for Upington using least squares reduction.

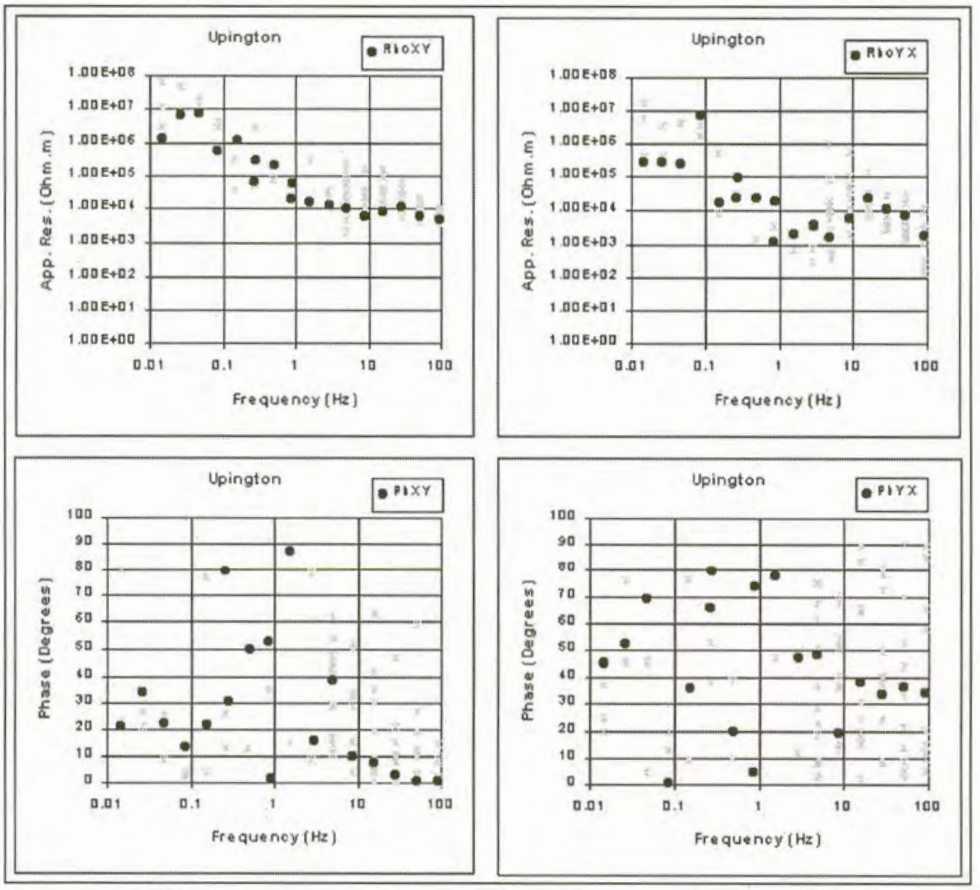

Figure 6.21(d). Curves estimated for Upington using robust M-estimation.

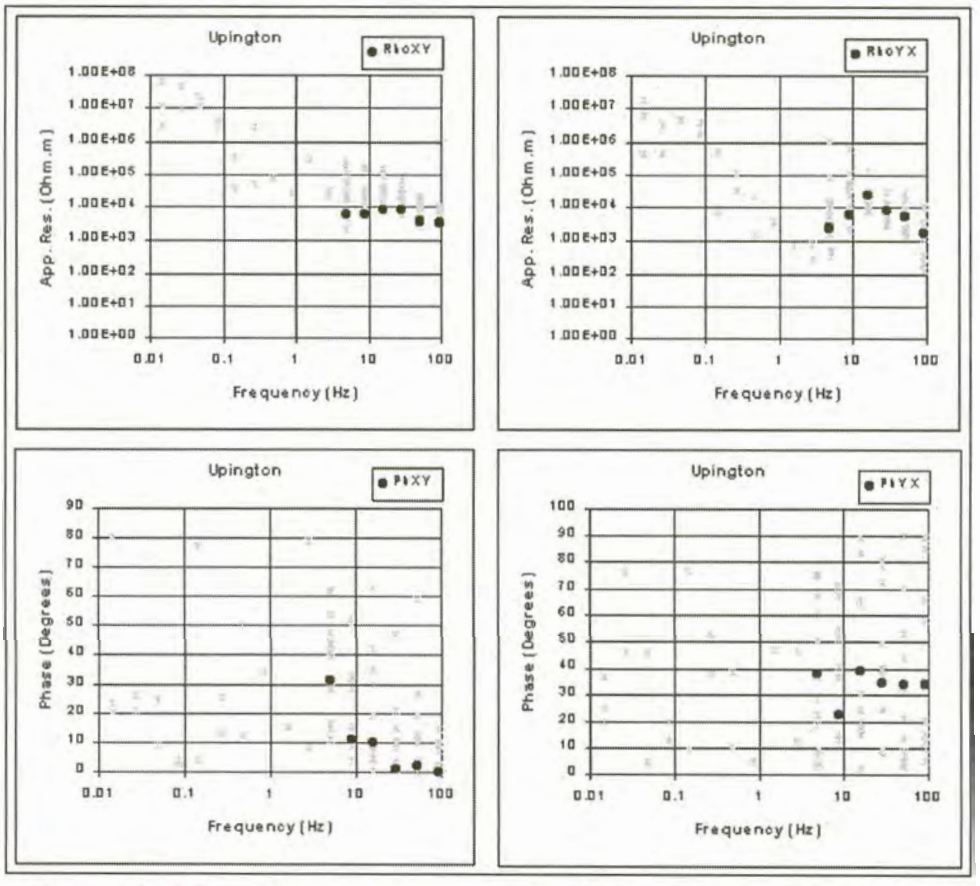

Figure 6.21(e). Curves estimated for Upington using adaptive L_p norm reduction (Sposito et al., 1983).

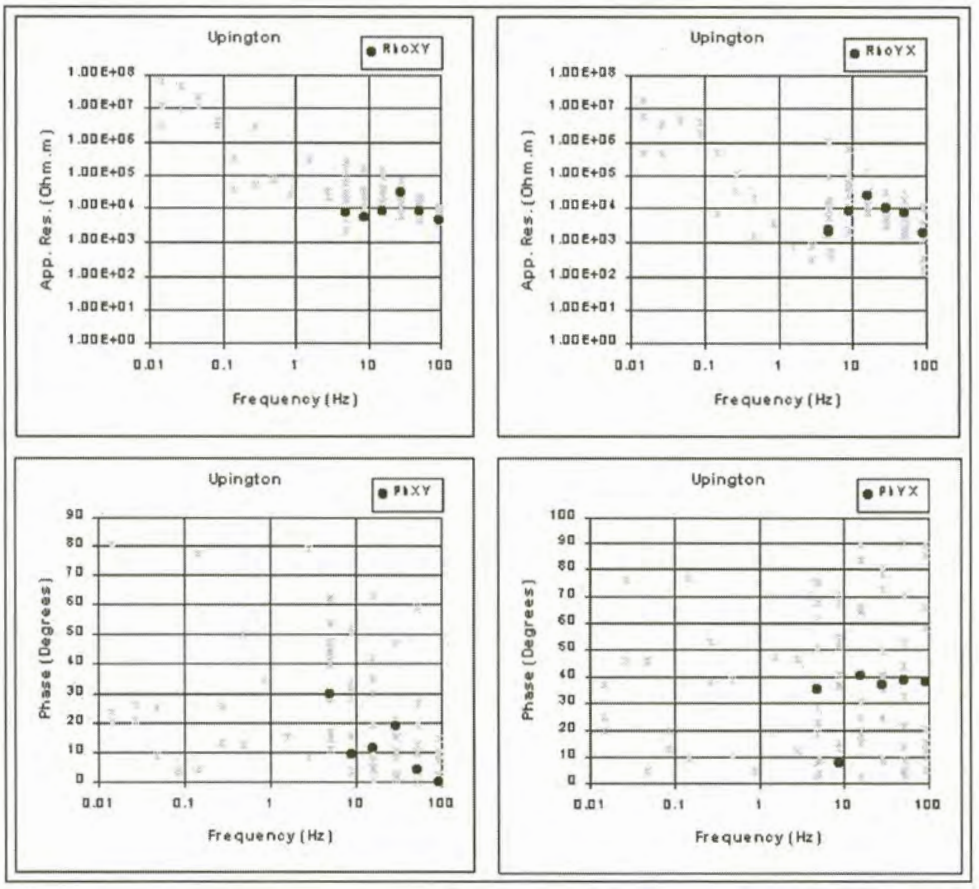

Figure 6.21(f). Curves estimated for Upington using adaptive L_p norm reduction (Money et al., 1982).

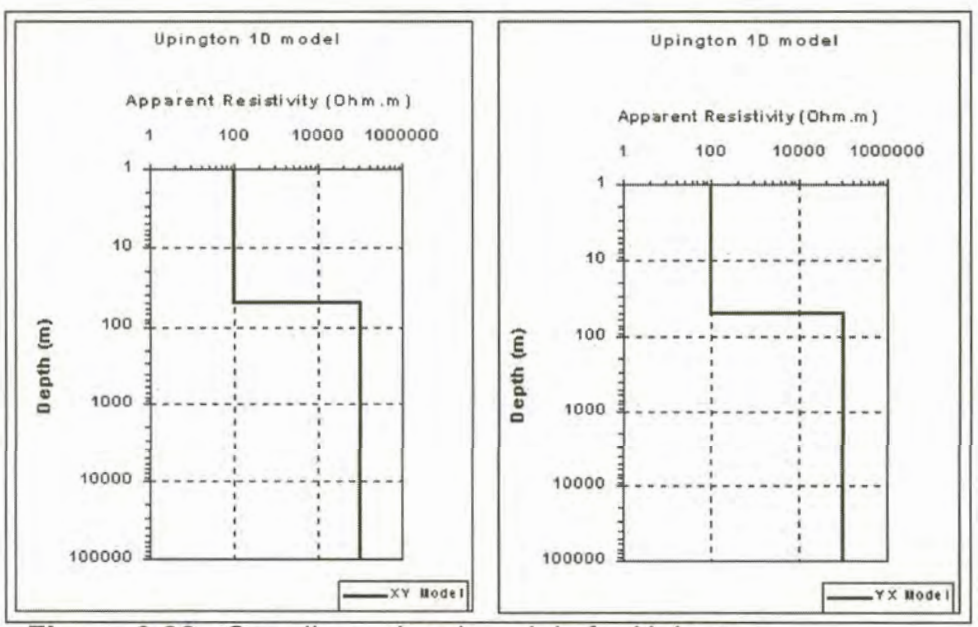

Figure 6.22. One dimensional models for Upington.

6.3.11. Dyason's Klip

An electrode spacing of 150m was used at this station. The distance between the local and remote stations was 450m. Data in the yx-direction are more scattered than data in the xy-direction (Figure 6.23(a)). The quality of the phase data in both directions are extremely poor.

Results of statistical reduction

The curves fitted through the ρ_{xy} data differ quite substantially depending on the reduction technique used. None of the methods yielded curves that fitted the data between 0.3 Hz and 5 Hz. The least squares (Figure 6.23(c)) and robust M-estimation (Figure 6.23(d)) methods produce curves that indicate the presence of a conductor between 1 and 10 Hz while the adaptive L_p norm (Sposito et al., 1983) (Figure 6.23(e)) yielded a curve that is close to being a straight line.

The curves calculated in the yx-direction approximates the data more closely. The adaptive L_p norm techniques (Figures 6.23(e) and (f)) yield very bad results at frequencies above 1 Hz due to a lack of data. It seems as though least squares minimisation (Figure 6.23(c)) produce the best result.

Interpretation

Apparent resistivities start in the vicinity of 1000 Ohm.m at high frequencies and increase with depth. Between 0.1Hz and 2 Hz the ρ_{xy} curve seems to flatten out somewhat before increasing again at lower frequencies. In the yx-direction the resistivity stay nearly constant at high frequencies and starts to increase from 1 Hz and lower. From the data and one-dimensional models (Figure 6.24) it can be interpreted that the underlying earth is more isotropic at greater depths, but become more inhomogeneous at shallower depths.

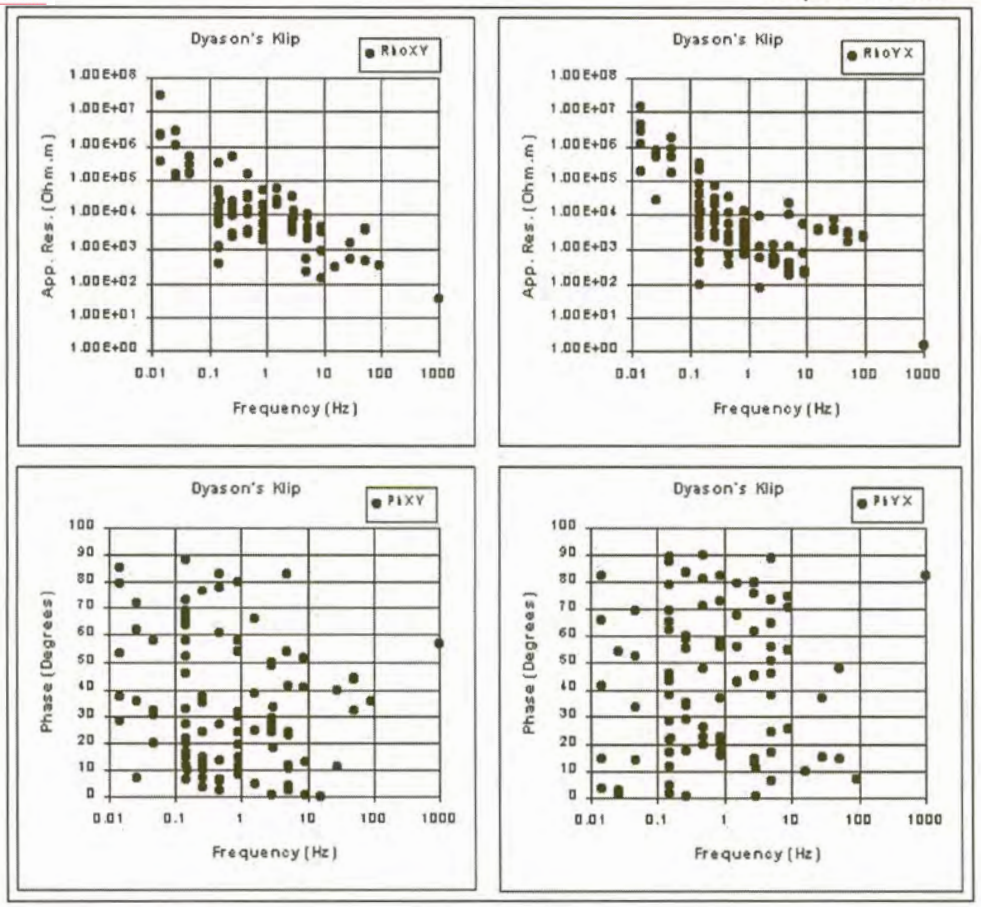

Figure 6.23(a). Apparent resistivity and impedance phase versus frequency curves for Dyason's Klip.

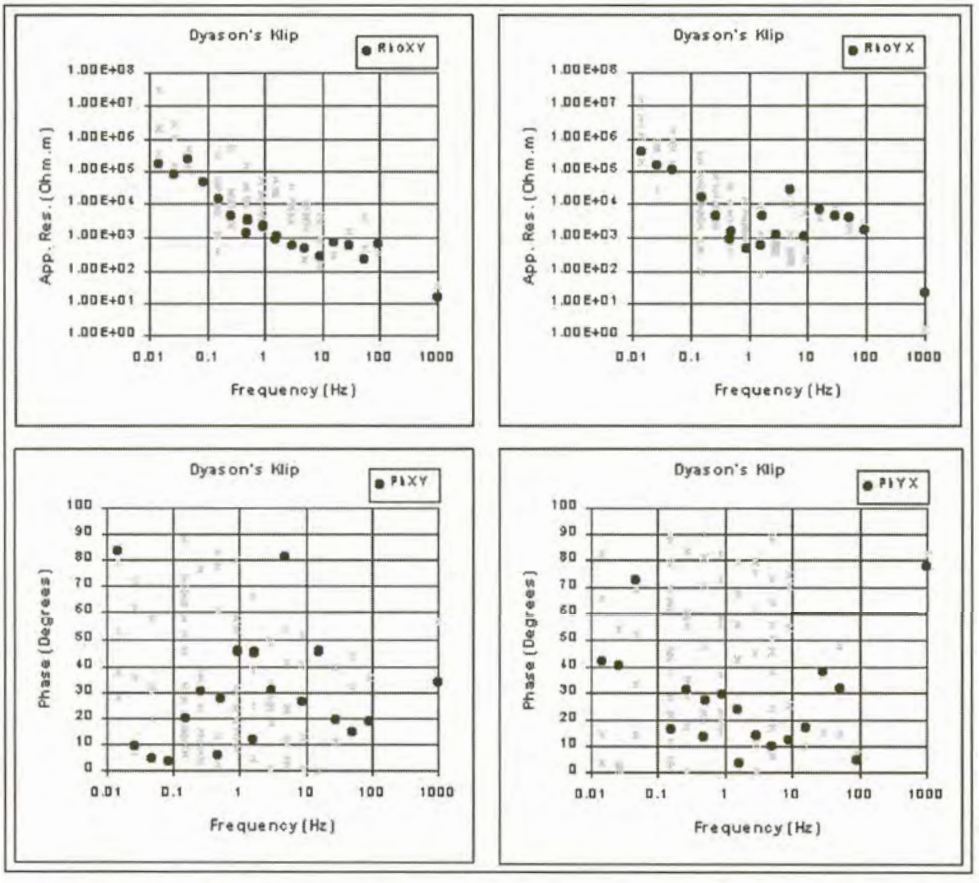

Figure 6.23(b). Curves estimated for Dyason's Klip using L_1 norm reduction.

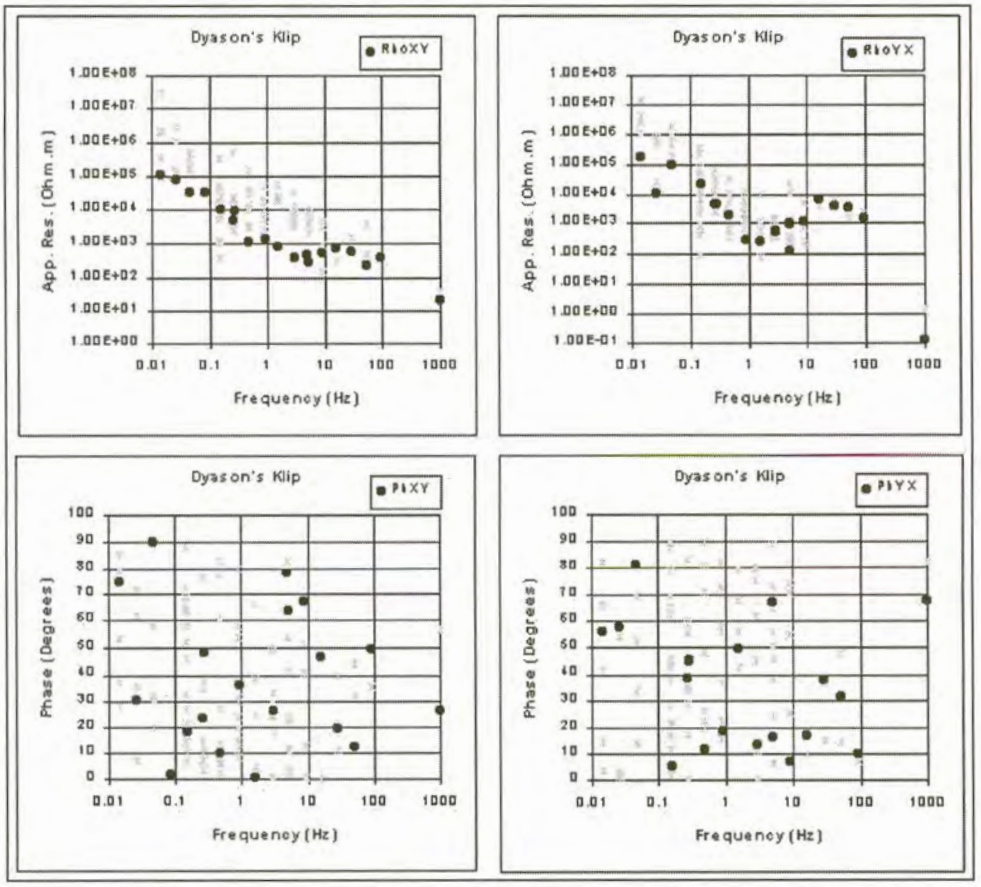

Figure 6.23(c). Curves estimated for Dyason's Klip using least squares reduction.

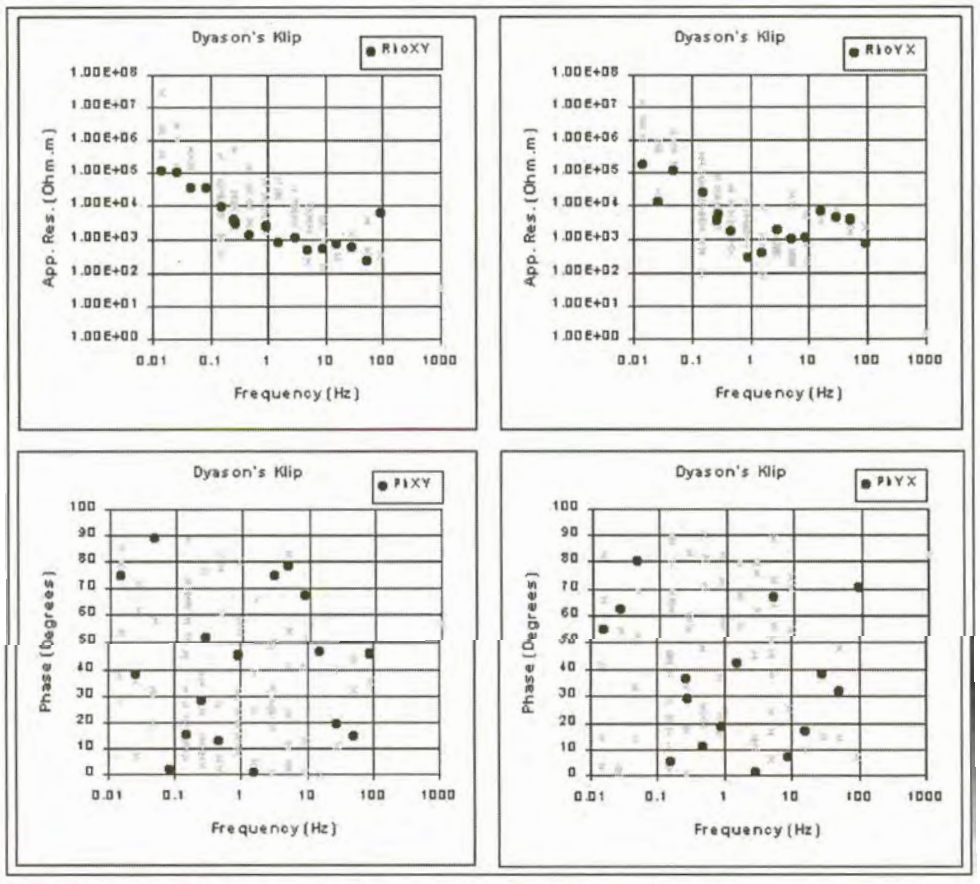

Figure 6.23(d). Curves estimated for Dyason's Klip using robust M-estimation.

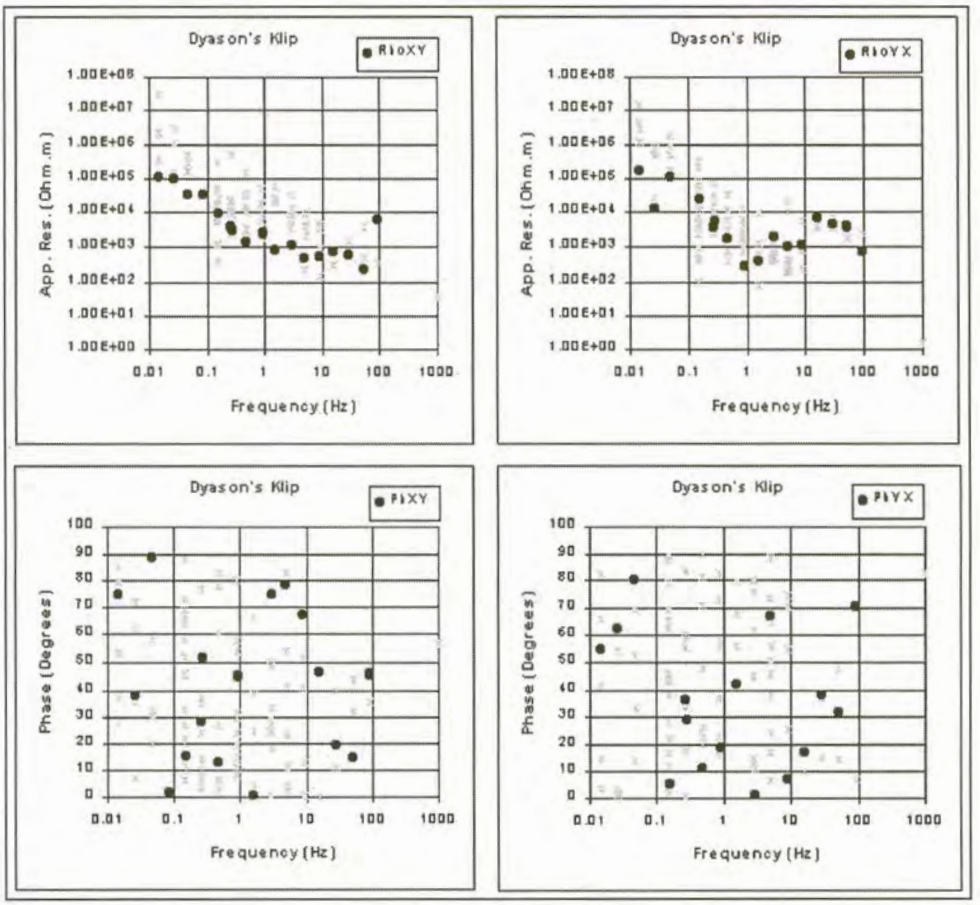

Figure 6.23(e). Curves estimated for Dyason's Klip using adaptive L_p norm reduction (Sposito et al., 1983).

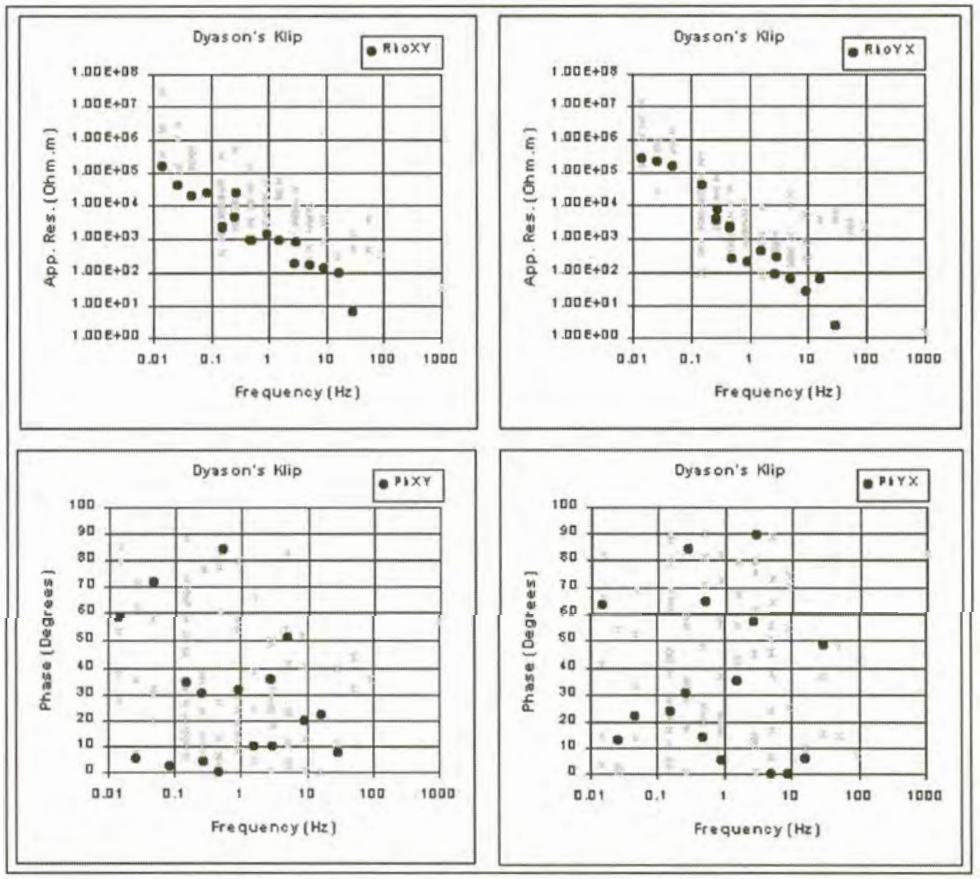

Figure 6.23(f) Curves estimated for Dyason's Klip using adaptive L_p norm reduction (Money et al., 1982).

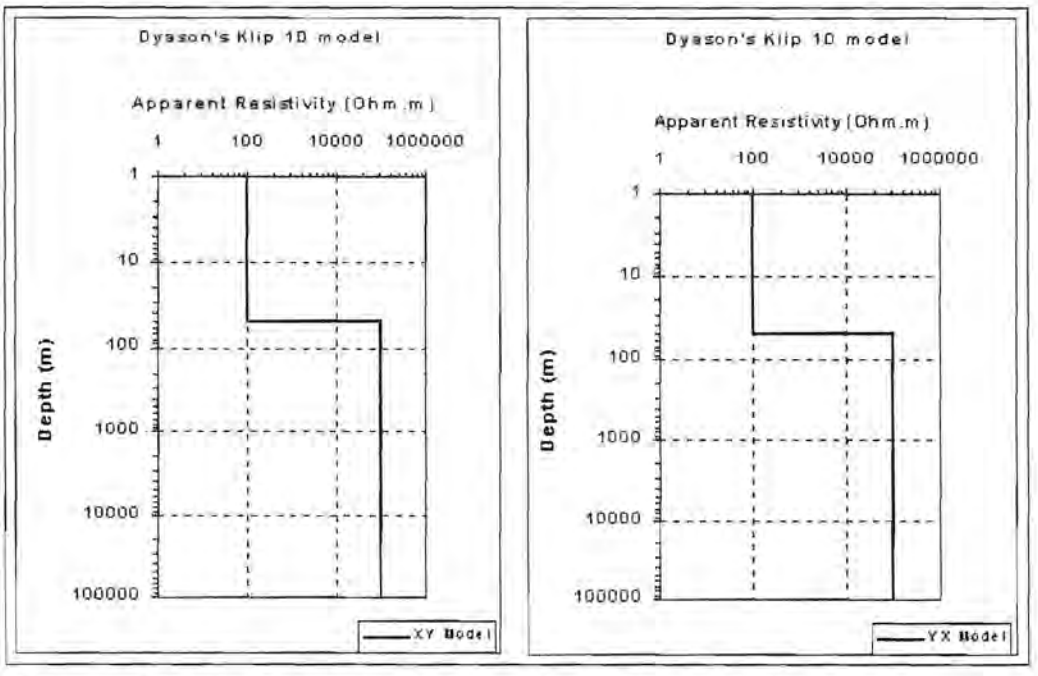

Figure 6.24 One dimensional models for Dyason's Klip.

6.4. TWO DIMENSIONAL MAGNETOTELLURIC MODEL

Figure 6.25 shows the two dimensional magnetotelluric model constructed along the Sishen-Keimoes line. The highly resistive material (20 000 Ωm) represents the basement material. A conductive zone (100 Ωm) separates the basement rocks from less resistive (6700 Ωm) material. It may be caused by conductive seafloor material wedged between resistive cratonic material in the east and a more fractured terrain in the west.

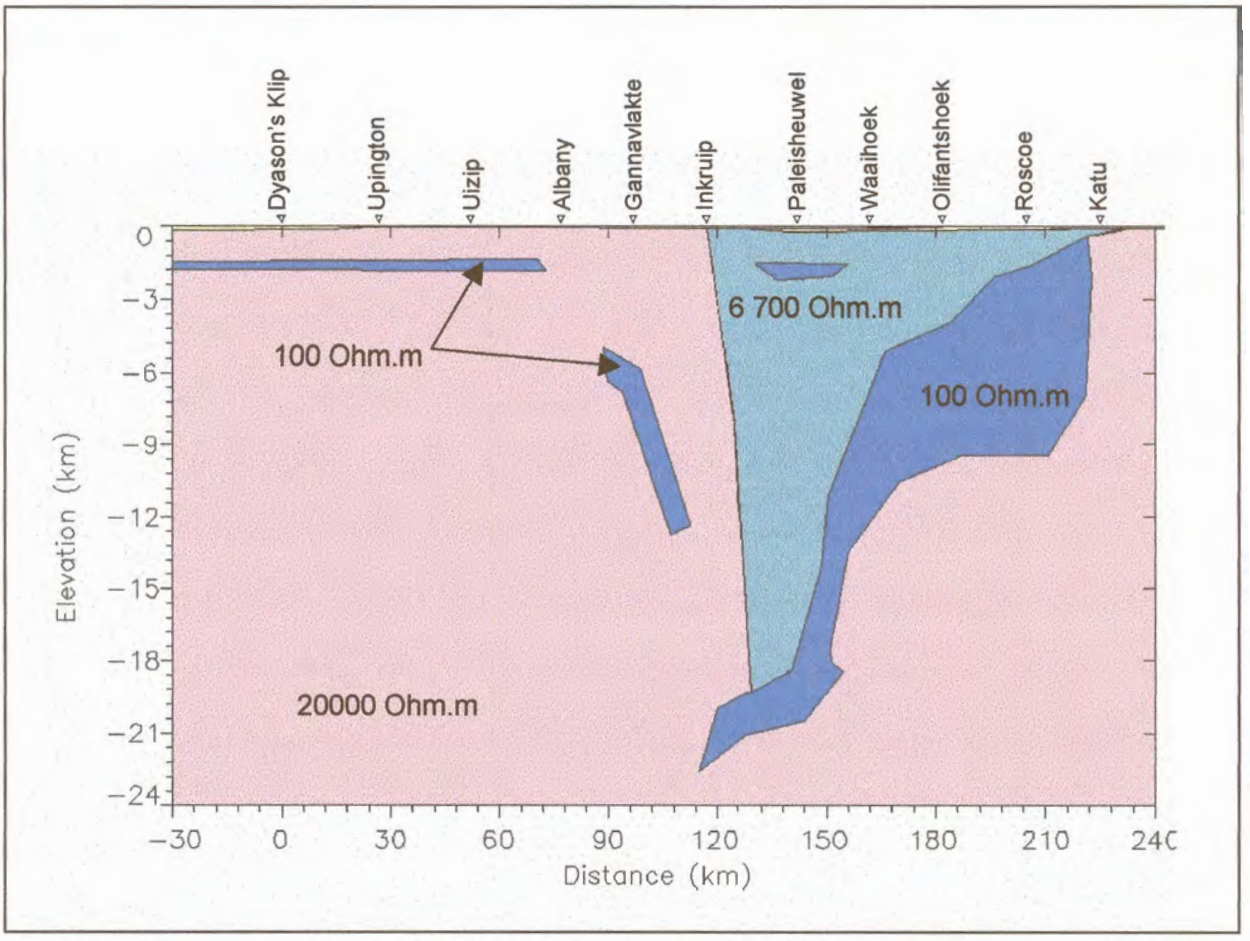

Figure 6.25. Two dimensional model constructed from the magnetotelluric data.

6.5. GRAVITY DATA

Gravity data covering the region of interest (Figure 6.26) were extracted from the regional gravity data set that covers the whole of South Africa. The data were collected at roughly one station every 10 – 12 km^2. Additional measurements were made every 0.5 km along the seismic route. Gravity measurements were conducted with La Coste and Romberg gravimeters and elevations were determined by micro-barometers. Bouguer anomaly values were calculated assuming a mean density of 2670 kg/m^3. The measurements were tied to the International Gravity Standardisation Net values (Morelli et al., 1974) and were referred to the gravity formula based on the 1967 geodetic reference system (Moritz, 1968). A maximum error in a regional Bouguer

anomaly value is calculated by combining an inaccuracy of ~ 2m (~4 gravity units) in the barometrically determined elevation with a maximum error in the observed gravity of 2 g.u. and a positional error of 150m in a north south direction (1 g.u.). This worst case error amounts to approximately 7 g.u.

The data are not terrain corrected since the area is mostly flat. Isostatic equilibrium exists in this area.

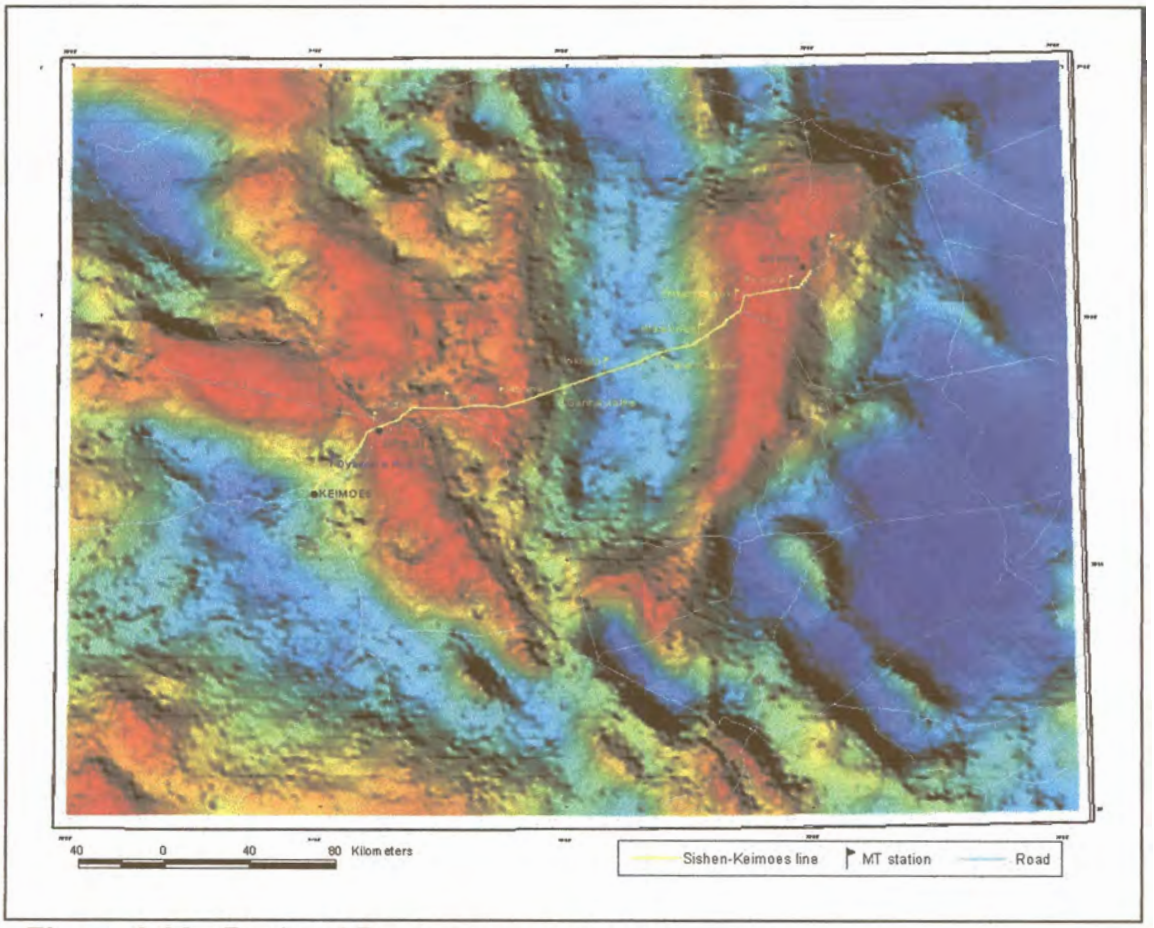

Figure 6.26. Regional Bouguer anomaly map.

Bouguer values were extracted along the road between Sishen and Keimoes and modelled (Figure 6.27). A regional field representing a horizontal line through the minimum of the Bouguer anomaly values was removed. This line would reflect the Bouguer values if only granitic crust of 2670 kg/m^3 was present.

The model shows a thick succesion of dense material in the east. Dense material of the Transvaal and underlying Ventersdorp Supergroups can only

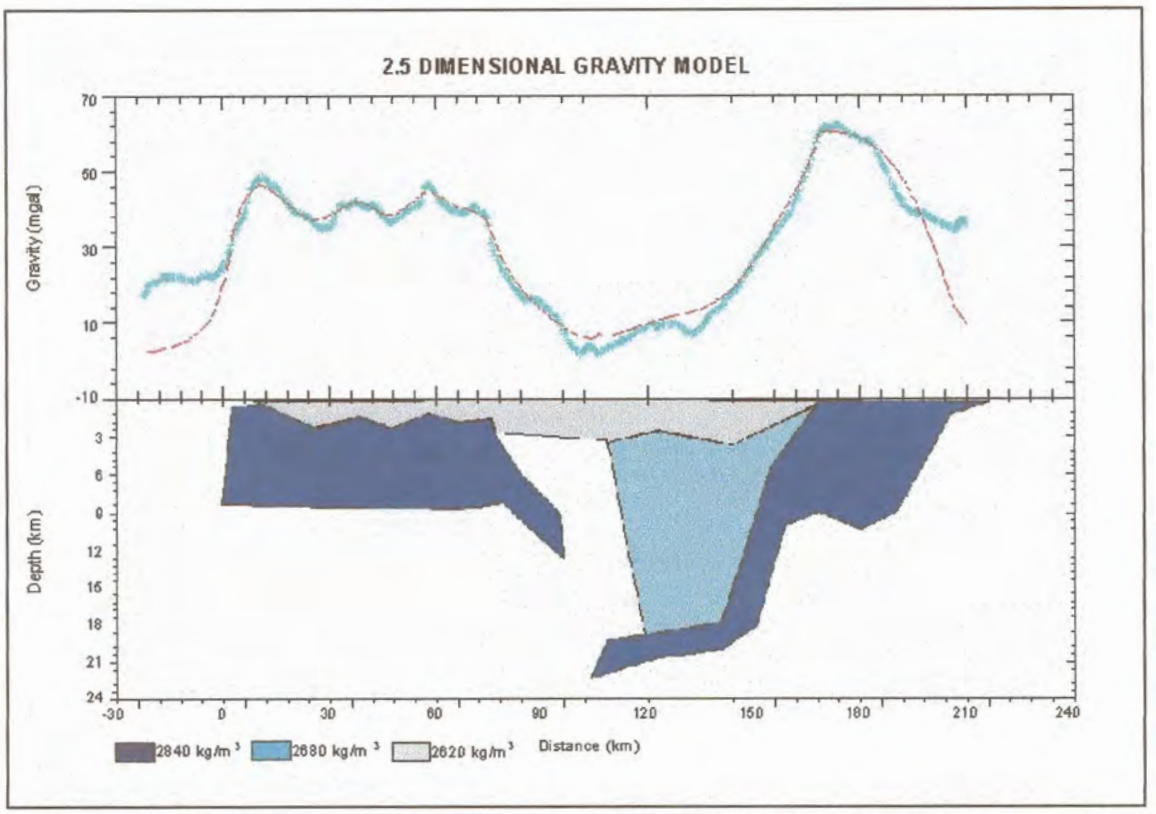

Figure 6.27. Two dimensional model constructed from the gravity data.

account for approximately the top five kilometres of this dense unit. The 2680 kg/m^3 material to the west of the dense body can be attributed to the metamorphosed Kheis basement, or dense units in the granitic Kheis material. A dense body in the west correlates with metamorphosed material belonging to the Namaqua Metamorphic Complex. Olifantshoek Supergroup sediments may constitute the less dense cover.

6.6. MAGNETIC DATA

The aeromagnetic data (Figure 6.28) was collected at a height of 100 ± 15 metres and a 1 km line spacing. The cycling time of the magnetometer was 1 second that, at an aircraft speed of 250 km/h amounts to a total magnetic field measurement about every 63m.

Highly magnetic banded iron formation and jaspillite of the Transvaal Supergroup are partly responsible for the prominent anomaly in the east (Figure

6.29). Similar to the gravity model, the causative body extends to a much greater depth that can be explained by the known geology. The 0.008 cgs units in the centre may be greenstones of the Wilgenhoudtsdrif Group. A highly magnetic body in the west cannot be explained by the mapped geology and is probably related to the Namaqua Metamorphic Complex.

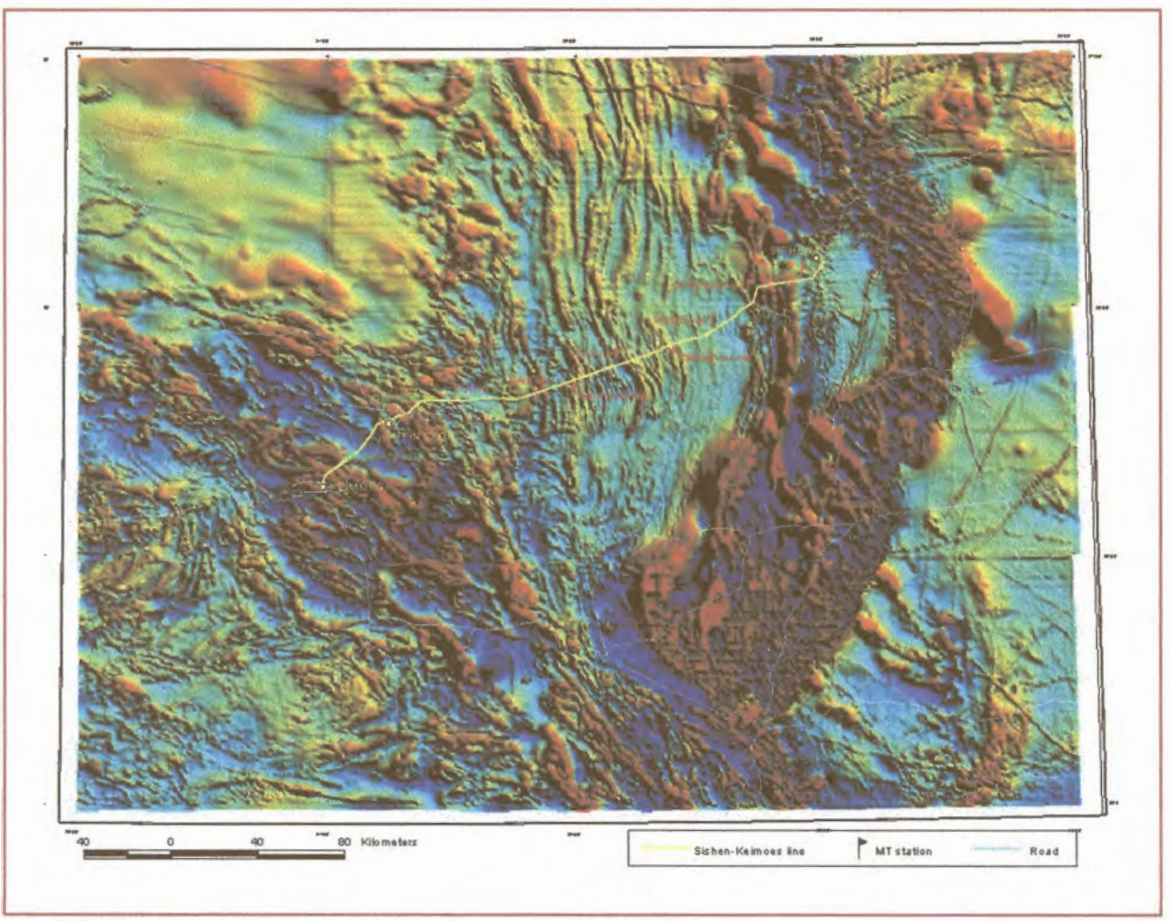

Figure 6.28. Total field aeromagnetic data.

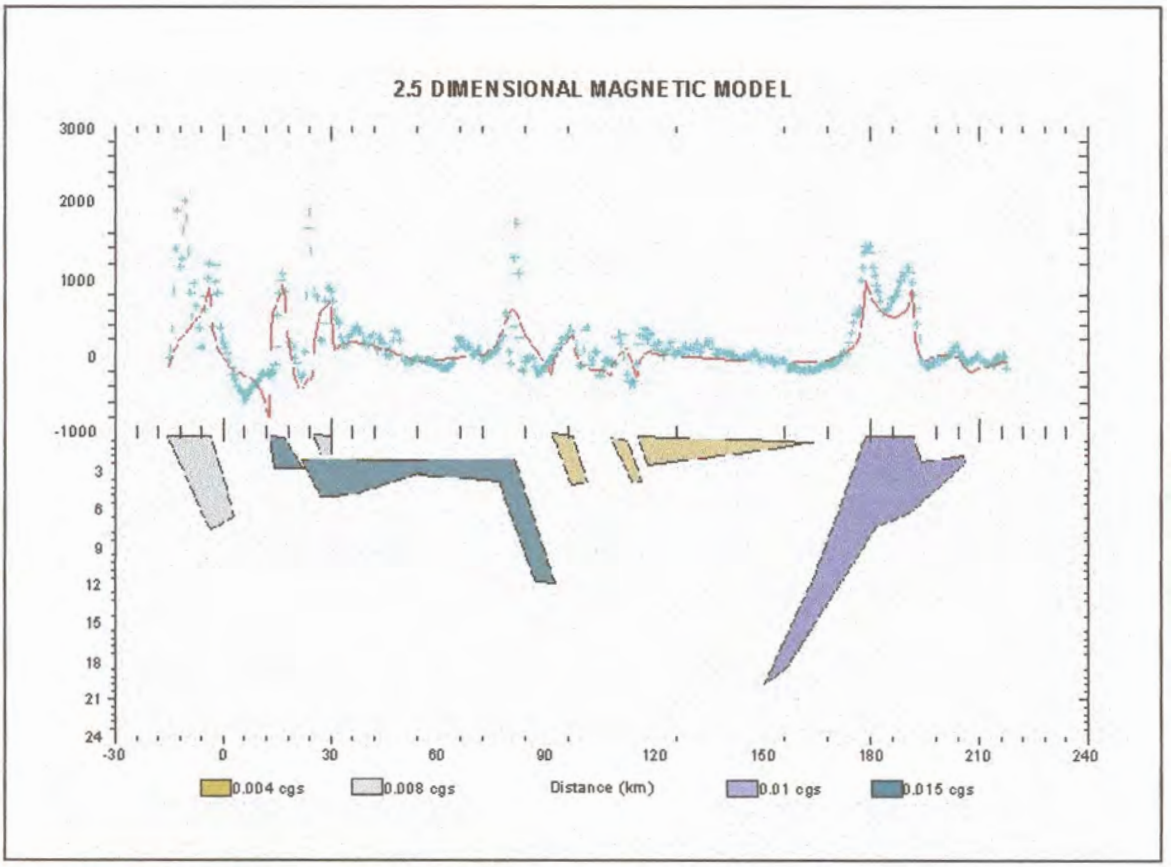

Figure 6.29. Two dimensional model constructed from the magnetic data.

6.7. DEEP REFLECTION SEISMICS

Figure 6.30 shows the migrated deep reflection seismic line recorded between Sishen and Keimoes. The major reflectors are highlighted. The distinct package of dipping reflectors visible on the eastern side of the record can only partially be explained by the Ventersdorp and Transvaal Supergroups. Elongated lens-like reflector packages may indicate thrusting at the edge of the Kaapvaal Craton. Doubling of the crustal layers by thrusting could explain the extensive reflector package. Alternative explanations may be a layered intrusion or an ophiolitic complex introduced by thrusting. Moving westward there is a dramatic decrease in the number of reflectors, and those that do occur dip in the opposite direction. These reflectors may be related to the boundary between the accreted Kheis Province in the east and the Rehoboth and Namaqua Terranes in the west.

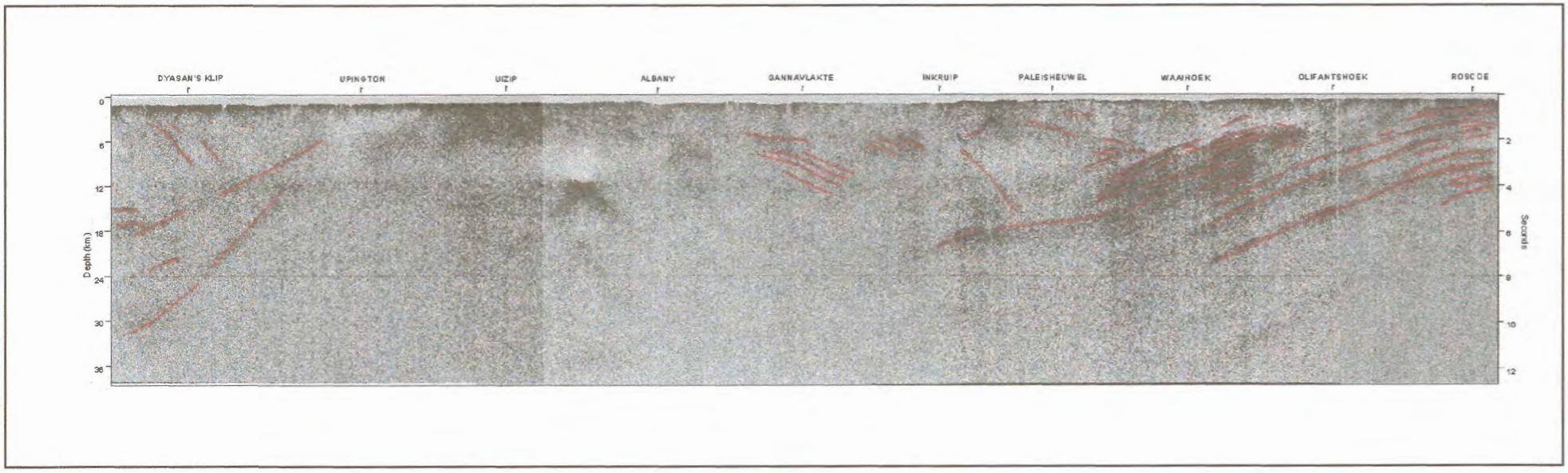

Figure 6.30. Deep reflection seismic section along the Sishen – Keimoes line.

6.8. SYNTHESIS

Considering all the geophysical interpretations we observe the following going from east to west :

(1) The westward dipping reflectors in the east correlate very well with the dense and conductive bodies present on the gravity and MT models. The top halve of the magnetic unit coincides with the dense and conductive bodies.
(2) The 2680 kg/m^3 and 6 700 ohm.m bodies west of the dense, conductive material coincide and their western edges line up with an eastward dipping reflector. We also note the absence of magnetic material in this area at greater depths.
(3) The top part of the dense body in the west correlates with highly magnetic material. At the eastern edge of the dense body, an eastward dipping lobe correlates with a similarly sloping part of the magnetic unit, conductive material and seismic reflectors.
(4) Shallow magnetic and conductive material overlap in the area between Paleisheuwel and Waaihoek.

Lense-shaped reflectors in the eastern reflective package may point to thrusting that took place at the western edge of the Kaapvaal Craton. Thrusting could result in stacking that would explain the thickness of the reflector sequence. Changes in the characteristics of the seismic, gravity and magnetotelluric data west of these reflectors are attributed to the transition to a different crustal terrane. The dense, conductive material that coincides with the reflective package therefore possibly demarcates the boundary between the Kheis Tectonic Province and the Kaapvaal Craton. This material is interpreted to be an ophiolitic sequence emplaced into an accretionary wedge that formed between the Kheis and Kaapvaal Craton during a proposed collisional event (1.75 Ga).

The eastward dipping dense, conductive material and reflectors west of the Kheis Province may similarly be accounted for by subducted seafloor material at the western edge of the Kheis Province. Very little is known about the period

between the Kheis and Namaqua events and whether accretion took place during this period. An explanation for the dense material to the west of the Kheis Terrane is that it constitutes again obducted seafloor material. The outcropping Jannelsepan ultramafic schists are probably a manifestation of this dense unit. Alternatively, these bodies may be explained by material that intruded into weak or fractured zones in the Kheis basement.

CHAPTER 7

CONCLUSIONS

7.1. COMPARISON OF DIFFERENT STATISTICAL REDUCTION TECHNIQUES

Applying different statistical reduction techniques to magnetotelluric data collected at eleven stations in the Northern Cape yielded disappointing results in many instances. The following points were noticed:

- For bad quality data, robust M-estimation and the adaptive L_p norm technique using Sposito et al's (1983) equation to calculate the value of p gave better results than L_1 -, L_2 – and adaptive L_p norm (using Money et al's (1982) equation) methods. Robust M-estimation was, however, superior in most of the cases albeit by a very small margin.
- For better quality data, all techniques gave similar results, with robust M-estimation and the adaptive L_p norm technique using Sposito et al's (1983) equation to calculate the value of p again somewhat better.
- The adaptive L_p norm method technique using Money's equation to calculate the value of p generally gave very bad results.

The effectiveness of the statistical techniques is dependent on the quality of the data. It is important to point out that the quality of the data used in the study was not always very good. Data were collected in batches between 1991 and 1998. During this period the acquisitioning system was in its main developmental phase and improvements were continuously made in an attempt to minimise electrical noise introduced by the equipment. The quality of data collected most recently (stations Albany, Uizip, Upington and Dyason's Klip) is significantly better than data collected earlier. As a consequence, statistical reduction techniques yielded better results for these stations.

7.2. COMPARISON OF MT RESULTS WITH RESULTS FROM OTHER GEOPHYSICAL METHODS

The magnetotelluric method was able to detect a conductive body that coincides with the western edge of a reflector package recorded on deep seismic reflection data. Bouguer anomaly data show a dense body at the same location. The magnetotelluric data provided valuable additional information that concurred with the other geophysical data and aided in gaining a better understanding of the geological structure of the area.

Given the high cost associated with deep reflection seismic surveys, it might be economically viable to do a magnetotelluric survey in addition to eg. gravity and magnetic surveys prior to embarking on a seismic survey. In this way areas of special interest may be identified and more intensive geophysical investigations can be localised to these areas. A magnetotelluric survey costs in the region of R10 000 a station.

ACKNOWLEDGEMENTS

I would like to thank the following people:

- Dr. C. Frick, Director of the Council for Geoscience, for permission to use MT data collected along the Sishen – Keimoes line in the case study.
- Dr. E.H Stettler of the Geophysics Business Unit for introducing me to MT and for all the valuable help and advice he has given me in order to gain a better understanding of the technique.
- Mr. Manfred Hauger for developing and continuously improving the equipment used during the MT surveys, and for numerous trips into the field to collect the data.
- P.J. Külper and I.A. van Vuuren for collecting the data.
- My mom, for all the support and encouragement and especially for giving me so many opportunities in life.
- My beloved husband Patrick, for being my inspiration.

REFERENCES

Altermann, W., Herbig, H.G., 1991. Tidal flats deposits of the lower Proterozoic Campbell Group along the southwestern margin of the Kaapvaal Craton, Northern Cape Province, South Africa: Journal of African Earth Sciences, **13**, 415-435.

Altermann, W., Siegfried, H.P., 1997. Sedimentology and facies development of an Archaean shelf: carbonate platform transition in the Kaapvaal Craton, as deduced from a deep borehole at Kathu, South Africa: Journal of African Earth Sciences, **24**, 391-410.

Bahr, K., 1988. Interpretation of the magnetotelluric impedance tensor: regional induction and local telluric distortion: J. Geophys., **62**, 119-127.

Bahr, K., 1991. Geological noise in magnetotelluric data: a classification of distortion types: Phys. Earth planet. Inter., **66**, 24-38.

Beukes, N.J., 1986. The Transvaal Sequence in Griqualand West, 819-828. *In*: Anhaeusser, C.R., Maske S. (Eds.) Mineral Deposits of Southern Africa 1, Geol. Soc. S. Afr., Johannesburg, 1020pp.

Beukes, N.J., Smit, C.A., 1987. New evidence for thrust faulting in Griqualand West, South Africa: implications for stratigraphy and the age of red beds: S. Afr. J. Geol., **90**, 378-394.

Cagnaird, L., 1953. Basic theory of the magnetotelluric method of geophysical prospecting: Geophysics, **18**, 605-635.

Chave, A.D., Thomson, D.J., Ander, M.E., 1987. On robust estimation of power spectra, coherences, and transfer functions: J. Geophys. Res., **92**, 633-648.

Claerbout, J.F., 1976. Fundamentals of geophysical data processing: McGraw-Hill Book Company, NY, 274pp.

De Villiers, P.R., Visser, J.N.J., 1977. The glacial beds of the Griqualand West Supergroup as revealed by four bore holes between Postmasburg and Sishen: Trans. Geol. Soc. S. Afr., **80**, 1-8.

Egbert,G.D., Booker, J.R., 1986. Robust estimation of geomagnetic transfer functions: Geophys. J. R. Astron. Soc., **87**, 175-194.

Ellis, R., Gulick, D., 1986. Calculus with analytic geometry, Third edition: Harcourt Brace Jovanovich Publishers, San Diego, 1059pp.

Frazier, K., 1985. Solar System: Time-Life Books, Amsterdam, 176pp.

Gamble, T.D., Goubau, W.H., Clarke, J., 1979. Magnetotellurics with a remote reference: Geophysics, **44**, 53-68.

Gosling, J.T., 1993. The solar flare myth: J. Geophys. Res., **98**, 18 937-18 949.

Gosling, J.T., McComas, D.J., 1987. Field line draping about fast coronal mass ejecta: a source of strong out-of-the-ecliptic interplanetary magnetic fields: Geoph. Res. Lett., **14**, 355-358.

Gosling, J.T., Bame, S.J., McComas, D.J., Phillips, J.L., 1990. Coronal mass ejections and large geomagnetic storms: Geoph. Res. Letters, **17**, 901-904.

Gosling, J.T., McComas, D.J., Phillips, J.L., Bame, S.J., 1991. Geomagnetic activity associated with earth passage of interplanetary shock disturbances and coronal mass ejections: J. Geophys. Res., **96**, 7831-7839.

Groom, R.W., Bailey, R.C., 1989. Decomposition of magnetotelluric impedance tensors in the presence of local three-dimensional galvanic distortion: J. Geophys. Res., **94**, 1913-1925.

Groom, R.W., Bailey, R.C., 1991. Analytic investigation of the effect of near-surface three-dimensional galvanic scatters on MT tensor decomposition: Geophysics, **56**, 496-518.

Hattingh, M., 1989. The use of data-adaptive filtering for noise removal on magnetotelluric data: Phys. Earth Planet. Inter., **53**, 239-254.

Hobbs, B.A., 1992. Terminology and symbols for use in studies of electromagnetic induction in the Earth: Surveys in Geophysics, **13**, 489-515.

Huber, P.J., 1981. Robust statistics: John Wiley and Sons Inc., New York.

Johnson, R.A., Wichern, D.W., 1998. Applied multivariate statistical analysis: Prentice Hall, New Jersey, 816pp.

Kaufman, A. A., Keller, G.V., 1981. The magnetotelluric sounding method: Elsevier Scientific Publishing Company, Amsterdam, 595pp.

Keyser, N., 1997. Geological map of the Republic of South Africa and the Kingdoms of Lesotho and Swaziland : Council for Geoscience.

Kijko, A., 1994. Seismological outliers: L_1 or adaptive L_p norm application: Bull. Of the Seismological Soc. Of America, **84**, 473-477.

Lundstedt, H., 1996. Solar origin of geomagnetic storms and prediction of storms with the use of neural networks: Surveys in Geophysics, **17**, 561-573.

Money, A.H., Affleck-Graves, J.H., Hart, M.L., Barr, G.D.I., 1982. The linear regression model: L_p norm estimation and the choice of p : Commun., Statist. – Computa., **11**, 89-109.

Moore, P., 1994. Atlas of the Universe: Reed International Books Limited, London, 272pp.

Moore, T.E., Delcourt, D.C., 1995. The geopause: Reviews of Geophysics, **33**, 175-209.

Morelli, C., Ganter, C., Honkasalo, T., McConnel, R.K., Szabo, B., Tanner, J.G., Uotila, U., Whalen, C.T., 1974, The international standardization net. 1971: Int. Assoc. Geod., Parks, 194pp.

Moritz, H., 1968, The Geodetic Reference System (1967): Allgem. Vermessungs-Nachrichten, 2-7.

Nelder, J.A., Mead, R., 1965. A simplex method for function minimization: Computer Journal, **7**, 308-312.

Press, W.H., Teukolsky, S.A., Vetterling, W.T., Flannery, B.P., 1992. Numerical recipes in C : The art of scientific computing : Cambridge University Press, Cambridge, 994 pp.

Pulkinnen, T.I., Baker, D.N., 1997. Global substorm cycle: what can the models tell us? : Surveys in Geophysics, **18**, 1-37.

Reddy, I.K., Rankin, D., 1974. Coherence functions for magnetotelluric analysis: Geophysics, **39**, 312-320.

Reid, G.C., 1964. A diffusive model for the initial phase of a solar proton event: J. Geophys. Res., **69**, 2659-2667.

Reitz, J.R., Milford, F.J., Christy, R.W., 1979. Foundations of electromagnetic theory: Addison-Wesley Publishing Company, Massachusetts, 534pp.

Sheeley, N.R., Howard, R.A., Koomen, M.J., Michels, D.J., Schwenn, R., Muhlhauser., K.-H., Rosenbauer, H., 1985. Coronal mass ejections and interplanetary shocks: J. Geophys. Res., **90**, 163-175.

Sims., W.E., Bostick, F.X. Jr., Smith, H.W., 1971. The estimation of magnetotelluric impedance tensor elements from measured data: Geophysics, **36**, 938-942.

Snyder, C.W., Neugebauer, M., Rao, U.R., 1963. The solar wind velocity and its correlation with cosmic-ray variations and with solar and geomagnetic activity: J. Geophys. Res., **68**, 6361-6370.

Spies, B.R., Eggers, D.E., 1986. The use and misuse of apparent resistivity in electromagnetic methods: Geophysics, **51**, 1462-1471.

Sposito, V.A., Hand, M.L., Skarpness, B., 1983. On efficiency of using sample kurtosis in selecting optimal L_ρ estimators: Commun. Statist. – Computa., **12**, 265-272.

Sutarno, D., Vozoff, K., 1989. Robust M-estimation of magnetotelluric impedance tensors: Expl. Geophys., **20**, 383-398.

Sutarno, D., Vozoff, K., 1991. Phase-smoothed robust M-estimation of magnetotelluric impedance functions: Geophysics, **56**, 1999-2007.

Swift, C.M. Jr., 1986. A magnetotelluric investigation of an electrical conductivity anomaly in the southwestern United States: *In* Magnetotelluric Methods, Ed. by K. Vozoff : Society of Exploration Geophysicists, 763pp.

Telford, W.M., Geldart, L. P., Sheriff, R.E., Keys, D.A., 1976. Applied geophysics: Cambridge University Press, Cambridge, 860pp.

Tikhonov, A.N., 1950. Determination of the electrical characteristics of the deep strata of the Earth's Crust: Dok. Akad. Naut., USSR, **73**, 295-297.

Tsurutani, B.T., Gonzalez, W.D., 1992. Tweaking the magnetosphere: Nature, **358**, 26.

Visser, D.J.L., 1989. Explanation: 1:1 000 000 geological map, Fourth edition,1984. The geology of the Republics of South Africa, Transkei, Bophuthatswana, Venda, Ciskei and the Kingdoms of Lesotho and Swaziland: Government Press, 494 pp.

Vozoff, K., 1972. The magnetotelluric method in the exploration of sedimentary basins: Geophysics, **37**, 98-141.

Walpole, R.E., Myers, R.H., 1989. Probability and statistics for engineers and scientists: Macmillan Publishing Company, New York, 765pp.

Young, H.D., 1962. Statistical treatment of experimental data: McGraw-Hill Book Company Inc., New York, 172pp.

Zhang, Y., Paulson, K.V., 1997. Enhancement of signal-to-noise ratio in natural source transient magnetotelluric data with wavelet transform: Pure appl. Geophys., **149**, 405-419.

Appendix A

PROVE THAT $\frac{1}{\sqrt{i}} = e^{-\frac{i\pi}{4}}$

$$\frac{1}{\sqrt{i}} = \sqrt{\frac{i}{i \cdot i}} = \sqrt{-i} = \sqrt{\frac{-2i}{2}} = \sqrt{\frac{(1-i)(1-i)}{2}} = \frac{1}{\sqrt{2}} \cdot (1-i) = \frac{1}{\sqrt{2}} - \frac{i}{\sqrt{2}}$$

$$= \cos\frac{\pi}{4} - i\sin\frac{\pi}{4}$$

$$= e^{\frac{-i\pi}{4}}$$